Advanced Light Source

Activity Report 2006

July 2007

Ernest Orlando Lawrence Berkeley National Laboratory | University of California | Berkeley, California, 94720 | LBNL-62841

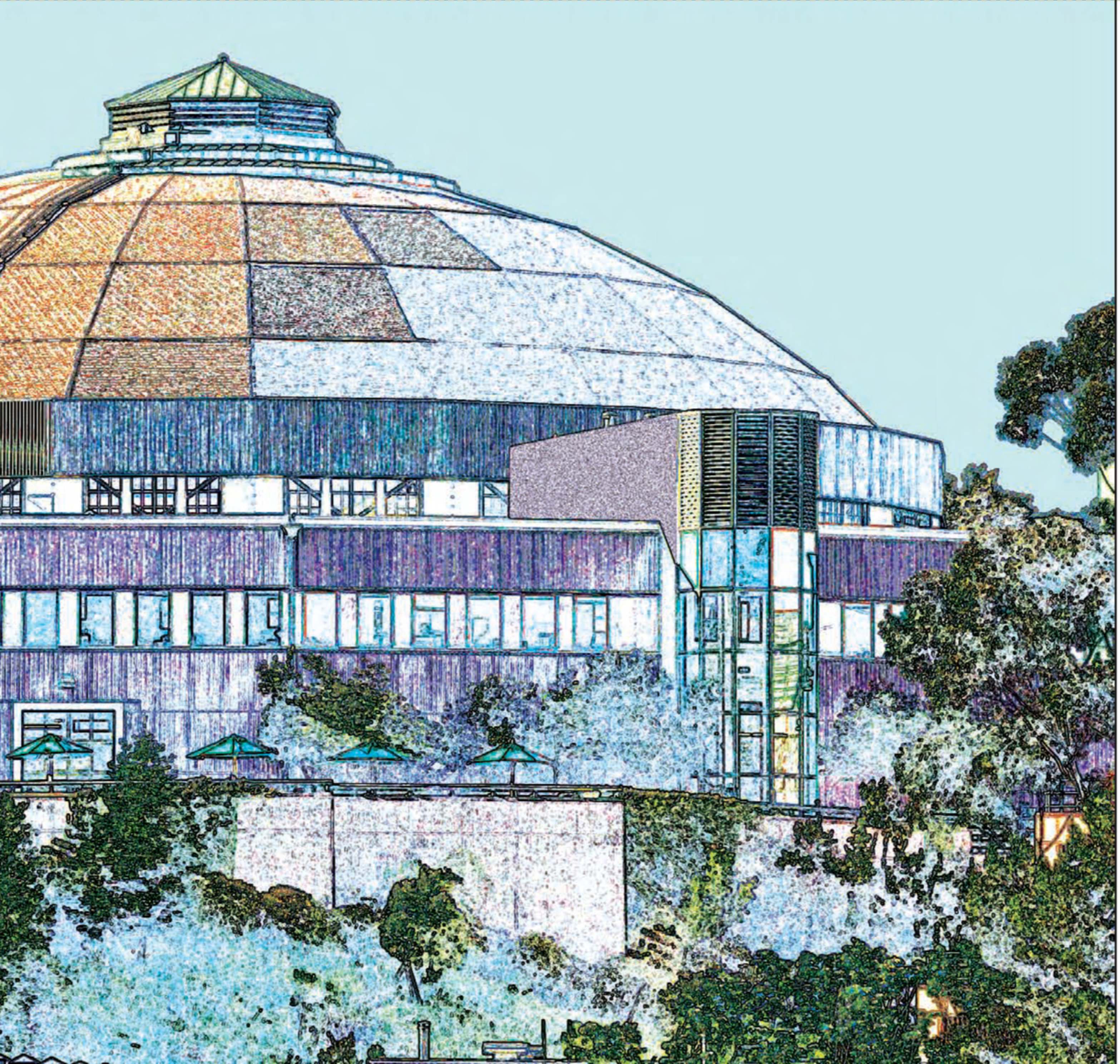

Editors:
Lori Tamura
Arthur Robinson
Elizabeth Moxon
Julie McCullough

Design, layout, photography, and additional writing provided by the Creative Services Office and the Communications Department of Berkeley Lab's Public Affairs Department.

The editors gratefully acknowledge the ALS users and staff for their contributions, advice, and patience.

Available to DOE and DOE Contractors from the Office of Scientific and Technical Communication, P.O. Box 62, Oak Ridge, TN 37831. Prices available from (615) 576-8401.

Available to the public from the National Technical Information Service, U.S. Department of Commerce, 5285 Port Royal Road, Springfield, VA 22161.

Advanced Light Source

Activity Report 2006

July 2007

Ernest Orlando Lawrence Berkeley National Laboratory | University of California | Berkeley, California, 94720 | LBNL-62841

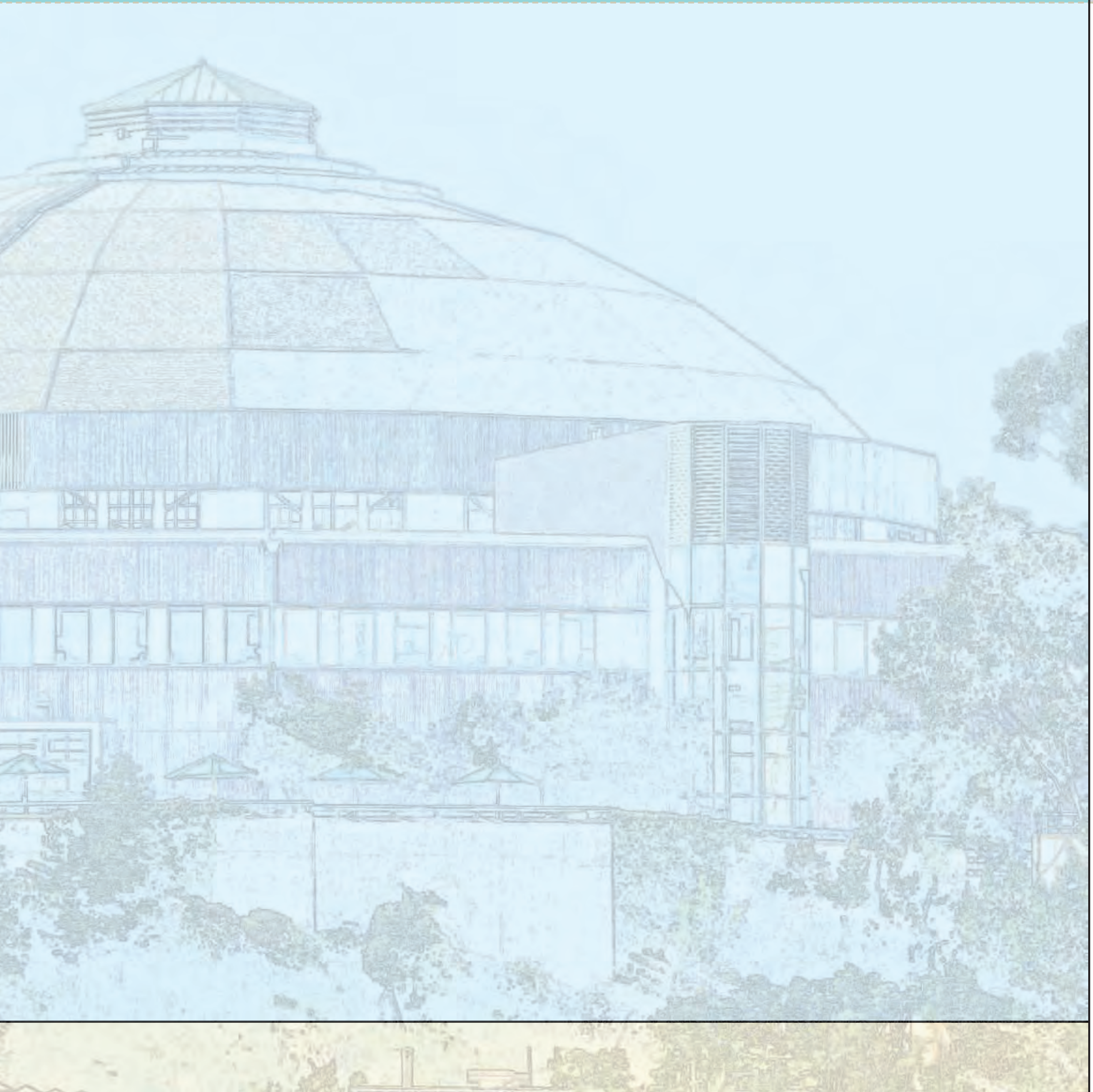

TABLE OF CONTENTS

WELCOME

Roger Falcone, ALS Director

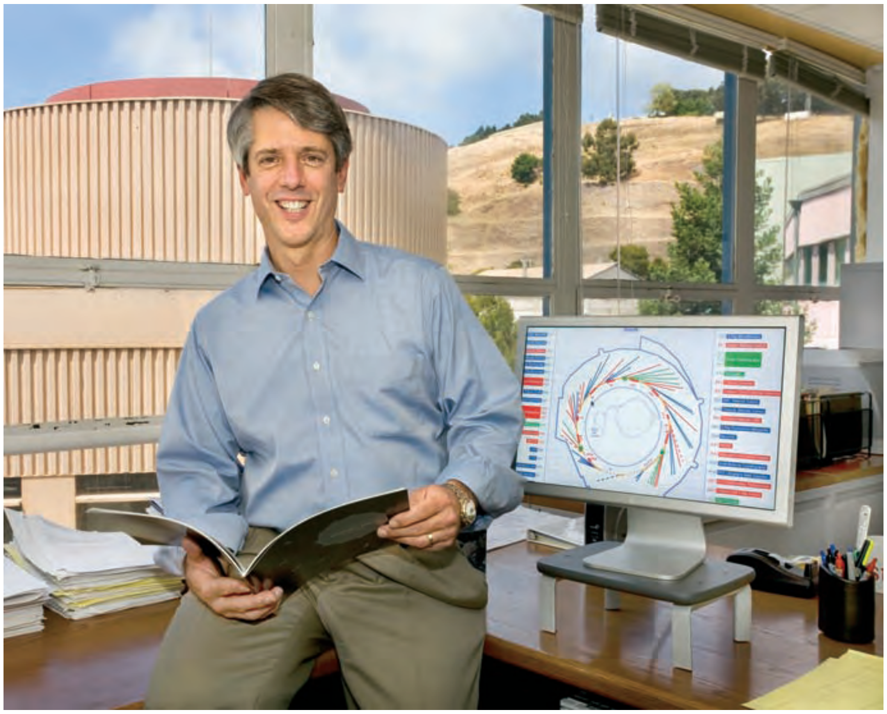

The ALS is a very dynamic facility, and the year 2006 continued a recent period of transition. In September, I moved from being an ALS user to being the ALS director, taking over from Janos Kirz. Janos served brilliantly as acting director, following Daniel Chemla, who stepped down from the directorship in July 2005. Both Janos and Daniel made enormous contributions to operations as well as planning at the ALS, and I look forward to building on their work in creating a vision for renewal of our light source. Fortunately, Janos has agreed to continue serving users of the ALS as our scientific advisor.

In August, we lost a dear friend and colleague, Neville Smith, to cancer. Neville was the ALS scientific director and had been with the ALS since 1994. His death was a shock, not just to the synchrotron community, but also to the larger scientific community, which knew him both as an authority in the field of photoemission and as a wise and warm colleague. He will be greatly missed.

Neville, Daniel, and Janos worked with users, ALS staff, and our advisory committees to craft a roadmap—a living document we call the ALS Strategic Plan (http://www-als.lbl.gov/als/ourorg/strategicplan.html). We will be guided by that creative plan, building on it as the needs of the facility evolve and we develop the financial and other resources necessary to enact it.

Our 2006 Users' Meeting was a great success in bringing together a diverse community of scientists from around the world, and I want to thank the Users' Executive Committee and especially the program chairs, Elke Arenholz and Hendrick Ohldag, for an excellent job of organizing it all. The meeting included 12 special workshops, an evening public science lecture, and a number of science highlights.

The future of the ALS includes the renewal and expansion of our technical capabilities and scientific goals as well as our physical environment. We are making progress on plans for a new user support building and a guest house. Expanded support from Washington is enabling us to hire new beamline scientists, as well as other ALS staff, to assist our ever-growing pool of users with their diverse studies, which range from understanding the structure of proteins and nanocrystals, to high-temperature superconductors and magnetic storage devices, to dust from space and aerosols that blow across the ocean and affect our weather. Plans have been made for new beamlines—which will, for example, probe electronic structure and image at the nanoscale—and for replacement of aging optics, electronics, and other hardware. We are moving forward rapidly to keep the ALS at the scientific frontier and serve the needs of researchers in wide-ranging fields. We are also augmenting our environmental, health, and safety activities, consistent with our mission, which is to "support users in doing outstanding science in a safe environment."

ALS UEC 2006 REVIEW

Clemens Heske, UEC Chair

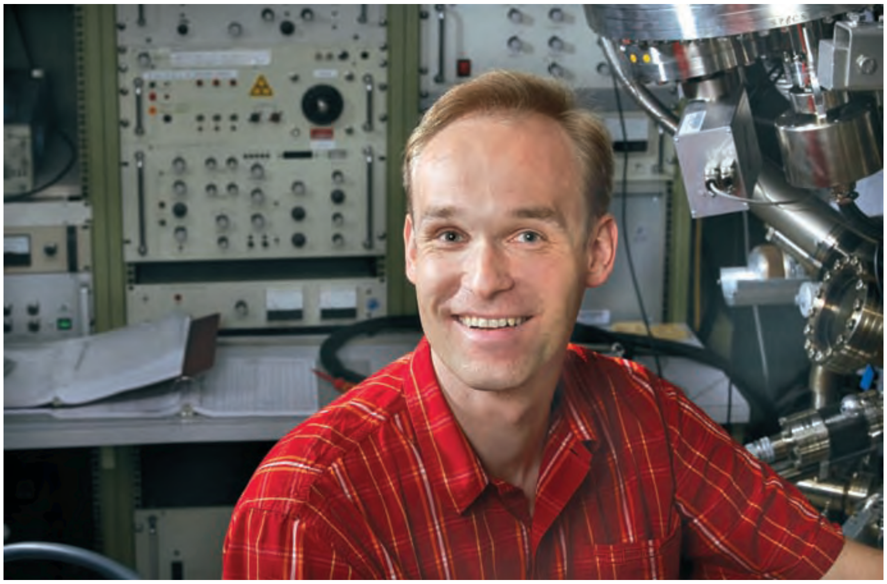

The ALS Users' Executive Committee (UEC) represents an ever-growing number of ALS users, and it has been my pleasure to serve as the 2006 UEC chair. The UEC not only very closely interacts with ALS management, but also represents ALS users to external visitors and reviewers and to various groups on Capitol Hill. In all of these capacities, the UEC addresses a large variety of topics and issues, ranging from facility access, safety regulations, user housing, ALS upgrades and parking to congressional support for DOE facilities and the general perception of basic science as a driver for future development in general.

And quite an eventful year it has been!

Several developments are now well underway that will significantly improve the "quality of life" for users at the ALS. In particular the User Guest House and the User Support Building are moving along nicely, thanks to the tireless efforts of Ben Feinberg, Steve Rossi, and especially Gary Krebs, who sadly passed away shortly before this report went to press in 2007. Safety and safety regulations have been a big topic in the past year, and the UEC has worked very closely with ALS management to ensure that the ALS and its users continue to operate in a safe and common-sense-based fashion. Jim Floyd has done an excellent job in implementing many improvements, including a revision of the safety training structure and many other important procedural aspects.

2006 was also the year of the unexpected and sad passing of our friend and colleague Neville Smith. He worked very closely with the UEC and had tremendous impact on all areas of user involvement at the ALS. At the 2006 Users' Meeting, "Bruce" was remembered with a special symposium and banquet session, and will remain very close to our hearts and thoughts.

The UEC-organized 2006 ALS Users' Meeting, put together by Elke Arenholz and Hendrik Ohldag with the help of Jeff Troutman and his outstanding team, was a great success, with exciting plenary sessions and jam-packed workshops.

2006 was also the year of change in leadership at the ALS. On behalf of the users at the ALS, I would like to express my sincere gratitude to Janos Kirz for his outstanding leadership at the ALS, and would also like to heartily welcome Roger Falcone as the new director. Both Janos and Roger have always surprised me with the intensity with which they were seeking the input and opinions of the users and the UEC.

Finally, 2006 was also the year of significant budget changes for the Office of Science. The UEC has played a humble, but active role in all of the activities that surround such developments, through email requests, personal visits, and—new in 2006—the installation of a permanent representative at the Synchrotron and Neutron Users' Group (SNUG), which coordinates group visits to Washington (Corie Ralston, cyralston@sff.net).

At the end of my tenure as UEC chair, I want to thank you for your support and help and ask you to work closely with Tony van Buuren (2007 UEC chair) and Hendrik Ohldag (2007 UEC vice chair) to ensure that the ALS continues to be an outstanding facility for synchrotron radiation science worldwide.

Science Highlights

Cometary Clues to Solar System Formation

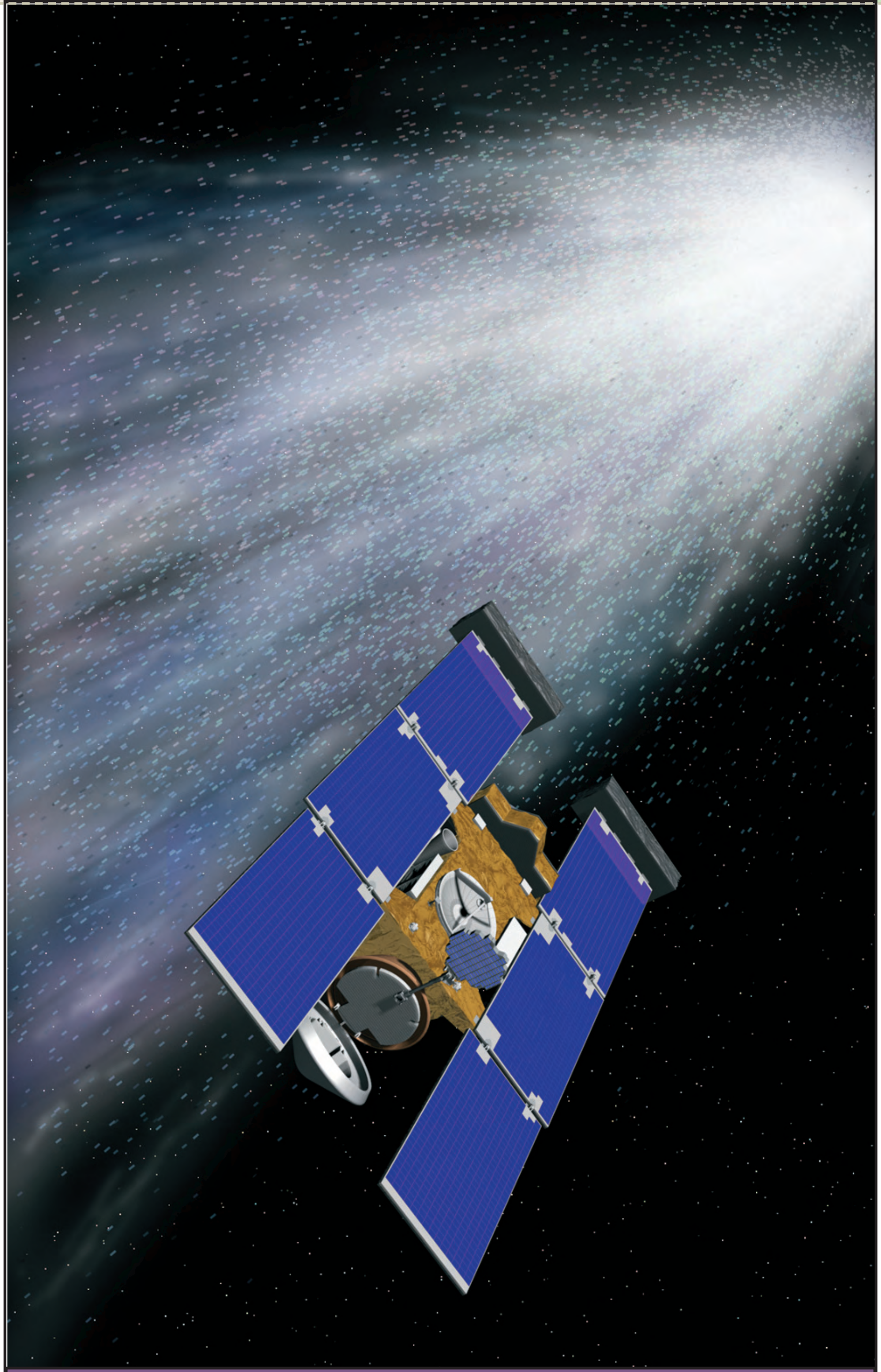

Particles from Comet 81P/Wild 2 Viewed by ALS Microscopes

Comets are widely believed to be the repositories of the building blocks of the Solar System. Astronomers theorize that a presolar dust cloud, perhaps after nudging by an outside shockwave, gradually collapsed under its own gravity to form a glowing star surrounded by an accretion disk, where protoplanets took shape. In them the constituents of the dust were subjected to heat and pressure and reactions with water, leading ultimately to the formation of planets. But comets that formed far from the Sun were believed to have preserved the original constituents of the Solar System in relatively unaltered form. In January 2006, the sample-return capsule from NASA's $200-million, seven-year-long Stardust mission to Comet 81P/Wild 2 parachuted to the Utah desert delivering the first solid samples from space since the 1970s moon missions. Hundreds of scientists and dozens of experimental techniques in facilities around the world contributed to the preliminary examination of the first samples. Four

ALS beamlines and the researchers using them contributed to many of the findings that are shedding new light on how the Solar System was formed. The Stardust results show that the mixing of materials throughout the disk started earlier in this process and was more extensive than previously thought.

FIGURE 1. Billows of exhaust fill Launch Pad 17-A, Cape Canaveral Air Station, as the Boeing Delta II rocket carrying the Stardust spacecraft launches at 4:04 P.M. EST, February 7, 1999. Image Credit: NASA.

Materials brought back from a known extraterrestrial source, such as the Apollo samples from the Moon in the 1970s, provide critical clues to the history of the Solar System and interpretation of extraterrestrial samples like meteorites and cosmic dust particles. When NASA's $200-million, seven-year-long Stardust mission returned to Earth thousands of tiny particles snagged from the coma of comet 81P/Wild 2, four ALS beamlines and the researchers using them were among the hundreds of scientists and dozens of experimental techniques in facilities around the world that contributed to the preliminary examination of the first samples.

Stardust's success depended on two technical achievements, a trajectory allowing it to pass within 240 km of the comet's nucleus at a speed of just 6 km/s (see sidebar, "NASA's Discovery Mission Stardust") and a special low-density material called aerogel molded into a collector grid (see sidebar, "Aerogel Cushions the Comet Particle Impact"). Particles were brought to a standstill as they penetrated into the aerogel with limited heating or alteration. Thousands of tiny particles were trapped, most of them smaller than 10 micrometers in size. The trails of perhaps two dozen larger particles are visible to the unaided eye. Stardust also collected interstellar dust samples.

After its launch in 1999 (Figure 1), Stardust reached the comet in 2004 (Figure 2), then returned its cargo to Earth in a capsule on January 15, 2006. At NASA's Johnson Space Center in Houston, a few of the captured particles were quickly distributed for inspection by multi-institutional preliminary examination teams (PETs) across the United States. Before any of these high-powered tools could be deployed, the samples had to be removed from the aerogel. Wedges called "keystones" containing complete tracks and the terminal particles at their tips were removed under a

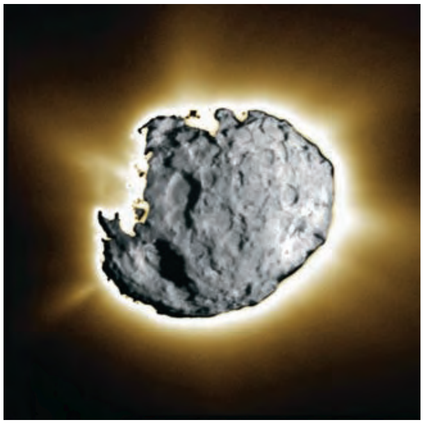

FIGURE 2. Composite image taken by Stardust's navigation camera during the close-approach phase of the January 2, 2004, flyby of comet Wild 2. Several large depressed regions can be seen. Comet Wild 2 is about five kilometers (3.1 miles) in diameter. To create this image, a short-exposure image showing considerable surface detail was overlaid on a long-exposure image taken just 10 seconds later showing jets. Together, the images show an intensely active surface, jetting dust and gas streams into space and leaving a trail millions of kilometers long. Image Credit: NASA/JPL-Caltech.

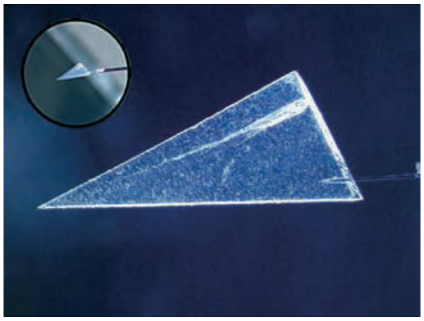

FIGURE 3. One of several ways scientists have begun extracting comet particles from the Stardust spacecraft's collector. First, a particle and its track are cut out of the aerogel collector material in a wedge-shaped slice called a keystone. A specialized silicon pickle fork is then used to remove the keystone from the remaining aerogel for further analysis. Image credit: NASA/JPL-Caltech/UC Berkeley.

microscope with the help of computer-driven micromanipulators that sliced the aerogel with glass needles, a technique pioneered at UC Berkeley's Space Sciences Laboratory (Figure 3). In some cases, slices were cut through the track at right angles.

Upon entering the aerogel, the particles typically excavated a carrot-shaped track, bulbous at the top and thinning to a point. The particles themselves mostly came to rest at this point, but on the way in, depending on its makeup, a particle might shatter and leave multiple tracks (Figure 4). They also shed outer layers and—because the collision and deceleration generated lots of heat—vaporized some of their more volatile components.

Synchrotron radiation facilities were major contributors to the findings of the various PETs. These included the four DOE light sources (ALS, APS, NSLS, and SSRL), the European Synchrotron Radiation Facility (ESRF), and SPring-8 in Japan. At the ALS, measurements were made at four beamlines: 1.4.3, 5.3.2, 10.3.2, and 11.0.2.

Minerals were the main target of studies at Beamline 10.3.2. The team used a combination of three spatially resolved techniques for mapping the bulk chemistry and mineralogy of the Wild 2 samples. With the x-ray microprobe, one can observe the whole track, still in the aerogel keystone, and look for all elements simultaneously, everything from sulfur up to selenium that may be present at each specific spot. Maps showing the spatial distribution and concentration of single elements (Figure 5) or multiple elements (Figure 6) result from scanning the probe over the sample surface. It is important to be able to distinguish which particles are from the comet and which from the aerogel. In Figure 6, particle 2 contains iron, calcium, titanium, and manganese. Calcium and titanium are elements that tend to occur together in the sort of high-temperature minerals that have attracted interest because their existence shows that material from the inner Solar System became incorporated into a comet formed in the outer Solar System. The bright blue spot (particle 3) contains calcium and little or no manganese or titanium; it is aerogel contaminant.

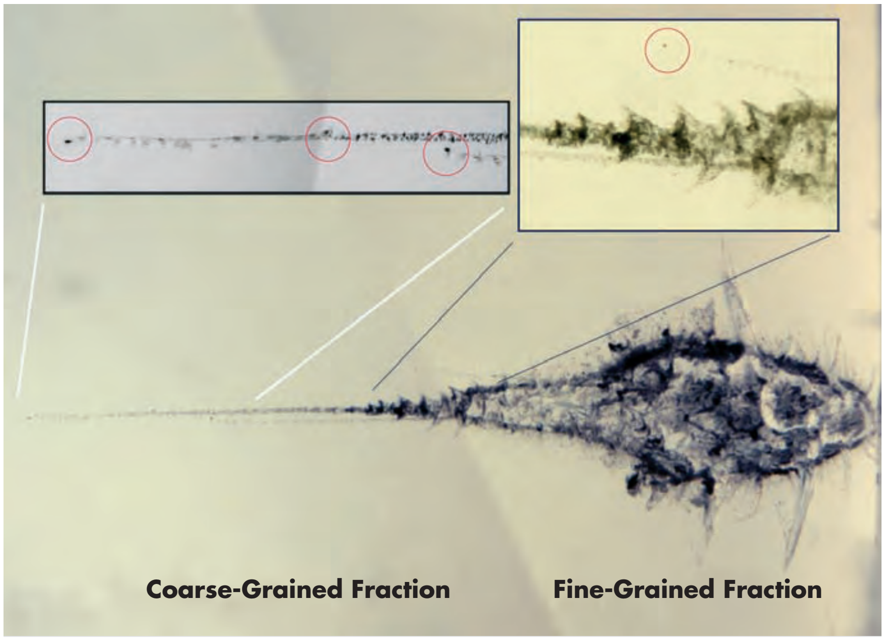

FIGURE 4. Aerogel tracks. When a particle hits the aerogel, it buries itself in the material, creating a carrot-shaped track up to 200 times its own length as it slows down and comes to a relatively gradual stop. Scientists use these tracks to find the tiny particles. Image credit: S. Sandford, NASA-Ames Research Center.

By means of x-ray absorption near-edge spectroscopy (XANES) and the related technique of extended x-ray absorption fine structure (EXAFS)

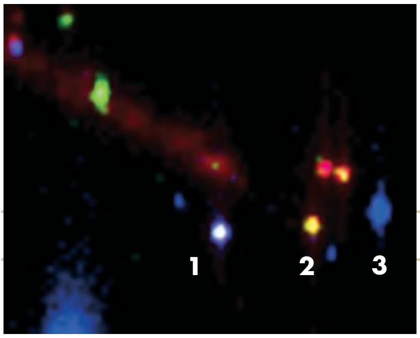

FIGURE 6. The problem: Which spots from x-ray microfluorescence maps are really from the comet? In this close-up of the "trapezium" region, titanium is mapped in red, manganese in green, and calcium in blue. Particle 2 in these pictures contains iron, calcium, titanium, and manganese and comes from the comet. The bright blue spot (particle 3) contains calcium and little or no manganese or titanium; it is aerogel contaminant. Note that the vertical "wings" on the brightest spots are artifacts of the microprobe. Image credit: S. Fakra and M. Marcus, ALS.

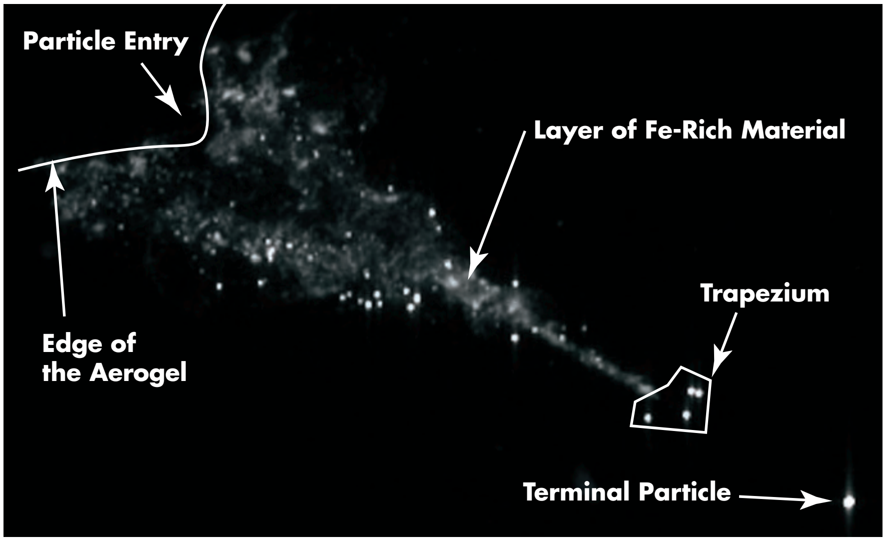

FIGURE 5. X-ray microprobe image of iron in comet particle track. The solid line is the edge of the aerogel collector. The diffuse-looking layer of iron-rich material consists of many nanosize particles of metals and metal sulfides, mixed with melted aerogel, coating the hollow interior of the track. The four particles in the trapezium are all of different compositions (see Figure 6). The terminal particle is the remaining large chunk of particle. Image credit: S. Fakra and M. Marcus, ALS.

spectroscopy, one can also determine the atomic environment of specific elements. For example, one mineral found in the material brought back by Stardust was olivine, a mixed iron–magnesium silicate that is a primary component of the green sand found on some Hawaiian beaches. It is among the most common minerals in the universe, but scientists were surprised to find it in cometary dust. The Wild 2 samples also had other high-temperature materials containing calcium, aluminum, and titanium.

One form of mineral that challenged the mineralogy team at Beamline 10.3.2 took the form of calcium–aluminum inclusions. The problem was that many other calcium-rich particles were found in the aerogel by x-ray microprobe mapping that were not from the comet. These particles could be distinguished from comet particles by the chemical state of the calcium they contained, as determined by XANES when using as spectral references particles found outside the tracks and therefore known to be extraneous. (Figure 7).

Because XANES yields a distinctive spectral signature for each chemical constituent in a sample, it is particularly useful for identifying organic compounds. At Beamlines 5.3.2 and 11.0.2, it was possible to combine this technique with the scanning transmission x-ray microscope (STXM) to image the spatial distribution of the compounds with high resolution (Figure 8).

Once again, aerogel contamination was a major issue, with carbon being the bad actor in this case. The supposedly pristine silica aerogel tiles had either become contaminated during the manufacturing process, or microtomed slices of the particles themselves had become contaminated with carbon compounds from being embedded in epoxy. The team had to sort out what carbon came from the aerogel, what came from epoxy, what came from the comet.

The breakthrough came when team

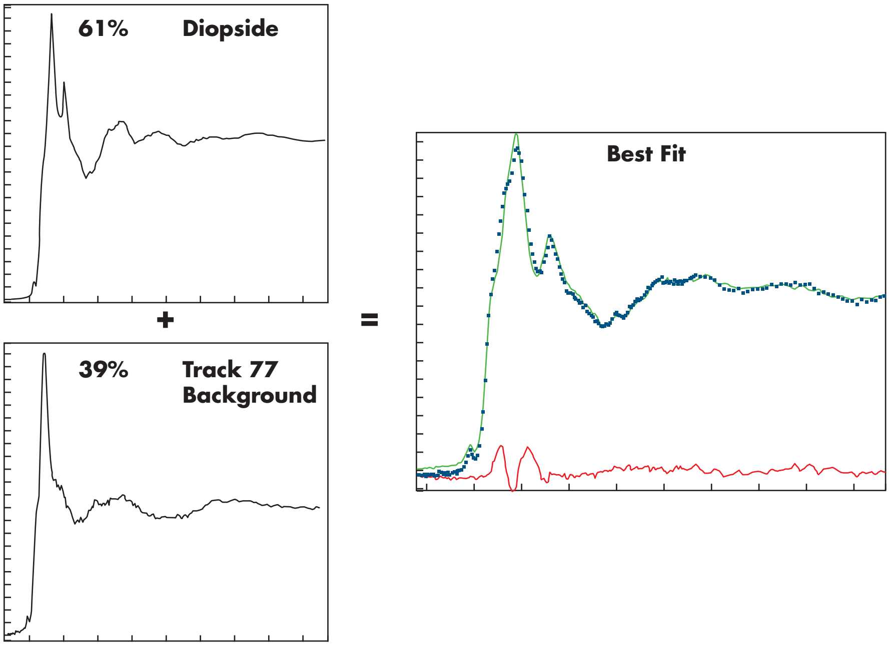

FIGURE 7. Calcium XANES best-fit process applied to particle 1 in Figure 6. XANES spectra of known contaminants, such as calcium hotspots in blank aerogel, can be used as fingerprints to recognize XANES spectra of other contaminant spots. Such spectra are also needed for the analysis of "real" calcium-bearing spots because the beam also hits aerogel. Image credit: M. Marcus, ALS.

members were able to examine transverse slices through the track, with cometary fragments inside it and a diffusion of volatile constituents into the neighboring aerogel, and then distinguish these signals from the aerogel far outside the track. Since the beamline can look at most elements, including silicon, researchers were able to correlate silicon with carbon in the aerogel. Carbon in the samples that wasn't correlated with silicon was not coming from the aerogel.

Infrared (IR) spectroscopy was expected to be useful for comparing the Wild 2 particles to astronomical observations of comets and interstellar dust, where minerals like crystalline silicates and organic compounds have been revealed using ground- and space-based telescopes for IR spectroscopy. Initially it was planned to do IR microspectroscopy at Beamline 1.4.3 only on the terminal particles. Initial IR measurements made of aerogels not used on Stardust had shown organic residue from the aerogel fabrication, initially killing any hope for detecting organics.

But after comparing those measurements to Stardust aerogels that had actually seen the comet, the IR team noticed different types of carbon–hydrogen molecules present along some of the particle tracks. Then, looking not just at the terminal particle but instead scanning the IR beam along the whole length of the track in the aerogel wedges, they found the track coated with different organics, left behind when whatever was carrying them—ice, for example—melted and vaporized.

It was because the aerogel slowed the particles relatively gently that team members were able to capture volatile organics along most of the length of the track and do IR imaging at each point. Building up a two-dimensional image of the different organics at different stages of entry (Figure 9), they found the distribution of organics to be nonuniform along the tracks. Not every track showed organics, but all showed OH bonds: oxygen–hydrogen bonds indicating the former presence of ice.

Taken together, the early analyses of the comet dust particles surprised scientists, who have long thought of comets as cold, billowing clouds of ice, dust, and gases formed on the edges of the Solar System. From the

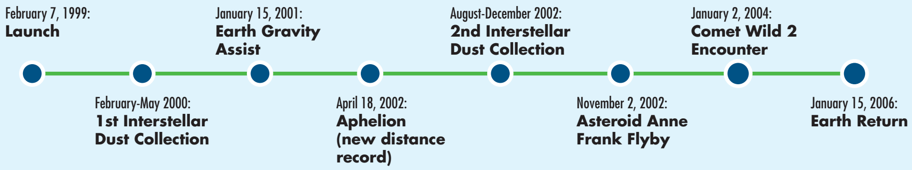

Figure 1. Stardust timeline.

NASA's Discovery Mission Stardust

In the early 1990s, NASA established the Discovery program aimed at low-cost Solar-System-exploration missions with highly focused science goals. Following on the heels of Mars Pathfinder, the Near Earth Asteroid Rendezvous, and the Lunar Prospector, the Stardust mission was selected in late 1995 to be the fourth Discovery mission and was the first U.S. mission dedicated solely to a comet and the first to return extraterrestrial material from outside the orbit of the Moon.

The Stardust spacecraft was launched on February 7, 1999, from Cape Canaveral Air Station, Florida, aboard a Delta II rocket. The primary goal of Stardust was to collect dust and carbon-based samples during its closest encounter with Comet Wild 2—pronounced "Vilt 2" after the name of its Swiss discoverer—in a rendezvous scheduled to take place in January 2004, after nearly four years of space travel (Figure 1). The Stardust spacecraft was also to bring back samples of interstellar dust, including recently discovered dust streaming into the Solar System from the direction of Sagittarius. Believed to consist of ancient presolar interstellar grains that include remnants from the formation of the Solar System, interstellar dust samples were expected to yield important insights into the evolution of the Sun, its planets, and possibly even the origin of life itself.

During its voyage, the spacecraft made three loops around the Sun (Figure 2). The seven-year, three-loop, Earth-gravity-assist trajectory was designed with four goals in mind: to fly by Wild 2 at a low velocity, to maximize the time for favorable collection of interstellar dust, to minimize the escape energy from Earth and trajectory correction requirements for the mission so that a smaller launch vehicle could be used, and to have a low velocity relative to Earth upon return.

On the second loop, the spacecraft trajectory passed close to comet Wild 2. During the meeting, Stardust recorded counts of comet particles encountered and made real-time analyses of the compositions of these particles and volatiles. A collector array containing a silica-based substance called aerogel enabled Stardust to capture samples and safely store them for the long journey back to Earth. On January 15, 2006, Stardust executed a precise cargo return by parachuting a reentry capsule weighing approximately 125 pounds to the Earth's surface.

Throughout the course of the entire mission up to that point, Stardust had flown a total of 5.2 billion kilometers (3.2 billion miles). In early 2007, however, communications were resumed with the spacecraft to determine its health for a follow-on mission to the comet Tempel 1. After extracting all the recorded data from a year's worth of space travel, including a close approach to the sun and an encounter with a solar flare, NASA placed the spacecraft in hibernation until the final decision is made concerning a possible Stardust-NExT follow-on mission, an encounter with the comet Tempel 1 in 2011 to image the crater made by the Deep Impact mission.

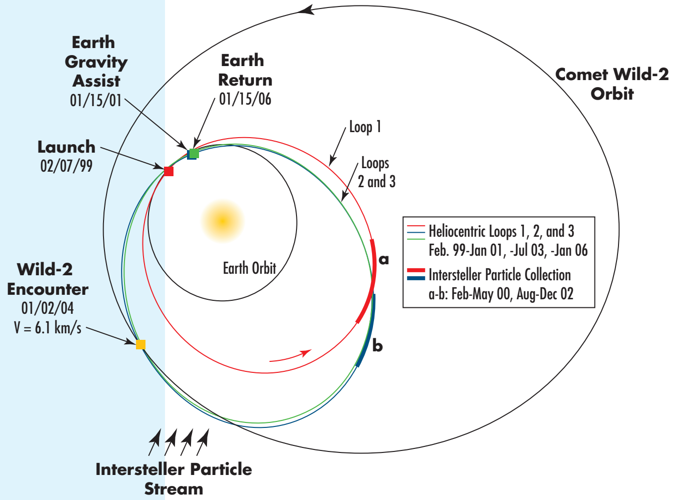

Figure 2. Trajectory of the Stardust spacecraft. Image credit: NASA/JPL-Caltech.

SOURCES

"Stardust: Mission to a comet—mission overview," www.nasa.gov/mission_pages/stardust/mission/index.html and related links.

"Stardust: NASA's comet sample return mission—mission overview," stardust.jpl.nasa.gov/mission/index.html and related links.

A. Chevront, "Stardust: Mission news—Stardust status report," www.nasa.gov/mission_pages/stardust/news/stardust-20070201.html.

Figure 1. An aerogel tile of the type used in the Stardust collector. Though having a ghostly hologram-like appearance, aerogel is very solid. To the touch, it feels as hard as styrofoam. Image credit: NASA.

Aerogel Cushions the Comet Particle Impact

The Stardust mission captured both cometary samples and interstellar dust. To collect the high-speed particles without damaging them, Stardust used an extraordinary substance called aerogel, a silicon-based solid with a porous, sponge-like structure that is 99.8 percent empty space. When a particle hits the aerogel, it buries itself in the material, creating a carrot-shaped track up to 200 times its own length as it slows down and comes to a relatively gradual stop. Scientists use these tracks to find the tiny particles.

It is often assumed that aerogels are recent products of modern technology. In reality, the first aerogels were prepared in 1931. Of the many scientists who have worked with aerogels since then, all of them owe a debt of gratitude to Samuel Stephens Kistler, a scientist at the University of the Pacific who prepared the first aerogels and spent decades studying their properties and uses.

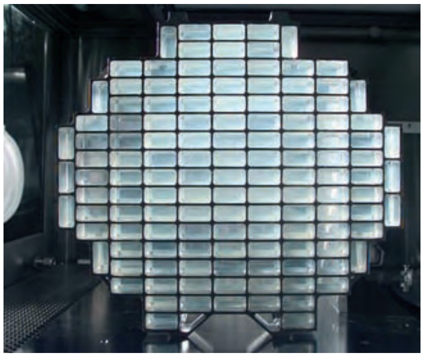

Figure 2. Aerogel array. The Stardust particle collector consisted of 260 tiles of aerogel, 130 on each side of a tennis-racket-shaped grid. One side was exposed during Stardust's flight through the interstellar dust stream between February and May 2000 and August and December 2002; the other collected cometary particles during the spacecraft's flight through Wild 2's coma on January 2, 2004. Image credit: NASA.

Aerogel is not like conventional foams; it has extreme microporosity on a micron scale. Individual features only a few nanometers in size are linked in a highly porous network-like structure. Aerogel is up to 1,000 times less dense than glass, and it is nearly transparent (unless deliberately dyed), with only a slight blue-grey tinge making it visible. When held, it feels nearly weightless but unmistakably solid and unyielding (Figure 1).

This exotic substance has many unusual properties, notably low thermal conductivity, in addition to its exceptional ability to capture fast-moving dust. Aerogel is made by critical-point drying at high temperature and pressure a gel composed of colloidal silica filled with solvents. For Stardust, the aerogel was prepared and flight qualified at the Jet Propulsion Laboratory (JPL).

For the Stardust mission, tiles of aerogel were fitted into a tennis-racket-shaped collector that was unfolded from the protective sample-return capsule to expose it during space flight (Figure 2). One side of the collector turned to face the streams of interstellar dust encountered during the journey to Comet Wild 2, while the other faced towards the cometary particles as the spacecraft passed through the coma surrounding the nucleus.

To capture both types of particles, JPL had to produce different types of aerogel for each side of the collector: heavier and denser aerogel on the cometary side subject to bombardment by relatively large grains, some even visible to the naked eye, and lighter, more porous aerogel on the interstellar dust side, where the particles would be no more than a few microns in diameter. Even more challenging, the aerogel tiles had to be of varying density: very light and porous on the surface of the collector, but increasingly dense towards the back.

When the Stardust spacecraft encountered Comet Wild 2, the impact velocity of the particles was up to six times the speed of a rifle bullet. This high-speed capture could alter their shape and chemical composition—or even vaporize them entirely. But as particles struck the collector, the aerogel absorbed them like a cushion of feathers and brought them to a halt within the space of a few dozen microns (in the case of interstellar dust), or just 1 or 2 centimeters (in the case of the cometary particles).

SOURCES

A. Alexander, "Aerogel: The 'frozen smoke' that made Stardust possible," www.planetary.org/programs/projects/stardustathome/aerogel.html (November 8, 2006).

"Aerogel: Catching comet dust," stardust.jpl.nasa.gov/tech/aerogel.html (last updated March 31, 2005).

A. Hunt and M. Ayers, "History of silica aerogels," eetd.lbl.gov/ECS/aerogels/sa-home.html (last updated April 2004).

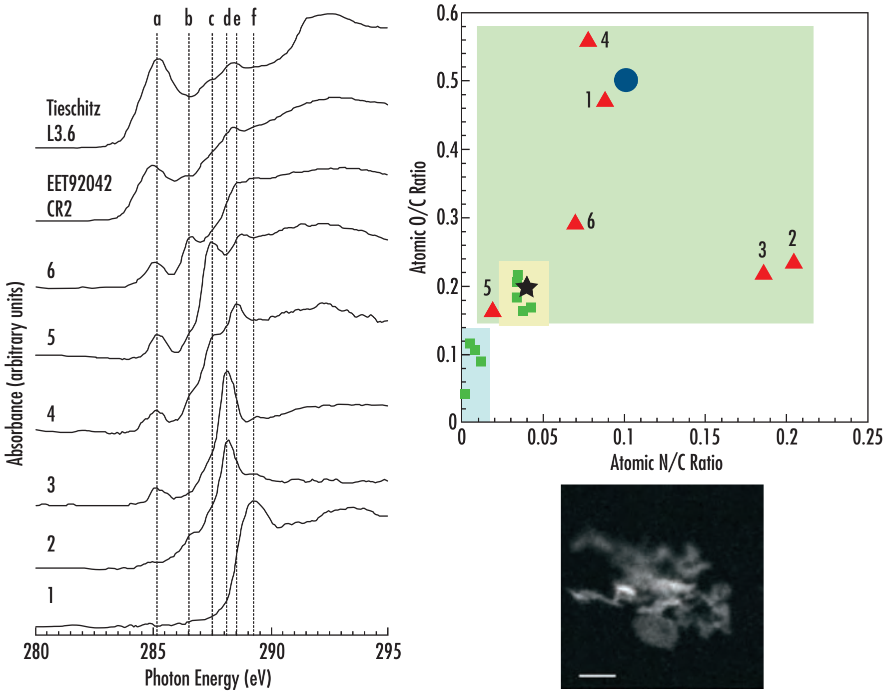

FIGURE 8. Left: Carbon XANES spectra of six thin-section samples (1 to 6) compared with spectra of primitive (EET92042, CR2) and moderately processed (Tieschitz, L3.6) chondritic organic matter. Samples represent various tracks and grains. Specific organic functional groups are highlighted by dashed lines: a) C=C, b) C=C–O, c) C=O, d) N–C=O, e) O–C=O, and f) C–O. Top right: Atomic oxygen/carbon and nitrogen/carbon ratios for samples 1 to 6 from C, N, and O XANES analysis (red triangles) are compared with chondritic organic matter (green squares), comet Halley particles (black star), and stratospheric interplanetary dust particles (blue circle). Bottom right: High-resolution (40-nm pixel size) STXM optical density image (scale bar = 1 µm) on the C 1s absorption edge for a thin section from sample 5. Image credit: D. Kilcoyne, ALS.

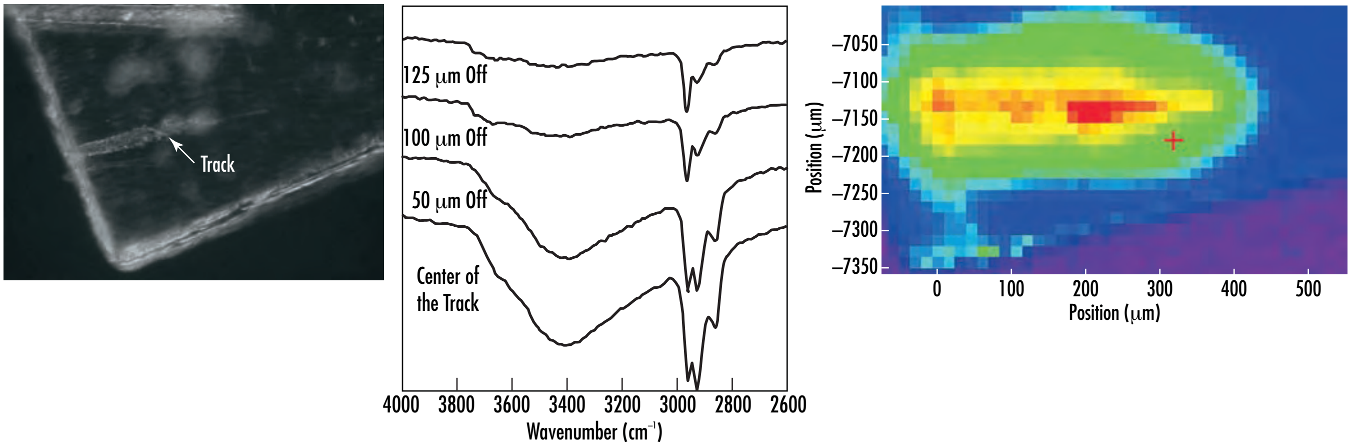

FIGURE 9. IR microspectroscopy of some particle tracks (left) revealed shedding of organic compounds and their diffusion into the surrounding aerogel. The spectra (center) show the intensities of a methylene group peak on the track and at various distances away. The methylene peak distribution is mapped in the false color image (right). The peak, which comes from organics, is most intense on the track (red is the most intense, purple the least) and decreases as one moves away but is still detectable 100 µm from the track. Image credit: S. Bajt, Lawrence Livermore National Laboratory.

Comet Wild 2 data, for example, comets apparently are not composed entirely of volatile rich materials but rather are a mixture of materials formed at all temperature ranges (such as high- and low-temperature minerals from olivine to low- and high-calcium pyroxenes) at places very near the early sun and at places very remote from it.

One of the major discoveries from the analysis of the comet samples was finding particles rich in organic matter. Comets are believed to have brought water and organic matter—necessary ingredients for the origin of life—to the early Earth. One of the first analyses obtained on the Stardust samples showed abundant hydrocarbons in many of the particles. The comet organics collected by Stardust are more "primitive" than those seen in meteorites and may have formed by processes in nebulae, either in space clouds between the stars, or in the disk-shaped cloud of gas and dust from which our Solar System formed.

Though the Wild 2 samples proved to be highly variable, the picture that nonetheless emerged is of cometary particles containing primarily silicate materials formed within the Solar System, including some grains born in the high temperatures existing only close to the Sun. These particles then were carried (perhaps by strong bipolar gas jets coming out of the early Sun) to the outer reaches of the accretion disk where the planets of the Solar System had their birth, corresponding to the Kuiper belt region outside Neptune's orbit, where they were incorporated into Comet Wild 2 along with organic compounds and other volatile materials. Added to recent advances in cometary science showing the important role played by mixing of materials, the first round of Stardust results suggests that the mixing started earlier in the planetary formation process and was more extensive than previously thought.

INVESTIGATORS

Research conducted by members of the Stardust preliminary examination team.

PUBLICATIONS

D. Brownlee et al., "Comet 81P/Wild2 under a microscope," *Science* **314,** 1711 (2006).

S.A. Sandford et al., "Organics captured from Comet 81P/Wild 2 by the Stardust spacecraft," *Science* **314,** 1720 (2006).

L.P. Keller et al., "Infrared spectroscopy of Comet 81P/Wild 2 samples returned by Stardust," *Science* **314,** 1728 (2006).

G.J. Flynn et al., "Elemental compositions of Comet 81P/Wild 2 samples collected by Stardust," *Science* **314,** 1731 (2006).

FUNDING

National Aeronautics and Space Administration and other institutions supporting the members of the Stardust preliminary examination team.

Condensed Matter Physics

FIRST DIRECT OBSERVATION OF SPINONS AND HOLONS

Just as the body and wheels of a car are thought to be intrinsic parts of the whole, incapable of separate and independent actions, i.e., the body goes right while the wheels go left, so, too, are electrical charge and spin intrinsic components of an electron. Except, according to theory, in one-dimensional solids, where the collective excitation of a system of electrons can lead to the emergence of two new quasiparticles called "spinons" and "holons." A spinon carries information about an electron's spin and a holon independently carries information about its charge. The splitting of an electron's properties into spinons and holons in one-dimensional systems is expected to have an impact on spintronics, where the storage and movement of data is based on electron spin, rather than on charge alone. Another area in which spinons and holons could play an important role is the development of nanowires, one-dimensional hollow tubes where electron movement is so constrained that quantum effects dominate. And, central to many leading theories about high-temperature superconductivity is the existence of spin–charge separation in one-dimensional systems. Beyond technological applications, the confirmation by Kim et al. of the idea of spin–charge separation is important because it reveals deep insights into the quantum world—and the beauty and subtleties associated with it.

Spin and charge are inseparable traits of an electron, but in one-dimensional solids, a 40-year-old theory predicts their separation into "collective" modes—as independent excitation quanta called spinons and holons. Angle-resolved photoemission spectroscopy (ARPES) should provide the most direct evidence of this spin–charge separation, as the single quasiparticle peak splits into a spinon–holon two-peak structure. However, despite extensive ARPES experiments, the unambiguous observation of the two-peak structure has remained elusive. Working at the ALS, a team of researchers from Korea, Japan, and the U.S. has now observed electron spin–charge separation in a one-dimensional solid. These results hold implications for future developments in several key areas of advanced technology, including high-temperature superconductors, nanowires, and spintronics.

The idea behind spin–charge separation is that electrons behave differently when their range of motion is restricted to a single dimension. Ordinarily, the removal of an electron from a crystal creates a hole, a vacant positively charged energy space. This hole can move freely throughout the crystal in two or three dimensions, carrying with it information on both the electron's spin and charge, as observed in a single peak of an ARPES spectrum. When restricted to one dimension, however, it becomes theoretically possible for the hole (carrying a positive charge) to propagate in one direction while the spin propagates in the opposite direction, or at a different speed (Figure 1). If this spin–charge separation occurs, the hole is said to decay into a spinon and a holon, and two peaks in the ARPES spectrum would be observed.

ARPES is an excellent tool for observing spin–charge separation and other collective effects involving electrons. By measuring the energy and momentum of emitted electrons, ARPES provides a detailed picture of the electron energy spectrum and important information about electron dynamics, such as the speed of the

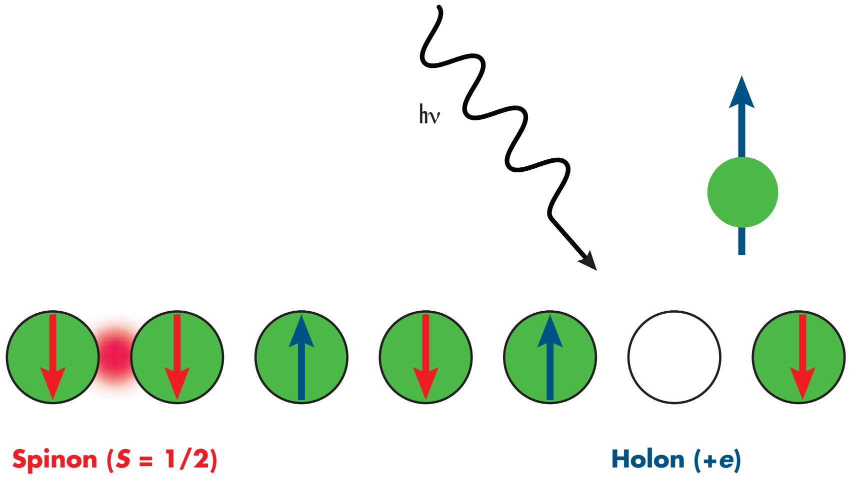

FIGURE 1. Schematic view of electron removal in the case of a one-dimensional system with antiferromagnetic correlation. Removal of a spin-up electron results in a positively charged hole (holon) that moves along the chain as neighboring electrons fill the empty space. The "closing up" of the initial hole leaves two spin-down electrons adjacent to each other. This magnetic disorder can be thought of as a quasiparticle (spinon) that propagates along the chain, independently of the holon, through the flipping of successive spins.

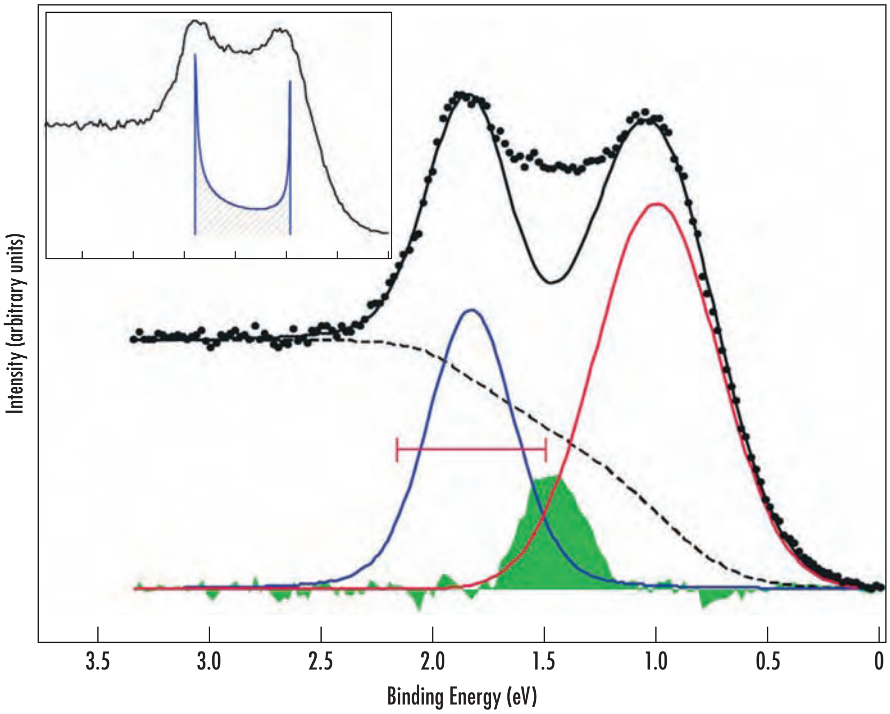

FIGURE 2. Two discrete peaks in the ARPES data form the signature of a spin–charge separation event. The raw data (black dots) are fitted with Gaussian peaks for the holon (blue) and the spinon (red) with an integrated background (dashed line). The solid black line is the sum of the two Gaussian peaks and the background. The inset compares the data with the calculated spectral function, and the shaded green area indicates the extra intensity predicted by theory. The red bar shows that the spinon peak is wider than the holon peak.

electrons and their effective mass. However, despite extensive studies of various one-dimensional systems, previous efforts to observe the two-peak spectrum proved unsuccessful or ambiguous. The materials in these earlier studies were complex enough to allow for alternative explanations for the peaks, and independent estimates of the spinon and holon energy scales—a valuable check on the interpretation of the data—were not available.

The current observations are direct and the results are unambiguous because they were obtained from a simple material that left little room for misinterpretation. The researchers examined the ARPES spectrum of $SrCuO_2$, which has a double Cu–O chain structure but is an ideal one-dimensional compound because of very weak interchain coupling. Furthermore, the values of its spinon and holon energy scales can be estimated from optical and neutron data as well as band theory. The observations were made at the Electronic Structure Factory endstation at ALS Beamline 7.0.1, which is able to survey a relatively large range of momentum and energy values to locate the interesting correlated effects. The data not only show a clear separation of ARPES peaks (Figure 2), but the spinon and holon energy scales of ~0.43 and 1.3 eV, respectively, are in quantitative agreement with theoretical predictions. In addition, deviation of the data from a simple two-peak structure (shaded green in figure) is also predicted by theory.

The researchers credit their breakthrough to the use of high photon energies that suppressed the effects of the main valence band, whose spectral "tail" obscured the holon peak in previous efforts. The only aspect of the data that remains unexplained is the broadness of the peaks; one clue may lie in the fact that the spinon peak is wider than the holon peak.

The clear-cut nature of this landmark study not only strengthens and deepens our understanding of the collective behavior of a system of particles, it also points the way to future investigations.

INVESTIGATORS

B.J. Kim and S.-J. Oh (Seoul National University, Korea), H. Koh and E. Rotenberg (ALS), H. Eisaki (National Institute of Advanced Industrial Science and Technology, Japan), N. Motoyama and S. Uchida (University of Tokyo, Japan), T. Tohyama (Tohoku University, Japan), S. Maekawa (Tohoku University and Japan Science and Technology Agency), Z.-X. Shen (Stanford Synchrotron Radiation Laboratory), and C. Kim (Yonsei University, Korea).

PUBLICATION

B.J. Kim, H. Koh, E. Rotenberg, S.-J. Oh, H. Eisaki, N. Motoyama, S. Uchida, T. Tohyama, S. Maekawa, Z.-X. Shen, and C. Kim, "Distinct spinon and holon dispersions in photoemission spectral functions from one-dimensional $SrCuO_2$," *Nature Physics* **2,** 397 (2006).

FUNDING

Korea Science and Engineering Foundation and U.S. DOE BES.

CONTROLLING GRAPHENE'S ELECTRONIC STRUCTURE

Graphene, a perfect two-dimensional structure, exists in our three-dimensional universe, despite the belief, based on theory, tradition, and experiment, that it cannot. Two years ago, scientists isolated the material by repeated exfoliation (peeling) of nanometer-scale pieces of graphite. This single layer of hexagonally arranged carbon atoms forms a two-dimensional "chicken-wire" sheet and serves as the baseline system of many carbon-based materials, including graphite (used in lead pencils), large fullerenes (also known as "buckyballs"), and carbon nanotubes, which can be created by rolling single sheets of graphene into cylinders. The semiconductor industry is always looking for a material that has superconductive properties. Carbon, with its ability to conduct electricity with almost no resistance, fits the bill. For a while, it was thought that carbon nanotubes (CNTs) would be a natural next-generation material to replace silicon. However, it has been difficult to get CNTs of consistent sizes, with consistent electronic properties. When working at the scales required for electronic devices, this is a major problem. Graphene, however, has the advantages of CNTs but does not appear to have the problems of consistency. In addition, we already have the microelectronics manufacturing technology that can be adapted for producing semiconductor graphene sheets.

Graphene, because of its unusual electronic properties, reduced dimensionality, and scale, has enormous potential for use in ultrafast electronic transistors. It exhibits high conductivity and an anomalous quantum Hall effect (a phenomenon exhibited by certain semiconductor devices at low temperatures and high magnetic fields). Among its novel properties, graphene's electrical charge carriers (electrons and holes) move with effectively zero mass and constant velocity, like photons. Graphene's intrinsically low scattering rate from defects implies the possibility of a new kind of electronics based on the manipulation of electrons as waves rather than particles. The primary technical difficulty has been controlling the transport of electrical charge carriers through the sheet. This area of research is known as band-gap engineering. While band-gap engineering is the basis of semiconductor technology, it is only now being applied to graphene. Using angle-resolved photoemission spectroscopy (ARPES) at ALS Beamline 7.0.1, a team of scientists from the ALS and Germany characterized the electronic band structure and successfully controlled the gap between valence and conduction bands in a bilayer of graphene thin films deposited on a substrate of silicon carbide. This was done by doping one sheet with adsorbed potassium atoms, creating an asymmetry between the two layers.

Graphene's unique electronic structure is characterized by conical valence and conduction bands that meet at a single point in momentum space (the Dirac crossing energy). The researchers demonstrated that through selective control of the carrier concentration in the graphene layers, the band structure can be easily tuned near the Dirac crossing (Figure 3). Similar control can be achieved in principle by varying the electric field across the bilayer film in an atomic-scale switching device.

If undoped, a bilayer of graphene sheets is considered a semimetal, a material in which the conduction and valence bands slightly overlap in energy. When the researchers first syn-

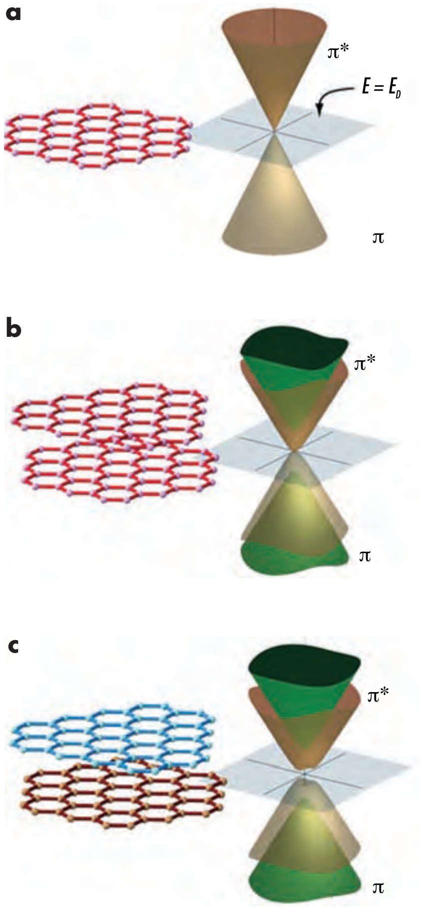

FIGURE 3. Electronic structure of a single layer (a), symmetric double layer (b), and asymmetric double layer (c) of graphene. The energy bands depend only on in-plane momentum because the electrons are restricted to motion in a two-dimensional plane. The Dirac crossing points are at energy E_D.

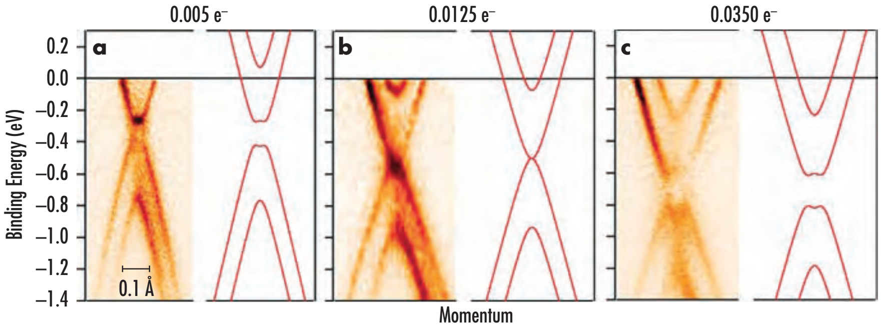

FIGURE 4. Evolution of gap closing and reopening by changing the doping level by potassium adsorption. Experimental and theoretical bands for an as-prepared graphene bilayer (a) and with progressive adsorption of potassium (b, c) are shown. The number of doping electrons per unit cell, estimated from the relative size of the Fermi surface, is indicated at the top of each panel.

thesized their bilayer graphene films onto the silicon carbide substrate, the graphene became a weak n-type semiconductor, having a slight excess of negatively charged electrons; the interface layer acquired an excess of conduction electrons from the substrate, creating a small band gap.

Potassium atoms deposited onto the graphene donated their lone valence electrons to the graphene's surface layer, initially closing the band gap. However, as the potassium deposition continued, the band gap was reopened by the excess of electron charge-carriers on the graphene's surface layer (Figure 4). Progressive potassium deposition further enhanced the n-type doping.

These results demonstrate that by controlling the carrier density in a bilayer of graphene, the occupation of electronic states near the Fermi level (E_F) and the magnitude of the gap between the valence band and conduction band can be manipulated. This control over the band structure suggests the potential application of bilayer graphene to switching functions in electronic devices with a thickness of only two atomic layers.

This experiment was a tour de force on multiple levels. In addition to characterizing and controlling the graphene band gap, the researchers found the current capacity to be surprisingly high. At a temperature of 30 K, cold enough to preclude any conduction through the substrate, they were able to pass 400 mA through a macroscopic sample. This corresponded to a current of about 20 million amps per square centimeter, the same order of magnitude reported for single-walled carbon nanotubes and graphene multilayers.

The results of this experiment showcase ARPES and the techniques developed at Beamline 7.0.1. This ability to obtain detailed information about changes that occur on a small scale in momentum space, and which are induced by only a small, dispersed distribution of atoms, means that useful information can be obtained not only for electronic applications but also for chemical applications (such as sensors). The researchers are now focusing on combining this capability with future high-spatial-resolution photoemission to derive useful information from real-world devices.

INVESTIGATORS

T. Ohta (ALS and Fritz-Haber-Institut der Max-Planck-Gesellschaft, Germany), A. Bostwick and E. Rotenberg (ALS), K. Horn (Fritz-Haber-Institut der Max-Planck-Gesellschaft, Germany), and T. Seyller (Universität Erlangen-Nürnberg, Germany).

PUBLICATION

T. Ohta, A. Bostwick, T. Seyller, K. Horn, and E. Rotenberg, "Controlling the electronic structure of bilayer graphene," *Science* 313, 951 (2006).

FUNDING

U.S. DOE BES, Max Planck Society, and European Science Foundation.

FIRST DIRECT EVIDENCE OF DIRAC FERMIONS IN GRAPHITE

Why are scientists suddenly interested in graphite? It is, after all, a common utilitarian material used for centuries in that humble invention, the pencil. And even in that application, it has been rendered practically obsolete by silicon, the signature material of the Information Age. It is our ability to manipulate electrons as they move through semiconductors such as silicon that is at the heart of modern solid-state electronics. Recently, however, scientists have discovered remarkable conducting properties in a two-dimensional form of graphite called graphene: here the electrons behave as though they are massless; they also travel long distances without scattering and have been clocked at speeds about 300 times below the speed of light in vacuum—much higher than the typical speed of electrons in semiconductors. Here, Zhou et al. show that this unusual behavior is present in three-dimensional, multilayer graphite as well, a critical finding if real-world graphite-based devices are to be realized. From a broader perspective, the work also demonstrates how graphite can be a convenient testing ground for studying exotic phenomena as we transition from two to three dimensions.

The recent surge of interest in the electronic properties of graphene—that is, isolated layers of graphite just one atomic layer thick—has largely been driven by the discovery that electron mobility in graphene is ten times higher than in commercial-grade silicon, raising the possibility of high-efficiency, low-power, carbon-based electronics. Scientists attribute graphene's surprising current capacity (as well as a number of even stranger phenomena) to the presence of charge carriers that behave as if they are massless, "relativistic" quasiparticles called Dirac fermions. Harnessing these quasiparticles in real-world carbon-based devices, however, requires a deeper knowledge of their behavior under less-than-ideal circumstances, such as around defects, at edges, or in three dimensions—in other words, in graphite. At the ALS, a team of researchers using angle-resolved photoemission spectroscopy (ARPES) have now produced the first direct evidence of massless Dirac fermions in graphite coexisting with quasiparticles of finite effective mass and defect-induced localized states.

An electron moving through a conventional solid is often described as having a small but finite effective mass (m^*) that takes into account the drag on its momentum from the surrounding crystal lattice as well as from interactions with other particles. The energy (E) of such an electron depends quadratically on its momentum (p), as given by the equation $E = p^2/2m^*$. In graphene, however, it has been discovered that electrons behave as if they are massless, "relativistic" particles (like photons traveling in free space at the speed of light) that exhibit a linear dispersion relationship given by the equation $E = vk$, where the wavenumber (k) represents momentum and the Fermi velocity (v) stands in for the speed of light. Because these electrons obey the Dirac equation—a description of fermions (e.g., electrons) that combines quantum mechanics with special relativity—they are called Dirac fermions.

Dirac fermions have been invoked recently to explain various peculiar phenomena in condensed-matter physics, including the novel quantum Hall effect in graphene, the magnetic-field-driven metal–insulator-like transition in graphite, superfluidity in ^{3}He, and the exotic pseudogap phase of high-temperature superconductors. Despite their proposed key role in these highly interesting systems, direct experimental evidence of Dirac fermions has been limited. Furthermore, although several experiments have seemed to point to the existence of these relativistic particles in graphite, no direct observations have previously been reported.

At ALS Beamlines 12.0.1 and 7.0.1, researchers studied the nature of quasiparticles in single-crystal graphite by performing high-resolution ARPES experiments (Figure 5). ARPES is unique in that it allows us to directly probe electronic structure using both energy and momentum information not accessible through any other type of measurement. The results provide the first direct experimental proof that Dirac fermions indeed exist in the low-energy dynamics of graphite. ARPES intensity maps taken near corner H of the Brillouin zone (BZ) show the linear dispersion characteristic of Dirac fermions (Figure 6). Near BZ corner K, however, a parabolic dispersion indicates the coexistence of quasiparticles with finite effective mass, probably due to interactions between the different graphene layers.

The experiment also revealed the presence of defect-induced localized states in the proximity of zig-zag edge structures (Figure 7), indicating that graphite's electronic structure is strongly affected by the network structure of sp^2 carbon, as is the case for fullerenes and carbon nanotubes.

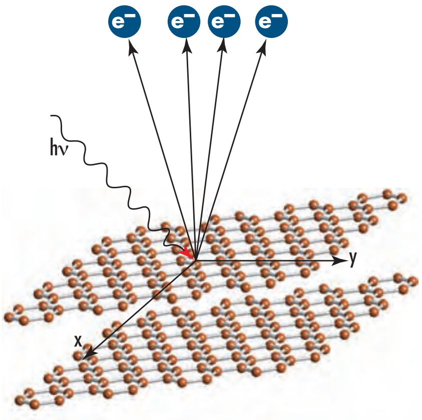

FIGURE 5. Photoemission geometry and crystallographic structure of two graphene layers.

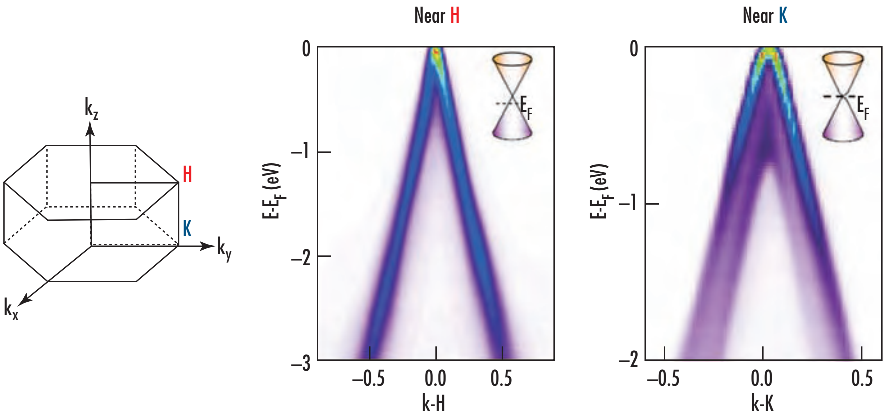

FIGURE 6. Left: Diagram of the Brillouin zone of graphite. Center: Dirac fermions in momentum space near corner H of the Brillouin zone are characterized by a sharply linear Λ-shaped dispersion relation, similar to that found in graphene. Right: As a result of interlayer interactions, other regions of momentum space (near corner K) display a parabola-shaped dispersion, signifying the existence of quasiparticles with finite mass whose energy is quadratically dependent on momentum.

This kind of information will be of fundamental importance if we eventually hope to engineer graphite down to the nanometer scale for possible use in electronic devices.

Graphite is a unique system in which three different types of excitations—massless Dirac fermions, quasiparticles with finite effective mass, and defect states—coexist. These special ingredients add an exotic flavor to the low-energy electron dynamics of this familiar yet surprising material that combines the realms of nonrelativistic condensed matter physics on the one hand and relativistic particle physics on the other.

INVESTIGATORS

S.Y. Zhou, C.D. Spataru, D.-H. Lee, S.G. Louie, and A. Lanzara (UC Berkeley and Berkeley Lab); G.-H. Gweon (UC Berkeley); J. Graf and A.V. Fedorov (Berkeley Lab); R.D. Diehl (Pennsylvania State University); and Y. Kopelevich (Universidade Estadual de Campinas, Brazil).

PUBLICATION

S.Y. Zhou, G.-H. Gweon, J. Graf, A.V. Fedorov, C.D. Spataru, R.D. Diehl, Y. Kopelevich, D.-H. Lee, S.G. Louie, and A. Lanzara, "First direct observation of Dirac fermions in graphite," *Nature Physics* **2**, 595 (2006).

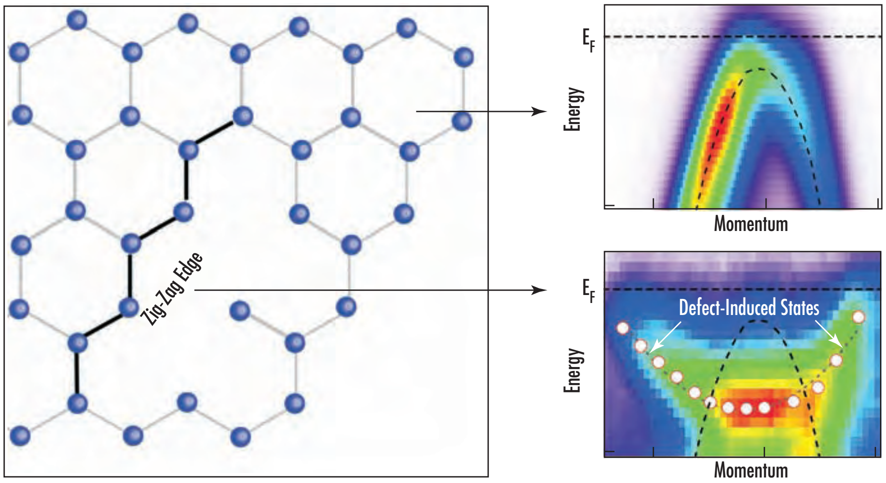

FIGURE 7. Left: A typical graphite layer, in which honeycomb structures coexist with zig-zag edge regions. Right: Intensity maps as a function of energy and momentum. The top map shows the parabolic dispersion intrinsic to graphite. The bottom map, measured near a zig-zag edge, shows a large electron pocket due to defect-induced states.

FUNDING

National Science Foundation, U.S. DOE BES, and Berkeley Lab Laboratory Directed Research and Development program.

NATURE AND ORIGIN OF THE CUPRATE PSEUDOGAP

Ever since the discovery of high-temperature superconductors (HTSCs), researchers have wrestled with not only theory, but application. One of the main problems is critical temperature, the temperature below which electrons can move within a material without resistance. The first HTSCs conducted electricity at 35 K. Researchers keep pushing this limit, and today HTSCs can superconduct at 138 K. However, until a material is found that superconducts above 300 K, a cooling system is required. Despite the temperature limitations, complexity of materials, and unanswered theoretical questions, many applications are being researched and developed for HTSCs. A significant area of focus is energy transmission. Since 2000, several transmission projects have used cryogenically cooled HTSC cable to provide electricity off of commercial power grids. In 2001, 150,000 residents of Copenhagen, Denmark, began receiving electricity through HTSC cable. That same year, three 400-foot HTSC cables were installed for Detroit Edison at the Frisbie Substation that could deliver 100 million watts of power. Sumitomo Electric's HTSC cable was connected to the Niagara Mohawk Power Corporation's power grid and since July 2006 has been supplying power to approximately 70,000 households. These successful projects are proof that HTSC use in power transmission is a practical reality.

The workings of HTSC materials are a mystery wrapped in an enigma. However, a team of researchers from the ALS, Brookhaven National Laboratory, and Cornell University has taken a major step in understanding part of this mystery—the nature and origin of the pseudogap. Using angle-resolved photoemission spectroscopy (ARPES) and scanning tunneling microscopy (STM), they have determined the electronic structure of $La_{2-x}Ba_xCuO_4$ (LBCO), a unique system in which superconductivity is strongly suppressed and static spin and charge orders develop near a doping level of $x = 1/8$.

In conventional superconductors, which operate at temperatures near absolute zero, the appearance of an energy gap in the electronic spectrum indicates pairing of electrons into Cooper pairs, global phase coherence, and a simultaneous transition into a macroscopic superconducting state. This gap is known as the superconducting gap. In contrast, in HTSCs (which have nonsuperconductive, mixed, and superconductive matter states), an energy gap is already present at the Fermi surface in the normal, nonsuperconductive, state. This is known as a pseudogap, and its origin and relationship to superconductivity is one of the most important open issues in the physics of HTSCs and represents the focal point of current theoretical debate. According to one view, this pseudogap is really a pairing (superconducting) gap, reflecting the existence of Cooper pairs without global phase coherence. The superconducting transition then occurs at some lower temperature, when phase coherence is established. In an alternative view, the pseudogap represents another state of matter entirely that competes with superconductivity. However, the order associated with such a competing state has never been unambiguously detected.

Cuprates are well-known HTSCs, but in the cuprate compound LBCO, superconductivity is strongly suppressed and static spin and charge orders, or "stripes," develop near a low doping level of $x = 1/8$ (at a point when one-eighth of the electrons have been removed). Previous measurements have shown that these stripes, an alternating arrangement of electrons about four atoms wide, somehow inhibit superconductivity. This absence of superconductivity at $x = 1/8$ enabled the researchers to "peek" into the normal ground state of an HTSC material for the first time.

The researchers measured the electronic excitations and detailed momentum dependence of the single-particle gap in the ordered state of LBCO (Figures 8, 9, and 10). Using ARPES at ALS Beamline 12.0.1, they detected an energy gap at the Fermi surface in the nonsuperconducting LBCO that looks the same as the energy gap at the Fermi surface in superconducting cuprates. This pseudogap, like the superconducting gap, has a magnitude consistent with d-wave symmetry (a form of electron pairing in which the electrons travel together in quantum waves shaped like a four-leaf clover), and vanishes at four nodal points on the Fermi surface. Using STM at the ultralow vibration laboratory of Cornell University, they found that the density of states $DOS(E) \propto |E|$, with zero-DOS falling exactly at the Fermi energy. Furthermore, the gap has a surprising doping dependence, with a maximum at $x \approx 1/8$, precisely where T_c has a local minimum and the

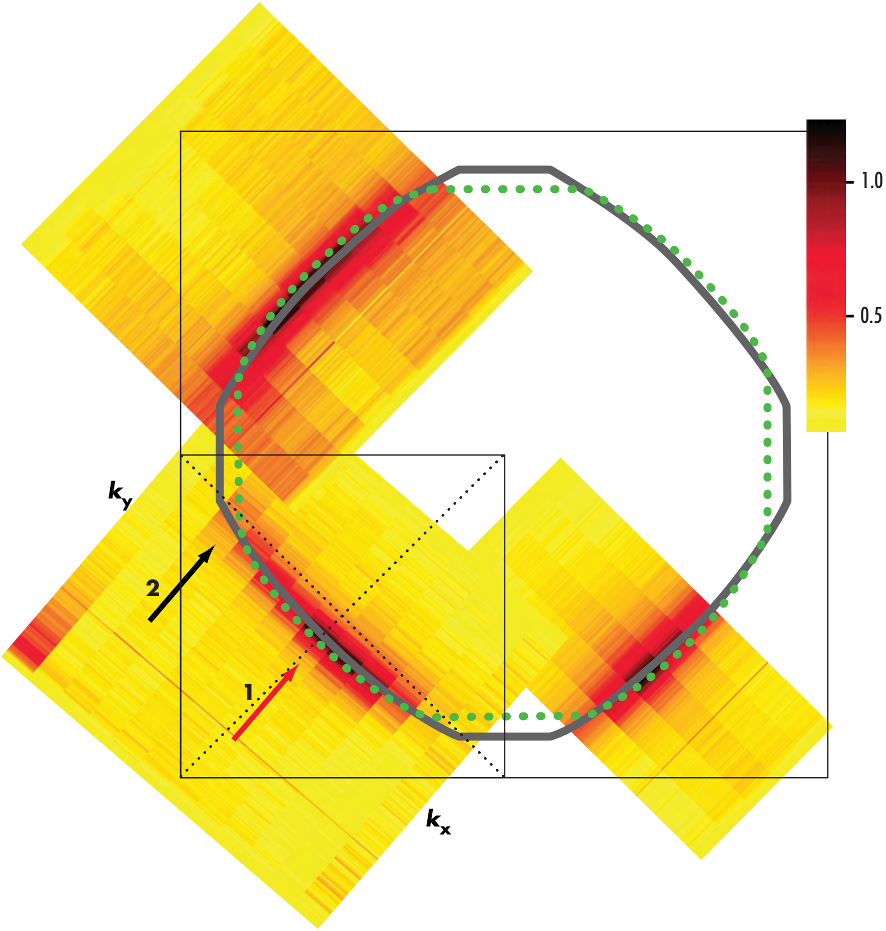

FIGURE 8. Photoemission from LBCO at x = 1/8. Photoemission intensity from a narrow interval around the Fermi level (ω = 0 ± 10 meV) as a function of the in-plane momentum. High intensity represents the underlying Fermi surface. Lines represent fits to the positions of maxima in spectral intensity at the Fermi level for LBCO (x = 0.125) (solid line) and LSCO (x = 0.07) (dashed line).

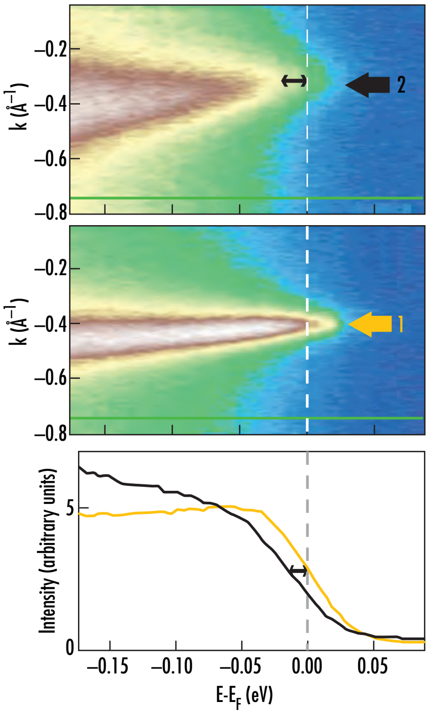

FIGURE 9. Top: Photoemission intensities from LBCO sample as a function of binding energy along the two momentum lines 1 and 2 indicated in Figure 8 by arrows. Bottom: Energy distribution curves of spectral intensity integrated over a small interval $k_F \pm \Delta k$ for lines 1 and 2. The arrow represents the shift of the leading edge. The spectra were taken in the charge-ordered state at T = 16 K.

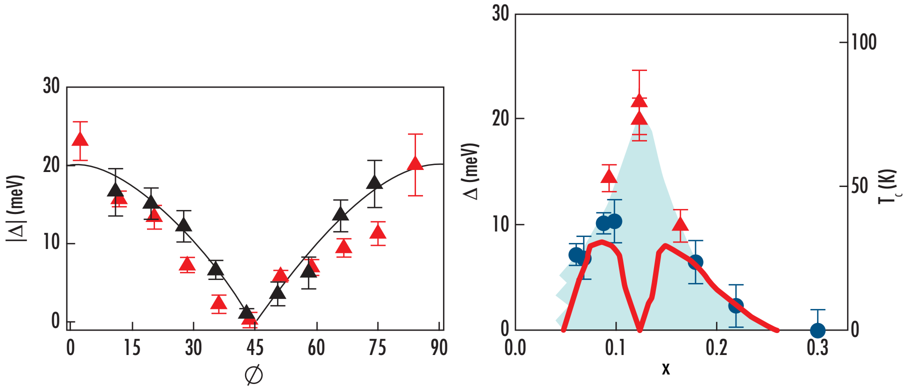

FIGURE 10. Left: Magnitude of single-particle gap for two LBCO samples (red and black triangles) as a function of angle around the Fermi surface. The line represents a d-wave gap amplitude, $\Delta_0|\cos(2f)|$ with Δ_0 = 20 meV. Right: Doping dependence of Δ_0 in LBCO (red triangles) and LSCO (blue circles). Red line represents doping dependence of T_c for LBCO.

charge/spin order is established between two adjacent superconducting domes. These findings reveal the pairing origin of the pseudogap and imply that the most strongly bound Cooper pairs at $x \approx 1/8$ are most susceptible to phase disorder and spatial ordering. Thus, the nonsuperconducting, "striped" state at $x = 1/8$ is consistent with a phase incoherent d-wave superconductor whose Cooper pairs form spin/charge-ordered structures instead of becoming superconducting.

Although with both ARPES and STM, low-energy electronic signatures were the same in both states, it is not yet clear how the superconducting state relates to the striped state. However, the fact remains that the same materials in two very different states appear to have identical energy-gap structures.

INVESTIGATORS

T. Valla and G.D. Gu (Brookhaven National Laboratory), A.V. Fedorov (ALS), and J. Lee and J.C. Davis (Cornell University).

PUBLICATION

T. Valla, A.V. Fedorov, J. Lee, J.C. Davis, and G.D. Gu, "The ground state of the pseudogap in cuprate superconductors," *Science* **314,** 1914 (2006).

FUNDING

U.S. DOE BES, Office of Naval Research, and Cornell University.

UNTANGLING THE ELECTRONIC STRUCTURE OF BNCO/CCO SUPERLATTICES

High-temperature superconductors exhibit complex electronic behavior and material structure. The mingling of these attributes makes it difficult to determine a mechanism for high-temperature superconductivity. High-T_c superconductors start out as insulating materials and ultimately become superconducting as they are doped with charge carriers—electrons and holes (the positive vacancies in the valence-band electron population). However, the doping process by which high-temperature superconductivity is achieved is still not well understood. Researchers at the ALS recently looked at a cuprate compound to understand how hole doping affects superconductivity. Pulsed-laser-deposited molecular beam epitaxy (MBE) allowed them to independently fabricate the cuprate superlattices as well as their component superconducting and nonsuperconducting planes as separate samples. The superconducting plane is known as the infinite layer. The adjacent nonsuperconducting plane is known as the charge reservoir. It houses the charge carriers and controls the oxidation state of the neighboring superconducting plane. Resonant inelastic x-ray scattering (RIXS) revealed the charge-doping mechanism, showing evidence of charge transport from the charge reservoir layer to the infinite layer through a pyramid of hole-doped oxides. This suggests a strong link between superconductivity and both the interaction of the electrons (known as electron correlation) and charge transfer within the superlattices.

Cuprate high-temperature superconductors have two functional blocks: the charge reservoir (CR) stores charge carriers and the infinite layer (IL) contains the infinite-layer CuO_2 planes. It is widely held that superconductivity occurs primarily within this IL region. Recently, investigators at the ALS used high-T_c planarity to disentangle the electronic structure of a high-T_c material by studying $[(Ba_{0.9}Nd_{0.1})CuO_{2+\delta}]_2/[CaCuO_2]_2$ (BNCO/CCO) high-T_c superlattices (SLs) (Figure 11). The researchers applied x-ray absorption spectroscopy (XAS) and x-ray emission spectroscopy (XES) at Beamline 7.0.1 to compare independently fabricated BNCO/CCO superlattice, CCO IL, and BNCO CR samples, thereby attaining the first direct observation of Zhang-Rice singlets in artificial high-temperature superconducting heteroepitaxial structures.

The CCO IL and BNCO CR spectra (Figure 12) show little band overlap, confirming the insulating character of

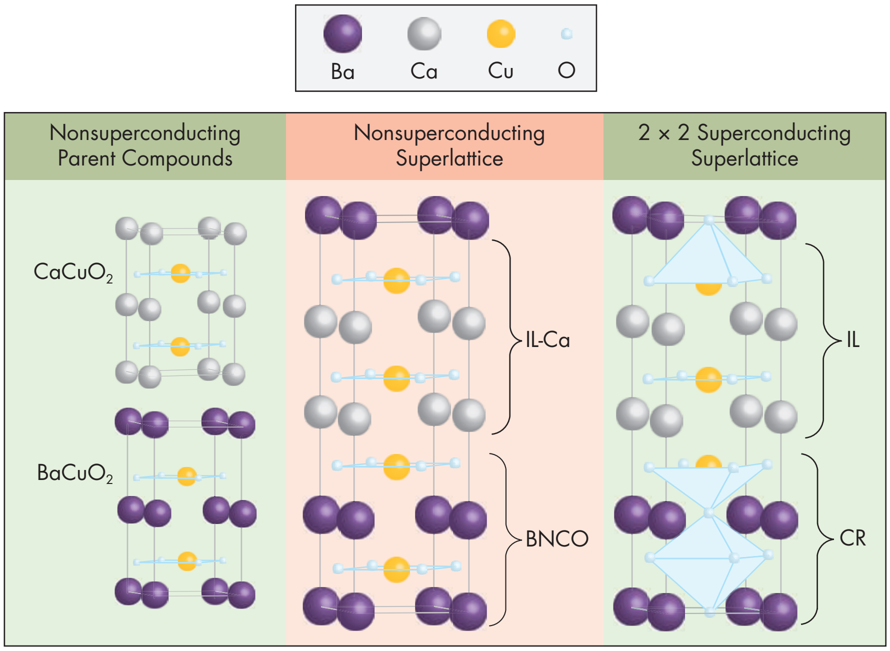

FIGURE11. Schematic of the BNCO and CCO parent compounds (left) and unit cells for nonsuperconducting (center) and superconducting (right) BNCO/CCO superlattices grown by pulsed-laser-deposited MBE starting from the parent compounds.

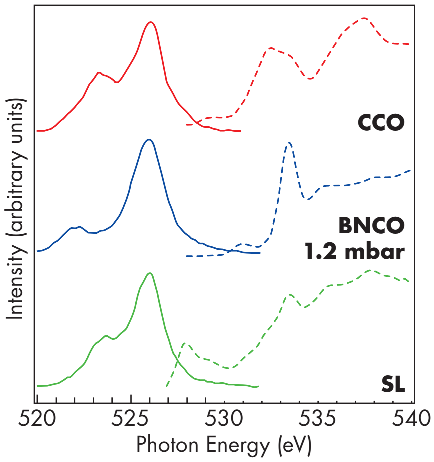

FIGURE 12. XES (solid lines) and XAS (dashed lines) of the infinite layer (CCO), charge reservoir (BNCO), and the superlattice (SL) reflect occupied and unoccupied densities of states near the Fermi level, respectively. Displaying XAS and normal XES data on a photon energy scale shows the gap between the valence and conduction bands.

the component materials. However, the SL spectra show a substantial band overlap, indicating metallicity. Examination of the SL density of states (DOS) spectra reveals a lowering of the conduction band minimum, meaning the top spectral feature of the conduction bands develops at a lower energy than similar CR and IL features. Conduction-band lowering indicates hole doping. SL formation in the 2 x 2 geometry results in a hole-doped oxide.

Using RIXS, the experimenters compared electronic information in all three materials. Directly tuning synchrotron radiation to the O 1s x-ray absorption edge yielded information about the partial unoccupied DOS and hole states. Both functional blocks possess a two-band character due to the O 2p main band and the O 2p$_{x,y}$–Cu 3d hybridization band, but clear differences are observable (Figure 13). The BNCO CR possesses resonant features assignable as dd electronic transitions and the charge transfer (CT) transition (where an electron transitions from the O 2p levels to the Cu 3d band). The CT excitation is dramatically enhanced when the upper Hubbard band is resonantly excited, characteristic of high-temperature superconductors. However, the CCO IL sample contains low-energy

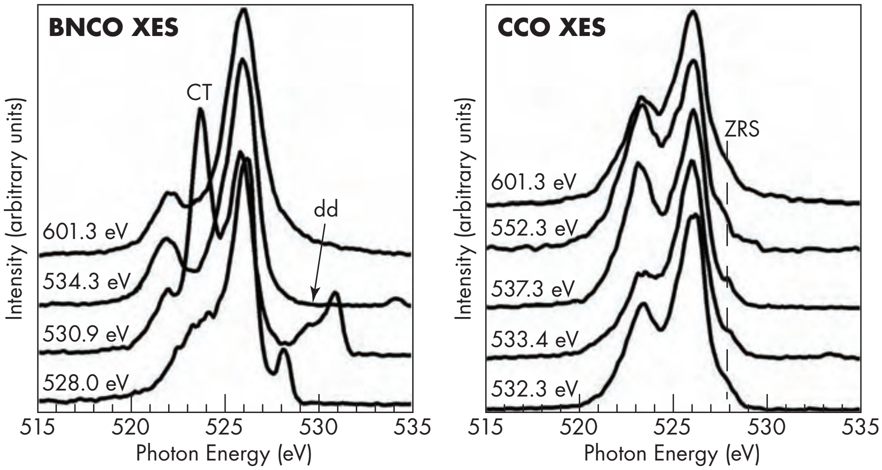

FIGURE 13. RIXS spectra from the CR and IL recorded at selected excitation energies. Left: XES spectra of BNCO thin film. Right: XES spectra of CCO thin film. The CT transition and dd energy loss excitation are observed in BNCO, and the Zhang-Rice singlet (ZRS) is observed in the CCO film.

electronic excitations on the high-energy side of the O 2p main-band peak. These features are the Zhang-Rice singlet band—the coupled state of an O 2p hole and Cu 3d hole on a CuO_4 plaquette (i.e., the ground state of a CuO_2 plane to which a hole is added).

RIXS spectra of the SL show oxygen main-band features and spectral changes associated with the O $2p_{x,y}$ bands. In addition, ZRS-like spectral weight undergoes a diminution compared with ZRS features in the IL, clearly indicating spectral weight transfer.

The mechanism of charge transport from the CR into the IL is based upon the Jahn-Teller distortion of the octahedral cage within the CR region. There is no octahedral distortion for the thin-film CR samples, explaining the clear spectral difference between the SL and CR. The high-T_c SL has two extra oxygen atoms (not possessed by the BNCO region of a nonsuperconducting SL) that are apical to Cu in the CuO plane, accounting for the in-plane CT feature in the SL. These oxygen atoms are pyramidally coordinated around Cu near the CR–IL interface, and there is a distorted octahedral cage around Cu within the BNCO unit cell. The Jahn-Teller distortion of the CuO_6 octahedron gives a d_{z^2} character to doping holes on apical oxygen atoms—i.e., the hole character of BNCO is different from that of superlattice BNCO. As a result, the BNCO CT excitation involving the planar Cu $d_{x^2-y^2}$ hole is delocalized as the newly formed hole state couples to the CCO region.

Hole doping proceeds from the CR to the IL through the apical oxygens. The researchers propose that these holes are transported into the superconducting region, where they may reduce the antiferromagnetic ordering of the CuO_2 planes. The experimental findings point to a possible mechanism of high-T_c superconductivity—hole doping of an antiferromagnetic insulator in which ZRS singlets are already present. The use of RIXS reveals the charge-doping mechanism and relationship of the Zhang-Rice singlets to doping.

INVESTIGATORS

B. Freelon and J.-H. Guo (ALS); A. Augustsson (Uppsala University); and P.G. Medaglia, A. Tebano, and G. Balestrino (National Research Council–Institute for the Physics of Matter, Italy, and University of Rome, Tor Vergata).

PUBLICATION

B. Freelon, A. Augustsson, J.-H. Guo, P.G. Medaglia, A. Tebano, and G. Balestrino, "Electron correlation and charge transfer in $[(Ba_{0.9}Nd_{0.1})CuO_{2+\delta}]_2/[CaCuO_2]_2$ superconducting superlattices," *Phys. Rev. Lett.* **96,** 017003 (2006).

FUNDING

U.S. DOE BES and Swedish Research Council.

ELECTRONS IN A TRIANGULAR LATTICE: QUANTUM-COHERENCE-DRIVEN PHASE TRANSITIONS

For electrons, two isn't company and three is decidedly a crowd. Being of like charge, they like to keep their distance from one another, and when they must be neighbors, in a crystal lattice, for instance, they insist on having opposite spin orientations. In a lattice with rectangular symmetry, adjacent electrons can always have opposite spins, but in a triangular lattice, two out of three neighbors in each triangle must share the same orientation. That's when "quantum spin frustration" sets in, as three electrons compete over two possible spin states. In sodium cobaltate (Na_xCoO_2), whose triangular lattice sandwiches sodium ions between layers of CoO_2, the combination of an ambivalent electronic state and strong coulombic interaction produces a wealth of unusual properties, including superconductivity, antiferromagnetism, and thermoelectricity. In experiments on Beamlines 12.0.1 and 10.0.1, researchers from Princeton University, Berkeley Lab, and the Chinese Academy of Sciences found a jump in thermopower in Na_xCoO_2 at $x = 1/2$. This corresponded with a boost in quasiparticles often associated with superconductivity, raising the intriguing possibility of a material that is both superconducting and highly thermoelectric, a combination that has potential applications in spintronics, nanoscale cooling devices for semiconductors, thermoelectric power, and compact energy supplies for spacecraft.

Strong coulomb interaction between electrons, known as the Mott phenomenon, is a well-known cause of metal-to-insulator phase transitions and can lead to unusual quantum mechanical effects, such as high-temperature superconductivity, when the underlying band is close to half-filled (spin 1/2) and electron transport is largely two-dimensional with square lattice symmetry. Cobaltates, Na_xCoO_2, are a recently discovered class of materials in which two of these conditions, spin 1/2 and two-dimensional transport, are present on the cobalt–oxygen layers. However, because the lattice symmetry is triangular rather than square, quantum spin frustration is also a factor. As a result, cobaltates exhibit not only superconductivity, magnetic order, non-Fermi-liquid transport, and charge order, but also new phases such as spin-thermopower. This rare combination of effects may have potential applications in spintronics, thermoelectric power, and energy-related compact device applications in spacecraft.

In Na_xCoO_2, thermopower exhibits a jump at around x = 1/2, which is in the vicinity of an unusual quantum phase transition along the doping axis (Figure 14). Considering the symmetry of the lattice, x = 1/2 does not represent an electron density commensurate with the triangular geometry, as would x = 1/3 or 2/3. The researchers have thoroughly investigated this unusual phase of this thermoelectric material

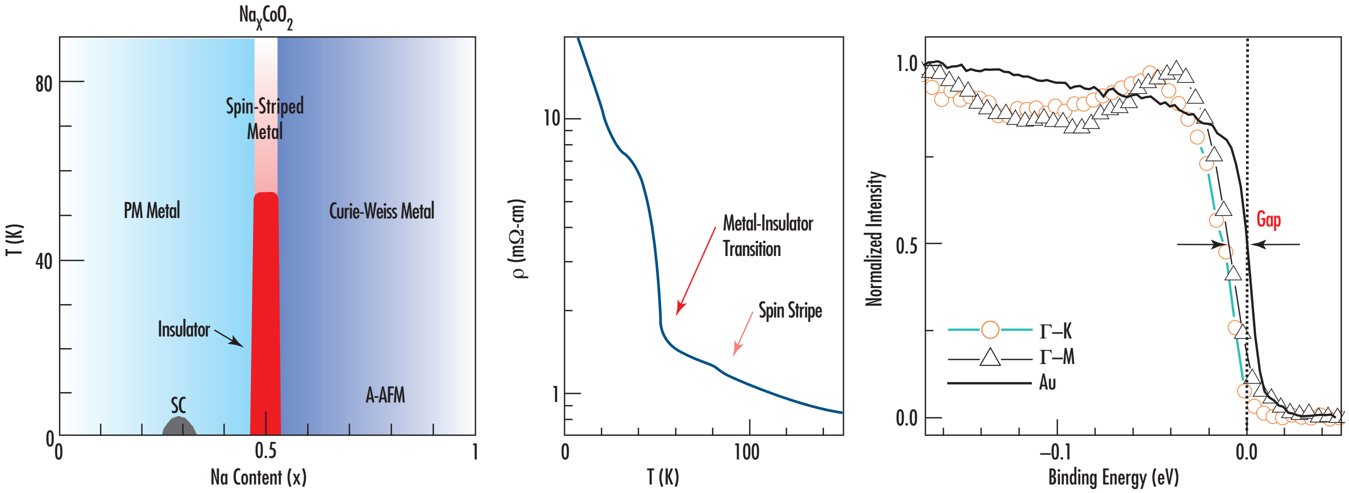

FIGURE 14. Left: Phase diagram of Na_xCoO_2. Doping values of x = 1/3 and x = 1/4 correspond to the boundaries of the supercomputing (SC) state, and an insulating phase only appears at x = 1/2—not at the magic numbers of a triangular lattice, 1/3 or 2/3. Center: Resistivity profile for x near 1/2. Right: Observation of a quasiparticle gap in ARPES experiements.

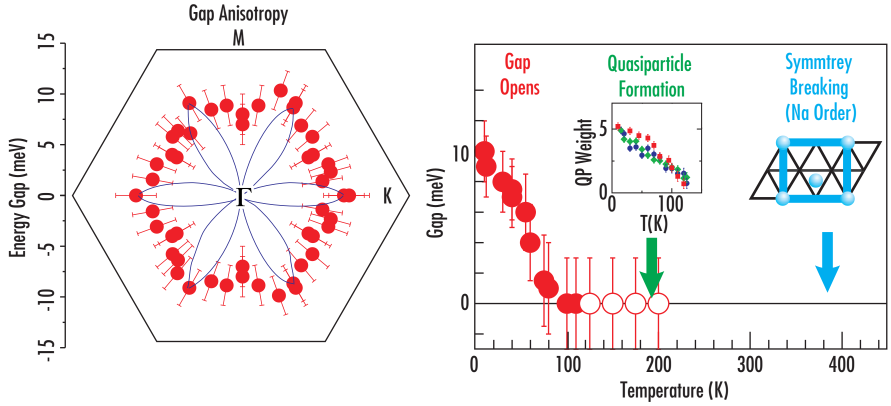

FIGURE 15. Left: Anistropy of charge gap in the unusual low-temperature insulating phase. Right: The insulating gap opens at close to 80 K, far below the sodium charge-ordering transition. Quasiparticle spectral weight is observed below 200 K, and increases significantly as temperature drops to the insulating state onset.

using angle-resolved photoemission spectroscopy (ARPES) at ALS Beamlines 12.0.1 and 10.0.1.

They observed that the opening of the gap occurs at a much lower temperature than the onset of breaking of symmetry related to charge ordering or spin-stripe ordering (Figure 15). Another key observation is that both phase transitions are realized only at temperatures that are low enough for quasiparticles to have gained substantial weight and become able to undergo interference. The researchers have measured the anisotropy of the gap in the insulating phase of this material. Such a gap structure cannot be explained in a conventional Fermi surface nesting picture; quasiparticle coherence, sodium charge order, and Fermi surface topology collectively conspire to bring about such a unique phenomenon. Results suggest that, unlike most other cases in quantum condensed matter physics, a broken symmetry does not necessarily guarantee a concomitant phase transition. Electrons only undergo phase transitions at a lower temperature when they form waves. This is the first strongly correlated material where such an effect has been observed.

Photoemission data show that the gap only appears below 80 K, roughly 300 degrees below the onset of sodium order, thus ruling out the simplest model of a reduced-periodicity Brillouin zone. It therefore becomes significant that the integrated spectral weight of the quasiparticle in $Na_{0.5}CoO_2$ is only apparent below about 200 K and increases at lower temperatures. Increased quasiparticle coherence at low temperature has been associated with the appearance of the superconducting gap in cuprates and is thought to be caused by stabilization through out-of-plane coupling. In this case, it is exciting to consider that the same physics can lead to both the onset of some form of charge-density wave state and to a competing instability, superconductivity.

INVESTIGATORS

D. Qian, L. Wray, D. Hsieh, R.J. Cava, L. Viciu, and M. Z. Hasan (Princeton University); D. Wu, J.L. Luo, and N.L. Wang (Beijing National Laboratory for Condensed Matter Physics); A. Kuprin and A. Fedorov (ALS).

PUBLICATIONS

D. Qian, L. Wray, D. Hsieh, D. Wu, J.L. Luo, N.L. Wang, A. Kuprin, A. Fedorov, R.J. Cava, L. Viciu, and M.Z. Hasan, "Quasiparticle dynamics in the vicinity of metal-insulator phase transition in Na_xCoO_2," *Phys. Rev. Lett.* **96,** 046407 (2006).

D. Qian, D. Hsieh, L. Wray, Y.-D. Chuang, A. Fedorov, D. Wu, J.L. Luo, N.L. Wang, L. Viciu, R. J. Cava, and M.Z. Hasan, "Low-lying quasiparticle states and hidden collective charge instabilities in parent cobaltate superconductors," *Phys. Rev. Lett.* **96,** 216405 (2006).

D. Qian, L. Wray, D. Hsieh, M. Viciu, R.J. Cava, J.L. Luo, D. Wu, N.L. Wang, and M.Z. Hasan, "Complete d-band dispersion relation in sodium cobaltates," *Phys. Rev. Lett.* **97,** 186405 (2006).

FUNDING

National Science Foundation, Natural Science Foundation of China, and U.S. DOE.

NEW QUANTUM PROPERTIES OF ELECTRONS NEAR THE SURFACE OF A SEMICONDUCTOR

Semiconductor compounds made by mixing and matching elements from the periodic table's groups III (e.g., aluminum, gallium, indium) and V (e.g., nitrogen, phosphorus, arsenic) have been the subject of intense scrutiny for many years because of their use in light-emitting diodes (LEDs) and other optoelectronic devices. Much recent attention has focused on indium nitride, where, because of improved film-growth methods, the energy of the fundamental band gap underwent a remarkable revision in the last five years from the previously accepted value of approximately 1.9 eV to the much lower value of approximately 0.65 eV. The size of the band gap is what determines the color of the light emitted (or absorbed, in the case of solar cells). The unexpectedly small band gap gives device designers a great deal of flexibility, because by gradually replacing the indium with gallium (and thus increasing the band gap), they can cover the spectrum from near-infrared to ultraviolet using a single material. Studies of electron behavior in such materials is important for progress, whether toward a highly efficient solar cell that can absorb sunlight of many wavelengths or a next-generation video display covering the entire visible spectrum.

Electron accumulation is a phenomenon observed in certain semiconductors whereby a higher density of electrons is observed in a layer near the surface of the solid. The narrow-gap semiconductor indium nitride (InN) is an unusual material in that there is strong experimental evidence for the existence of an intrinsic electron accumulation layer near the surface when in thin-film form. It is postulated that the surface region has a higher charge density than the bulk due to donor states. This causes the surface Fermi level (E_F) to lie in the conduction band. Researchers have now for the first time directly observed an electron accumulation layer near the surface of InN using high-resolution angle-resolved photoemission spectroscopy (ARPES). They have discovered that not only are electrons observed far above the conduction band minimum, but that they are quantized perpendicular to the surface; that is, the electrons in the accumulation layer reside in quantum-well states.

Prior evidence for an accumulation layer has come from high-resolution electron-energy-loss spectroscopy studies, which indicated a higher electron density within 80 Å of the surface than in the bulk. Further evidence comes from sheet carrier density measurements as a function of film thickness, capacitance-voltage measurements, a photoemission study of defective InN coated with titanium, and recent tunneling spectroscopy experiments. Reported here is the direct observation of electron accumulation in InN using high-resolution ARPES at the ALS (Beamline 12.0.1) and NSLS. The thin-film samples were grown using molecular-beam epitaxy at Boston University.

Figure 16 presents an ARPES photocurrent intensity map of emission from the states within 1.5 eV of E_F, recorded with an incident photon energy of 69 eV, from a sample annealed in ultrahigh vacuum (UHV) to 300°C for 30 minutes. The sample was held at 177 K during measurement. The horizontal axis is the angle of emission, converted to momentum at each point, while the vertical axis is the binding energy. The intensity at any given point reflects the photocurrent for that particular combination of binding energy and momentum. The momentum direction is parallel to the surface plane. Two well-resolved, nested bands are clearly observed. These states, although derived from the conduction band, arise from the

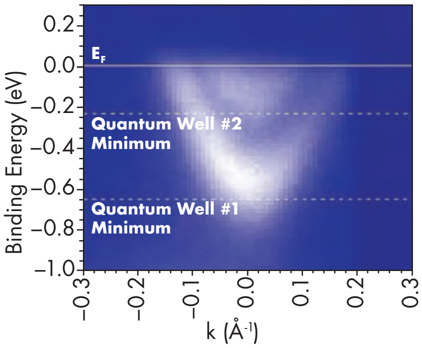

FIGURE 16. ARPES photocurrent intensity map of states within 1.5 eV of E_F. The two quantum-well minima are indicated by dashed lines.

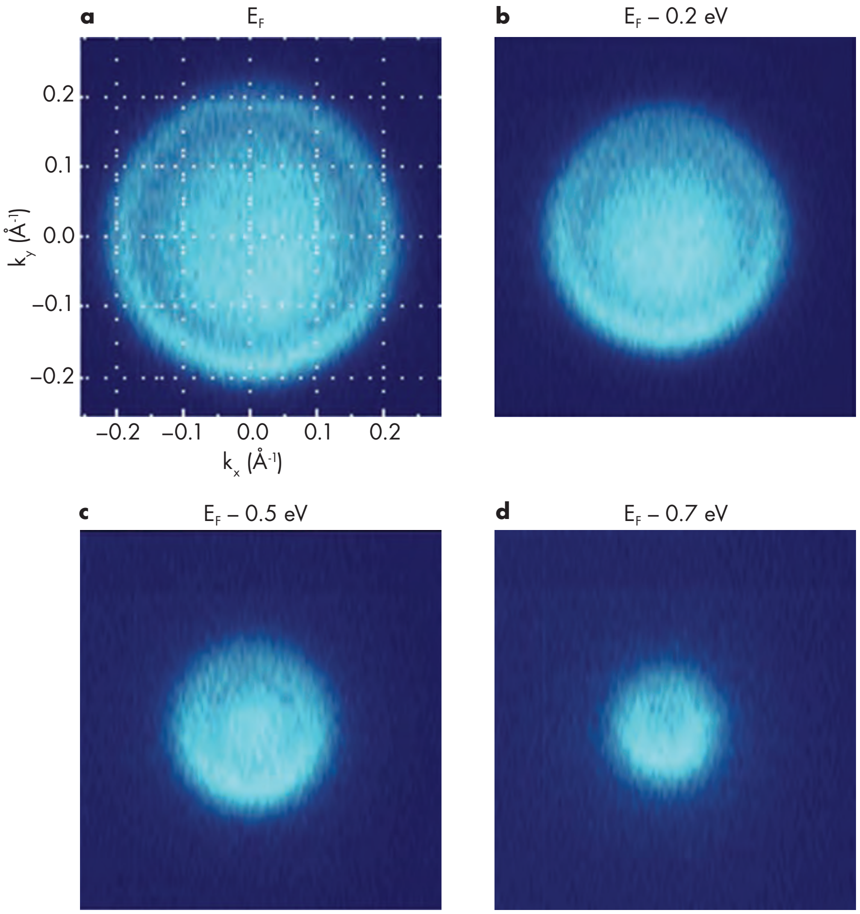

FIGURE 17. Constant-binding-energy contours extracted from ARPES data. Contours are for binding energies of 0, 0.2, 0.5, and 0.7 eV below the Fermi level, E_F. A hexagonal structure appears as the distance from E_F increases.

existence of a potential well perpendicular to the film surface. Downward band bending forms a one-dimensional potential well, and the resulting two-dimensional electron gas is quantized along the direction normal to the surface.

The researchers also examined constant-binding-energy contours below the Fermi level, E_F. Figure 17 presents a series of constant-binding-energy contours—horizontal slices taken at various distances below E_F—extracted from a data set similar to that in Figure 16. These Fermi surfaces were found to consist of concentric, perfectly circular structures associated with each of the two quantum-well states, but as the binding energy gets farther below E_F, a hexagonal structure appears, most clearly seen in Figure 17c. Although the researchers note that the orientation of the hexagonal structure is identical to that of InN's measured low-energy electron diffraction (LEED) pattern reflecting the surface unit-cell symmetry, calculated constant-energy contours are required for further analysis.

The researchers also point out that the Fermi level and the size of the Fermi surface for these quantum-well states could be controlled by varying the method of surface preparation. ARPES spectra taken from two different samples showed fundamental differences in the energies of the subband minima. These differences are directly related to the charge densities in the conduction bands. The sample surface in one case was prepared by simply annealing in UHV; in the other case, the surface was prepared by two cycles of N_2^+ bombardment and UHV annealing. Clearly, the latter method of surface preparation led to a higher density of charge donors, most likely N vacancies.

INVESTIGATORS

L. Colakerol, H.-K. Jeong, L. Plucinski, A. DeMasi, T. Learmonth, P.-A. Glans, S. Wang, Y. Zhang, T.-C. Chen, T.D. Moustakas, and K.E. Smith (Boston University); T.D. Veal, L.F.J. Piper, P.H. Jefferson, and C.F. McConville (University of Warwick, UK); and A. Fedorov (ALS).

PUBLICATION

L. Colakerol, T.D. Veal, H.-K. Jeong, L. Plucinski, A. DeMasi, T. Learmonth, P.-A. Glans, S. Wang, Y. Zhang, L.F.J. Piper, P.H. Jefferson, A. Fedorov, T.-C. Chen, T.D. Moustakas, C.F. McConville, and K.E. Smith, "Quantized electron accumulation states in indium nitride studied by angle-resolved photoemission spectroscopy," *Phys. Rev. Lett.* **97,** 237601 (2006).

FUNDING

National Science Foundation, Army Research Office, and Air Force Office of Scientific Research.

BEYOND THE LONE-PAIR MODEL

Perfect symmetry can be beautiful, but boring. In some materials, it is the slight imperfections found on the atomic scale that can lead to the most interesting—and potentially valuable—macroscopic properties. In semiconductors, the introduction of dopants provides the extra electrons or holes needed to conduct electricity. Ferromagnetism occurs when unpaired electrons in incompletely filled shells are free to align their spins in a particular direction. And, as discussed below, ferroelectricity arises in materials whose crystal structures are a bit out of alignment, creating an asymmetric charge distribution (i.e., polarization) in the bulk material. The coupling of the latter two phenomena, ferromagnetism and ferroelectricity, in composite materials or even in a single "multiferroic" material, offers the exciting prospect of devices in which electric polarization can be induced by a magnetic field and magnetization can be induced by an electric field—providing an extra "degree of freedom" for device designers. As we get better at synthesizing complex nanostructures that mix and match these properties, studies such as this one by Payne et al. become increasingly important in helping us to understand and exploit the possibilities inherent in Nature's imperfections.

"Ferroelectricity," by analogy to ferromagnetism, is defined as the presence of spontaneous electrical polarization in a material, often arising from distortions in the material's crystal structure. In oxides of the metals lead and bismuth, such distortions were for many years attributed to the existence of "lone pair" electrons: pairs of chemically inert, nonbonding valence electrons in hybrid orbitals that leave noticeable voids in the crystal structure. At the ALS, researchers from the U.K., Ireland, and the U.S. have now obtained definitive experi-

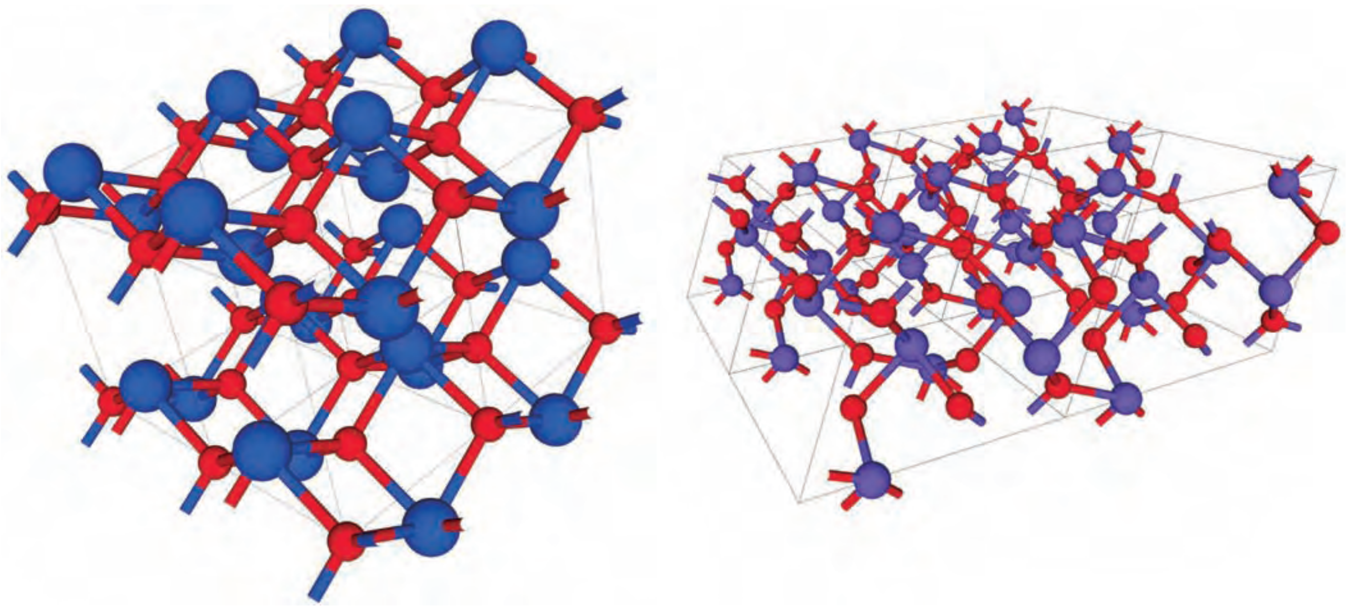

FIGURE 18. Left: In the low-temperature phase of lead oxide (α-PbO), each lead atom (blue) forms a tetragon with four oxygen nearest neighbors (red) on one side. Right: In monoclinic bismuth oxide (α-Bi_2O_3), the two distinct bismuth ions (blue) both have five oxygen near neighbors (red), creating a distorted square pyramidal coordination geometry.

mental evidence that this lone-pair model must be revised. High-resolution x-ray photoemission spectroscopy (XPS) and soft x-ray emission spectroscopy (XES) have clarified the subtle electronic origins of the prototypical distortions in these crystal structures. The results have important implications for the tantalizing possibility of spintronic or superconducting devices combining ferroelectric and ferromagnetic properties.

The asymmetrical crystal structures of the metal oxides α-PbO and α-Bi_2O_3 (Figure 18) were for many years explained by the hybridization of the metals' 6s and 6p orbitals, which are occupied by metal 6s electrons, assumed to lie close to the Fermi energy (E_F) in the solid state. This conventional "lone-pair" model, however, has recently been called into question on the basis of density functional theory (DFT) calculations that suggest that the majority of the 6s population in α-PbO is in fact found

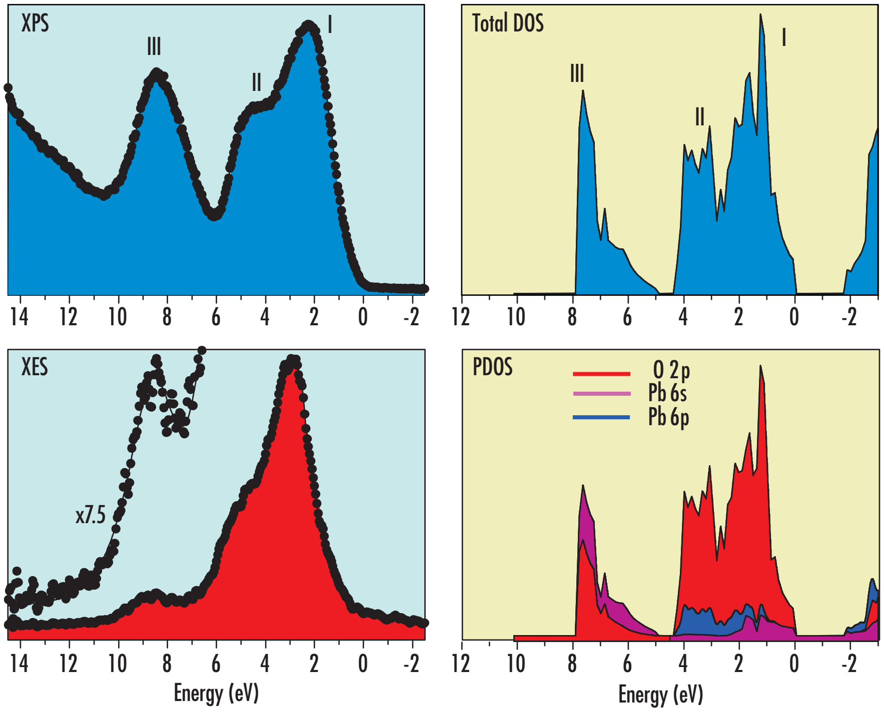

FIGURE 19. XPS (top left) and XES (bottom left) spectra of α-PbO compared to DFT calculations of the total density of states (DOS, top right) and partial density of states (PDOS, bottom right) with the contributions from the various O and Pb states indicated. The XPS data correspond to the total DOS while XES measures the O 2p PDOS. The spectra are all presented on a binding energy scale referenced to the top of the valence band. (The results for α-Bi_2O_3 are similar.)

at the bottom of the main valence band, about 10 eV below E_F. However, definitive experimental evidence supporting this idea has been lacking.

In this study, the investigators showed that consideration of the relative intensities of valence-band components in O K-shell XES, obtained at ALS Beamline 7.0.1, provides a simple but incisive experimental approach to investigating the nature of lone-pair states in metal oxides, especially when compared with the intensities of features in XPS obtained from an aluminum Kα x-ray source. Both XPS and XES spectra (and the corresponding DFT calculations) show a well-defined band (labeled III) that lies about 10 eV below the top of the valence band (Figure 19). However, this band diminishes dramatically in the XES data. Since O K-shell XES is governed by a very strict selection rule that allows only states of O 2p character to decay into the O 1s core hole, the XES data directly measures the O 2p partial density of states (PDOS).

The conclusion, fully supported by DFT calculations, is that there can be little O 2p character in this band, and by default, the associated electronic states must have dominant metal 6s character. These findings confirm that the structural distortions in α-PbO and α-Bi_2O_3 should not be attributed to the direct hybridization of metal orbitals close to E_F, resulting in purely metal-based 6s-6p lone pairs. Instead, the dominant contribution to the metal 6s PDOS is found at the bottom rather than the top of the valence band, and *indirect* mixing between 6s and 6p states is mediated by hybridization with oxygen 2p states at the top of the valence band.

It follows that qualitative textbook explanations of structural distortions in many heavy post-transition-metal compounds should be revised, with important implications for understanding the structural physics of, for example, magnetic ferroelectric materials such as $BiMnO_3$ and $BiFeO_3$. The results are also of general significance in relation to the electronic structures of ternary lead and bismuth oxides, including the many high-temperature superconducting phases that contain these heavy cations. It has in the past been assumed that the 6s states lie close to E_F and therefore contribute significantly to the states responsible for conduction in metallic phases. The present findings demonstrate that this viewpoint is not correct. Again, this will have an impact on our understanding and tuning of the physical properties of these and related materials.

INVESTIGATORS

D.J. Payne and R.G. Egdell (Oxford University); A. Walsh and G.W. Watson (Trinity College); J. Guo (ALS); and P.-A. Glans, T. Learmonth, and K.E. Smith (Boston University).

PUBLICATION

D.J. Payne, R.G. Egdell, A. Walsh, G.W. Watson, J. Guo, P.-A. Glans, T. Learmonth, and K.E. Smith, "Electronic origins of structural distortions in post-transition metal oxides: Experimental and theoretical evidence for a revision of the lone pair model," *Phys. Rev. Lett.* **96,** 157403 (2006).

FUNDING

U.K. Engineering and Physical Sciences Research Council, Higher Education Authority (Ireland), and U.S. DOE BES.

ELECTRON-STATE HYBRIDIZATION IN HEAVY-FERMION SYSTEMS

Anisotropy is a fancy word for a simple concept: dependence on direction. For example, you can get lost in a forest of isotropic trees (they look the same in every direction), but not if you know that moss grows on them anisotropically (only on the north side). An even better method for getting your bearings is to measure the directionality (anistropy) of the Earth's magnetic field (using a compass). Modern technology is replete with examples of anistropy at work. Polarized lenses in sunglasses filter light waves that oscillate in a certain direction. Flat-screen televisions utilize liquid crystals whose molecules line up under the influence of electric fields. High-performance read-write drives exploit the directionality of properties such as electrical conductivity and resistance. In this work, Molodtsov et al. examine the momentum dependence (i.e., the anisotropy) of electron-state hybridization in a heavy-fermion compound containing the rare-earth element, ytterbium (Yb). Their findings are of high importance for both the understanding and the tailoring of the anisotropic electronic, transport, and magnetic properties of heavy-fermion superconducting, thermoelectric, and ultrafast optomagnetic devices.

Heavy-fermion systems are characterized by electrons with extremely large effective masses. The corresponding heavy-electron "quasiparticle" states are close to the Fermi energy and govern the thermodynamic, transport, and, in part, magnetic properties of these materials. In the case of rare-earth compounds, the quasiparticle states arise from the interactions (hybridization) of valence states with strongly localized 4f states (Figure 20). The question as to whether it is sufficient to treat the f states as localized impurities (single-impurity Anderson model) or whether the periodic crystal symmetry must be considered (periodic Anderson model) has been the subject of extensive debate. An international team of researchers from Germany, Ukraine, India, and the U.S. has performed angle-resolved photoemission spectroscopy (ARPES) studies of the heavy-fermion system $\mathrm{YbIr_2Si_2}$. The results show a strong momentum (directional) dependence of the hybridization that clearly rules out the single-impurity model in favor of the lattice model.

The 14 "rare-earth" elements following lanthanum in the periodic table are characterized by the successive filling of inner 4f states with electrons while the number of valence electrons remains almost constant. Since the 4f shell lies relatively close to the atomic core, the f orbitals do not contribute to chemical bonding and tend to retain their atomic-like properties in solids. This holds particularly for their high magnetic moments. As a consequence, a number of rare-earth compounds belong to the strongest hard magnetic species frequently used as permanent magnets and magnetic storage materials. However, at temperatures below a critical temperature (the Kondo temperature, T_K), the 4f magnetic moments can be fully screened by the spins of itinerant electrons. This interaction retards the itinerant electrons and greatly increases their effective mass. Within the Anderson model, the phenomenon may be described by electron hopping between the states.

Most direct experimental insight into this problem may be expected from ARPES, which reflects the momentum-resolved response of the electronic system (i.e., electron energy dispersion). Expected features in the spectrum of a heavy-fermion system include a sharp virtual bound state (below T_K, called the Kondo resonance) and narrow, 4f-derived quasiparticle bands near the Fermi level (E_F). ARPES studies of heavy-fermion narrow-band compounds are only possible, however, under superior conditions with high-photon-flux experimental equipment providing ultrahigh energy (several meV) and angle resolution (a few tenths of a degree).

At ALS Beamline 10.0.1, ARPES spectra of $\mathrm{YbIr_2Si_2}$ were taken at 20 K (below $T_K \sim 40$ K) and 55-eV photon energy for different emission angles Θ. The results demonstrate for the first time the strong angle (i.e., momentum) dependence of the hopping interactions in a heavy-fermion system. Two valence bands are visible, one of which intersects with the Yb 4f surface emission at 0.6-eV binding energy (Figure 21). In the region of the interaction, the 4f state splits into two

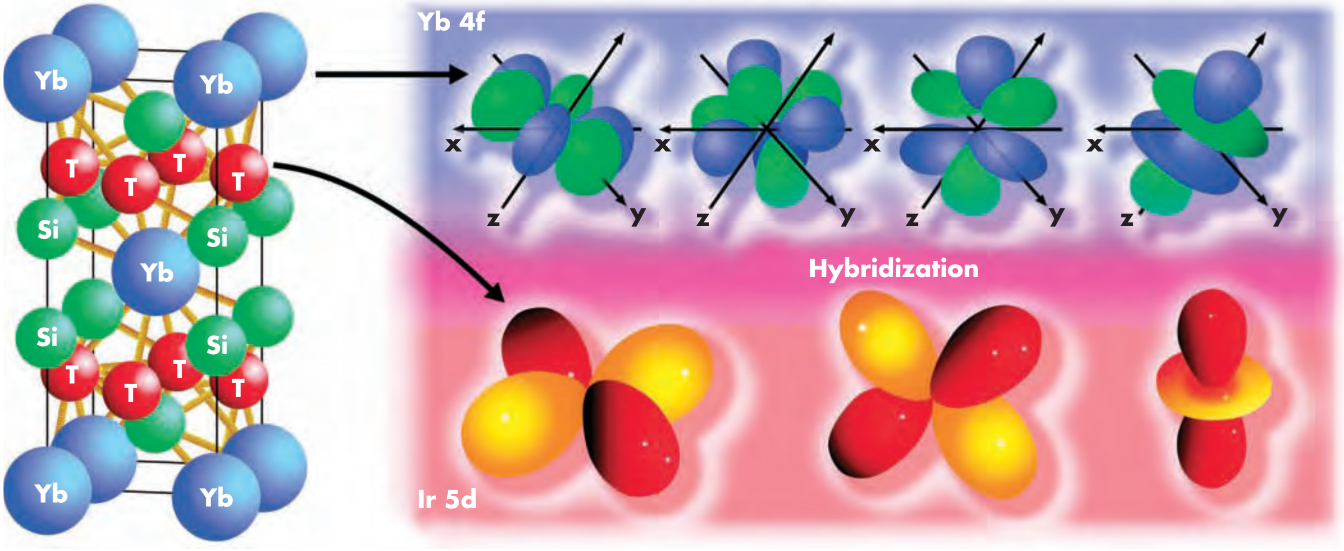

FIGURE 20. Representation of the crystal structure of $\mathrm{YbIr_2Si_2}$ (the letter T represents a transition metal, in this case, Ir) and the shapes of the Yb 4f and Ir 5d orbitals involved in hybridization.

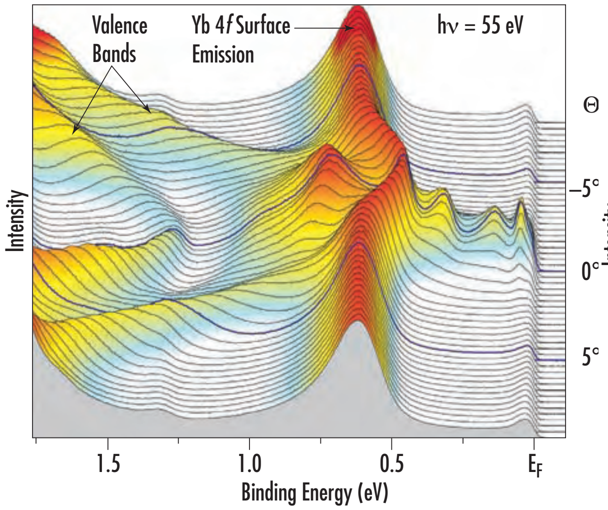

FIGURE 21. ARPES spectra of the heavy-fermion system $YbIr_2Si_2$ showing two parabola-shaped valence bands on the left, one of which intersects the 4f surface emission of the rare-earth element Yb. Signal in the region of E_F reveals strongly anisotropic behavior.

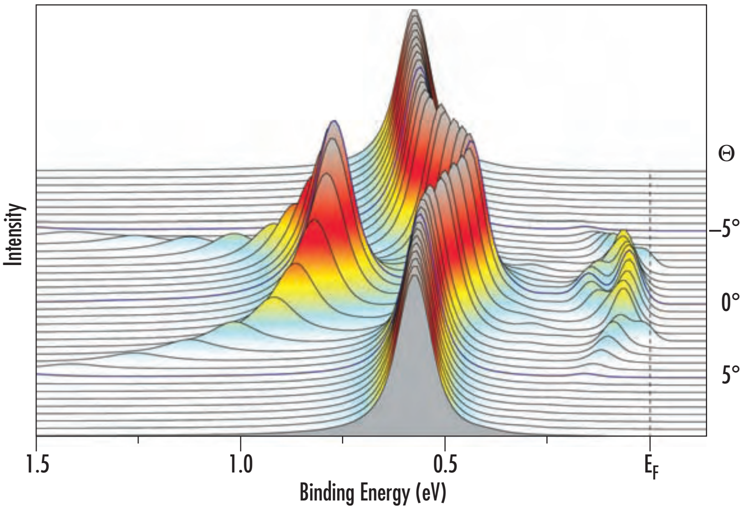

FIGURE 22. ARPES spectra calculated on the basis of the periodic Anderson model nicely reproduce all 4f characteristic features of the experiment.

components separated by up to 0.25 eV. At the same emission angles, further peaks appear at lower binding energy, including a signal in the region of the Kondo resonance immediately at E_F.

Since a proper description of rare-earth systems by means of conventional approximations used in band structure theory is not possible because of strong Coulomb repulsions between the electrons in the relatively compact 4f shells, the data were analyzed within the framework of a simplified periodic Anderson model: starting from valence bands obtained from the calculation of an isostructural La/Ba compound and two Yb 4f states close to E_F and at 0.6-eV binding energy, the 4f emission spectra were obtained within the periodic Anderson model assuming momentum conservation upon electron hopping. The calculated 4f ARPES spectra nicely reproduce all 4f characteristic features of the experiment (Figure 22). The results, obtained for the compound $YbIr_2Si_2$, can readily be used to understand the properties of other heavy-fermion systems in which momentum-dependent anisotropies may be of primary importance in future electronic and magnetic applications.

INVESTIGATORS

S. Danzenbächer, C. Laubschat, D.V. Vyalikh, and S.L. Molodtsov (Dresden University of Technology); Y. Kucherenko (Dresden University of Technology and National Academy of Sciences of Ukraine); Z. Hossain (Max Planck Institute for Chemical Physics of Solids and Indian Institute of Technology); C. Geibel (Max Planck Institute for Chemical Physics of Solids); X.J. Zhou, W.L. Yang, and N. Mannella (Stanford University and ALS); Z. Hussain (ALS); and Z.-X. Shen (Stanford University).

PUBLICATION

S. Danzenbächer, Y. Kucherenko, C. Laubschat, D.V. Vyalikh, Z. Hossain, C. Geibel, X.J. Zhou, W. Yang, N. Mannella, Z. Hussain, Z.-X. Shen, and S.L. Molodtsov, "Energy dispersion of 4f-derived emissions in photoelectron spectra of the heavy-fermion compound $YbIr_2Si_2$," *Phys. Rev. Lett.* **96**, 106402 (2006).

FUNDING

German Research Foundation, German Ministry for Education and Research, U.S. DOE BES, National Science Foundation, and Office of Naval Research.

BRIDGING THE GAP BETWEEN MOMENTUM SPACE AND REAL SPACE

The Heisenberg uncertainty principle tells us that it is possible to know either the momentum or the position of a quantum mechanical state, but not both. Conventional solid state physics revolves around using the momentum of electrons to describe and derive material properties. In materials where very strong interactions interfere with this picture, the behavior of electrons on the other side of the uncertainty principle becomes important. A high-temperature superconductor, in which strong correlations drive the superconducting transition temperature up to 150 K, is a good example of such a system in which what happens spatially may have a strong impact on the material's properties. A team of researchers has here introduced a new technique that allows us to peer across the uncertainty principle from momentum space (where each point in space represents a momentum value as opposed to a position value) into real space. This new approach allows us to extract the elastic scattering susceptibility of a material and to predict what happens when disorder in the material scatters electrons, a fundamental property for many materials.

In investigating materials such as high-temperature superconductors, two probes have proven invaluable: angle-resolved photoemission spectroscopy (ARPES), which probes systems by their momentum properties, and scanning tunneling microscopy (STM), which probes systems by their spatial properties. In the work described here, a collaboration of researchers from Berkeley and Japan have introduced a new technique for using the momentum-resolved probe ARPES to peer across the uncertainty principle into real space and predict what happens when disorder scatters electrons. They found excellent agreement between the position-resolved and momentum-resolved behaviors in two samples of the high-temperature superconductor, Bi2212, one sample optimally doped and the other underdoped. This result is encouraging news for a novel tool that bridges the momentum–position divide represented by Heisenberg's principle.

In recent work, real-space measurements by STM have revealed a great deal of complex structure in the local density of states (a measure of where electrons sit in a material from atom to atom). These results can be interpreted in a couple of ways: as indications of a new state of matter in which the real-space organization of electrons plays a role or as the response of wave-like electronic states with well-defined momentum scattering off of defects in the crystal structure like ripples in a pond. Resolving which aspects of these real-space patterns result from the scattering of momentum states is crucial to solving this mystery.

To make a direct comparison between the real- and momentum-space properties of a high-temperature superconductor, the researchers used ARPES measurements of Bi2212 taken at the ALS (Beamlines 10.0.1 and 12.0.1) and SSRL. In ARPES, high-energy photons are used to eject electrons from the surface of a material; the energy and angle distribution of the electrons is then mapped out. Using conservation laws, this data can be converted into a map of the electrons' energy and momentum distribution while they were still in the material, before the ejection. However, a way to relate this momentum information to real-space measurements is needed.

The momentum-space autocorrelation (AC) is a mathematical transformation that takes an ARPES image and searches it for regions where there are many states off of which to scatter. The transformation then returns a map, in momentum space, that shows the susceptibility of the material (within a simple model) for scattering a given momentum. For this transformation to reproduce the real-space STM results, the Bi2212 would have to be responding in a rather traditional way, where single-electron-like momentum states are sufficient to describe the physics. In fact, a comparison of the AC-ARPES and STM data shows excellent agreement (Figure 23). This indicates that the low-energy electronic states of these complex materials indeed behave in a traditional manner and that STM and ARPES are consistent measurements of the same underlying physical phenomena.

In addition to being to consistent with each other, the two spectroscopic probes are also complementary. One aspect of STM results that has not been well characterized is the

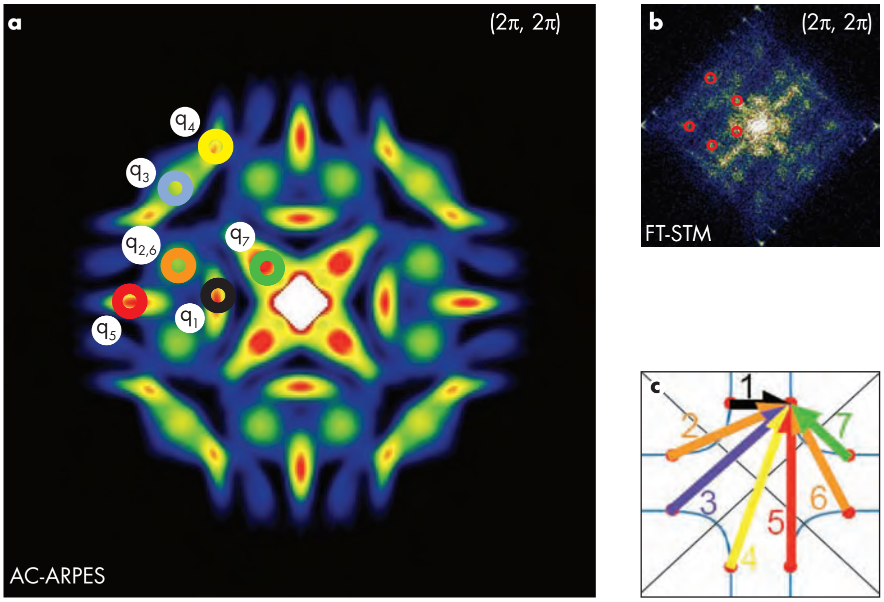

FIGURE 23. A comparison between the Fourier transform (FT) of the electronic structure of the high-temperature superconductor Bi2212 as measured by (a) AC-ARPES and (b) FT-STM at –10 meV. Circles mark the peaks associated with a simple single-electron model. The corresponding scattering vectors and Fermi surface are shown in (c).

so-called matrix element. The matrix element governs which types of electrons are visible to a given probe. In STM it is something that is poorly understood and over which experimenters have little control. On the other hand, ARPES has a well-understood matrix element that can be controlled by experimental geometry. By comparing different ARPES geometries with STM results, the approximate form of the matrix element can be found. In general, this novel analytical technique also has broad applicability to other materials, as it allows us to map out the reaction that a material will have to different types of perturbations. Doing this can lead to predictions for scattering and susceptibility to particular interactions, by relating the momentum space of a material to its real-space response.

INVESTIGATORS

K. McElroy and J. Graf (Berkeley Lab), G.-H. Gweon and S.Y. Zhou (UC Berkeley), S. Uchida (University of Tokyo), H. Eisaki (National Institute of Advanced Industrial Science and Technology, Japan), H. Takagi (University of Tokyo, Japan Science and Technology Agency, and Japan Institute of Physical and Chemical Research), T. Sasagawa (University of Tokyo and Japan Science and Technology Agency), and D.-H. Lee and A. Lanzara (Berkeley Lab and UC Berkeley).

PUBLICATION

K. McElroy, G.-H. Gweon, S.Y. Zhou, J. Graf, S. Uchida, H. Eisaki, H. Takagi, T. Sasagawa, D.-H. Lee, and A. Lanzara, "Elastic scattering susceptibility of the high temperature superconductor $Bi_2Sr_2CaCu_2O_8{+}_\delta$: A comparison between real and momentum space photoemission spectroscopies," *Phys. Rev. Lett.* **96,** 067005 (2006).

FUNDING

U.S. DOE BES, National Science Foundation, and Sloan Foundation.

Magnetism and Magnetic Materials

MAGNETIC VORTEX CORE REVERSAL BY LOW-ENERGY EXCITATIONS

The consumer electronics industry seems to have an endless supply of "must-have" products, and to sell, each new gizmo must be smaller, or faster, or have quadzuple the capacity of the old model. Is there a physical limit to how far this process can go? At the heart of each digital device is a way to physically store data in binary form. For magnetic media, binary digits (bits) take the form of grains of magnetic material in which the spins are aligned. As we increase the number of bits in a finite area (areal density), a point is reached (the superparamagnetic limit) where thermal vibrations are no longer negligible and can knock bits out of alignment. While advances in technology have forestalled this limit for now (areal densities of up to 400 gigabits per square inch have been achieved in a laboratory setting), scientists are looking farther down the road at completely new ways to encode binary information. Magnetic vortex cores, being thermally stable and measuring just 10 nm across, offer one tantalizing possibility. Not only are these structures useful for applications such as data storage, they also form an interesting playground for fundamental studies of magnetism on a microscopic level.

In micrometer-sized magnetic thin films, the magnetization typically adopts an in-plane, circular configuration known as a magnetic vortex (Figure 1). At the vortex core, the magnetization turns sharply out of the plane, pointing either up or down. Magnetic data storage based on this binary phenomenon is an intriguing concept, but it would require the ability to flip the vortex cores on demand. Because these structures are highly stable, very strong magnetic fields of around half a tesla (approximately one-third the field of the strongest permanent magnet) were previously thought to be necessary to accomplish this. At the ALS, a team of researchers from Germany, Belgium, and the U.S. has used time-resolved scanning transmission x-ray microscopy (STXM) to observe vortex motion and demonstrate the feasibility of using weak magnetic fields as low as 1.5 millitesla (mT) to reverse the direction of a vortex core. The observed switching mechanism, which can be understood within the framework of micromagnetic theory, gives insights into basic magnetization dynamics and their possible application to data storage technologies.

In magnetic thin films, magnetostatic interactions usually force the magnetization to lie parallel to the film plane. When further constrained to an area of about a square micrometer or less, the magnetic moments will form rotationally symmetric patterns that follow closed flux lines. At the center, the tightly wound magnetization cannot lie flat, because the short-range exchange interaction favors a parallel

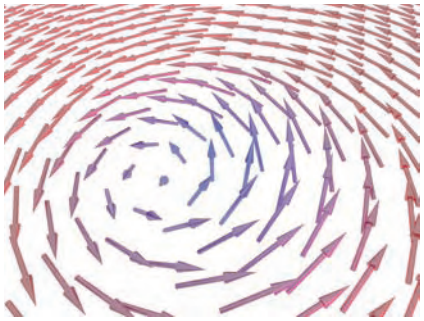

FIGURE 1. Representation of a magnetic vortex.

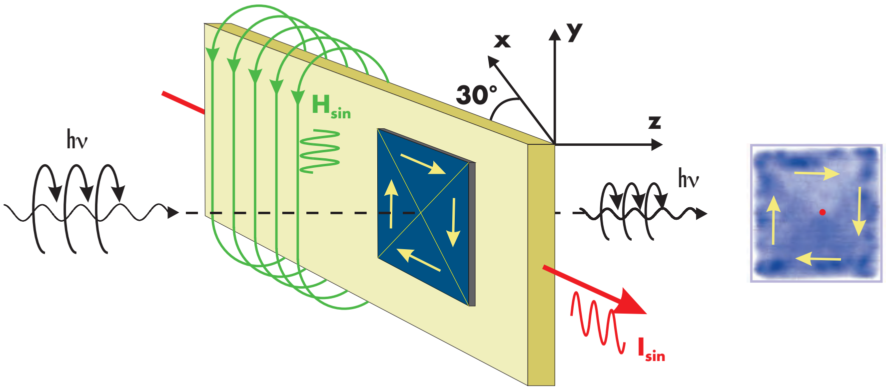

FIGURE 2. Schematic of the sample setup. An alternating current I_{sin} generates an in-plane magnetic field H_{sin}. Circularly polarized x-ray photons are selectively absorbed by the magnetic domains of the sample. An example of the magnetic contrast is shown at the right. The yellow arrows indicate the magnetization in the four domains.

alignment of neighboring magnetic moments. The direction of the out-of-plane component is defined as the polarization of the vortex core. Moreover, the vortex structure can be set into gyrotropic motion by the application of a small magnetic field, and the sense of the gyration (clockwise or counterclockwise) is determined by the vortex core polarization. Thus, a change in the sense of gyration unambiguously indicates a change in the vortex core polarization.

In this experiment, the researchers applied a small (0.1-mT) sinusoidal magnetic field to induce gyrotropic motion in a square Permalloy ($Ni_{80}Fe_{20}$) sample. The excitation frequency was set at 250 MHz, close to the resonance frequency of the system (about 244 MHz) derived from micromagnetic simulations. The excitation field was synchronized with flashes of circularly polarized x rays from ALS Beamline 11.0.2 to produce dynamic STXM images, with x-ray magnetic circular dichroism (XMCD) providing the contrast mechanism (Figure 2). A short (4-ns) burst of 1.5 mT was applied, superimposed on the weak alternating field. The results show that the vortex core follows an elliptical trajectory, and a change in the sense of the gyration (and thus the vortex core polarization) can be clearly seen after the burst (Figure 3).

This vortex core switching, observed experimentally for the first time, was also reproduced by micromagnetic simulations (Figure 4). The simulations show that the burst distorts the out-of-plane vortex structure and creates a region of opposite out-of-plane magnetization at the edge of the original vortex core. This opposite magnetization grows and eventually splits into a vortex–antivortex pair with equal polarizations. The newly formed vortex and antivortex move apart, and the antivortex moves toward the original vortex. When the antivortex meets the original vortex, they annihilate each other, emitting spin waves in the process, until only one vortex, having a reversed polarization, remains in the structure.

These results show that properly tuned bursts of only 4 ns can be used to switch the polarization of a vortex core. Because the resonance frequency of the gyrotropic mode scales inversely with the lateral dimensions, much shorter pulses should be sufficient for switching the core polarization of smaller elements. Although their practical realization is still far off, data storage systems based on this core-switching scheme could have several advantages, including high thermal stability, insensitivity to external static fields, and minimal crosstalk between neighboring patterns, all of which are indispensable features for ultrahigh-density magnetic storage devices.

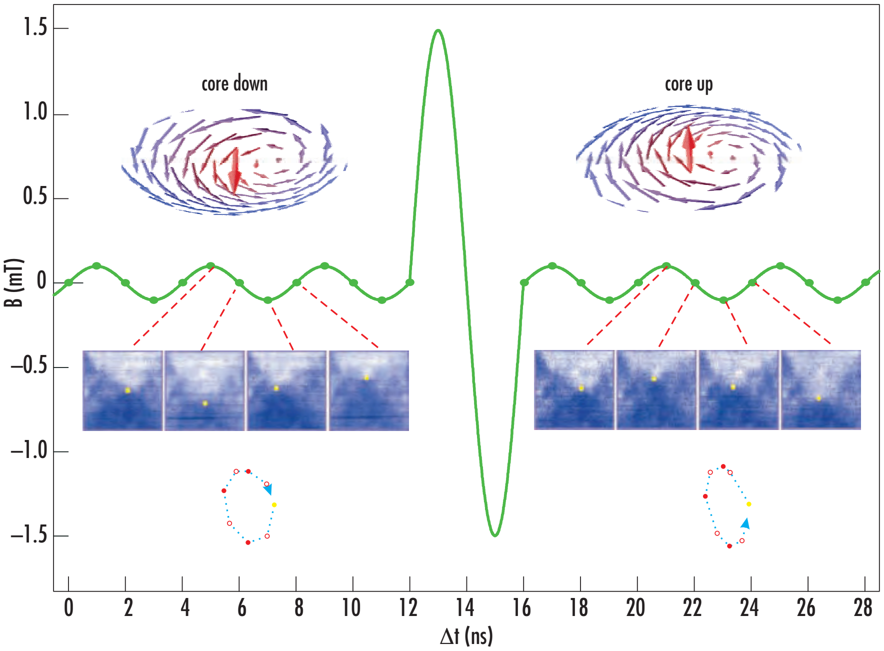

FIGURE 3. Points on the sinusoidal magnetic field (green curve) correspond to x-ray flashes that record individual frames of the vortex-core movie. When the frames are strung together, they reveal the sense of gyration of the vortex core. Before the burst, the gyration is clockwise, corresponding to a vortex core polarization pointing down. After the burst, the gyration is reversed, and the vortex core polarization points up.

INVESTIGATORS

B. Van Waeyenberge (Max Planck Institute for Metals Research and Ghent University, Belgium); A. Puzic, H. Stoll, K.W. Chou, M. Fähnle, and G. Schütz (Max Planck Institute for Metals Research); T. Tyliszczak (ALS); R. Hertel (Research Centre Jülich, Germany); H. Brückl, K. Rott, and G. Reiss (Bielefeld University, Germany); and I. Neudecker, D. Weiss, and C.H. Back (University of Regensburg, Germany).

PUBLICATION

B. Van Waeyenberge, A. Puzic, H. Stoll, K.W. Chou, T. Tyliszczak, R. Hertel, M. Fähnle, H. Brückl, K. Rott, G. Reiss, I. Neudecker, D. Weiss, C.H. Back, and G. Schütz, "Magnetic vortex core reversal by excitation with short bursts of an alternating field," *Nature* **444,** 461 (2006).

FUNDING

German Research Foundation.

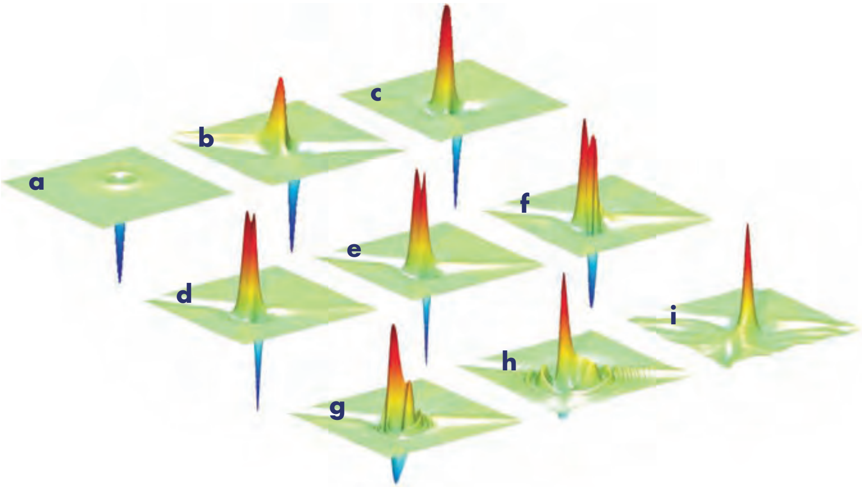

FIGURE 4. Micromagnetic simulation of the reversal of the vortex core excited with a short magnetic field pulse. In the initial state, the vortex core is pointing down (a). Under influence of the external field, a region forms with opposite magnetization (b) and reaches full amplitude (c) before a double peak is created: a vortex–antivortex pair (d). The antivortex moves toward the original vortex (e) and annihilation occurs, creating spin waves (f–h). A vortex core with opposite polarization remains (i).

ULTRAFAST MAGNETIC SWITCHING OF NANOELEMENTS WITH SPIN CURRENTS

Spintronics is a word we will probably hear more often in the coming years. Already, hard drives incorporating spin valves in giant magnetoresistance (GMR) read heads have become commonplace in such consumer electronics products as notebook computers, smartphones, handhelds, and MP3 players. Spin-transfer structures, or "spin valves," in these devices are designed to sense the external magnetic field on a hard drive. The next step is a magnetic random-access memory (MRAM) device that stores the information magnetically without moving parts. Like flash memory, MRAMs would retain their state without a power supply but would rival the performance of volatile RAM. Understanding the behavior of spin-polarized currents at the nanoscale will be essential in developing practical MRAM and will pave the way for a variety of future devices, such as all-spintronic processors and hybrid optical-spintronic devices.

Time-resolved images of the magnetization switching process in a spin-transfer structure, obtained by ultrafast x-ray microscopy, reveal a complex picture of how this switching works. Instead of a coherent magnetization reversal, researchers observed switching by lateral motion of a magnetic vortex across a nanoscale element. Their measurements reveal the roles played independently by charge and spin currents in breaking the magnetic symmetry on picosecond time scales.

In experiments at ALS Beamline 11.0.2, an unpolarized charge current was sent through a lithographically manufactured pillar containing two magnetic layers (Figure 5). The polarizer creates a spin-polarized current either in transmission or in reflection, depending on the direction of current flow through the pillar. The polarizer is separated from a second ferromagnetic (FM) layer, the sensor, by a nonmagnetic spacer layer. The goal is to reliably switch the magnetization of the sensor layer by reversing the direction of current flow.

X-ray images were recorded using scanning transmission x-ray microscopy (STXM) with a spatial resolution of

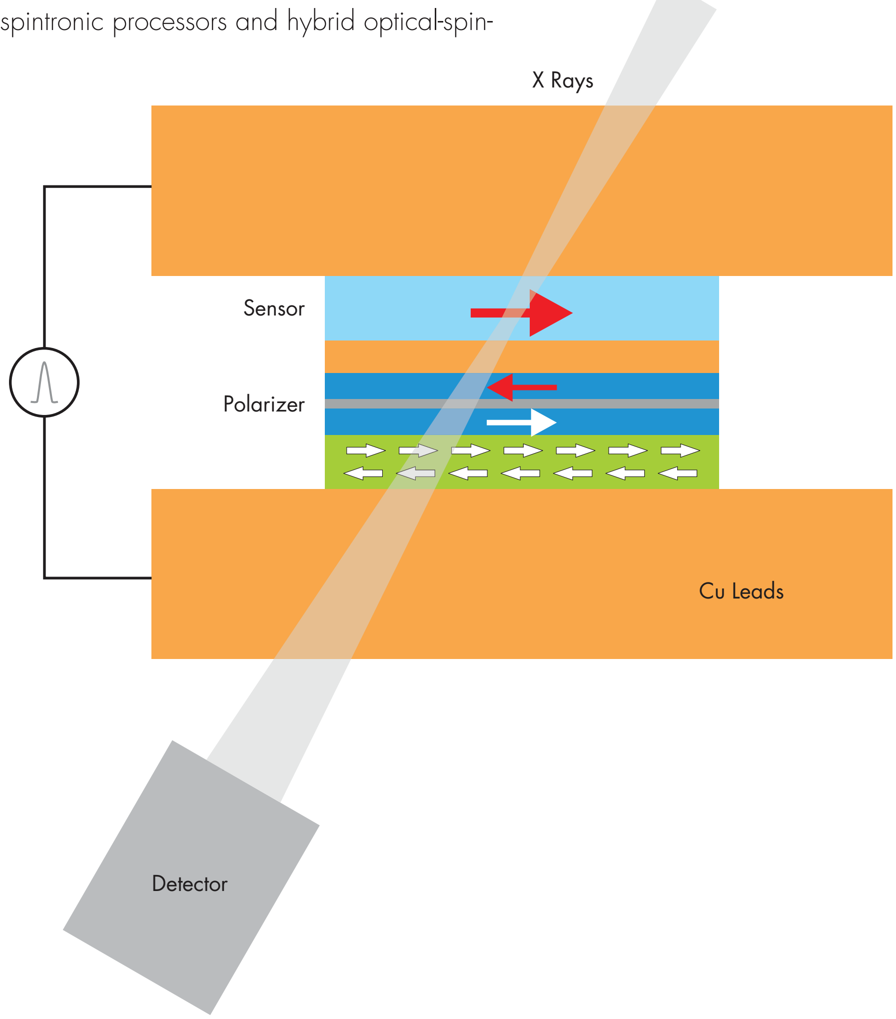

FIGURE 5. Schematic of the pillar structure, showing the ferromagnetic layers in blue, an antiferromagnetic pinning layer in green, and copper leads and spacer layers in orange. The bottom two FM layers are coupled into a fixed antiferromagnetic arrangement by a ruthenium spacer layer, and their magnetization direction is pinned by exchange coupling to the green antiferromagnet shown at the bottom.

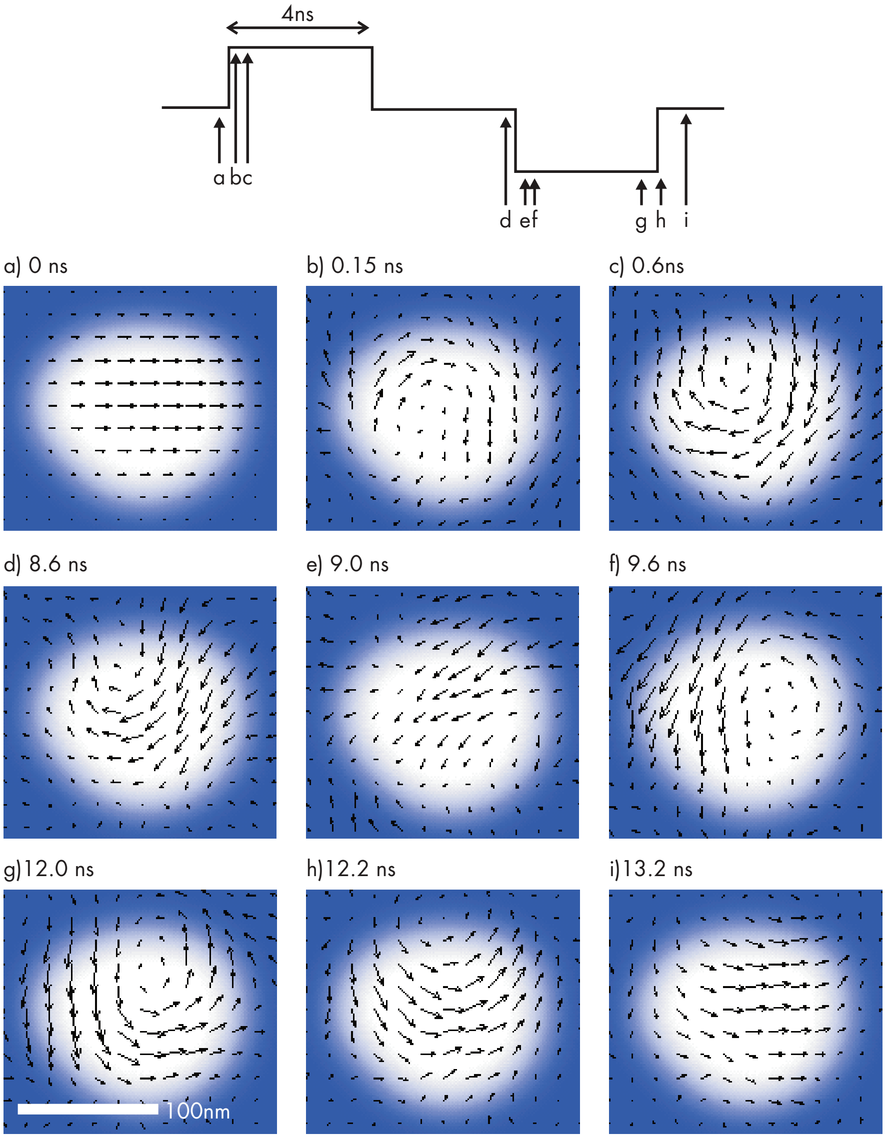

a) 0 ns b) 0.15 ns c) 0.6ns

d) 8.6 ns e) 9.0 ns f) 9.6 ns

g)12.0 ns h)12.2 ns i)13.2 ns

FIGURE 6. Top: Pulse sequence. Bottom: The uniform antiparallel configuration (a) is switched into a C state with a parallel M_x component (c). The switching process involves motion of a magnetic vortex through the sensor later, visible in (b). The C state is metastable after the falling edge of the pulse (d) and is reversed by the set pulse into another C state (f). The switching of one C state into another is caused by lateral vortex motion as well, leaving a uniformly magnetized area in the center of the sensor layer (e). The C state with its horizontal x component antiparallel to the polarizer is unstable and relaxes into the uniform state (g)–(i). This relaxation is deterministic but comparatively slow.

about 30 nm. Circularly polarized x rays from the beamline's variable polarization undulator were incident at an angle of 30° from the surface normal of the sample. Images for two orthogonal azimuthal sample orientations relative to the fixed x-ray direction were the basis for arrow plots of the in-plane magnetization directions in the $Co_{0.86}Fe_{0.14}$ sensor layer.

The switching process, and even the final switched states, turn out to be more complicated than can be accounted for by spin injection alone. Oersted fields, which accompany the flow of a charge current, are present inside and outside the pillar, with a zero value at the center of the pillar and maximum value at its periphery. The curl associated with these fields may be important in initiating the spin injection switching process and may result in nonuniform switching and even a curled static magnetization in the sensor—an undesirable outcome, since curled states reduce or even eliminate GMR.

A pump–probe technique allowed isolation of the small magnetic signal from the 4-nm-thick sensor layer. Opposite-polarity-current "pump" pulses of 4-ns duration and separation were synchronized with the x-ray pulses from the storage ring. The x-ray "probe" pulses of about 100 ps FWHM were separated by 2 ns. For a given sample position in the beam, the transmitted x-ray intensity was recorded separately for eight consecutive x-ray probe pulses. This cycle was repeated to accumulate adequate signal-to-noise ratios. The sample was then moved to a new position and the procedure was repeated to produce a complete set of magnetic images of the sensor layer.

The results in Figure 6 indicate that only the reset spin-injection pulse leads to a uniform magnetization direction. All other cases reveal a curled state, caused by the Oersted field. The curled states observed during the set pulse, shown in (c), and after the pulse, shown in (d), are almost identical. This shows that the magnetization remains in the same curled state when the current is switched off.

Oersted fields clearly accompany spin injection for samples of size near 100 nm. This is an unexpected result. The Oersted fields have important consequences. The curled Oersted field breaks the mirror symmetry along the spin direction and creates a nonzero torque on the sensor layer magnetization immediately after the rising edge of the current pulse, so that no thermal fluctuations are needed to initiate switching. In response to the Oersted field, a C-state is formed. The spin-polarized current then forms and shifts the vortex core to one side of the sample, resulting in a preferred magnetic alignment direction. This curled state may persist or straighten out into a linear uniform state. Finally, the observed nonthermally initiated switching process is deterministic and therefore desirable in switching applications.

INVESTIGATORS

Y. Acremann, B.H.C. Siegmann, and J. Stöhr (SSRL); J.P. Strachan, V. Chembrolu, S.D. Andrews, and M. Clemens (Stanford University); T. Tyliszczak (ALS); and J.A. Katine and M.J. Carey (Hitachi Global Storage Technologies).

PUBLICATION

Y. Acremann, J.P. Strachan, V. Chembrolu, S.D. Andrews, T. Tyliszczak, and J.A. Katine, M.J. Carey, B.M. Clemens, H.C. Siegmann, and J. Stöhr, "Time-resolved imaging of spin transfer switching: Beyond the macrospin concept," *Phys. Rev. Lett.* **96**, 217202 (2006).

FUNDING

U.S. DOE BES and National Science Foundation.

ELECTRONIC STRUCTURE AND MAGNETISM IN DILUTED MAGNETIC SEMICONDUCTORS

"When will this finally be as easy as switching on the light?" many people ask themselves as they wait for their computer operating system and programs to load from the hard drive into RAM. The answer might be "soon." Currently, most information is stored in a nonvolatile way in magnetic bits on hard drives that use electrons' spin (their orientation up or down), while semiconductor devices like RAM operate by manipulating electron charge. But the ability to manipulate electrons' spin and charge together could create new capabilities for computers—like eliminating the need for lengthy boot-up times. This is the topic of an exciting research field known as "spintronics." Manipulating an electron's magnetic state in a semiconductor device is the key to successful spintronics, and the simplest way to do that is by using a semiconductor material such as gallium arsenide (GaAs) that incorporates magnetic elements like manganese (Mn). A major obstacle is creating magnetic semiconductor materials that work at room temperature. In their research, Edmonds et al. correlate the electronic and magnetic characteristics of electrons in manganese-doped gallium arsenide. Their results are crucial for understanding and further development of a new class of semiconductors—dilute magnetic semiconductors.

The possibility of using electrons' spins in addition to their charge in information technology has created much enthusiasm for a new field of electronics popularly known as "spintronics." An intensely studied approach to obtaining spin-polarized carriers for data-storage devices is the use of diluted magnetic semiconductors created by doping ions like Mn, Fe, or Co having a net spin into a semiconducting host such as GaAs, ZnO, or GaN (Figure 7). The interaction among these spins leads to ferromagnetic order at low temperatures,

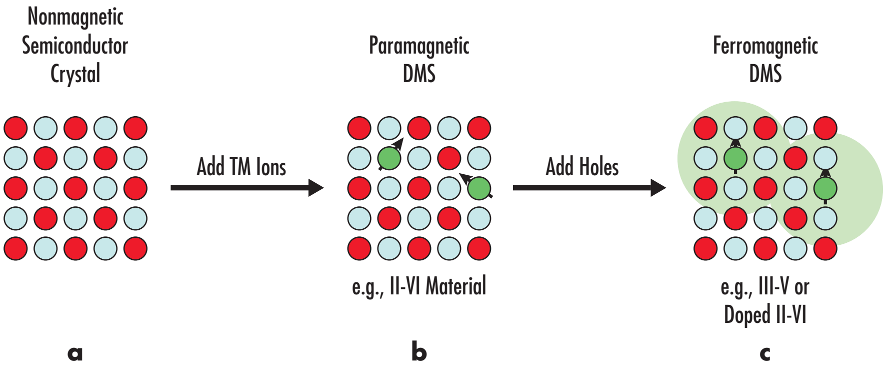

FIGURE 7. Three types of semiconductors: (a) nonmagnetic semiconductor, which contains no magnetic ions; (b) diluted magnetic semiconductor (DMS), i.e., a cross between a nonmagnetic semiconductor and a magnetic transition-metal (TM) element, in a paramagnetic state; (c) DMS with ferromagnetic order mediated by charge carriers (holes).

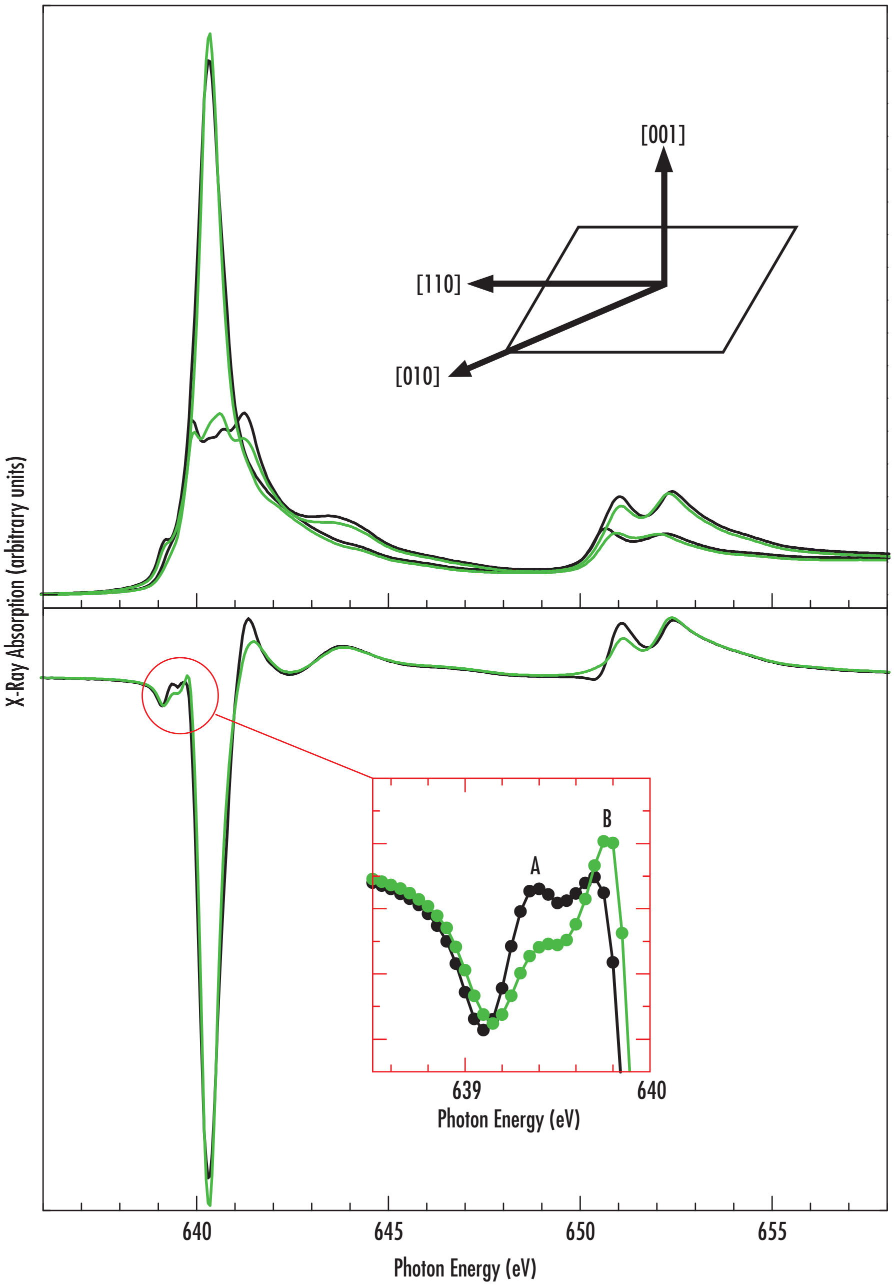

FIGURE 8. Top: Mn $L_{2,3}$ absorption spectra for parallel and antiparallel alignment of polarization and magnetization when the magnetization is aligned along the [001] (black) and [111] (green) directions. Bottom: XMCD spectra for magnetization along [001] (black) and [111] (green). The pronounced differences between the absorption spectra and the observed anisotropy in the pre-edge features in the XMCD signal (shown in the inset) are most remarkable.

which is necessary to create spin-polarized carriers. A research team working at ALS Beamline 4.0.2 and European Synchrotron Radiation Facility Beamline ID8 made a big leap forward in clarifying the microscopic picture of magnetism and anisotropy in Mn-doped GaAs by resolving localized and hybridized d states using angle-dependent x-ray magnetic circular dichroism (XMCD) measurements.

Mn-doped GaAs, in which the Mn dopant provides both a magnetic moment and a spin-polarized charge carrier, has attracted considerable interest as a spintronics material. However, the microscopic picture of magnetism and magnetic anisotropy (direction dependence of the magnetic properties) in this system is still hotly disputed. Are the Mn states localized, strongly hybridized with the GaAs valence band, or do they form a separate impurity band? To further understand this system, researchers used x-ray absorption spectroscopy (XAS) and XMCD to study (Ga,Mn)As samples. XAS measures excitation from the Mn 2p to 3d levels, thus probing the unoccupied valence states with Mn 3d character. XMCD measures the difference (dichroism) between absorption spectra obtained with opposite alignments of the sample magnetization direction and x-ray helicity vector.

XAS and XMCD spectra measured along two directions—[111] and [001]—show pronounced differences (Figure 8). Detailed study of the angular dependence illustrates that almost all spectral features, including pre-edge feature peak A, exhibit cubic symmetry about the crystalline axes. Only the pre-edge feature peak B shows a gradual increase going from out-of-plane to in-plane magnetization in both the (100) and (110) planes—i.e., uniaxial symmetry.

In annealed (Ga,Mn)As, Mn occupies Ga sites with tetrahedral symmetry. However, the (Ga,Mn)As/GaAs(001) films are placed under compressive strain, breaking the symmetry between in-plane and out-of-plane directions. This leads to a large uniaxial magnetic anisotropy. Thus, while almost all spectral features share the cubic symmetry of the Mn site, peak B reflects uniaxial symmetry of the strain field.

To determine the origin of peak B, the researchers compared experimental results to atomic multiplet calculations, which reproduce almost all of the multiplet structure of the Mn $L_{2,3}$ XMCD and correctly predict the angular dependence of those features (Figure 9), with one notable exception. The calculated spectra only show a single peak in the pre-edge region, peak A. Peak B in the experimental spectrum is not reproduced by the atomic calculation, so it must be of a different origin. Studying the size of peak B versus hole concentration, ρ, obtained from Hall measurements, shows a clear correlation, with peak B becoming more negative with increasing ρ. The intensity of peak B is thus dependent on the Fermi level position (level of the least tightly held electrons), indicating that this feature corresponds to transitions to states at or just above Fermi energy (E_F).

The uniaxial anisotropy and the correlation with hole density indicate peak B is due to hybridization of Mn d states with strain-split GaAs valence states at E_F. The results are clear evidence of a small, but finite, density of unoccupied Mn d states close to E_F. Thus, both localized atomic-like states lying far above the Fermi level and Mn 3d states strongly hybridized with the valence bands of the GaAs host are observed. The ability to separately resolve localized and hybridized d states makes angle-dependent XMCD a powerful method for determining the electronic structure of magnetic semiconductors.

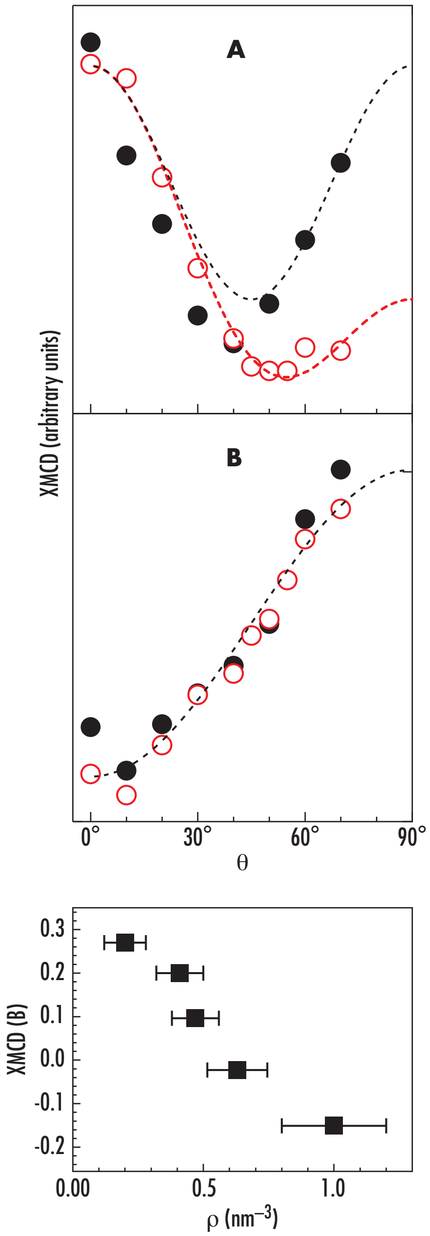

FIGURE 9. Dependence of the XMCD signal of spectral features A and B on the out-of-plane (001) angle θ. Open circles represent the angular dependence in the (110) plane, solid symbols indicate the results for the (100) plane. Dashed lines show the angular dependence expected in cubic (uniaxial) anisotropy. At the bottom is the dependence of the pre-edge features in Mn $L_{2,3}$ XMCD spectra on the hole density obtained from Hall measurements.

INVESTIGATORS

K.W. Edmonds, A.A. Freeman, N.R.S. Farley, R.P. Campion, C.T. Foxon, and B.L. Gallagher (University of Nottingham, U.K.); G. van der Laan and T.K. Johal (Daresbury Laboratory, U.K.); and E. Arenholz (ALS).

PUBLICATION

K.W. Edmonds, G. van der Laan, A.A. Freeman, N.R.S. Farley, T.K. Johal, R.P. Campion, C.T. Foxon, B.L. Gallagher, and E. Arenholz, "Angle-dependent x-ray magnetic circular dichroism from (Ga,Mn)As: Anisotropy and identification of hybridized states," *Phys. Rev. Lett.* **96**, 117207 (2006).

FUNDING

U.K. Engineering and Physical Sciences Research Council, U.K. Council for the Central Laboratory of the Research Councils, Royal Society, and U.S. DOE BES.

PARALLEL AND ANTIPARALLEL INTERFACIAL COUPLING IN AF–FM BILAYERS

Imagine getting up in the morning and finding that everything around you either is upside down or runs backwards—your bed hangs from the ceiling or the sun is going down. You would be justifiably confused, and you would certainly demand to know what was going on. The perplexity you experience is very similar to what scientists must have thought when they first studied magnetic interactions between thin layers of certain magnetic materials and found behavior upside down or backwards relative to everything they had known up to then about the magnetic properties of so called "antiferromagnetic–ferromagnetic exchange-coupled" systems. Because these systems are at the heart of many of today's most modern magnetic storage disk technologies, the bewilderment involved more than just pride. Ohldag et al. have now provided direct experimental evidence that supports a subsequently proposed explanation. Moreover, they have begun to unravel a situation that is even more complex than imagined, showing that the magnetic properties at the boundary between an antiferromagnet and ferromagnet are the result of complicated and competing processes.

Cooling an antiferromagnetic–ferromagnetic bilayer in a magnetic field typically results in a remanent (zero-field) magnetization in the ferromagnet (FM) that is always in the direction of the field during cooling (positive M_{rem}). Strikingly, when FeF_2 is the antiferromagnet (AF), cooling in a field can lead to a remanent magnetization opposite to the field (negative M_{rem}) (Figure 10). A collaboration led by researchers from the Stanford Synchrotron Radiation Laboratory working at ALS elliptically polarizing undulator Beamline 4.0.2 has verified a proposed explanation involving a small magnetic moment at the AF interface, but in the process also found both positive and negative moments and a way to distinguish them.

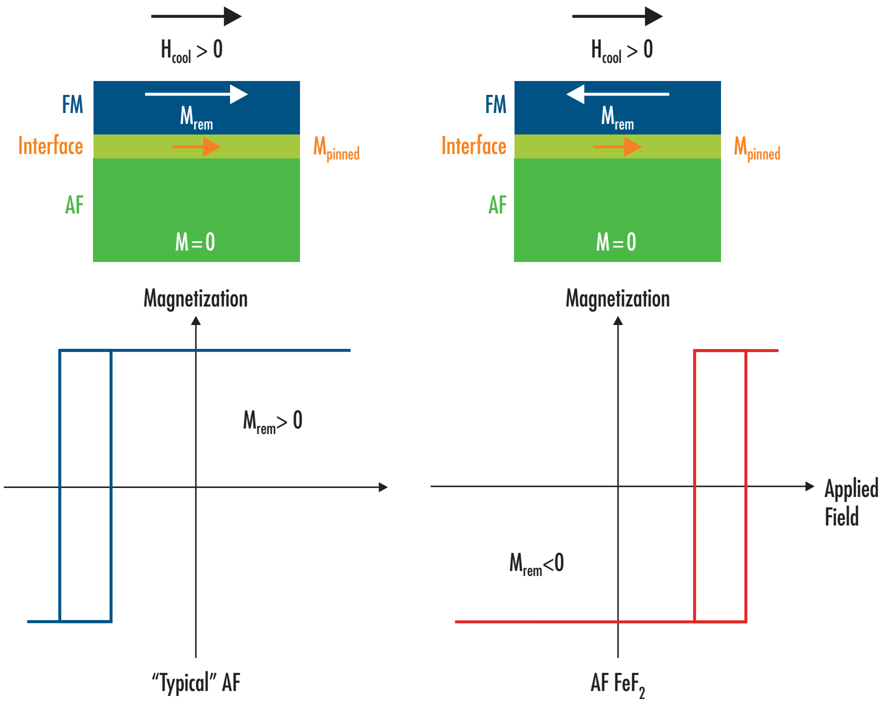

FIGURE 10. Ideal hysteresis loops (magnetization vs. applied magnetic field) for the FM component of "typical" field-cooled AF–FM bilayers with "positive" remanent magnetization (left) and of FeF_2–FM bilayers with "negative" remanent magnetization (right). The magnetizations in each of the component layers and the interface are represented by the arrows in the diagrams.

To understand the occurrence of either preferred direction, one has to assume that the AF layer exhibits a small magnetic moment at the interface that can be aligned by the cooling field. After cooling, this moment will not change its direction, even upon reversal of the external field, since it is now strongly anchored (pinned) in the magnetic system of the AF. This very small moment at the interface then aligns the FM via an internal magnetic field called magnetic exchange coupling. This exchange-bias phenomenon is useful in modern magnetic devices.

Two years ago, the Stanford group

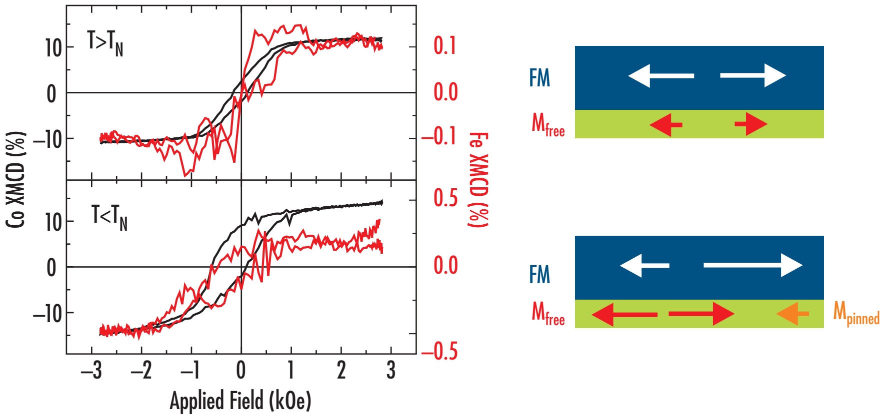

FIGURE 11. Left: Element-specific cobalt (black) and iron (red) hysteresis loops (as measured by XMCD) acquired at 300 K and 15 K after cooling in a weak field that only partially aligns the surface moment. Right: Schematic of moments in the cobalt and at the interface.

was able to provide the first direct experimental evidence for the existence of this small interfacial moment in the AF by using Beamline 4.0.2. To explain the anomalous behavior with FeF$_2$, it has been postulated that the coupling between the pinned moment in FeF$_2$ and a FM layer is not parallel but antiparallel and thus reverses the favored direction of the FM. In the new experiment, the researchers verified this proposition in a high-quality 2.5-nm FeF$_2$–Co bilayer grown at West Virginia University. They used x-ray absorption dichroism spectroscopy, a technique that can selectively detect the magnetic properties of sites close to the interface and distinguish between the magnetic properties of cobalt and iron atoms.

Hysteresis loops (magnetization vs. applied magnetic field) of the interfacial iron spins and the FM cobalt layer taken at 300 K (well above the ordering temperature, T$_N$ = 78 K) for FeF$_2$ show that both loops are symmetric and the entire moment at the FeF$_2$ interface follows the Co moment (Figure 11). Since one would expect the orientations of all iron moments within the FeF$_2$ lattice to be in constant motion above T$_N$, it is clear that the magnetic moment of the cobalt layer can be used to induce magnetic order in the topmost layer of the FeF$_2$.

At 15 K, the investigators observed a partial shift in the cobalt hysteresis loop indicating a positive remanent magnetization. Most of the spins at the interface simply seem to follow the FM Co layer as they do above T$_N$, and the overall shape of the interfacial hysteresis loop closely resembles that of the cobalt layer. However, it appears that the interfacial iron loop shifts down towards negative magnetization. This shows that a small fraction of the spins at the interface generate a magnetic moment that always points opposite to the favored magnetization of the FM.

In sum, the group found that a small fraction of interfacial magnetic moments tend to align the FM layer opposite to their moment, which can lead to a reversal of the preferred magnetization direction of the FM with respect to the cooling field. These moments appear only below the antiferromagnetic ordering temperature. On the other hand, the FM is able to align some of the moments at the AF surface so that they point in the same direction as the FM even above T$_N$. All in all, the magnetic properties at AF–FM interfaces are the result of complicated and competing processes. The present results provide clear evidence to distinguish between these two type of coupling mechanisms.

INVESTIGATORS

H. Ohldag and J. Stöhr (SSRL), H. Shi and D. Lederman (West Virginia University), and E. Arenholz (ALS).

PUBLICATION

H. Ohldag, H. Shi, E. Arenholz, J. Stöhr, and D. Lederman, "Parallel versus antiparallel interfacial coupling in exchange-biased Co/FeF$_2$ bilayers," *Phys. Rev. Lett.* **96,** 027203 (2006).

FUNDING

National Science Foundation and U.S. DOE BES.

ANISOTROPY TRANSITION IN ANTIFERROMAGNETIC FILMS: NiO/Fe(100)

Devices that use magnetic data storage, such as the read heads in computer hard drives, depend on antiferromagnetic (AF) thin films in combination with ferromagnetic (FM) layers. When the read head passes over the spinning hard disk, it senses the orientation of magnetic domains (bits of information) on the disk, causing the head's electrical resistance to change. Antiferromagnets act as magnetic references by pinning the magnetization direction of adjacent ferromagnetic layers. This property, known as exchange bias or exchange anisotropy, is not fully understood. Precise characterization of the magnetic structure between AF and FM layers—the interface—is crucial for improved performance and efficiency in future magnetic applications, such as magnetic RAM memory cells. The ALS photoemission electron microscope, PEEM2, can determine the magnetic properties of individual layers in structures with multiple AF and FM layers. X rays or extreme ultraviolet light can be tuned to knock large quantities of electrons out of a sample and into a phosphor screen so that a PEEM2 CCD camera can acquire a visible-light image for analysis. This is a high-resolution technique with the spatial resolution required to image nanometer- to micrometer-sized magnetic domains in AF thin films.

The study of magnetic instabilities in antiferromagnetic (AF) thin films interacting with ferromagnetic (FM) substrates has led to advances in magnetic recording heads, novel permanent magnets, spin valves, and magnetic tunnel junctions for high-density data storage in nonvolatile magnetic memory cells. To further develop the technological potential of AF–FM systems, researchers from Italy, the ALS, and UC Berkeley used the ALS photoemission electron microscope, PEEM2, to increase understanding of magnetic orientations when AF thin films interact with FM substrates. The results demonstrated, for the first time, a coupling transition between AF and FM anisotropy axes as the thickness of the AF layer was changed.

Magnetic instabilities in the rotation of the magnetic anisotropy axis are well known for low-dimensional FM systems and have been the subject of extensive research. The reduced coordination number at the FM surface, the hybridization with the substrate, and the presence of tensile forces can drive such instabilities, influencing the interplay between the exchange interaction, the magnetocrystal anisotropy, the magnetostriction, and the dipolar magnetic field.

Magnetic instabilities in AF thin films have received much less attention, and experimental evidence describing the occurrence of such phenomena is very scarce, although they might be important in defining the magnetic properties of heterogeneous systems in which a FM material interacts with an AF partner. Thanks to studies performed at the PEEM2 microscope on ALS Beamline 7.3.1.1, the researchers were able to observe magnetic instabilities in NiO thin films epitaxially grown on Fe(001). In particular, thin NiO films show a sudden phase transition from an in-plane perpendicular (low NiO thickness) to an in-plane collinear (high NiO thickness) coupling between the NiO anisotropy axis and Fe magnetization. (Although a subsequent study has found that the direction of the coupling is actually reversed, this is not, by itself, relevant to the conclusions of this experiment.) The ALS PEEM apparatus can image the electrons excited from the sample upon absorption of linearly polarized x rays. In fact, the absorption coefficient across a core threshold depends on the relative orientation between the light electric field and the direction of the local spins (x-ray magnetic linear dichroism, or XMLD), thus providing a source of magnetic contrast with chemical sensitivity both for FM and AF materials.

Figure 12 displays asymmetry images obtained at the Ni and Fe L_2 edges showing the magnetic contrast in the NiO wedged thin film and in the Fe(001) substrate. The asymmetry images have been obtained in such a way as to have dim areas corresponding to local magnetic moments aligning collinear to the light electric field, while bright areas indicate a perpendicular alignment, both for NiO and Fe. We conclude that the magnetization of the dark domain (topmost) is parallel to the [100] crystallographic axis, while the bright domain (lowermost) is magnetized parallel to the [010] axis.

The observation of a magnetic con-

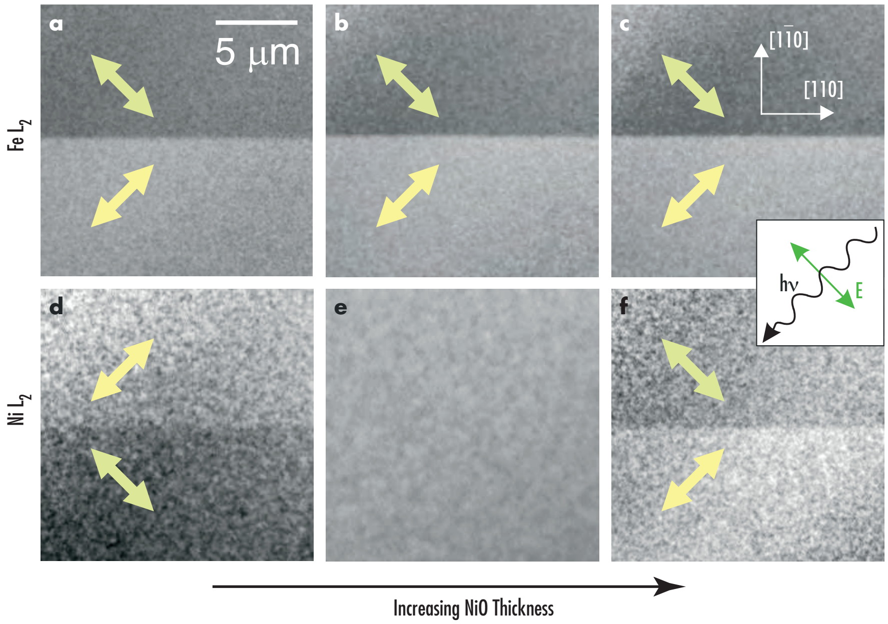

FIGURE 12. PEEM images of XMLD asymmetry obtained at the Fe (top) and Ni (bottom) L_2 edge on a NiO/Fe(001) wedged thin film. The indicated crystallographic directions refer to the Fe substrate. The NiO thickness increases from the left side to the right side of the figure and ranges between 12 and 24 Å. In the upper panels, two different Fe magnetic domains are clearly visible for the substrate, separated by a domain wall parallel to the [110] direction. The Fe easy axes belong to the ⟨100⟩ family, while the Fe(001) substrates have a strong in-plane magnetic shape anisotropy.

trast at the Ni L_2 edge proves that the NiO overlayer develops uniaxial anisotropy in the (001) plane. At very low coverage, the NiO contrast is reversed with respect to Fe (see panels on the left side of Figure 12, average NiO thickness = 12 Å), indicating that the interfacial coupling between the Fe substrate magnetization and the NiO overlayer anisotropy axis is perpendicular. Moving to higher NiO thickness values (central panels in Figure 12, corresponding to a sample region where the average NiO thickness is about 18 Å), the contrast disappears. Moving the PEEM field of view to a region where the NiO coverage is even higher (right-hand panels in Figure 12, average NiO thickness = 24 Å), a magnetic contrast is clearly retrieved on NiO. In this region, the XMLD has the same sign for both Ni and Fe, indicating that the NiO uniaxial anisotropy axis has rotated, and the type of interfacial coupling has turned from perpendicular to collinear.

INVESTIGATORS

M. Finazzi, A. Brambilla, P. Biagioni, and L. Duò (Politecnico di Milano, Italy); J. Graf, G.-H. Gweon, and A. Lanzara (UC Berkeley); and A. Scholl (ALS).

PUBLICATION

M. Finazzi, A. Brambilla, P. Biagioni, J. Graf, G.-H. Gweon, A. Scholl, A. Lanzara, and L. Duò, "Interface coupling transition in a thin epitaxial antiferromagnetic film interacting with a ferromagnetic substrate," *Phys. Rev. Lett.* **97,** 097202 (2006).

FUNDING

Fondo Italiano per la Ricerca di Base, National Science Foundation, and U.S. DOE BES.

IMAGING MAGNETISM AT FUNDAMENTAL LENGTH AND TIME SCALES WITH SOFT X RAYS

As in other areas of modern solid state physics, small and fast are at the forefront of research on magnetism, with distances being measured in nanometers and times in femtoseconds (quadrillionths of a second). So-called nanomagnetism is a scientifically rich and very attractive area because of novel magnetic phenomena occurring only in ultrasmall materials (proximity and confinement effects) and the ability to tailor novel magnetic materials by controlling size and composition. These features also make nanomagnetism the basis of magnetic recording and sensor devices used in modern information technology. The shrinking size of a magnetic bit in which one unit of digital information is stored has reached a level where both the reading and the writing of information are now limited by fundamental parameters, including the sizes of the grains making up the magnetic media and the time it takes the magnetization representing the magnetic bit to change orientation. Kim et al. have exploited recent advances in x-ray optics to demonstrate x-ray microscopy of a typical magnetic alloy with a spatial resolution of 15 nm. Femtosecond time resolution awaits the availability of new ultrafast x-ray sources.

Magnetic soft x-ray microscopy is already a powerful analytical tool for imaging nanomagnetism, and a clear path toward spatial resolution below 10 nm and time resolution down to femtoseconds promises an even brighter future. Recent achievements with Fresnel zone-plate technology at Berkeley Lab's Center for X-Ray Optics (CXRO) have revealed a glimpse of this future, yielding a spatial resolution better than 15 nm at the full-field soft x-ray microscope XM-1 at Beamline 6.1.2 (Figure 13). This capability has now been applied to studies of magnetization-reversal processes at the nanoscale in a 50-nm-thick thin film of a nanogranular cobalt–chromium–platinum alloy.

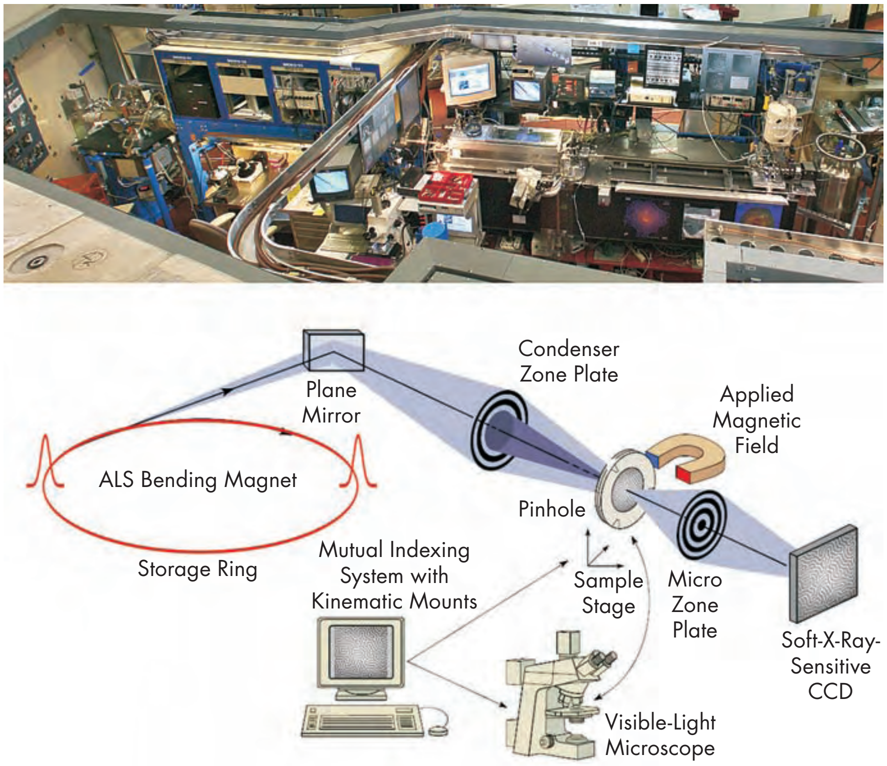

FIGURE 13. Top: View of the full-field soft x-ray microscope XM-1 at Beamline 6.1.2. Bottom: Schematic optical layout for magnetic imaging. Note the Fresnel micro zone plate primarily determines the spatial resolution, whereas the electron bunch length in the ALS storage rings determines the x-ray pulse length and hence the temporal resolution.

A detailed understanding of the microscopic origin of magnetization reversal is still mostly lacking with no answers to such questions as: Is the nucleation of magnetic domains a stochastic process? Does the system show a memory effect for identical applied external fields in a hysteresis cycle? Is there a microscopic symmetry in the hysteresis loop? How does the system follow microscopically the virgin magnetization loop? By taking advantage of recent experimental evidence from high-resolution magnetic microscopies, researchers are just now starting to develop theoretical models describing these scenarios.

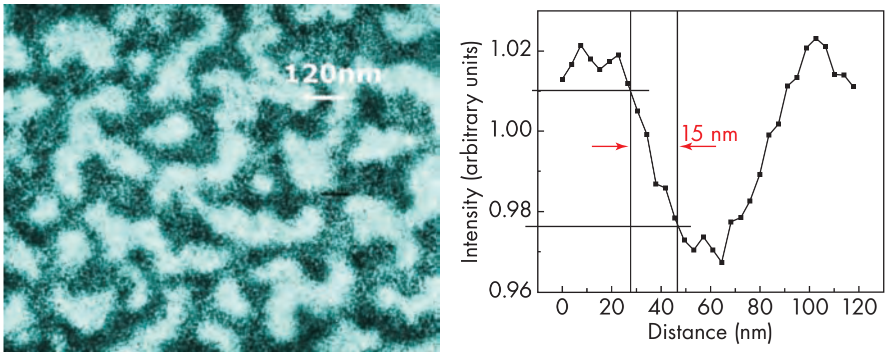

FIGURE 14. Left: Magnetic domains in a $(Co_{83}Cr_{17})_{87}Pt_{13}$ layer imaged at the cobalt L_3 absorption edge (777 eV). Right: Intensity scan across a domain boundary (indicated by the white bar in the microscopy image) showing a 15-nm spatial resolution as derived from the distance over which there is a drop in intensity between the 90% and 10% levels.

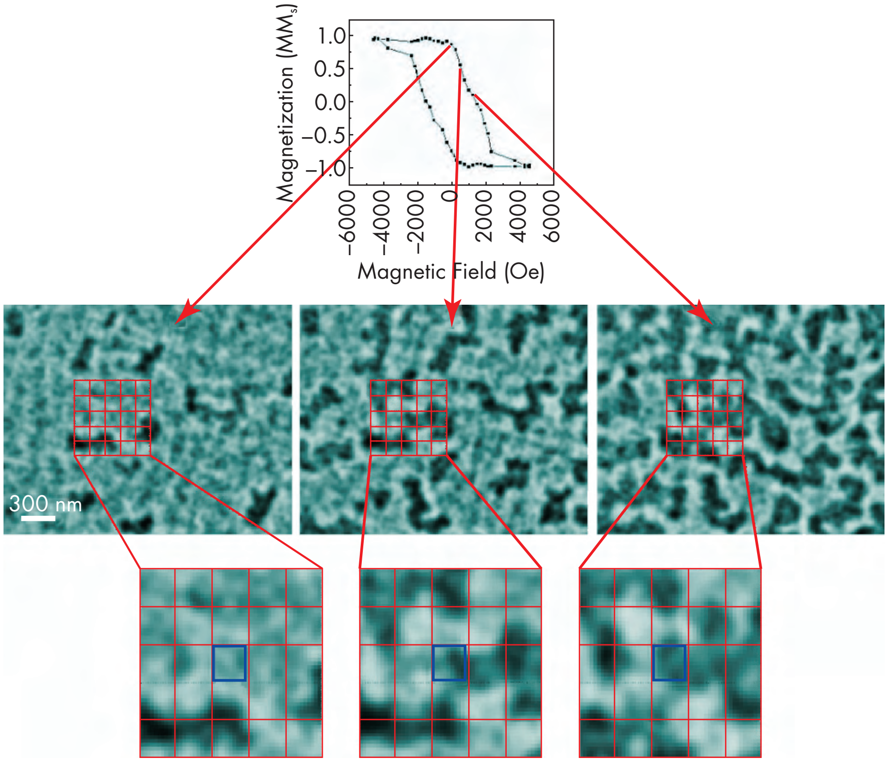

FIGURE 15. Top: Global hysteresis loop derived from averaging the intensity across the field of view. Center: Evolution of the local magnetic domain pattern in varying applied magnetic fields. Bottom: Zooming into the images allows the determination of local hysteresis behavior. Each grid square corresponds to approximately 100 x 100 nm^2 (15 x 15 pixels).

Illustrating the capability now becoming available, a team from CXRO and two Korean institutions recorded images of the magnetic domain structure of a nanogranular $(Co_{83}Cr_{17})_{87}Pt_{13}$ alloy thin film at the cobalt L_3 absorption edge at 777 eV using x-ray magnetic circular dichroism (XMCD) as an element-specific magnetic-contrast mechanism. CoCrPt films exhibit a strong perpendicular magnetic anisotropy and are used in perpendicular magnetic-storage technology.

The grain-size distribution obtained from transmission electron microscopy analysis yielded an average grain size of about 20 nm. A 15-nm spatial resolution in the x-ray microscopy images therefore provides insight into the nucleation process at the granular level. A typical high-resolution x-ray image (Figure 14) shows an irregular magnetic-domain structure. An intensity scan across the domain structure clearly proves that a 15-nm spatial resolution was obtained in this experiment.

Recording images in varying external magnetic fields allowed a detailed study of the magnetization-reversal process. Interestingly, repetitive measurements and careful analysis provided a strong indication of statistical nucleation behavior. Since the XMCD contrast scales with the projection of the local magnetization onto the photon propagation direction, and the two were chosen to be parallel, the nanoscale hysteresis behavior of the specimen could be deduced from the x-ray microscopy images by analyzing the magnetic contrast in local areas of the sample (Figure 15). Technologically, the switching field distribution in media is a parameter in storage technology that becomes even more important with increasing storage density. Such information can also be extracted from high-resolution magnetic soft x-ray microscopy images without ambiguity.

Apart from the ability to image nanomagnetism with a spatial resolution close to fundamental length scales, soft x-ray microscopy can today achieve a time resolution below 100 ps, thus allowing us to image fast spin dynamics with elemental sensitivity. The electron bunch length at the ALS is 70 ps, which is adequate for precessional and relaxation phenomena with GHz frequencies as well as domain-wall propagation in nanowires with velocities around 100 m/s. However, the limited number of photons per bunch requires the use of a stroboscopic pump–probe scheme and also poses the severe constraint of perfect repeatability in the dynamic processes that are accessible.

The spatial resolution will improve with progress in x-ray optics. However, while current Fresnel zone-plate designs already allow imaging with short pulses down to the subfemtosecond regime, achieving this time resolution has been largely limited by the time structure of soft x-ray sources. But with the upcoming availability of femtosecond sources (e.g., free-electron lasers), it is worth planning for ultrafast, full-field, soft x-ray microscopy snapshot imaging of spin dynamics, such as fluctuations, at fundamental (fs/as) time scales with nanoscale spatial resolution.

INVESTIGATORS

P. Fischer, D.-H. Kim, M.-Y. Im, B.L. Mesler, W. Chao, E.H. Anderson, J.A. Liddle, and D.T. Attwood (Berkeley Lab); S.-C. Shin (Korea Advanced Institute of Science and Technology); and S.-B. Choe (Seoul National University, Korea).

PUBLICATIONS

P. Fischer, D.H. Kim, W. Chao, J.A. Liddle, E.H. Anderson, and D.T. Attwood, "Soft x-ray microscopy of nanomagnetism," *Materials Today* **9,** 26 (2006).

D.-H. Kim, P. Fischer, W. Chao, E. Anderson, M.-Y. Im, S.-C. Shin, and S.-B. Choe, "Magnetic soft x-ray microscopy at 15-nm resolution probing nanoscale local magnetic hysteresis," *J. Appl. Phys.* **99,** 08H303 (2006).

FUNDING

U.S. DOE BES.

Organic Compounds and Biomolecules

NUCLEOBASE ORIENTATION AND ORDERING IN SINGLE-STRANDED DNA ON GOLD

A simple test in the doctor's office reveals what is making a patient sick and what drug treatment will work best. A similar test checks a suspicious powder for dangerous biowarfare agents. Science fiction? Only because the latest biotech marvel—the "DNA chip"—still needs a few years to become part of everyday life. DNA chips start with a piece of glass or silicon (sometimes coated with gold) about the size of a digital camera's light-sensitive chip. Instead of electronics, however, DNA chips are covered with up to half a million "pixels" of microscopic droplets of DNA. When the "probe DNA" in each pixel recognizes a particular "target DNA," they combine to form the famous double helix (hybridization). For this to work, each strand of probe DNA must stand up on the surface while being firmly attached by one end tagged with a "linker" chemical. Petrovykh et al. have found a way to adapt methods normally used to study clean, solid surfaces to obtain information about how DNA strands attach to DNA chips. This ability will become increasingly important for the development of future generations of smaller and more complex chips and related devices.

DNA microarrays are small metal, glass, or silicon chips covered with patterns of short single-stranded DNA (ssDNA) (Figure 1). These "DNA chips" are revolutionizing biotechnology, allowing scientists to identify and count many DNA sequences simultaneously. They are the enabling technology for genomic-based medicine and are a critical component of advanced diagnostic systems for medical and homeland security applications. Like digital chips, DNA chips are parallel, accurate, fast, and small. These advantages, however, can only be realized if the fragile biomolecules survive the attachment process intact. Furthermore, biomolecules must be properly oriented to perform their biological function. In other words, the DNA literally must stand up to be counted. Understanding both the attachment and orientation of DNA on gold surfaces was the goal of recent experiments performed at ALS Beamline 8.0.1 by an international collaboration of scientists.

The cornerstone of molecular biology is the study of the *structure* and *function* of biomolecules in solution. Likewise, the modified behavior of biomolecules on the surface of a chip or nanoparticle is the foundation of many areas of bio- and nanotechnology. However, characterizing the interactions between biomolecules and surfaces requires new measurement techniques, because most current bioanalytical methods are hindered by the inherently small number of molecules bound to a surface. Complementary surface-sensitive spectroscopies come to the rescue (Figure 2). X-ray photoelectron spectroscopy (XPS) provides *quantitative* information about elemental composition and surface chemistry. Fourier-transform infrared (FTIR) spectroscopy adds molecular fingerprints and orientational information. Near-edge x-ray absorption fine-structure (NEXAFS) spectroscopy probes electronic transitions between core levels and valence orbitals.

Short strands of synthetic ssDNA typically used in bio- and nanotechnology are called *oligonucleotides* or *oligos*. Oligos with "trivial" sequences

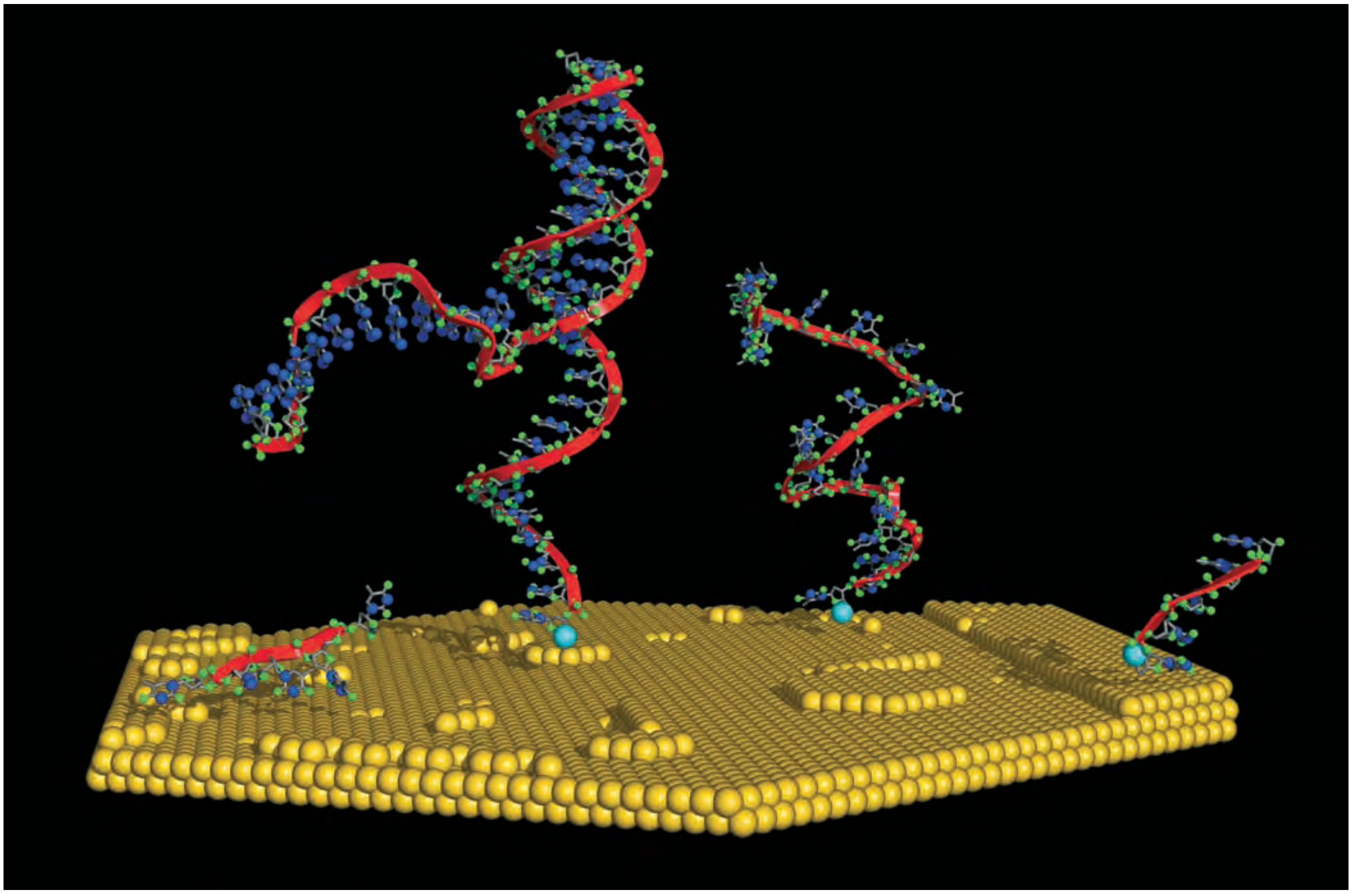

FIGURE 1. Schematic of DNA structures in various conformations on a gold surface. Differences in overall structure and orientation are emphasized by color-coding of DNA structural elements: phosphate backbone (red), nitrogen (blue), oxygen (green), and sulfur linker (cyan). Upright orientation is required for efficient hybridization with a complementary strand from solution.

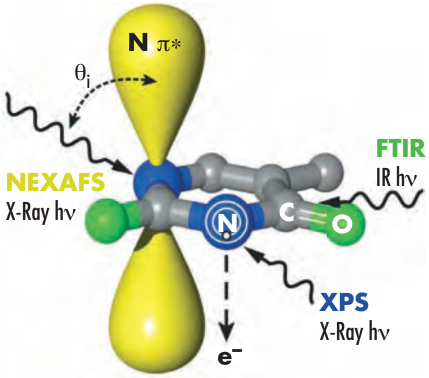

FIGURE 2. XPS and NEXAFS techniques use incident x rays to probe the core levels of nitrogen atoms (blue) in nucleobases (thymine shown). FTIR spectroscopy adds vibrational fingerprints of submolecular structures such as the C=O groups. NEXAFS and FTIR use linearly polarized incident photons and thus are sensitive, via the dipole selection rule, to the orientation of nitrogen π* orbitals (yellow) and C=O ligands, respectively.

composed of only one letter of the DNA alphabet (A, C, G, or T) provide simplified spectroscopic signatures while maintaining realistic DNA structure. Thymine (T) has the simplest nucleobase structure and provides nitrogen atoms and carbonyl groups suitable for complementary measurements by XPS, FTIR, and NEXAFS. Furthermore, features in thymine spectra allow one to distinguish DNA strands lying down on the surface from those standing up.

In excellent agreement, all three techniques showed that strands of five Ts (T5), synthesized without special "linker" groups for surface attachment, lay flat against the surface, while strands modified with a thiol (T5-SH and T25-SH) stood upright, anchored by strong sulfur–gold bonds. Furthermore, signatures of internal molecular ("secondary") structure could be observed by NEXAFS for the upright T5-SH and T25-SH strands (Figure 3). The nitrogen π* orbitals within the T bases could be selectively excited by photons with energies around the nitrogen absorption edge. The polarization dependence of the nitrogen π* intensities then provided information about the orbital orientations, from which the T-base orientations could be deduced. Only minimal preferential orientation was observed for Ts in T25-SH films, consistent with a random-coil-like secondary structure. The Ts in T5-SH, however, showed a surprisingly strong orientation parallel to the surface. This result was corroborated by XPS and FTIR.

The significance of these results goes beyond the structure of a few DNA oligos. For DNA, RNA, and particularly proteins, secondary structure strongly affects function and contains valuable information about molecular interactions. Therefore, the researchers are already extending these analysis methods to larger biomolecules, such as proteins, on surfaces.

The consistent structural information from all three ex situ methods can be best understood if it reflects the common initial in situ structure, thus providing an affirmative answer to the long-standing question, "Can ex situ measurements provide relevant information about biomolecules on surfaces?" Furthermore, both FTIR and NEXAFS with fluorescence detection (as used in this work) can be performed in situ, opening the possibility of studying biomolecules on surfaces using a label-free method that provides a revolutionary combination of chemically specific, structurally sensitive, quantitative results.

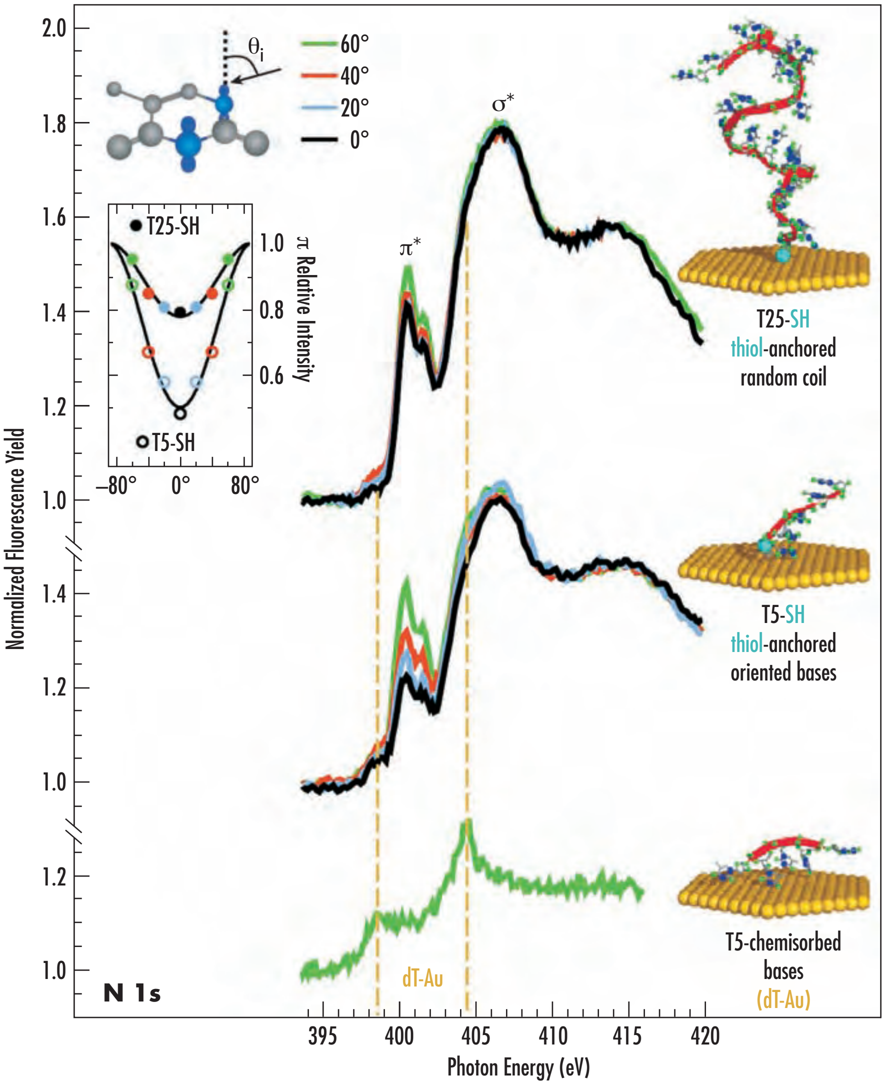

FIGURE 3. Fluorescence yield NEXAFS was used to determine the structure of DNA on gold surfaces. The changes in intensity of the nitrogen π* peaks as a function of the incident angle θ_i (inset) indicate strong preferential orientation of thymine bases in T5-SH monolayers but a nearly random distribution of orientations in T25-SH monolayers. For thymine nucleotides chemisorbed directly on gold—the dominant structure in T5 monolayers—the spectral features are shifted to lower photon energies (dashed gold lines, dT-Au).

INVESTIGATORS

D.Y. Petrovykh (University of Maryland and Naval Research Laboratory); A. Opdahl, H. Kimura-Suda, and M.J. Tarlov (National Institute of Standards and Technology); V. Pérez-Dieste and F.J. Himpsel (University of Wisconsin); J.M. Sullivan (Northwestern University and Naval Research Laboratory); and L.J. Whitman (Naval Research Laboratory).

PUBLICATION

D.Y. Petrovykh, V. Pérez-Dieste, A. Opdahl, H. Kimura-Suda, J.M. Sullivan, M.J. Tarlov, F.J. Himpsel, and L.J. Whitman, "Nucleobase orientation and ordering in films of single-stranded DNA on gold," *J. Am. Chem. Soc.* **128,** 2 (2006).

FUNDING

Air Force Office of Scientific Research, Office of Naval Research, National Research Council, U.S. DOE BES.

PROBING ORGANIC TRANSISTORS WITH INFRARED BEAMS

Heeger, MacDiarmid, and Shirakawa shared the 2000 Nobel Prize in Chemistry for showing how plastic can be made to conduct electric current. They found that if electrons were removed from certain types of long polymer chains that make up plastics, the "holes" left behind could act as positive charge carriers, increasing conductivity by a factor of up to ten million. The prospect of electronic devices incorporating lightweight, moldable, relatively cheap plastic has since stimulated intensive research and development toward a wide variety of applications, including large-area flat-screen displays, chemical and biological sensors, and environmentally friendly solar cells. Semiconducting organic polymers can also be used in field-effect transistors (FETs), solid-state electronic devices used to amplify wireless and other weak electromagnetic signals. But the ability to do this depends upon the density of the charge carriers that can be introduced into the transistor's conducting channel. This channel is confined to a nanometer-thick layer at the interface between the device's semiconducting and insulating layers, thus its intrinsic properties are very difficult to interrogate experimentally. Li et al. take a novel approach to probing the electronic characteristics of organic FETs, using infrared light to map the density of charge carriers under various conditions.

Silicon-based transistors are well-understood, basic components of contemporary electronic technology. In contrast, there is growing need for the development of electronic devices based on organic polymer materials. Organic FETs are ideal for special applications that require large areas, light weight, and structural flexibility. They also have the advantage of being easy to mass produce at very low cost. However, even though this class of devices is finding a growing number of applications, electronic processes in organic materials are still not well understood. A group of researchers from the University of California and the ALS has succeeded in probing the intrinsic electronic properties of the charge carriers in organic FETs using infrared spectromicroscopy. The results of their study could help in the future development of sensors, large-area displays, and other plastic electronic components.

Arguably, one of the main challenges in achieving these goals is finding a means of investigating the intrinsic electronic properties of the charge carriers in organic FETs without the need for metallic contacts that could interfere with the properties under study. In FETs, the charge carriers are confined to a nanometer-thick layer at the semiconductor–insulator interface, buried under several layers of the device (Figure 4). This makes it difficult to experimentally study injected charge carriers using some of the most informative experimental techniques in the arsenal of physicists and chemists, including scanning tunneling microscopy, photoemission spectroscopy, and inelastic x-ray and neutron scattering.

In this research, the scientists instead employed infrared light to study the electronic processes in organic FETs that are based on poly(3-hexylthiophene), a semiconducting polymer featuring exceptionally high charge-carrier mobility. In such materials, charge carriers can induce infrared vibrations of the polymer chain. In addition, when these charges are displaced under the influence of an electric field, they drag the local polarization cloud of the molecular chains with them, forming so-called polarons. The scientists have been able to employ infrared spectroscopy to directly probe the vibrational modes and polarons in a functional organic FET device (Figure 5). This information is difficult or impossible to obtain using other experimental techniques.

Furthermore, infrared spectromicroscopy can also be used to explore the distribution of charges in the conducting channel of the FETs with high spatial resolution, made possible by the exceptionally high brightness and small focal-spot size of the infrared beams at the ALS. Using the infrared Beamline 1.4.3, the researchers were able to acquire infrared spectra from individual spots less than 10 microns in diameter. By scanning the beam over the conducting channel of the device and measuring the infrared spectra in different areas, they were able to map out the density of the charge carriers in different regions and examine its evolution as the applied voltage is increased (Figure 6). Comparisons were made between FETs having insulating layers of either SiO_2 or TiO_2. The latter, having a high dielectric constant, are much desired in FETs because they allow for a much higher density of charge carriers in their channels than SiO_2-based FETs.

However, the measurements re-

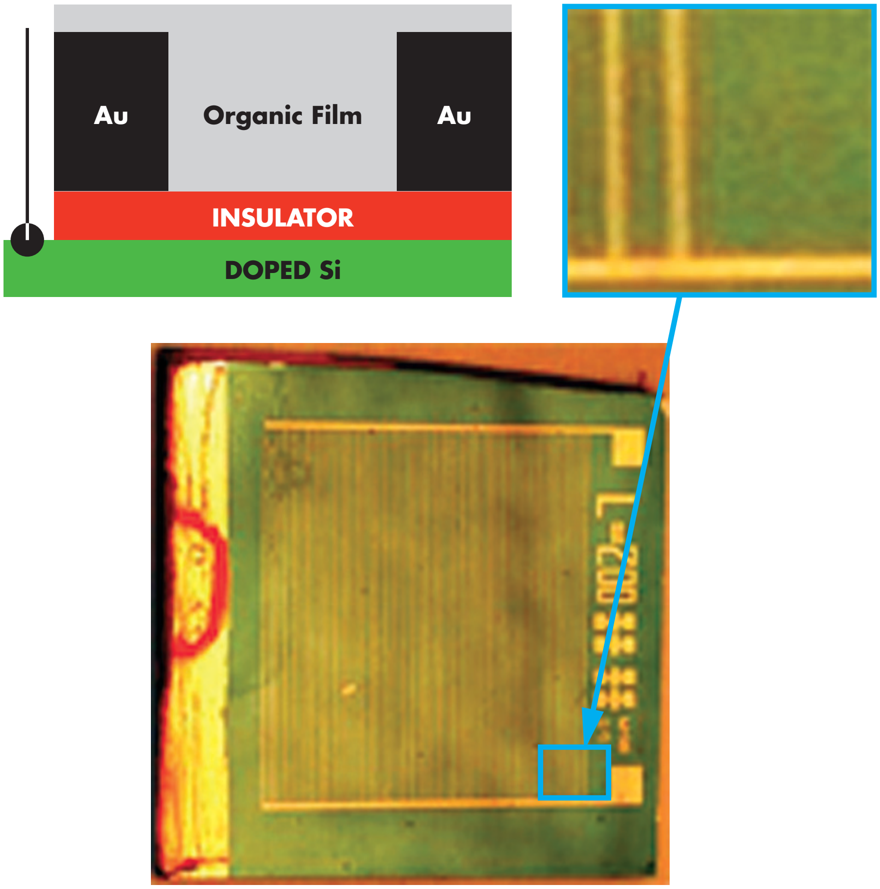

FIGURE 4. Top left: A fragment of the cross section of a "grid-electrode" organic FET. The organic material in this study is poly(3-hexylthiophene) and the insulator is a high-dielectric-constant material, TiO_2. Bottom: A photograph of an actual device with dimensions 10 x 14 mm^2. Inset: Close-up of the area to be studied.

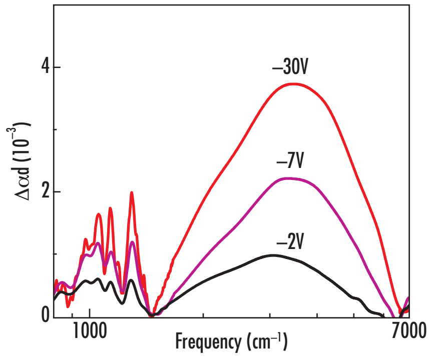

FIGURE 5. The voltage-induced infrared absorption spectra ($\Delta\alpha d$) of the device. Employing infrared spectroscopy, the researchers were able to directly probe the electronic excitations associated with the injected carriers in a functional organic FET device: infrared active vibrational modes of the polymer chain (sharp resonances in the 1,000–1,500 cm^{-1} range) and polarons (broad absorption band centered at 3,500 cm^{-1}).

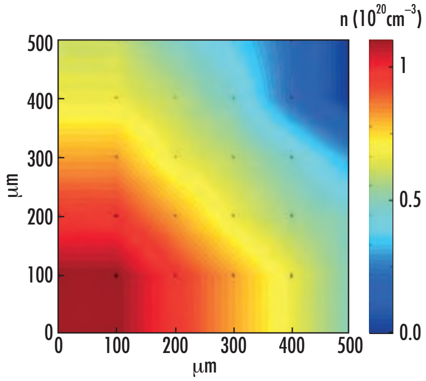

FIGURE 6. The variation of carrier density away from the injection contacts in the area shown by the blue square in Figure 4, obtained by spatially monitoring the spectroscopic fingerprints of the injected charges using infrared microspectroscopy.

vealed severe restrictions of the charge-carrier channel length for TiO_2-based devices, a significant departure from the behavior expected for an "ideal" FET, in which the charge density increases linearly with voltages and is uniform in the channel. This is particularly important if one wants to use these insulators in chemical or biological sensors. In general, these experiments indicate that infrared spectroscopy and spectromicroscopy offer researchers unique tools to explore physical phenomena at the nanoscale occurring at the semiconductor–insulator interface in organic FETs. The team hopes to employ the same techniques in the study of other materials in FET devices, including polymers, organic molecular crystals, and transition-metal oxides.

INVESTIGATORS

Z.Q. Li, N. Sai, M. Di Ventra, and D.N. Basov (UC San Diego); G.M. Wang, D. Moses, and A.J. Heeger (UC Sant Barbara); and M.C. Martin (ALS).

PUBLICATION

Z.Q. Li, G.M. Wang, N. Sai, D. Moses, M.C. Martin, M. Di Ventra, A.J. Heeger, and D.N. Basov, "Infrared imaging of the nanometer-thick accumulation layer in organic field-effect transistors," *Nano Letters* **6**, 224 (2006).

FUNDING

National Science Foundation, Petroleum Research Fund, and U.S. DOE BES.

MAPPING THE NANOSCALE LANDSCAPE

Fossil fuel is a form of stored solar energy. The energy of the sun is "captured" through photosynthesis, plants and animals are converted over eons to fossil fuel, then we extricate it from geologic deposits. However, fossil fuel use contributes to increases in CO_2 emissions, leading to global warming. So why not go directly to the source? No messy extraction, just direct conversion of photons into electricity. Organic solar cells (OSCs) are the most promising new candidates for low-cost photovoltaics. Presently, OSCs and LEDs based on blends of semiconducting polymer and fullerene derivatives exhibit power conversion efficiencies of 3% under solar conditions and quantum efficiencies of up to 70%. The performance of these devices involves a complex balance between charge generation and charge transport. Studying the active layers of OSCs logically follows upon the nanometer characterization of TFB/F8BT-based LED devices and will be critical to the improvement of performance and energy efficiencies. Although just a third as efficient as fossil fuel, clean green OSCs have the potential for large-area solar collection—on rooftops of buildings and other unused spaces. And every increase in efficiency will reduce the amount of device space needed.

For the first time, researchers have successfully mapped the chemical structure of conjugated polymer blend films with a spatial resolution of better than 50 nm using scanning transmission x-ray microscopy (STXM). This is not just another application of STXM. It is a breakthrough experiment on several levels. Correlating local composition to electronic/optical device characteristics will pave the way to characterizing a whole new class of materials with STXM—multicomponent organic electronic devices that have intrinsically nanoscale dimensions. Understanding where charge transport and recombination occur in these materials helps explain the efficient performance of polymer-based LEDs and will lead to a new avenue of research on organic electronic devices, supporting emerging technologies such as molecular computing and promoting increased efficiencies in existing organic technologies (organic LEDs and solar cells).

Conjugated polymer blends are good candidates for low-cost optoelectronic devices because of their stability, efficient electroluminescence, and photovoltaic performance. Spin-coating demixes the two polymers, pro-

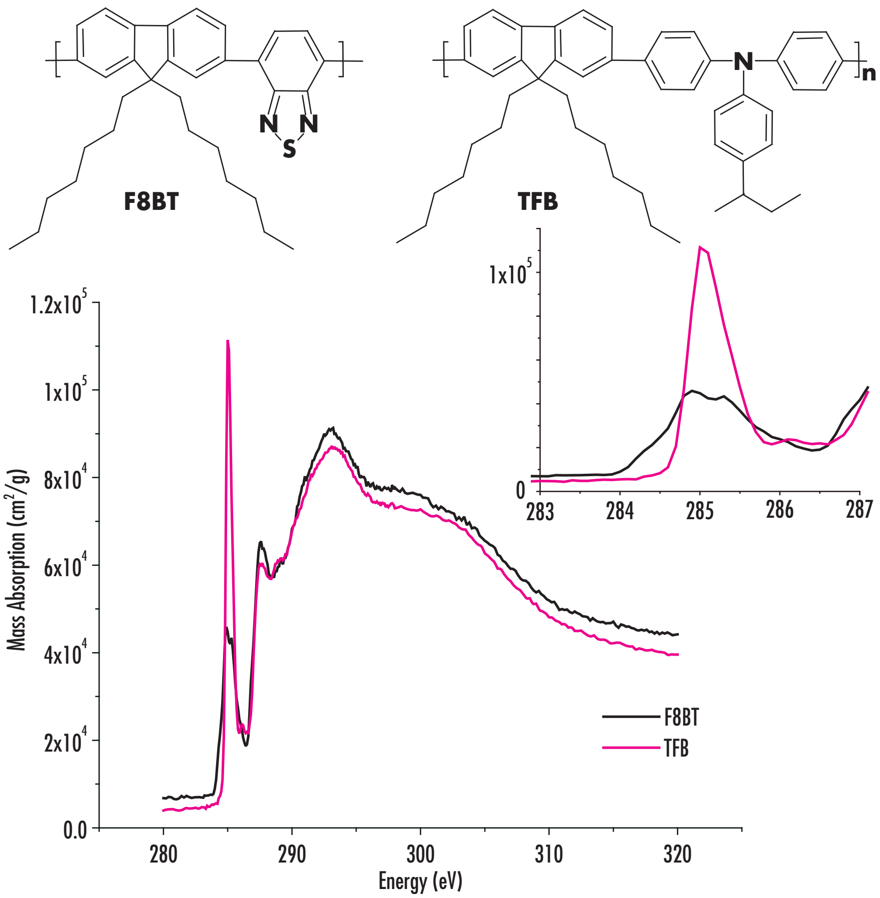

FIGURE 7. Chemical structures of F8BT and TFB along with their NEXAFS spectra. Although TFB and F8BT exhibit similar NEXAFS spectra above 287 eV, between 283 and 287 eV, the π^* absorption peak of F8BT has a broader, weaker structure with a lower absorption onset, consistent with the deeper lowest unoccupied molecular orbital of F8BT compared to TFB. (These spectra analyses formed the basis for the observed chemical contrast in the STXM maps.)

ducing a distributed heterojunction structure with interfaces for charge recombination (LEDs) or charge separation (solar cells). These films, however, have a complex nonequilibrium structure, making device function interpretation difficult. To better understand this structure, an international group of scientists performed STXM measurements at Beamline 5.3.2 at the ALS on blend films of poly(9,9-dioctylfluorene-*co*-*N*-(4-butylphenyl) diphenylamine) (TFB) and poly(9,9′-dioctylfluorene-*co*-benzothiadiazole) (F8BT). STXM, in conjunction with the chemical sensitivity of near-edge x-ray absorption fine-structure (NEXAFS) spectroscopy, allows for quantitative determination of submicron polymer blend composition (Figure 7).

At a lateral resolution of 50 nm, the researchers mapped three thickness layers (65 nm, 95 nm, and 150 nm) of subsurface chemical structure (Figure 8). Within the enclosed TFB domains, there is little lateral variation in composition (e,h). In the F8BT region, however, F8BT concentration near the domain interface is high (d,g), measuring 90% (although a TFB wetting layer between blend and substrate indicates this concentration is even higher). F8BT concentration falls to 60% further from the interface and into the domain. The domain interface measures 200 nm, but may be sharper due to additional three-dimensional structure. Such a large decrease in F8BT concentration is not caused by the presence of a TFB surface capping layer, since it would be too thick. These features arise from variations in bulk intermixing between F8BT and TFB.

These results will help clarify nanoscale mechanisms of electroluminescence in LEDs based on these blends. Previous studies showed that injection of electrons from a cathode is most efficient into an F8BT-rich domain near a domain interface not covered by a TFB capping layer. The injection of holes in contrast is facilitated by a TFB wetting layer that covers the entire anode, providing efficient injection across the plane of the device. As demonstrated here, however, the F8BT-rich domain is almost pure near the domain boundary, thus the efficient injection of electrons into the near-domain F8BT-rich region is accompanied by efficient charge transport through this almost pure bulk region of the film. Charge capture is then facilitated by charge recombination at either the interface between the micrometer-sized domains or at the horizontal interface between the TFB-rich wetting layer and the nearly pure near-domain F8BT-rich region. As injection of electrons and electron transport are efficient only near the domain interface, both charge capture mechanisms could explain why electroluminescence is only observed near the micrometer-sized domain interface by optical microscopy.

Interfacial enrichment of F8BT, which facilitates efficient charge transport, and interface sharpness, which promotes charge capture and recombination, help explain the efficient performance of TFB/F8BT-based LEDs and demonstrate the exciting potential for this technique to probe the composition, morphology, and electronic processes of polymer films.

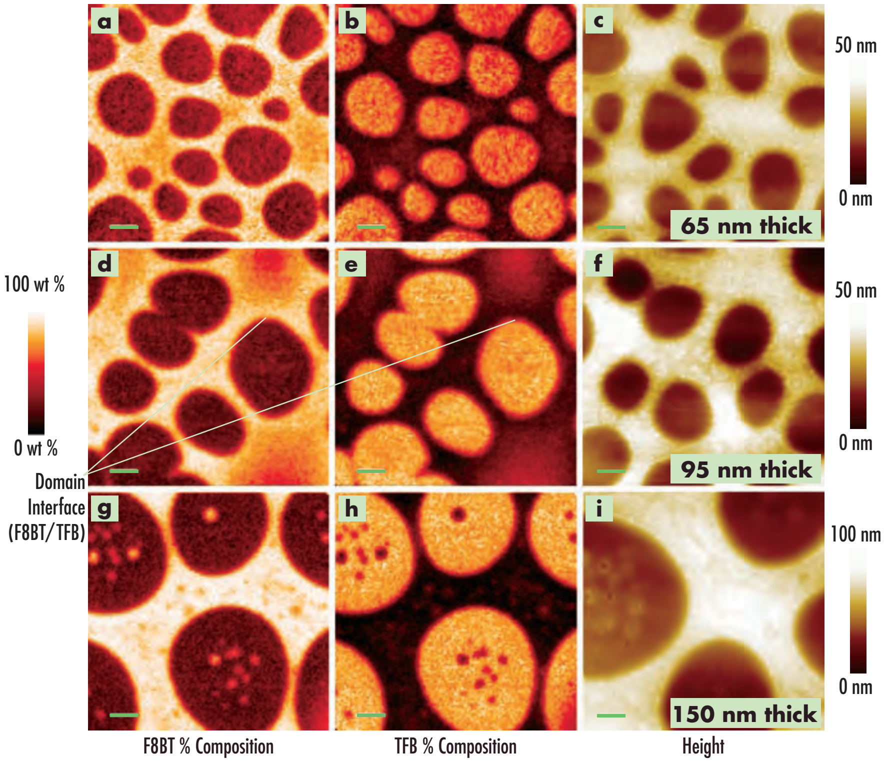

FIGURE 8. STXM composition maps (5 μm x 5 μm) of F8BT:TFB blend films (left and center). Comparative atomic-force microscopy (AFM) surface images (right) reveal micrometer-sized domains in blend films deposited from xylene. Both AFM and STXM show similar coarse domain sizes, 1 to 5 μm, confirming domain structures are columnar and round. The left column corresponds to F8BT weight % composition maps; the center to TFB weight % composition maps. (a), (b), and (c) are of a 64-nm-thick film; (d), (e), and (f) are of a 95-nm-thick film; (g), (h), and (i) are of a 150-nm-thick film. The scale bar is 1 μm.

INVESTIGATORS

B. Watts, L. Thomsen, W.J. Belcher, and P.C. Dastoor (University of Newcastle, Australia); C.R. McNeill and N.C. Greenham (University of Cambridge, U.K.); and A.L.D. Kilcoyne (ALS).

PUBLICATION

C.R. McNeill, B. Watts, L. Thomsen, W.J. Belcher, N.C. Greenham, and P.C. Dastoor, "Nano-scale quantitative chemical mapping of conjugated polymer blends," *Nano Letters* **6,** 1202 (2006).

FUNDING

U.K. Engineering and Physical Sciences Research Council, Australian Research Council, and Commonwealth of Australia.

THE FIRST STEP IN REFORMING METHANE

Hydrogen is responsible for about 75% of the elemental mass in the universe. Ironically, finding a cheap and clean way to extract hydrogen for bulk energy storage and transport has been a challenge. Steam reforming of methane is the least expensive and most commonly used commercial method, although costs are still high. However, there are three pluses to steam-reforming technology that make it a viable near- and midterm energy solution: because 95% of the hydrogen produced in the U.S. is made via natural gas reforming in large central plants, a pipeline delivery infrastructure already exists; it is one of the most efficient (65%–75%) of the current commercially available production methods; and greenhouse gas emissions in hydrogen-fuel-cell-powered vehicles are lower than in gasoline-powered internal combustion engine vehicles. Steam reforming also has possibilities as a hydrogen production/distribution technology for fuel-cell-powered vehicles. A methanol tank and steam reforming unit could replace the bulky pressurized hydrogen tanks presently in use. Öström et al. looked at the first step in steam reforming to determine how the chemical bonds changed when methane interacted with metal. Understanding these interactions could lead to lower costs and greater efficiencies in bulk hydrogen production.

A major challenge for our society is how to handle the pollution problems stemming from the use of fossil fuels, such as climate changes, while at the same time seeking alternative solutions because of the shrinking availability of this form of energy. Using angle-resolved x-ray absorption spectroscopy (XAS) at ALS Beamline 8.0.1, a team of researchers from Sweden and the U.S. looked at one alternative, natural gas. This energy source has been largely unused because of the high cost of converting its main constituent, gaseous methane, into compounds that are cheaper to handle. The researchers focused their attention on steam reforming of methane, which is presently the least expensive and most commonly used commercial method for producing bulk hydrogen and is used in several important chemical processes, such as petroleum refining and the industrial synthesis of ammonia for fertilizer. It is also a promising method of fuel production for hydrogen fuel cells.

Methane adsorption at single-crystal metal surfaces has often been used as a well-defined model system to study this important reaction. To gain knowledge about methane–metal interactions, the team investigated the metal-induced changes in the methane electronic structure. Their findings demonstrate unexpectedly large chemical interactions and preparation for bond cleavage already occurring at low temperatures before dehydrogenation.

Steam reforming of methane occurs at high temperatures in the presence of a metal-based catalyst. The rate-limiting step is the activated adsorption that leads to dehydrogenation at transition-metal surfaces. The industrial process takes place at temperatures of up to 1000 °C and pressures as high as 25–35 bar, where methane can be efficiently dehydrogenated. The challenge is to find effective catalytic pathways that dehydrogenate methane without leading to the formation of atomic carbon, which poisons the metal catalyst. To accomplish this, a fundamental understanding of every step in the process is important. The researchers focused on the first step, where the molecule is in a weakly physisorbed state prior to the dissociation process that leads to dehydrogenation.

The team performed XAS of adsorbed methane at low temperature and pressure, where no chemical interaction was anticipated. This experiment allowed them to monitor the electronic structure of the intact molecule at the metal surface to see how the chemical bonds changed when the molecule interacted with the metal. Mixing of electronic states between the metal surface and methane molecule was observed, indicating direct chemical interaction, as well as a broken molecular symmetry (Figure 9). With the aid of density functional theory spectrum calculations, the data were interpreted and a distortion of the molecular geometry was found. This distortion consisted of the stretching of a C–H bond by as much as 8% of the original bond length. The interaction with the surface induced a mixing between bonding and antibonding C–H orbitals, causing a charge polarization from the hydrogen to the carbon, which was accompanied by a weakening of the C–H chemical bond (Figure 10).

No evidence was found of a covalent chemical bond to the metal surface. The electronic interaction was instead driven by the minimization of Pauli repulsion to optimize the conditions for van der Waals bonding. However, the results of this experiment show that the methane molecule is already interacting chemically with the surface at low temperature. The C–H bond, which is already in the weakly adsorbed state, can be viewed as a precursor step to the dissociation. The molecule is thereby prepared for the dehydrogenation that takes place under catalytic conditions.

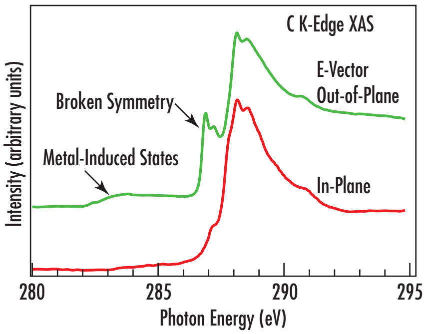

FIGURE 9. Angle-dependent XAS spectra of adsorbed methane. The intensity in the region between 283 and 286 eV arises as a consequence of orbital mixing between the molecule and the metal. The molecular symmetry is broken at the surface, leading to the appearance of the state at 287 eV, which corresponds to the symmetry-forbidden lowest unoccupied molecular orbital of gas-phase methane.

INVESTIGATORS

H. Öström, L.-Å. Näslund, and L.G.M. Pettersson (Stockholm University); H. Ogasawara (SSRL); and A. Nilsson (SSRL and Stockholm University).

PUBLICATION

H. Öström, H. Ogasawara, L.-Å. Näslund, L.G.M. Pettersson, and A. Nilsson, "Physisorption-induced C–H bond elongation in methane," *Phys. Rev. Lett.* **96**, 146104 (2006).

FUNDING

Swedish Foundation for Strategic Research, Swedish Natural Science Research Council, and U.S. DOE BES.

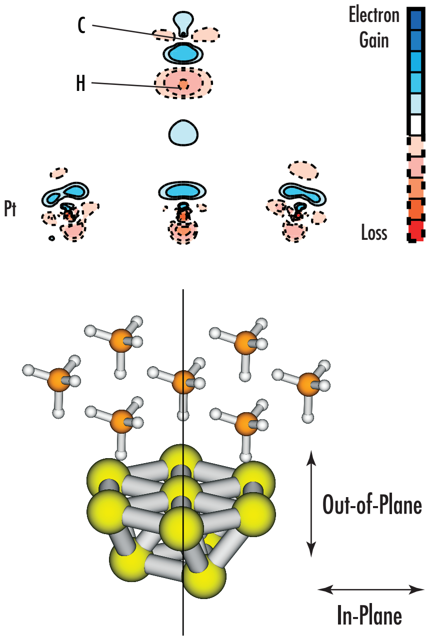

FIGURE 10. Top: Computer charge-density difference plot shows electrons polarized toward the carbon atom. This effect arises as a consequence of the interaction with the metal surface and leads to the weakening of the C–H bond. Solid lines in the plot denote electron charge buildup and dashed lines denote charge depletion. Bottom: Methane molecules above row of first layer of Pt atoms. Vertical line shows the cutting plane of the two-dimensional charge-density difference plot.

SUBSTRATE EFFECT ON THE CRYSTALLIZATION AND MELTING OF POLYETHYLENE THIN FILMS

Low-density polyethylene—a strong, flexible form of plastic composed of linear chains of ethylene (C_2H_4) molecules—has a wide range of commercial uses, from shrink-wrap packaging and plastic shopping bags to landfill caps and pond liners. It is mostly used in film or sheet form because of its tensile strength and impact and puncture resistance. Its behavior on solid substrates has also been studied for decades because of its uses in adhesive, wear-resistant, and lubricant coatings. Recently, the properties of ultrathin (below 100-nm) polymer films in confined geometries have received a great deal of attention because of potential uses in electronic components where miniaturization is becoming increasingly important. Designing polymer thin films with specific surface properties requires a detailed understanding of the underlying physical principles and the ability to control interfacial interaction parameters. This requires state-of-the-art synthesis, characterization, and imaging instrumentation capable of observing chemical and morphological variation on the nanometer scale. In this work, Wang et al. bring to bear a number of tools, including x-ray microscopy at the ALS, to help explain the falling melting point of ultrathin polyethylene films on various substrates.

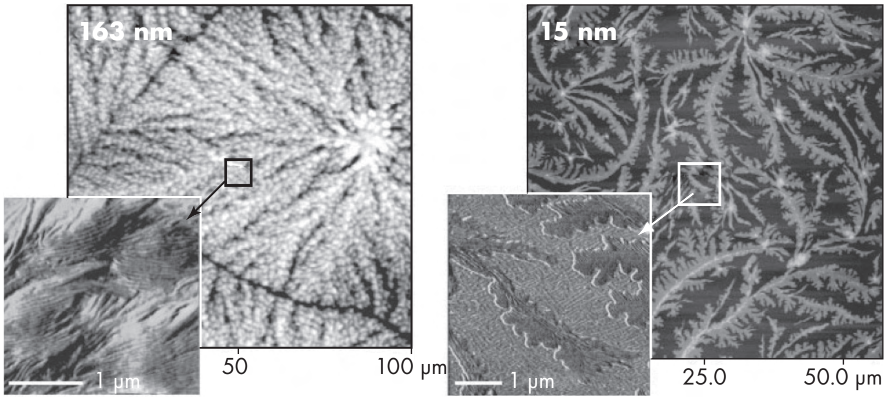

FIGURE 11. Scanning probe microscopy images of PE thin films on Si. The crystals are highly ordered, with clear spherulitic structure in the thicker film, but with axial structures in the thinner film. The friction images (insets) indicate that a transition from mainly edge-on to mainly flat-on lamellar orientation may be occurring with decreasing film thickness.

The crystallization of thin polymer films on solid substrates has been a topic of intensive interest because geometric confinement and interfacial interaction can change the properties of polymer films in comparison to the bulk state. Numerous groups have demonstrated that the rate of crystallization, crystal orientation, and density of nucleation can be very different for thin films versus the bulk material. A previous study has shown that thin (less than 100-nm) polyethylene (PE) films melt at 5–38 °C lower than the bulk material, depending on film thickness. Since melting is a well-defined first-order transition and an intrinsic property of a material, it is important to obtain a fundamental understanding at the molecular level of the factors that affect this process.

In this work, researchers investigated thin films of linear low- and medium-density PE. Semicrystalline PE films, with thicknesses from 160 to 15 nm, were produced by the spin-casting of solutions of varying polymer concentrations onto three substrates—silicon (Si), aluminum (Al), and polyimide (PI). Calculated substrate–polymer interfacial energies indicated that silicon has the greatest degree of interfacial interactions with PE.

The morphologies of the films were measured by atomic force microscopy (Figure 11). On the Si substrate, big two-dimensional spherulites (crystal aggregates with radial fibril structure) were observed in the thicker film (~160 nm). A detailed scan within the spherulites revealed well-organized lamellae (layered scale-like structures) oriented edge-on. In the thinner film (~15 nm), axial structures with flat-on lamellae were observed. For the films on the Al and PI substrates, the crystallites were randomly ordered, and the lamellae were edge-on regardless of film thickness.

The films on Si were also measured using scanning transmission x-ray microscopy (STXM) at ALS Beamline

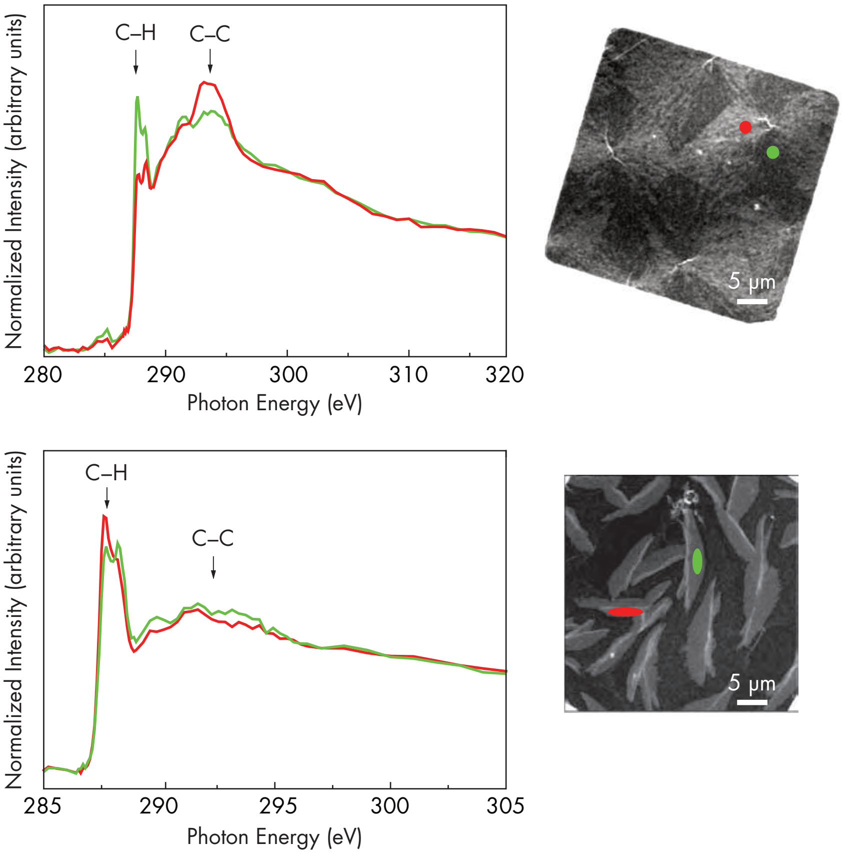

FIGURE 12. NEXAFS chain-orientation measurements of PE thin films with thicknesses of ~60 nm (top), and ~25 nm (bottom) from locations as indicated in the inset optical density images.

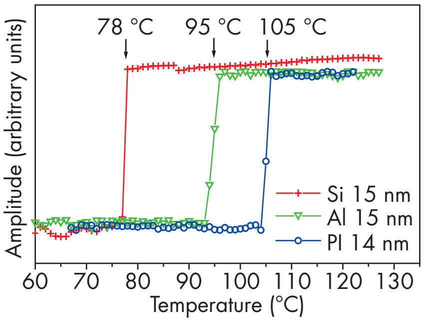

FIGURE 13. Shear modulus force microscopy curves for PE films with thicknesses below 20 nm on Si, Al, and PI substrates. The temperature at which the amplitude increases abruptly is the melting temperature.

5.3.2. In this technique, the near-edge x-ray absorption fine structure (NEXAFS) spectra were collected with the x-ray beam linearly polarized in the film plane. Because C–H absorption at 288 eV is maximized for x-ray polarization perpendicular to the polymer chain and C–C absorption at 290–295 eV is maximized for polarization parallel to the chain, the chain orientation can be determined by varying the x-ray polarization direction (Figure 12). For the thicker film, spectra were taken from two fibrils of the same spherulite. The results indicated that the chains were oriented parallel to the substrate and perpendicular to the crystal fibril radiation direction. For the thinner film, spectra were taken at two spots within the flat lamellae. Both showed a strong C–H feature but a weak C–C feature, indicating that the chains were oriented perpendicular to the film plane.

Finally, the melting temperature (T_m) of the films was measured with shear modulus force microscopy. The results (Figure 13) demonstrated a depression in T_m for the films on Si below a certain critical thickness, and the largest depression was ~38 °C. For the films on Al or PI, T_m depression was also observed, but with a much more gradual tendency (22 °C for films on Al and 12 °C for films on PI). Given the greater degree of Si–PE interfacial interactions, it would seem that the substrate attraction force tends to break the order of the chains in the crystalline state by randomly adsorbing and pinning the chains. This reduces the free energy of the system, ultimately leading to a lower melting temperature.

In summary, this study showed how substrate interaction plays a crucial role in affecting the morphology, chain orientation, and melting temperature of polymer thin films, shedding light on our ability to control interfacial properties such as strength, adhesion, and thermal stability. The results will be useful in predicting the properties of polymers on substrates with known surface energies and in properly choosing the right substrates for prospective applications.

INVESTIGATORS

Y. Wang, M. Rafailovich, J. Sokolov, and D. Gersappe (Stony Brook University); T. Araki, Y. Zou, and H. Ade (North Carolina State University); A.L.D. Kilcoyne (ALS); Gad Marom (The Hebrew University of Jerusalem); and Arnold Lustiger (ExxonMobil Research and Engineering Company).

PUBLICATION

Y. Wang, M. Rafailovich, J. Sokolov, D. Gersappe, T. Araki, Y. Zou, A.D.L. Kilcoyne, H. Ade, G. Marom, and A. Lustiger, "Substrate effect on the melting temperature of thin polyethylene films," *Phys. Rev. Lett.* **96,** 028303 (2006).

FUNDING

National Science Foundation and U.S. DOE BES.

Structural Biology

STRUCTURE AND RECEPTOR SPECIFICITY OF AN AVIAN FLU ANTIGEN

The H5N1 avian influenza virus, commonly called “bird flu,” is a highly contagious and deadly pathogen in poultry. Since late 2003, H5N1 has reached epizootic levels in domestic fowl in a number of Asian countries, including China, Vietnam, Thailand, Korea, Indonesia, Japan, and Cambodia, and has now spread to wild bird populations. More recently, the H5N1 virus has spread to bird populations across much of Europe and into Africa. Although its spread to the human population has so far been limited, it has a high mortality rate, accounting for 191 deaths out of 315 documented severe cases (as of June 25, 2007, according to the World Health Organization). In this work, Stevens et al. analyze the structure of the hemagglutinin (HA) from a highly pathogenic Vietnamese H5N1 influenza virus. HA, the principal antigen on the viral surface, is the primary target for neutralizing antibodies and is responsible for viral binding to host receptors, enabling the virus to enter the host cell. As such, the HA is an important target for both drug and vaccine development.

To date, the H5N1 influenza viruses, which are currently circulating in domestic and wild birds on three continents, have only a limited ability to infect humans. However, with continued outbreaks of the virus in poultry and wild birds, the potential for the emergence of a human-adapted H5 virus, either by reassortment (the mixing of genetic material from similar viruses) or mutation, is seen as a major threat to public health worldwide. Of the three influenza pandemics of the last century, the 1957 (H2N2) and 1968 (H3N2) pandemic viruses were avian–human reassortments in which three and two of the eight avian gene segments, respectively, were reassorted into an already circulating, human-adapted virus. The origin of the genes of the 1918 influenza virus (H1N1), which killed about 50 million people worldwide, is unknown.

Although a number of viral factors can determine the host range restriction and pathogenicity of influenza A viruses, recent evidence suggests that HA, the principal antigen on the viral surface, is a critical factor for efficient human-to-human transmission. The HA homotrimer is responsible for viral binding to host receptors containing glycans (complex sugar chains) terminated by sialic acids; avian viruses preferentially bind to sugar receptors with sialic acid in an α2-3 linkage, whereas human-adapted viruses prefer sialic acids in an α2-6 linkage.

The researchers utilized a number of technologies to study the structure–function relationship of an HA from a highly pathogenic H5N1 influenza virus, A/Vietnam/1203/2004 (Viet04). Functional HA trimers were produced in a baculovirus expression system, eliminating the difficulty and hazard of extracting the HA from live influenza viruses. Three hundred and eighty-four crystallization conditions were tested using less than 6 μL of protein material. The most promising condition based on crystal quality was translated to sitting drop conditions, and subsequent optimization of these conditions yielded diffraction-quality crystals. The Viet04 HA structure was then solved by molecular replacement to 2.95-Å resolution from data collected at ALS Beamline 8.2.2 (Figure 1).

The resulting Viet04 HA trimer structure is very similar to other avian, human, and swine HAs, with a globular head containing the receptor binding domain and a vestigial esterase domain, and a membrane proximal domain with its distinctive, central alpha-helical stalk and HA1/HA2 cleavage site. Comparison of human, avian, and swine HA structures revealed that the Viet04 HA is more closely related to human 1918 H1 HA than to the other HA structures, including a related 1997 duck H5 HA (A/Duck/Singapore/3/1997).

The same HA protein can also be used to analyze HA receptor specificity using a recently described technique involving a glycan microarray—a glass slide imprinted with hundreds of different glycan chains to systematically analyze their binding properties. Glycan microarray analysis of Viet04 HA revealed a preference for binding to avian α2-3 sialic acid receptors (Figure 2, top). The introduction of mutations that can convert H1 serotype HAs to human α2-6 receptor specificity only enhanced or reduced affinity for avian-type receptors. However, the introduction of mutations at positions 226 and 228, which are known to convert avian H2 and H3 HAs to human receptor specificity, permitted binding to natural human biantennary α2-6 glycans (Figure 2, bottom).

FIGURE 1. Ribbon diagram of the Viet04 trimer. The three monomers are colored blue, green, and gray. The receptor binding site on one monomer is highlighted.

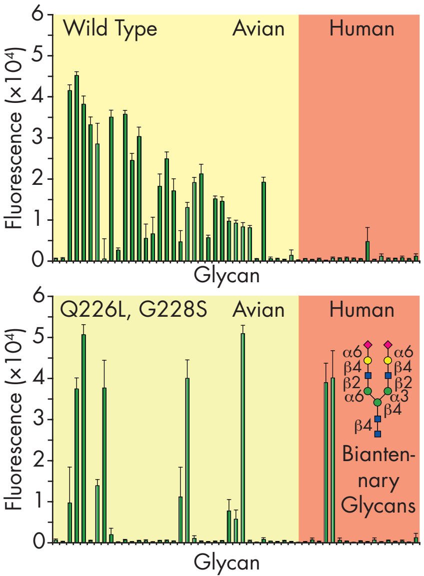

FIGURE 2. Top: Glycan microarray analysis of the wild-type Viet04 reveals avian preference. Bottom: Mutations at positions 226 and 228 result in a reduction in preference for avian receptor analogs and an increase in human biantennary glycans.

Thus, these mutations on the H5 HA not only reduced avidity to avian sialosides, they increased specificity for human α2-6–linked biantennary N-linked glycans, which could serve as receptors on lung epithelial cells. These combined effects could allow the Viet04 virus to escape entrapment by mucins in the lungs and increase binding to susceptible human epithelial cells. These mutations therefore provide only one possible route by which H5 viruses could gain a foothold in the human population, but other mutations are likely required to facilitate the complete switch in receptor specificity that appears to be critical for human-to-human transmission.

INVESTIGATORS

J. Stevens, O. Blixt, J.C. Paulson, and I.A. Wilson (The Scripps Research Institute); T.M. Tumpey (Centers for Disease Control and Prevention); and J.K. Taubenberger (Armed Forces Institute of Pathology).

PUBLICATION

J. Stevens, O. Blixt, T.M. Tumpey, J.K. Taubenberger, J.C. Paulson, and I.A. Wilson, "Structure and receptor specificity of the hemagglutinin from an H5N1 influenza virus," *Science* **312**, 404 (2006).

FUNDING

National Institutes of Health and Skaggs Institute for Chemical Biology.

STRUCTURE OF THE COMPLETE 70S RIBOSOME AT 3.7-Å RESOLUTION

The ribosome is the largest asymmetric macromolecular complex for which an atomic structure has been determined. The first all-atom structure of a ribosome was obtained by Cate and co-workers in 2005, using ALS data, for two different conformations of vacant *Escherichia coli* 70S ribosomes at 3.5-Å resolution. Comparison of the 3.7-Å structure of the tRNA-containing 70S ribosome complex with that of the vacant ribosome provides insight into the structural changes that occur upon binding tRNA. This has an important bearing on our understanding of the structural dynamics of the ribosome and tRNA during protein synthesis. Besides providing a sound structural foundation for attempting to understand the molecular mechanisms of protein synthesis, the new structure of a functional ribosome complex, together with other structures of 70S ribosomes and ribosomal subunits, can be used to understand the molecular basis of action of the many antibiotics that target bacterial ribosomes, leading to rational design of novel antibiotics.

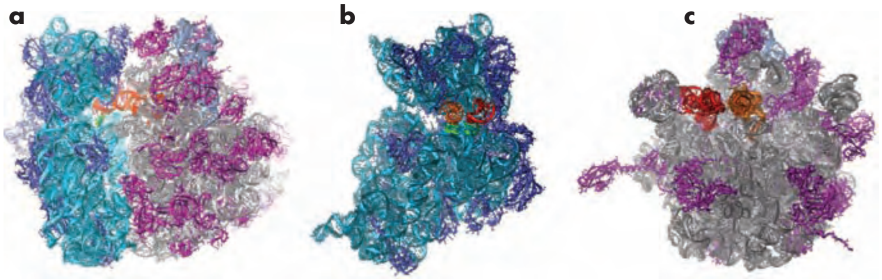

FIGURE 3. X-ray crystal structure of a 70S ribosome functional complex at 3.7-Å resolution. The complex contains a defined mRNA (green) and two tRNAs, bound to the P and E sites (orange and red) at the subunit interface. (a) The 30S subunit is shown on the left (16S rRNA in cyan, 30S proteins in dark blue) and the 50S subunit is on the right (23S rRNA in gray, 5S rRNA in gray-blue, and 50S proteins in magenta). (b) The 30S subunit. (c) The 50S subunit.

Ribosomes are RNA-based protein factories found in all living cells, responsible for translating the genetic information encoded in messenger RNA (mRNA) into proteins. The first x-ray structures of the complete 70S ribosome were determined in 1999 at 7.8 Å and in 2001 at 5.5 Å, using diffraction data collected at ALS Beamline 5.0.2. These structures showed how the ribosomal RNA and the more than 50 ribosomal proteins are organized to form the structure of the complete ribosome and the positions of the mRNA and transfer RNAs (tRNAs) in the ribosome. Now, using data collected at ALS Beamline 12.3.1, researchers from UC Santa Cruz have solved the structure of a *Thermus thermophilus* 70S ribosome functional complex at 3.7-Å resolution (Figure 3). Because of the large cell dimensions of ribosome crystals, they diffract weakly, and spots are crowded close together in the diffraction patterns.

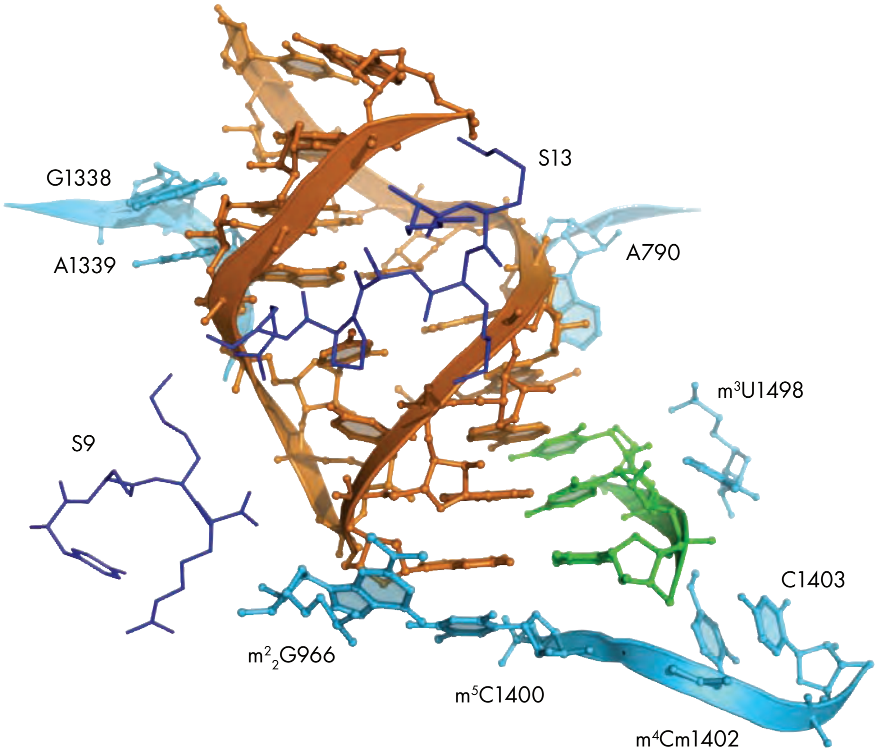

FIGURE 4. Interactions of the anticodon stem loop of elongator tRNA^{Phe} (orange) and mRNA (green) with 16S rRNA (cyan) and small-subunit proteins (blue) in the 30S subunit P site.

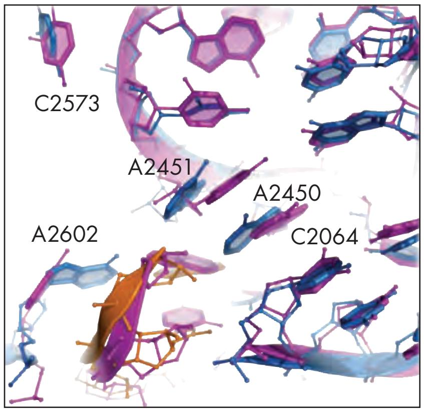

FIGURE 5. Structural changes in the peptidyl transferase center. View of the *T. thermophilus* 70S ribosomal complex containing deacylated tRNA bound to the P site (blue) compared with the *H. marismortui* 50S subunit model complex (magenta).

Consequently, the high-flux beams, sensitive large-area detectors, and well-focused, compact beam cross sections available at the ALS all played a crucial role in this work. Research in this area may lead to novel antibiotics targeting bacterial ribosomes that have developed resistance to current drugs.

The improved structure resolution allows construction of the first all-atom model of a ribosome functional complex containing its mRNA and tRNA substrates. This provided two kinds of information crucial to the understanding of the protein synthesis mechanism: (1) details of molecular interactions between the ribosome and its substrate RNAs, and (2) ways in which the structures of both the ribosome and the tRNAs are altered by their functional interactions.

During protein synthesis, the genetic code is used to translate the sequence of nucleotides in an mRNA into the sequence of amino acids in the protein. Groups of three nucleotides (codons) in the mRNA are read by base pairing with a complementary three-nucleotide sequence of nucleotides (anticodon) in the tRNAs, which carry the growing protein chain during synthesis. There are three binding sites for tRNA in the ribosome, called the A (aminoacyl), P (peptidyl) and E (exit) sites. In the crystals that were used for the structure determination, tRNA^{Phe} was bound to the P site and noncognate endogenous tRNA to the E site of the ribosome in addition to a 10-nucleotide mRNA fragment. The tRNA is bound most tightly to the ribosomal P site, which is responsible for maintaining the translational reading frame of the mRNA and for holding the growing protein chain in the ribosome via the peptidyl-tRNA. The structure reveals a high density of contacts between the tRNA and ribosomal RNA bases and backbone, as well as ribosomal proteins, explaining the high affinity of the P site for tRNA (Figure 4). Catalysis of peptide bond formation takes place on the 50S subunit by a ribosomal activity called peptidyl transferase. In the new structure, an intriguing structural rearrangement is observed in the peptidyl transferase center (Figure 5).

In the course of protein synthesis, tRNAs move through the ribosome, coupled to movement of mRNA like an assembly line, in a process called translocation. Translocation of tRNA from the P to the E site is crucial for the energetics of this process, and requires that the terminal nucleotide A76 of tRNA is deacylated—i.e., no

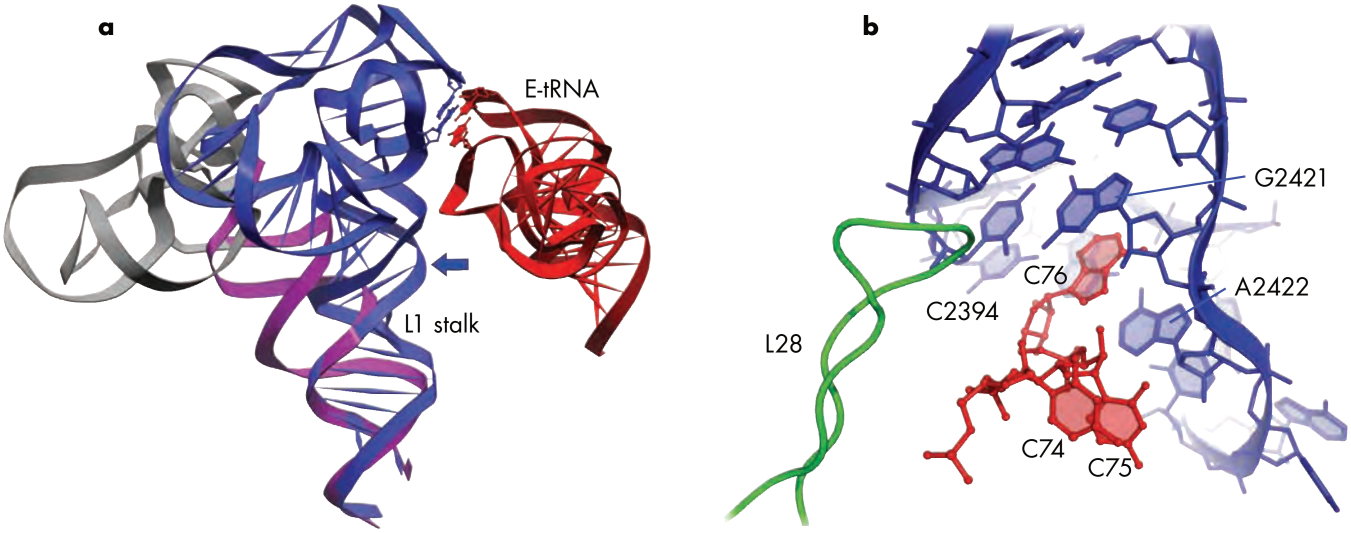

FIGURE 6. E-site tRNA interactions. (a) Interaction of the elbow of E-site tRNA (red) with 23S rRNA (blue) in the L1 stalk region, showing the large-scale displacement of the stalk relative to its position in the vacant ribosome, induced by tRNA binding. The blue arrow indicates the extreme compression of the major groove of helix 76 of 23S rRNA that accompanies this movement. (b) Interactions of the CCA tail of E-site tRNA with the large subunit.

longer contains a bound protein chain, which is its chemical state following peptide bond formation. The new structure explains this requirement, showing that binding of tRNA to the E site requires hydrogen bonding between the ribose moiety of A76 and C2394 of 23S rRNA (Figure 6); the presence of a peptidyl, aminoacyl, or even a methyl group bound to the terminal ribose would thus prevent these interactions.

Future ribosome structure studies that include functional states may eventually lead to an atomic-resolution three-dimensional "movie"—the ultimate description of the molecular mechanism of protein synthesis.

INVESTIGATORS

A. Korostelev, S. Trakhanov, M. Laurberg, and H.F. Noller (UC Santa Cruz).

PUBLICATION

A. Korostelev, S. Trakhanov, M. Laurberg, and H.F. Noller, "Crystal structure of a 70S ribosome-tRNA complex reveals functional interactions and rearrangements," *Cell* **126**, 1065 (2006).

FUNDING

National Institutes of Health and Agouron Institute.

ROLE OF THE TRIGGER LOOP IN TRANSCRIPTION

Every cell of the human body contains the same DNA. The variation in cell types—such as blood, nerve, and liver cells—comes from the selection of genes chosen to be copied by RNA polymerase from DNA into messenger RNA. This transcription process is the first step and the primary control point in gene expression, and the central enzyme involved in this process for eukaryotic cells—such as human cells—is RNA polymerase II (pol II). The structure of the 12-subunit pol II protein complex and its role in transcription regulation is the key to understanding the information flow from gene to protein. A pol II molecule slides along a DNA molecule, splitting the DNA helix as it goes, then synthesizes a complementary strand of RNA and checks the accuracy of the copied information. Pol II is capable of retracing its steps if it comes across damaged DNA. The basis for this highly accurate transcription lies in a structure called the trigger loop, which selects the correct RNA building blocks and places them in the right spot on the growing RNA strand, triggering a catalytic reaction. If the process goes well, healthy cell growth and differentiation is the result.

Protein crystallography studies at the ALS have helped researchers from the Stanford University School of Medicine identify how the RNA polymerase II (pol II) enzyme discriminates among potential RNA building blocks to ensure an accurate transcription process for turning DNA's genetic blueprint into working proteins. Pol II is the protein complex responsible for all messenger RNA production in eukaryotic cells, but the mechanism by which this enzyme chooses specific nucleotides and catalyzes the reaction that builds them into a growing RNA strand has not been understood until now. Working at the ALS Macromolecular Crystallography Facility (Beamlines 5.0.2 and 8.2.2), and SSRL (Beamlines 9-2 and 11-1), this team determined the structure and function of a trigger-loop mechanism in the pol II enzyme that couples nucleoside triphosphate (NTP) recognition and catalysis to ensure accurate transcription.

The fundamental mechanism of transcription is conserved among cellular RNA polymerases. Common features include an unwound region, or "transcription bubble," of about 15 base pairs of the DNA template and some eight residues of the RNA transcript hybridized with the DNA in the center of this bubble. Pol II is capable of both forward and backward movement on the DNA. Forward movement is favored by the binding of substrate—NTPs, in this case—while backtracking occurs when the enzyme encounters an impediment, such as damaged DNA. All NTPs can bind the entry (E) site of pol II, whereas only an NTP properly matched to the DNA template can enter the addition (A) site and be added to the growing RNA chain.

The mechanism by which the correctly matched and positioned NTP is recognized and leads to catalysis remained unanswered by previous studies. The energies of base pairing and stacking are insufficient for base selectivity, and the question arose as to why transient occupation of the A site by either incorrect NTP or 2′-dNTP substrates does not lead to erroneous RNA synthesis. Genetic and biochemical studies have implicated two conserved polymerase domains, termed F and G, in the transcription mechanism. Protein x-ray crystallography studies have identified these two domains with elements adjacent to the polymerase active site, now termed the bridge helix (F) and trigger loop (G). In the x-ray structures of transcribing complexes, however, no contact of these structural elements with NTP in the A or E sites has been observed. The present work describes a series of pol II transcribing complex structures that reveal such contacts and suggest the roles of these domains in the transcription mechanism (Figure 7).

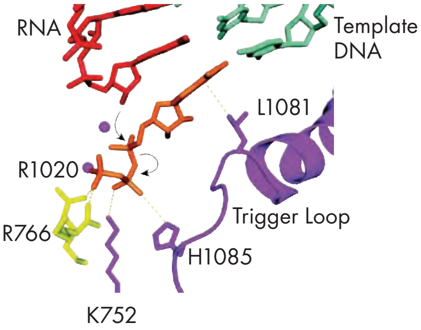

FIGURE 7. The pol II trigger loop is a mobile element, allowing entry of NTP into the E and A sites and sealing off the A site in the conformation reported here. When base, sugar, and phosphates are all correct, a histidine residue of the trigger loop is aligned with the ß-phosphate, facilitating nucleophilic attack by the RNA 3′-OH and phosphodiester bond formation. In this way, the trigger loop couples nucleotide selection to catalysis, reading out not only the chemical nature of the NTP but also the parameters of the DNA–RNA hybrid helix in the A site.

Two further features of trigger-loop interaction may be crucial for transcription. First, the contact of His1085 with the NTP β-phosphate may be key to catalysis. Second, trigger-loop interaction with NTP in the A site is evidently poised on the verge of stability, since the interaction could only be detected with improved data quality and analysis. If any feature of the NTP or its location is incorrect, the interaction will be lost.

The trigger loop may therefore couple nucleotide recognition to catalysis. In the presence of matched ribosomal NTP in the A site, it will swing into position and literally "trigger" phosphodiester bond formation. An incorrect NTP in the A site will not support trigger-loop interaction and so is unlikely to undergo catalysis. When reaction with a correct NTP does occur, the release of pyrophosphate disrupts contact with His1085, likely destabilizing trigger-loop interaction and freeing the DNA–RNA hybrid for translocation. Movement of the trigger loop, coupled to that of the bridge helix, may contribute to the translocation process.

INVESTIGATORS

D. Wang, D.A. Bushnell, K.D. Westover, C.D. Kaplan, and R.D. Kornberg (Stanford University).

PUBLICATION

D. Wang, D.A. Bushnell, K.D. Westover, C.D. Kaplan, and R.D. Kornberg, "Structural basis of transcription: Role of the trigger loop in substrate specificity and catalysis," *Cell* **127,** 941 (2006).

FUNDING

National Institutes of Health.

THE INITIATION OF BACTERIAL DNA REPLICATION

Billions of years ago, there were no plants, animals, or bacteria, just a "soup" of small free-floating molecules. The famous 1953 experiment by Miller and Urey, in which they made amino acids by applying sparks to hydrogen, methane, ammonia, and water, led to this "primordial soup" theory of life. Small molecules eventually came together and formed complex molecules. Eventually the first cell was formed. It is uncertain how that first cellular life form came into being. However, at the beginning was replication. And recently, scientists identified one of the first tools of replication, a helical substructure within a superfamily of proteins called AAA+, which spans all three domains of life—Archaea, Bacteria, and Eukarya. Studies of the bacteria *Aquifex aeolicus* and *Escherichia coli, Drosophila melanogaster* (the fruit fly), and earlier research identifying AAA+ proteins in archaeal organisms indicate that DNA replication is highly conserved, i.e, it comes from the last common ancestor of all extant life. Understanding replication in simpler life forms will help us understand such mechanisms in higher life forms. It may also help us understand how these mechanisms have been conserved and bring us closer to pinpointing how cells' ability to duplicate their genomes came into being.

For the first time, scientists have determined the structure of the initiator of bacterial DNA replication. It is already known that such replication is controlled by a protein known as DnaA, a member of the AAA+ superfamily of ATPases. What has now been discovered is that the core of the initiator is not the closed-ring structure expected for this system. Instead, DnaA forms an open right-handed helix. In addition, the architecture indicates that this AAA+ superhelix will wrap coils of the DNA around its exterior, causing the DNA double helix to deform as a first step in the separation and unwinding of its strands. Eukaryotic and archaeal initiators also have the structural elements that promote open-helix formation, indicating that a spiral, open-ring AAA+ assembly is a conserved element from a common evolutionary ancestor of Archaea, Bacteria, and Eukarya.

At the beginning of replication, ATP binds with DnaA, causing it to change from a monomer to a large oligomeric complex consisting of DnaA monomers bound to a series of DnaA "boxes" (9-base-pair sequences). Although this DnaA–DnaA-box interaction is highly conserved in all bacteria, the mechanism by which ATP activates DnaA oligomerization has been poorly understood. However, UC Berkeley researchers using ALS Beamline 8.3.1 have determined the structure of ATP-bound DnaA from

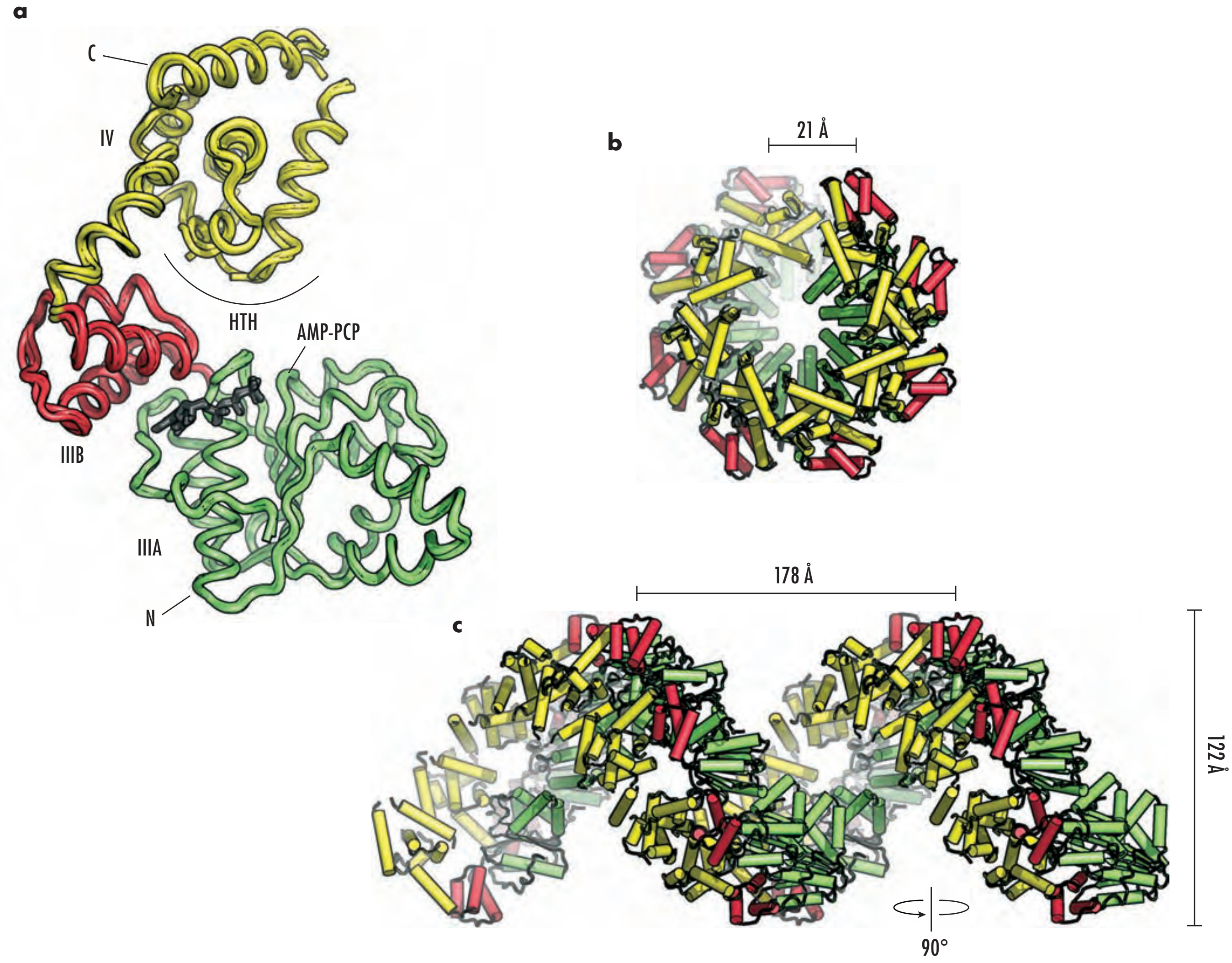

FIGURE 8. Structure of ATP–DnaA, which forms a right-handed helical filament with 8_1 symmetry. (a) Overlay of the four DnaA monomers in the asymmetric unit. The AAA+ module is colored green and red (domains IIIA and IIIB, respectively); domain IV, the DNA-binding element, is yellow. The ATP analog AMP-PCP is shown as black sticks. The helix-turn-helix (HTH) motif in domain IV and the N and C termini are labeled. Axial (b) and side (c) views of four symmetry-related DnaA tetramers are shown. Monomers are colored by domain as in (a).

the bacterium *Aquifex aeolicus.* Using data collected from a single crystal, they assembled a high-resolution model of an ATP-bound DnaA molecule (Figure 8) using an ATP analog (AMP-PCP). Each asymmetric unit contains four structurally similar DnaA molecules arranged in a head-to-tail manner.

Several important pieces of information came out of this study. First, by comparing the ATP–DnaA binding pocket to those of other AAA+ assemblies, it was determined that the ATP–DnaA active site is in a closed configuration, which allows it to bind nucleotides using conserved residues from neighboring AAA+ protomers. The precise geometry of these contacts depends on the subunit arrangement arising from the ATP–DnaA spiral, strongly supporting the physiological relevance of the helical filament architecture.

The researchers also discovered that a V-shaped α-helical steric wedge protrudes away from the core AAA+ fold and reorients the AAA+ interface, preventing a flat-ring assembly (Figure 9). This establishes the unique DnaA superhelix. While the steric wedge directs this helical architecture, an ATP-specific conformational change within the AAA+ domain accommodates and stabilizes subunit–subunit interactions necessary to

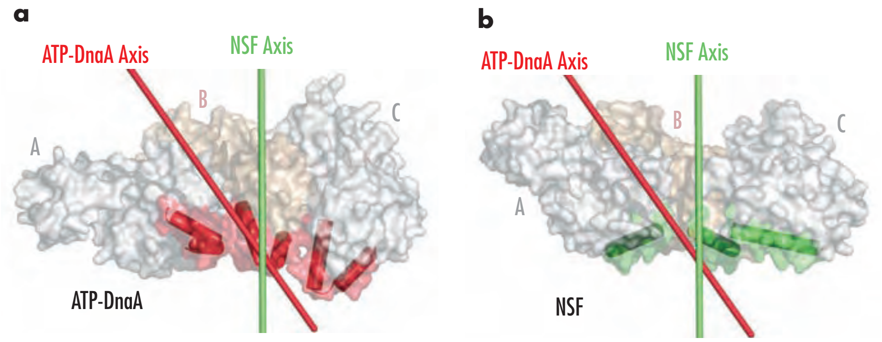

FIGURE 9. The initiator helical insert drives filament formation. Comparison of ATP–DnaA helix with a classic AAA+ protein such as NSF, which is a closed-ring assembly, reveals a novel AAA+ assembly mode. The central symmetry axes of each assembly are depicted as rods. Helices α3 and α4 of DnaA (a) form a V-shaped steric wedge that blocks assembly of DnaA domains into a closed, planar array like NSF (b).

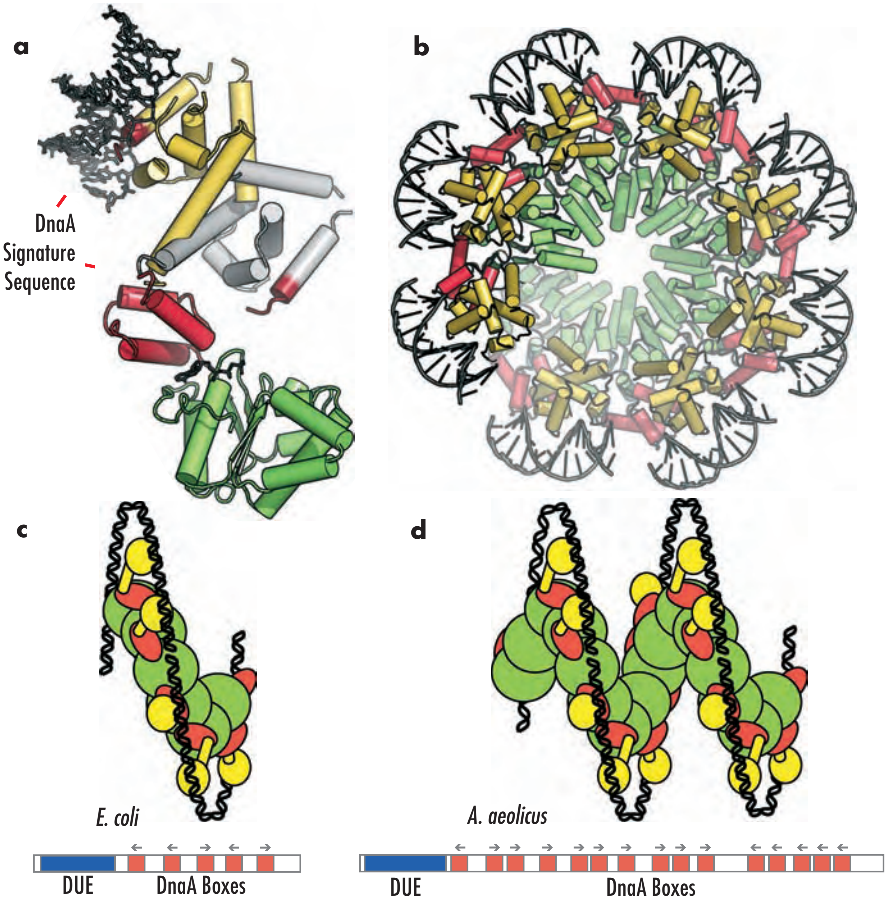

FIGURE 10. The DnaA filament in the context of the nucleoprotein complex. (a) DNA engagement by oligomerized DnaA requires a rotation of the DNA-binding domain (yellow) about the hinge at the base of the connector helix from its position in the filament (gray). DNA is modeled onto domain IV. (b) The outward rotation orients DNA on the outside of the helical assembly, as predicted from electron microscope (EM) and DNA-protection studies. (c,d) Modulation of filament size enables the engagement of origins of different lengths with highly diverse numbers of DnaA boxes (shown in red; orientations indicated by arrows), exemplified by the *E. coli* and *A. aeolicus* origins.

support oligomer formation at replication origins. This rearrangement adjusts for internal incompatibility and is crucial for filament creation.

The mechanism that allows DnaA to render an origin competent for replisome activity is the linker helix in domain IV of ATP–DnaA (Figure 10). This helix is bent at a ≥40° angle, and the ATPase and DNA binding domains of DnaA are tethered but conformationally uncoupled, allowing the origin DNA to wrap around the outside of a DnaA core (consistent with previous *E. coli* modeling studies).

Understanding replisome initiation allows us to start answering some long-held questions and start asking some new ones. Although the DnaA–DnaA-box interaction is highly conserved in all bacteria, the origins of different bacteria vary greatly. How does a conserved initiator protein accommodate this origin heterogeneity? A filamentous DnaA assembly provides a ready mechanism, as it could grow or shrink at either end depending on the size and organization of the origin.

The structural similarities of AAA+ in archaeal, eukaryotic, and bacterial initiators further suggest these proteins share substantial mechanistic properties. A recent classification of AAA+ proteins reveals that all initiators share a specific helical insert in their ATPase cores. We must then ask, do the AAA+ domains of archaeal and eukaryotic initiators assemble in a manner similar to that of bacterial ATP–DnaA? Recent EM reconstructions of the *Drosophila melanogaster* origin recognition complex reveal a helical feature within the initiator that accommodates a five-subunit, DnaA-like AAA+ assembly. This finding indicates that the DnaA oligomer is a useful model to further our understanding of higher-order initiator architecture and function.

INVESTIGATORS

J.P. Erzberger and M.L. Mott (UC Berkeley) and J.M. Berger (UC Berkeley and Berkeley Lab).

PUBLICATION

J.P. Erzberger, M.L. Mott, and J.M. Berger "Structural basis for ATP-dependent DnaA assembly and replication-origin remodeling," *Nat. Struct. Mol. Biol.* **13**, 676 (2006).

FUNDING

G. Harold and Leila Y. Mathers Charitable Foundation and National Institutes of Health.

FIRST MOLECULAR MODEL OF THE EGFR TYROSINE KINASE DOMAIN

Overactivation of epidermal growth factor receptors (EGFRs) is implicated in several forms of cancer, and EGFR inhibitors are becoming a powerful treatment option. They have been approved in the U.S. and other countries for treatment of advanced non-small-cell lung cancer after failure of chemotherapy. Two such options inhibit EGFR tyrosine kinase activity by competing with ATP for the ATP-binding site. Lapatinib, a broader-spectrum inhibitor, targets two EFGR family members, known for their roles in lung and breast cancer. Determining more precisely how EGFR works will lead to the design of better inhibitors. Researchers using information obtained from the ALS discovered that EGFR maintains itself in the "off" state. When a receptor is activated, it pairs up with another receptor—symmetrically, and nothing happens; asymmetrically, and one "pushes" an activation site in the other, sending signals that lead to cell growth. The researchers discovered that if initial EGFR activation is by specialized extracellular ligands, growth can proceed normally. However, if a mutation frequently found in lung cancer patients overactivates EGFR, it gets stuck in the "on" position. Their molecular model will help researchers design new approaches that block activation sites, shutting down overexpressed EGFRs and stopping rampant cell division.

Communication between individual cells is critical for the development and well-being of multicellular organisms. Intercellular communication in animals relies on antenna-like receptor molecules present on the cell surface. Small protein molecules specialized for signaling, such as insulin and growth hormone, are produced by one cell, then engage receptors on another cell and affect that cell's behavior through a process called signal transduction. The EGFR is one such receptor and is key in activating cell growth. It consists of an extracellular ligand-binding region, a single transmembrane segment, and an intracellular tyrosine kinase domain (EGFR's catalytic center). For the first time, a group of researchers using the tools of the ALS have constructed a detailed molecular model of this catalytic center.

When EGFR is activated by extracellular protein ligands, members of the EGFR family pair up (dimerize), which in turn activates the intracellular kinase domain. Activated EGFR phosphorylates several tyrosine residues in its C-terminal tail, triggering a series of downstream signaling events. Such signals play critical roles in regulating many important cellular functions. However, uncontrolled activation of EGFR by mutation or overexpression is associated with a variety of human cancers. To date, more than ten cancer drugs targeted to EGFR are being tested or are in clinical use. However, despite extensive studies, how the EGFR kinase domain is kept inactive prior to ligand engagement and how it is activated upon ligand-induced dimerization remained unknown.

Using diffraction data collected at ALS Beamlines 8.2.2, 8.3.1, and 12.3.1, a multi-institutional team (from Berkeley Lab, Howard Hughes Medical Institute, Johns Hopkins, and Northern Illinois University) has answered these questions by providing a detailed molecular structure of the EGFR switches at the kinase domain level. Their results show that the kinase domain is monomeric and possesses a low basal activity in solution. Increasing the local concentration by tethering the domain onto lipid vesicles results in a ~15-fold increase of kinase activity. A mutation (L834R) frequently found in human lung cancer increases the kinase activity by ~20-fold. These results establish that the EGFR kinase domain is autoinhibited (self-restrained), and that autoinhibition can be released by either ligand-induced dimerization or the L834R mutation.

Two crystal forms of the EGFR kinase domain had already been determined—the active conformation by researchers at Genentech and the inactive (complexed with lapatinib, a kinase inhibitor) by researchers at GlaxoSmithKline (Figure 11). The research team solved two crystal structures of the kinase domain, both having an active conformation identical to that seen in the Genentech active crystal structure. The fact that the kinase domain is inactive in solution but active in the crystallized form (except in the presence of lapatinib) suggests that the high concentration of kinase in the crystals mimics the high local concentration in dimerized receptors, leading to the formation of an activated dimer in the crystal lattice. The lapatinib-bound structure is likely to be trapped in an inactive conformation because lapatinib is in-

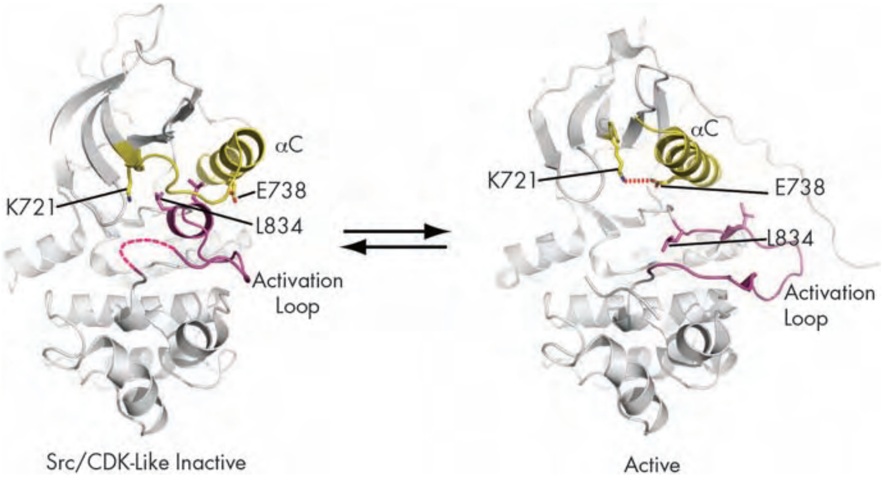

FIGURE 11. Comparison of the inactive and active conformations of the EGFR kinase domain.

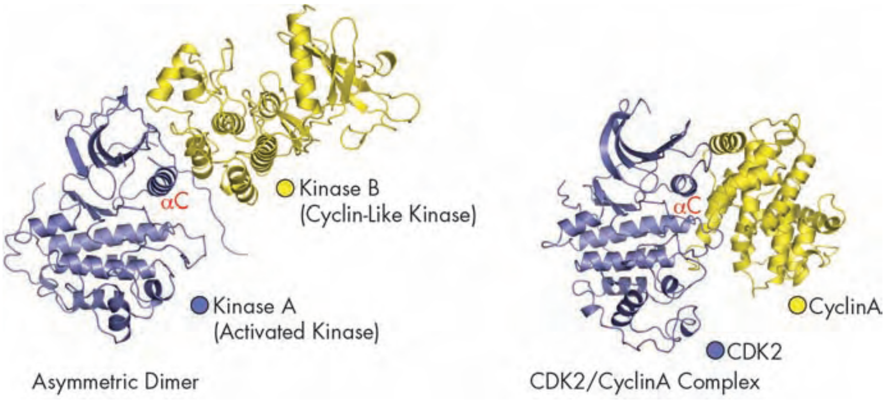

FIGURE 12. Comparison of the asymmetric dimer and the CDK2–cyclinA complex.

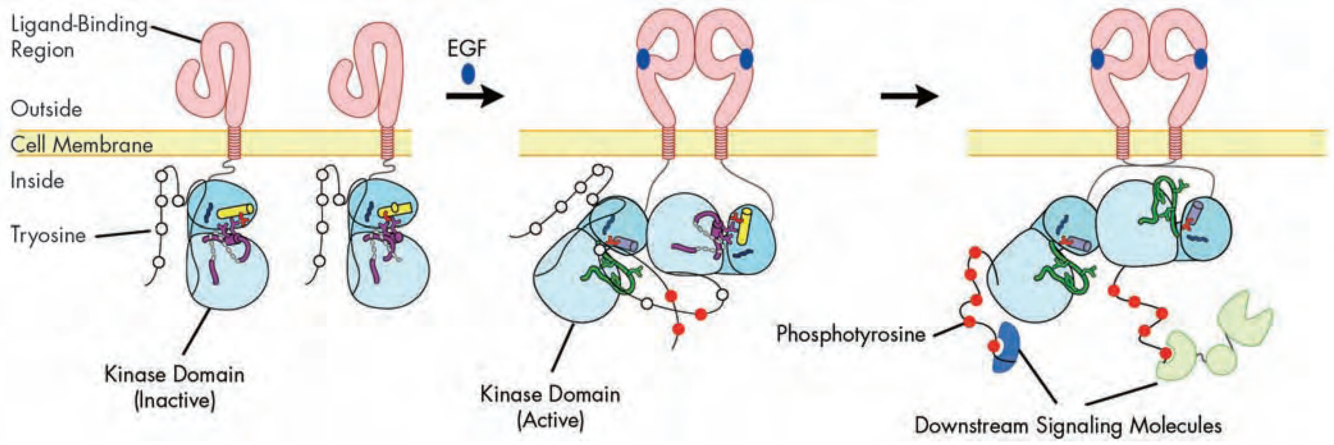

FIGURE 13. A general model of the activation mechanism for the EGFR family receptor tyrosine kinases. All the members in the family can act as the cyclin-like activator for the kinase-active members (EGFR, ErbB2, and ErbB4) after the EGF ligand induces homo- or heterodimerization.

compatible with the active conformation.

The research team identified two prominent intermolecular interactions in the crystal lattice associated with the active conformation—one corresponding to a symmetric dimer, the other to an asymmetric one. Extensive mutational analysis showed that the symmetric dimer is not relevant to EGFR activation. However, in the asymmetric dimer, the bottom of one kinase domain docks onto the top of the other, stabilizing the active conformation of the kinase domain (Figure 12). This activation mechanism strongly resembles cyclin, a well-understood signaling switch, which activates the protein kinase function in cyclin-dependent kinase (CDK), a cell-cycle regulator. The EGFR activation mechanism discovered here has one receptor molecule acting as the "cyclin" for the other (Figure 13). One important consequence of this work is that it provides a potential route for the inhibition of EGFR by blocking the cyclin-like interfacial region.

INVESTIGATORS

X. Zhang and J. Gureasko (UC Berkeley and Howard Hughes Medical Institute), L. Shen and P.A. Cole (Johns Hopkins University), and J. Kuriyan (UC Berkeley, Howard Hughes Medical Institute, and Berkeley Lab).

PUBLICATION

X. Zhang, J. Gureasko, K. Shen, P.A. Cole, and J. Kuriyan, "An allosteric mechanism for activation of the kinase domain of epidermal growth factor receptor," *Cell* **125**, 1137 (2006).

FUNDING

National Institutes of Health.

FIRST DETAILED LOOK AT RNA DICER

RNA interference is an ancient genetic process in which targeted genes—blueprints for producing certain proteins—can be "turned off." It is therefore a necessary step in many fundamental biological events, including genome rearrangement, stem-cell differentiation, brain development, and viral defense. The ability to control gene expression with flexibility and precision is a highly sought-after goal: by observing the effects of switching off a particular gene, scientists can infer the gene's function. Such basic knowledge is invaluable in itself, but can also be put to practical use in treating diseases such as cancer or improving the pest-resistance of agricultural crops. The Dicer enzyme is known to play a key role in RNA interference, but the details of how it functions have remained unclear. The Dicer structure solved by MacRae et al. not only provides an explanation of how the enzyme measures out lengths of RNA for slicing, it also suggests the possibility of tailoring those lengths as desired.

Scientists have gotten their first detailed look at the molecular structure of an enzyme that Nature has been using for eons to help silence unwanted genetic messages. A team of researchers with Berkeley Lab and UC Berkeley used x-ray crystallography at ALS Beamlines 8.2.1 and 8.2.2 to determine the crystal structure of Dicer, an enzyme that plays a critical role in a process known as RNA interference. The Dicer enzyme is able to snip a double-stranded form of RNA into segments that can attach themselves to genes and block their activity. With this crystal structure, the researchers learned that Dicer serves as a molecular ruler, with a clamp at one end and a cleaver at the other end a set distance away, that produces RNA fragments of an ideal size for gene-silencing.

RNA—ribonucleic acid—has long been known as a multipurpose biological workhorse, responsible for carrying DNA's genetic messages out from the nucleus of a living cell and using those messages to make specific proteins in a cell's cytoplasm. In 1998, however, scientists discovered that RNA can also block the synthesis of proteins from some of those genetic messages. This gene-silencing process is called RNA interference and it starts when a double-stranded segment of RNA (dsRNA) encounters the enzyme Dicer.

Dicer cleaves dsRNA into smaller fragments called short interfering RNAs (siRNAs) and microRNAs (miRNAs). Dicer then helps load these fragments into a large multiprotein

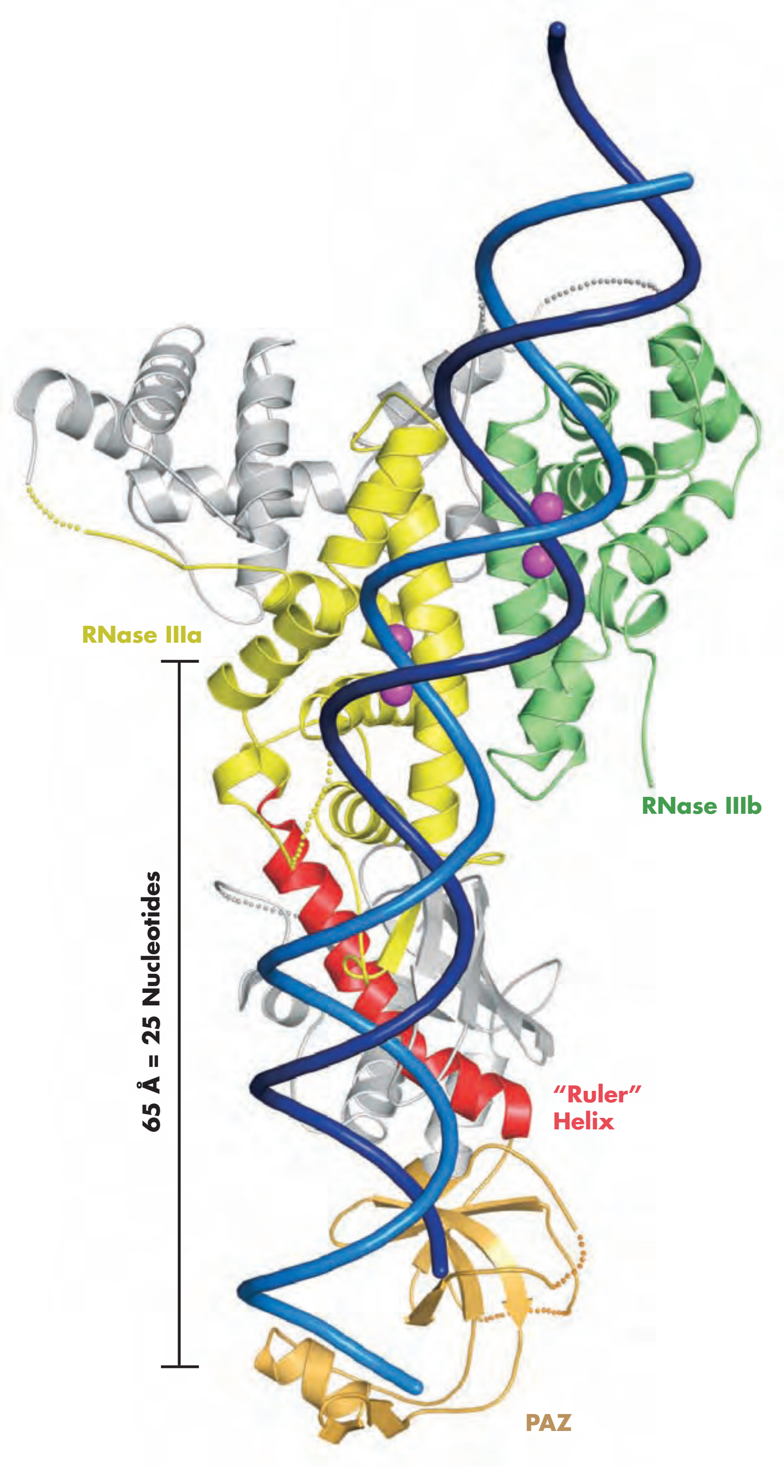

FIGURE 14. Front view of a ribbon representation of Dicer. The enzyme resembles an axe with the RNA clamp at the handle (the PAZ domain) and the cleaver at the blade (RNase IIIa and IIIb). A flat connector area measuring 65 Å is the ruler portion that is used to measure out segments of 25 nucleotides (bases) in length. A segment of double-stranded RNA (blue) is shown passing through the Dicer enzyme.

complex called RISC, for RNA-induced silencing complex. RISC can seek out and capture messenger RNA (mRNA) molecules (the RNA that encodes the message of a gene) with a base sequence complementary to that of its siRNA or miRNA. This serves to either destroy the genetic message carried by the mRNA outright or else block the subsequent synthesis of a protein.

Until now, it has not been known how Dicer is able to recognize dsRNA and cleave those molecules into products with lengths that are exactly what is needed to silence specific genes. The Berkeley researchers were able to purify and crystallize a Dicer enzyme from *Giardia intestinalis,* a one-celled microscopic parasite that can infect the intestines of humans and animals. This Dicer enzyme in *Giardia* is identical to the core of a Dicer enzyme in higher eukaryotes, including humans, that cleaves dsRNA into lengths of about 25 bases.

In this work, the researchers describe a front view of the structure as looking like an axe (Figure 14). On the handle end there is a domain that is known to bind to small RNA products, and on the blade end there is a domain that is able to cleave RNA. Between the clamp and the cleaver is a flat-surfaced region that carries a positive electrical charge. The researchers propose that this flat region binds to the negatively charged dsRNA like biological Velcro, enabling Dicer to measure out and snip specified lengths of siRNA. When you put the clamp, the flat area, and the cleaver together, you get a pretty good idea as to how Dicer works. The research team is now using this structural model to design experiments that might reveal what triggers Dicer into action.

In addition, one size does not fit all for Dicer: different forms of the Dicer enzyme are known to produce different lengths of siRNA, ranging from 21 to 30 base pairs in length or longer. Having identified the flat-surfaced positively charged region in Dicer as the "ruler" portion of the enzyme, the researchers speculate that it may be possible to alter the length of a long connector helix within this domain to change the lengths of the resulting siRNA products. The researchers would like to see what happens when you take a natural Dicer and change the length of its helix.

INVESTIGATORS

I.J. MacRae and K. Zhou (UC Berkeley and Howard Hughes Medical Institute); F. Li, A. Repic, A.N. Brooks, and W.Z. Cande (UC Berkeley); P.D. Adams (Berkeley Lab); and J.A. Doudna (UC Berkeley, Howard Hughes Medical Institute, and Berkeley Lab).

PUBLICATION

I.J. MacRae, K. Zhou, F. Li, A. Repic, A.N. Brooks, W.Z. Cande, P.D. Adams, and J.A. Doudna, "Structural basis for double-stranded RNA processing by Dicer," *Science* **311**, 195 (2006).

FUNDING

National Institutes of Health.

Atomic and Molecular Science

LOW-ENERGY NONDIPOLE EFFECTS IN MOLECULAR NITROGEN VALENCE-SHELL PHOTOIONIZATION

While quantum mechanics allows scientists to write equations governing quite complex assemblies of electrons and atoms in molecules, the interactions among these particles make the equations too difficult to solve. As a result, theorists introduce approximations expected to be applicable to molecules and that make the equations solvable or amenable to numerical modeling on a computer. The most widespread approach to the particular problem of the interaction of light (anything from microwaves to x rays) with electrons in the molecules is called the dipole approximation. Over the last forty years, experimentalists have sought, and more recently been finding, discrepancies between the predictions calculated using the dipole approximation, with the conclusion that such violations primarily occur at relatively short wavelengths in the x-ray region of the spectrum. Hemmers et al. have now shown that violations of the dipole approximation also occur at longer wavelengths down into the vacuum ultraviolet and are probably a widespread phenomenon that theorists will have to take into account.

Measured angular distributions of photoelectrons photoejected from molecules and other atomic aggregates have been commonly interpreted according to the dipole or uniform-electric-field approximation for interactions between radiation and matter. But considerable recent evidence indicates that this approximation can be inadequate for interpretations of photoelectron angular distributions at surprisingly low photon energies. A multi-institutional collaboration led by researchers from the University of Nevada, Las Vegas, has reported the first observations of nondipole effects in the valence-shell photoionization of molecular nitrogen (N_2). Significant nondipole behavior was observed over the entire spectral range studied that is attributable to interference between electric-dipole (E1) and electric-quadrupole–magnetic-dipole (E2, M1) terms in the angular distributions.

Interest in measurements of the angular-distribution patterns and their spectral variations has continued over the past four decades because they are particularly sensitive to attributes of the molecules studied and to the dynamical aspects of the photoionization process. The new results clearly contradict a pervasive notion that nondipole effects occur only at high photon energy in atoms and molecules. As molecular nitrogen serves as a prototypical example, it can now be expected that such considerations should apply to atoms, molecules, clusters, surfaces, and solids quite generally.

The present investigation complements the group's earlier K-shell studies performed at higher photon energy and momentum and provides an opportunity to compare the nondipole behavior of the more spatially extended valence orbitals in N_2 with those of the nearly degenerate compact $1\sigma_g/1\sigma_u$ core orbitals. Two independent sets of experiments were carried out at the University of Wisconsin's Synchrotron Radiation Center (SRC) and at the ALS.

The photon energy range from 26–100 eV was studied at the SRC undulator Beamline 071 with four

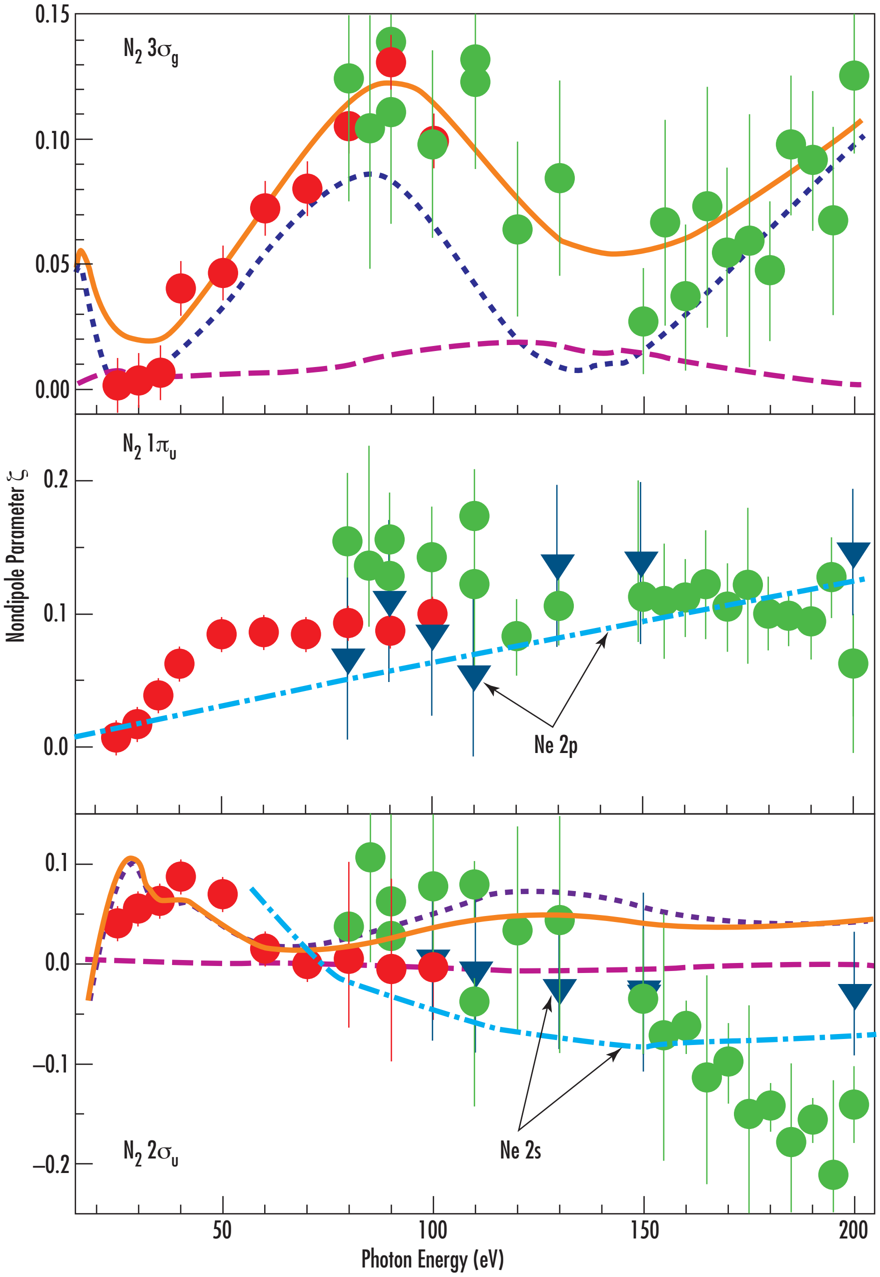

FIGURE 1. N_2 $3\sigma_g$, $1\pi_u$, and $2\sigma_u$ nondipole asymmetry parameters $\zeta = \Upsilon + 3\delta$ measured at the SRC (red circles) and the ALS (green circles) compared with calculations (ζ, orange curve; δ, magenta curve; ϒ, purple curve). The measured $1\pi_u$- and $2\sigma_u$-channel data are also compared with experimental 2p and 2s neon values (blue triangles) and with corresponding calculations (blue curve).

parallel-plate electron analyzers in a vacuum chamber doubly shielded by μ-metal. The analyzers operated at sufficient resolution to fully separate the three outer-valence N_2 peaks. Measurements over the photon energy range from 80–200 eV were made at the ALS on undulator Beamline 8.0.1 over several periods of two-bunch operation, which provide the timing mode crucial to the time-of-flight (TOF) method used. The endstation contains five electron-TOF analyzers that can measure photoelectron peaks at many kinetic energies and at multiple emission angles simultaneously.

The experimental data for the three valence channels in N_2 (Figure 1) show that the nondipole angular-distribution parameter ζ has values close to zero near threshold for all three valence lines and range between values of –0.2 and 0.2 over the photon energy range studied.

Theoretical studies have been performed to verify the experimentally determined nondipole parameters.

The spectral variation of the measured and calculated $3\sigma_g$ nondipole parameter is similar to that of the previously reported K-shell ($1\sigma_g$, $1\sigma_u$) nondipole parameter in N_2, although the peak magnitude for the K shell is about a factor of five larger than that of the $3\sigma_g$ result. The difference in peak heights is accounted for largely by the ratio of the different values of photon momenta.

In the absence of a theoretical determination of the N_2 $1\pi_u$-channel asymmetry parameter, a consequence of the higher-symmetry waves required in this case, experimental and previously reported theoretical neon 2p-channel parameters are used for comparison. The N_2 $1\pi_u$ molecular orbital, composed approximately of two in-phase $2p_N$ atomic orbitals perpendicular to the molecular axis, apparently gives rise to a nondipole asymmetry parameter that behaves similarly to that of an atomic $2p_{Ne}$ orbital at sufficiently high photon energies.

The $2\sigma_u$-channel results show general accord between theory and experiment. The negative values observed at higher photon energies are similar to the measured and calculated Ne 2s-channel asymmetry parameter, in agreement with the largely 2s antibonding character of the $2\sigma_u$ orbital.

INVESTIGATORS

O. Hemmers, R. Guillemin, A. Wolska, and D.W. Lindle (University of Nevada, Las Vegas); D. Rolles (ALS); E.P. Kanter, B. Krässig, and S.H. Southworth (Argonne National Laboratory); R. Wehlitz (University of Wisconsin); B. Zimmermann and V. McKoy (California Institute of Technology); and P.W. Langhoff (UC San Diego).

PUBLICATION

O. Hemmers, R. Guillemin, D. Rolles, A. Wolska, D.W. Lindle, E.P. Kanter, B. Krässig, S.H. Southworth, R. Wehlitz, B. Zimmermann, V. McKoy, and P.W. Langhoff, "Low-energy nondipole effects in molecular nitrogen valence-shell photoionization," *Phys. Rev. Lett.* **97,** 103006 (2006).

FUNDING

U.S. DOE BES and National Science Foundation.

VUV PHOTOIONIZATION STUDIES OF SMALL CARBON CLUSTERS

Clusters are a state of matter intermediate between individual atoms or molecules in a gas and bulk solids. They are found in the environment, interstellar space, and around massive stars, and they serve as laboratories for investigating molecular structure and bonding. The first spectroscopic observation of a cluster of carbon atoms was reported more than a century ago, when the amateur English astronomer Sir William Huggins investigated comets. Given their many roles, it is surprising that one of the most fundamental properties of any molecule, the energy required to remove (ionize) an electron from the outer or valence orbit, has never been directly measured for small carbon clusters, owing to the need to combine spectroscopy in a wavelength region difficult for lasers and to a complex sample-preparation process that must be integrated into the measurement apparatus. Nicolas et al. have solved these problems with a unique apparatus and the use of the ALS and applied it to the small carbon molecule C_3. Their apparatus is already being used by others to study ionization energies in many other molecules.

Given the importance of carbon clusters in molecular, environmental, and space science, it is surprising that one of the most fundamental properties of a molecule, the ionization energy, has never been directly measured for small carbon clusters. This deficiency has now been remedied by a Berkeley–French group that combined photoionization measurements and calculations to determine an ionization energy of 11.61 ± 0.07 eV between the neutral and ionic ground states of the carbon trimer C_3.

Clusters have always been used as a medium to understand the transition of chemical properties from the gas phase to the bulk. Small carbon clusters are ubiquitous in interstellar space, around massive stars, and in our own environment as critical intermediates in flame chemistry and soot formation. They have also been invoked as precursors of large carbon molecules including aromatic species and fullerenes, such as C_{60}. On a more fundamental level, carbon clusters provide a broad and interesting field from which molecular structure and bonding can be studied. As the size of the cluster increases, chain, cyclic, and branched structures can form, culminating in the three-dimensional cages of fullerenes.

Located in the vacuum ultraviolet (VUV) region, ionization energies are typically difficult to access with traditional laboratory-based laser sources. An added complication is that carbon clusters have to be prepared by methods such as laser ablation of graphite surfaces and subsequent cooling in supersonic molecular-beam expansions. Coupling sample preparation to a synchrotron light source was an experimental challenge that the group undertook in 2004.

The experiments were performed on a laser-ablation apparatus (Figure 2) coupled to the output of a 3-m monochromator on the Chemical Dynamics Beamline 9.0.2 at the ALS. The use of different buffer gases allowed better cooling of the electronically excited C_3 molecules that are formed during the ablation process. The ablation apparatus is now being used by a number of outside groups to measure ionization energies of metal oxides and carbides, larger carbon clusters, and novel radical species formed in reactions of carbon with hydrocarbons.

Carbon clusters were photoionized with tunable VUV radiation and the ionized species separated and detected in a time-of-flight mass spectrometer (Figure 3). Adding all the ion counts at a single mass peak at each

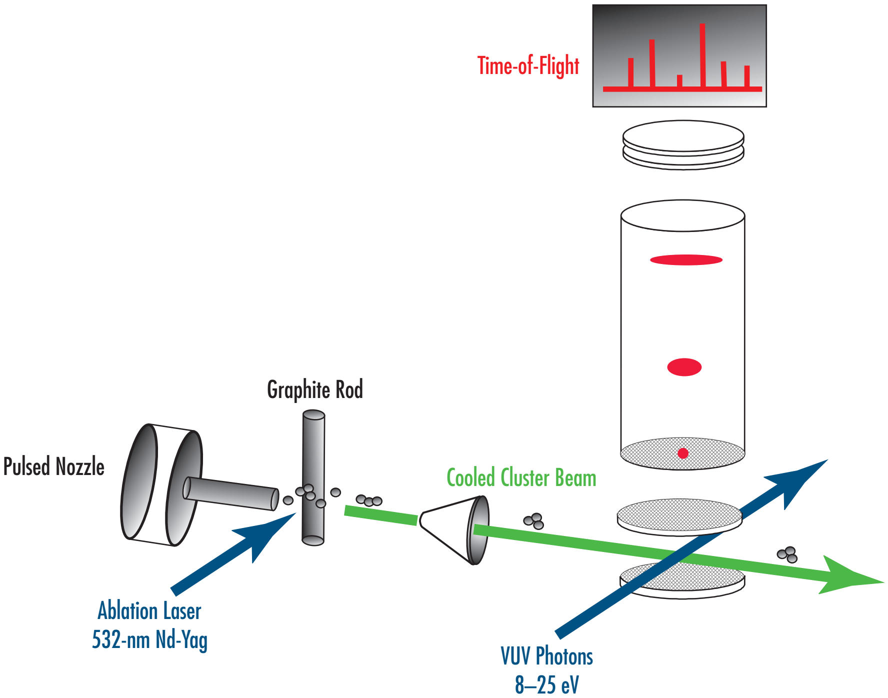

FIGURE 2. Schematic of the experiment showing (left to right) the cluster formation by laser ablation, formation of a cooled cluster beam by supersonic expansion of a carrier gas containing the clusters, and photoionization measurements by time-of-flight mass spectroscopy.

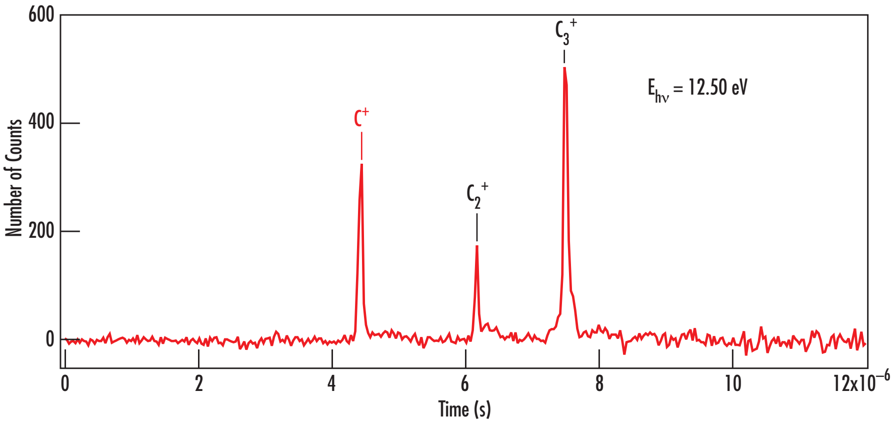

FIGURE 3. A time-of-flight mass spectrum of small carbon clusters photoionized at 12.5 eV. Peaks occurring at different times correspond to ions of different mass, as indicated in the figure.

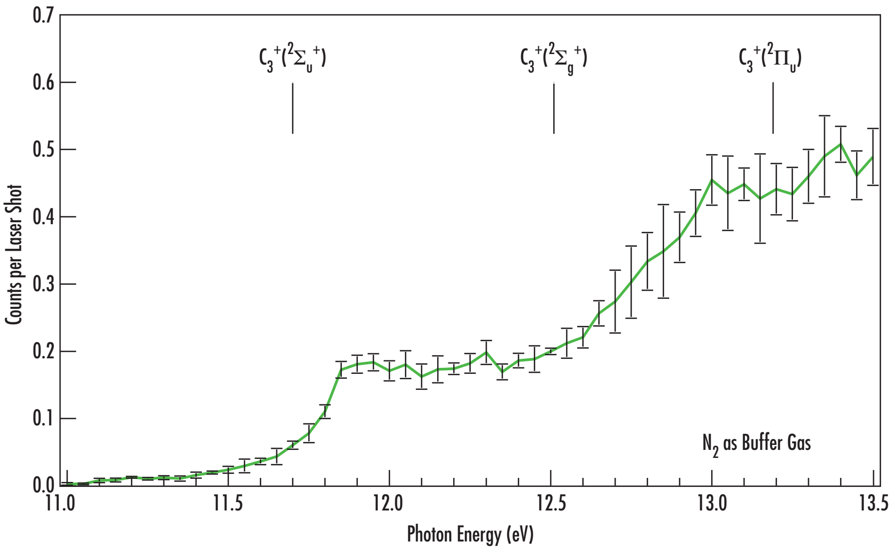

FIGURE 4. A PIE curve for C_3^+ obtained by integrating the counts for C_3^+ in the mass spectra. The energies of the three different C_3^+ states indicated were obtained from ab initio calculations.

photon energy, normalized by the photon flux and by the number of laser pulses used to form the cluster species, yielded a photoionization efficiency (PIE) curve. PIE curves for the C_3 molecule were measured from 11.0 to 13.5 eV (Figure 4).

To help interpret the experimental results, the investigators undertook high-level ab initio calculations to quantify the ionization energies and the electronically excited states present in the carbon clusters. For example, the step structure in the PIE curve, obtained with N_2 as the carrier gas, suggests an effective cooling of the neutral C_3 molecule into its linear ${}^1\Sigma_g^+$ ground state. And the second step in the PIE curve observed with N_2 as the buffer gas could be the first experimental evidence of the $C_3^+({}^2\Sigma_g^+)$ excited state. This state correlates to a stable ${}^2A_1$ state lying very close in energy to the already known ${}^2B_2$ ionic ground state.

Using the experimental results, complemented by the ab initio calculations, a state-to-state vertical ionization energy of 11.70 ± 0.05 eV between the $C_3(\tilde{X}^1\Sigma_g^+)$ and the $C_3^+(\tilde{X}^2\Sigma_u^+)$ states was obtained. New potential-energy surfaces with varying C–C distances and bending angles were also calculated for the doublet states of the cation. The calculations confirm the bent structure of C_3^+ in its ground state. Using these calculations in conjunction with our experimental results, an ionization energy of 11.61 ± 0.07 eV between the neutral and ionic ground states of C_3 was deduced.

INVESTIGATORS

C. Nicolas, J. Shu, D.S. Peterka, L. Poisson, and M. Ahmed (Berkeley Lab); M. Hochlaf (Université de Marne la Vallée, France); and S.R. Leone (UC Berkeley and Berkeley Lab).

PUBLICATION

C. Nicolas, J. Shu, D.S. Peterka, M. Hochlaf, L. Poisson, S.R. Leone, and M. Ahmed, "Vacuum ultraviolet photoionization of C_3," *J. Am. Chem. Soc.* **128**, 220 (2006).

FUNDING

U.S. DOE BES and Office of Advanced Scientific Computing Research.

EUV Optical Metrology

MICROFIELD EXTREME ULTRAVIOLET LITHOGRAPHY TOOL FOR FUTURE 15-nm CHIPS

As applied to the manufacture of computer chips, lithography refers to the process of transferring a circuit pattern from a mask to the surface of a silicon wafer, which after processing will be diced into tiny chips. In projection lithography, pattern transfer takes place with the aid of a refractive lens to focus the image created when shining ultraviolet light through the mask onto the wafer, which is covered with a light-sensitive polymer film (a resist). As the circuit features become ever smaller, numerous challenges arise, including reducing the wavelength of the ultraviolet to keep pace with the decreasing feature size, developing optics to image the tinier patterns, constructing masks without pattern-destroying defects, and devising resists that can retain with high fidelity the circuit pattern. The current feature-size frontier calls for the use of so-called extreme ultraviolet (EUV) light, whose wavelength is so short that conventional refractive optics no longer work. Naulleau et al. describe an EUV "microfield exposure tool" that is being used as a test bed for exploring these challenges.

Presently the nanoelectronics industry's state-of-the-art manufacturing process for memory chips is at the 65-nm level. As the industry eventually pushes to feature sizes of 32 nm and below, down to feature sizes as small as 15 nm or even smaller, conventional refractive lithography systems (including immersion systems) will no longer be feasible. EUV lithography, utilizing reflective optics and a wavelength of approximately 13 nm, is the leading candidate to meet the industry's needs. Despite the ongoing commercialization of this technology, significant challenges remain in areas including ultrahigh-resolution photoresists and defect-free masks. With sub-20-nm resolution, the microfield exposure tool using the unique beam properties of the ALS and developed by researchers at Berkeley Lab's Center for X-Ray Optics is arguably the world's most advanced test bed for studying these crucial issues.

The Berkeley tool is unique in that it is the only EUV lithography tool in the world to provide illumination with lossless programmable coherence. Programmability is important because the degree of coherence for optimum optical performance is not necessarily the same for all imaging tasks. Programmability is made possible by the use of intrinsically coherent radiation produced by undulator Beamline 12.0.1 at the ALS. This capability allows the Berkeley tool to support resolutions down to 11 nm, whereas similar tools with conventional illumination cannot support resolutions below approximately 25 nm. Given that EUV resolution is presently resist limited, however, it has not yet been possible to demonstrate printing at the tool's resolution limit, at least not with commercially viable chemically amplified resists.

In the exposure tool (Figure 1), undulator radiation is used to illuminate a pair of high-speed angular scanning mirrors that allow the phase-space of the illumination to be controlled in real time. A toroidal optic directs this coherence-controlled illumination to the lithographic mask. A 5x-reduced image of the mask is then projected onto a resist-coated silicon wafer by means of a 0.3-numerical-aperture EUV optic. Figure 2 shows two representative coherence functions as visu-

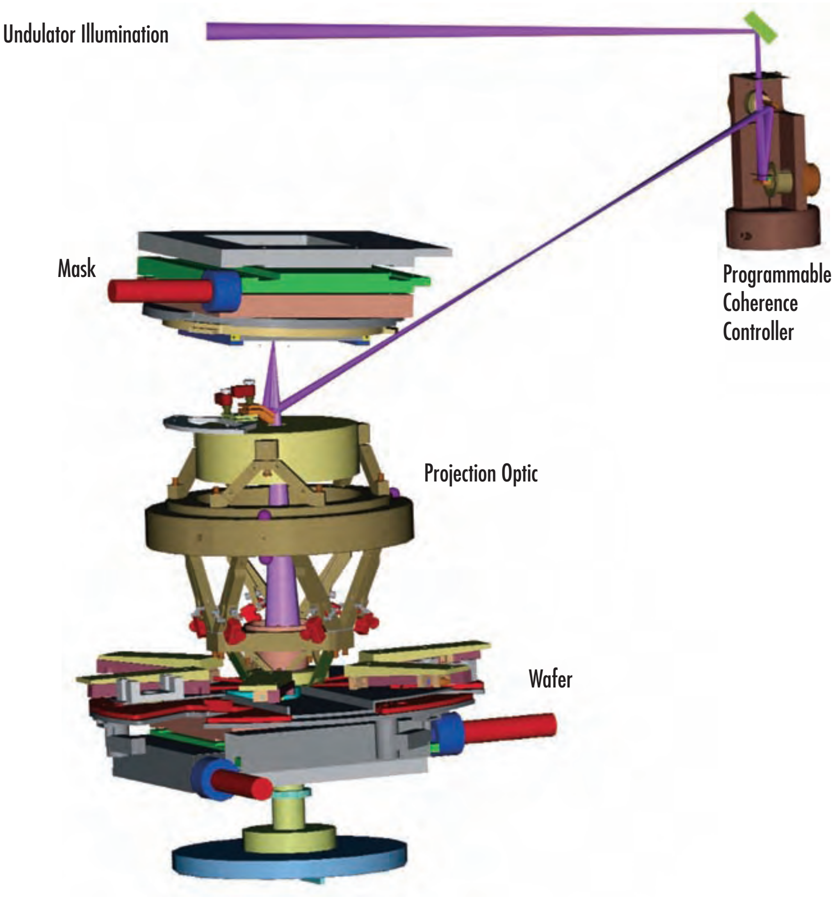

FIGURE 1. Schematic of the EUV microfield exposure tool at ALS Beamline 12.0.1.

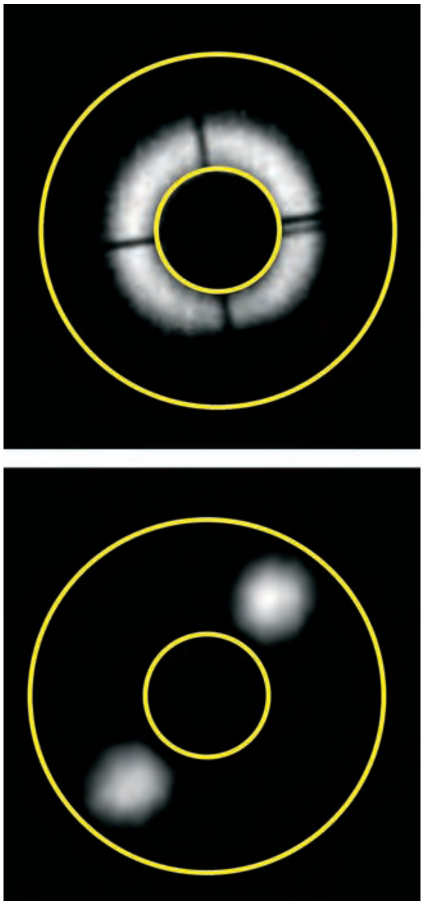

FIGURE 2. Two representative coherence functions as visualized in phase space at the pupil of the projection optic.

alized in phase space at the pupil of the imaging (projection) optic. The yellow lines represent the physical extent of the imaging optic pupil. The annular pattern is preferable for general-purpose imaging whereas the two-pole pattern is optimized for printing horizontal and vertical lines exclusively.

The Berkeley EUV exposure tool has enabled significant progress in EUV resists over the past few years. The past year has brought about the first demonstration of sub-30-nm equal-line-space printing from a projection EUV lithography tool. Specifically, with two experimental resists, resolutions down to 28-nm lines and spaces (Figure 3) have been attained. For both of these materials, the failure mechanism appears to be pattern collapse, a physical rather than a chemical failure, suggesting that the intrinsic resolution limit of the resist could support even finer lines and spaces. In many cases, for example in the manufacture of microprocessors, the relevant resolution metric is not equal lines and spaces, but rather semi-isolated lines. By this metric, the Berkeley tool has been used to demonstrate resolution down to 22.5 nm in a resist with an exposure sensitivity of 19 mJ/cm^2 (Figure 4).

The Berkeley EUV exposure tool plays a crucial role in the advancement of EUV resists. The unique programmable coherence properties of this tool enable it to achieve higher resolution than other EUV projection tools. As presented here, over the past year the tool has been used to demonstrate resist resolutions of 28-nm equal lines and spaces and 22.5-nm semi-isolated. Moreover, because the Berkeley tool is a true projection lithography tool, it also plays a crucial role in advanced EUV mask research. Examples of the work done in this area include defect printability, mask architecture, and phase-shift masks.

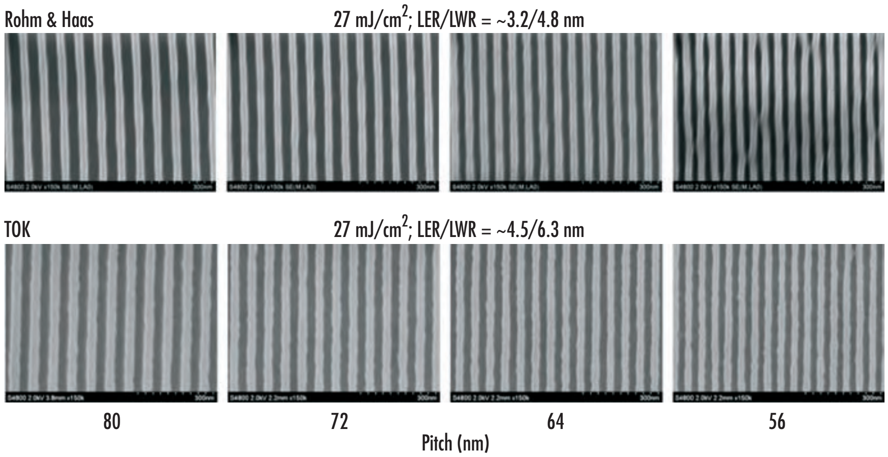

FIGURE 3. Results from two experimental resists (Rolm & Haas and TOK) at two exposure levels demonstrating resolution down to 28-nm lines and spaces with current materials technology. LER and LWR are line-edge and line-width roughness, respectively.

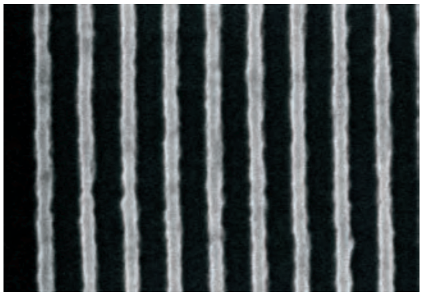

FIGURE 4. Example of 22.5-nm semi-isolated lines printed with the EUV microfield exposure tool.

INVESTIGATORS

P. Naulleau, P. Denham, J. Chiu, K. Goldberg, B. Hoef, and G. Jones (Berkeley Lab) and K. Dean (SEMATECH).

PUBLICATIONS

P. Naulleau, C. Anderson, B. La Fontaine, R. Kim, R. Sandberg, and T. Wallow, "Characterization of advanced EUV resists at the Berkeley MET facility," *Proceedings of SEMICON Korea 2007*, STS Volume 1, 27 (2007).

J. Cain, P. Naulleau, and C. Spanos, "Resist-based measurement of the contrast transfer function in a 0.3-numerical aperture extreme ultraviolet microfield optic," *J. Vac. Sci. Technol. B* **24,** 326 (2006).

P. Naulleau, C. Anderson, B. La Fontaine, R. Kim, and T. Wallow, "Lithographic metrics for the determination of intrinsic resolution limits in EUV resists," *Proc SPIE* **6517** (to be published 2007).

FUNDING

SEMATECH, AMD, IBM, Intel, and Samsung.

Facility Report

Tailored Terahertz Pulses

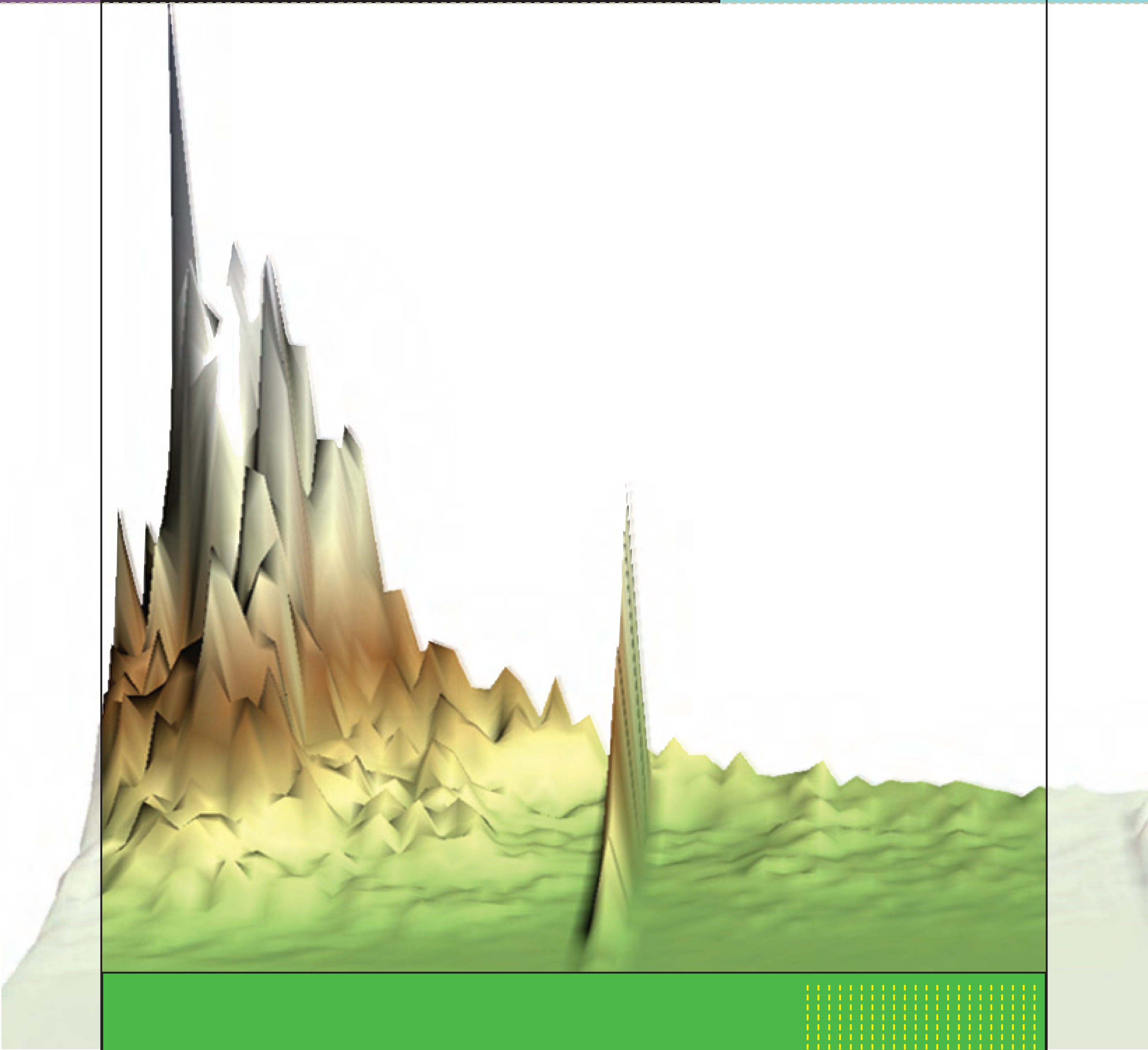

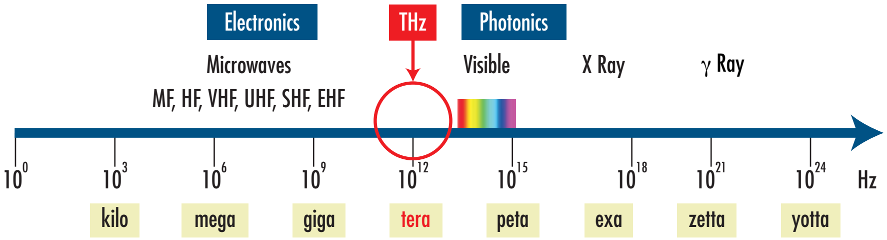

FIGURE 1. The electromagnetic spectrum. The scarcity of intense broadband sources of radiation in the 10^{12} hertz (terahertz) frequency range leaves us blind to a wide range of interesting phenomena.

High-Power Coherent Terahertz Radiation from Laser-Modulated Electron Beam

To "see" phenomena invisible to the naked eye—from galaxies to viruses and atoms—scientists have the entire electromagnetic spectrum at their disposal: radio waves, microwaves, and infrared light below the visible spectrum, and ultraviolet light, x rays, and gamma rays above it. However, between the microwave and infrared regions, where electromagnetic waves oscillate at a frequency of 10^{12} hertz (terahertz), we have a noticeable blind spot (Figure 1). Terahertz radiation with a wavelength from about 1 cm to about 100 microns would provide access to an almost limitless array of interesting phenomena, including orbiting electrons, rotating molecules, and vibrating proteins (see sidebar, "Looking at the World with T-Ray Vision"). The reason for this "terahertz gap" has been the scarcity of intense broadband sources of radiation in the terahertz frequency range. New findings by an ALS group could represent a significant step toward satisfying the need for powerful terahertz sources.

Terahertz waves, or "T-rays" as some prefer, are nothing new, being of the same late-nineteenth-century vintage as Röntgen's "X-rays." The first reported observation of terahertz rays is credited to Heinrich Rubens and Ernest Fox Nichols at the University of Berlin in 1896. The importance of Rubens' careful measurements as applied to the formulation of the law of black-body radiation was acknowledged by none other than Max Planck himself. Since black-body radiation is a broadband phenomenon that encompasses the terahertz regime, any object that is a nominal source of black-body radiation is also a source of terahertz waves. These "thermal" T rays, however, are very weak, and much brighter beams are required in order to mine the rich field of potential scientific and technological applications. Several desirable features of such beams include pulses shorter than 100 femtoseconds, synchronization to another ultrafast source ranging from infrared to x-ray wavelengths, and the ability to shape the time envelope of the pulse. Among the promising technologies under study is the relatively new development of coherent synchrotron radiation (CSR) generated by electron storage rings.

In 1982, F. Curtis Michel of Rice University published a paper in *Physical Review Letters* pointing out that electron storage rings, which produce *incoherent* short-wavelength (x-ray) radiation, should be able to produce *coherent* long-wavelength (terahertz) radiation, because the electron bunches in storage rings are very short compared to the wavelength of terahertz radiation and can effectively act as a macroparticle "point source," emitting many waves in phase (Figure 2). Moreover, the coherence of the radiation means that the waves interact constructively, and their power increases quadratically with the number of electrons in the bunch. In 2002, researchers at Jefferson Lab in Virginia used relativistic electrons in a free-electron laser (FEL) to produce terahertz radiation 20,000 times brighter than that generated from previously existing sources. Shortly thereafter, researchers at the BESSY synchrotron in Berlin succeeded in producing stable coherent terahertz radiation from an electron storage ring, where circulating electron bunches provide for a more stable beam with a higher signal-to-noise ratio.

This was all extremely encouraging to researchers at the ALS who, for the past several years, have also been exploring the ways coherent synchrotron radiation in the terahertz range is generated in electron storage rings. The group (Figure 3) includes J.M. Byrd, D.S. Robin, F. Sannibale, A.A. Zholents, and M.S. Zolotorev (Accelerator and Fusion Research Division, Berkeley Lab); Z. Hao and M.C. Martin (ALS); and R.W. Schoenlein (Materials Sciences Division [MSD], Berkeley Lab). In their most recent

FIGURE 3. ALS terahertz CSR research team. Clockwise from lower left: Michael Martin, Alexander Zholents, David Robin, Robert Schoenlein, Zhao Hao, John Byrd, Max Zolotorev, and Fernando Sannibale.

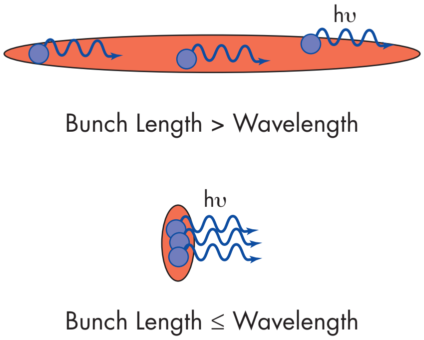

FIGURE 2. Effect of electron bunch length on coherence. When the bunch length is much greater than the emitted wavelength, the output radiation is out of phase. When the bunch length is comparable to or shorter than the wavelength, the emitted radiation is coherent.

work, these researchers have demonstrated a new method for generating tunable, coherent, broadband terahertz radiation at the ALS with tremendous pulse-shape flexibility through modulation by a femtosecond laser pulse. They also presented a physical model of how, under the proper conditions, the laser seeds an instability in the electron beam. Such a mechanism makes it possible to control the instability onset and to exploit its gain for the generation of pulses of coherent terahertz radiation of unprecedented power.

In 2000, the demonstration of femtoslicing at the ALS as a source of ultrafast x rays showed that we can manipulate the distribution of an electron beam using a short-pulse laser on a time scale of several hundred femtoseconds. One of the by-products of this technique is that femtoslicing can create very short "holes" in the time distribution of the electron bunch. While short electron bunches can radiate coherently, the researchers found that these "holes" in the electron bunch can radiate coherently as well, and that this technique could be extended to create a novel source of terahertz radiation. For example, by shaping the slicing laser pulse, we can tailor the shape of the hole that is "sliced" in the bunch and thus shape the electric field of the coherent terahertz pulse. This would make the terahertz radiation tunable.

Femtoslicing works by modulating the energy of electrons in the bunch using a high-power laser pulse copropagating with the electrons in a wiggler field. For example, the interaction of a 75-femtosecond laser pulse with an electron bunch results in the formation of "wings" in the bunch energy distribution (Figure 4). The projection of the distribution on the time axis represents the relative variation in the peak bunch current. As the bunch passes through the accelerator, the high- and low-energy "wings" of the bunch energy distribution slip backward and forward along the bunch, creating a "hole" in the center of the bunch that emits terahertz radiation. As the bunch continues around the storage ring, the "hole" quickly spreads and fills with electrons. Because of the short laser pulses that are used to slice the electron beam, the emission spectrum initially extends up to terahertz frequencies but shifts to lower frequencies as the hole spreads.

To observe these effects, the researchers used a liquid-helium-cooled bolometer sensitive to terahertz wavelengths and recorded bursts of coherent signal coincident with the slicing, which occurred at a 1-kHz repetition rate (Figure 5). The measurements were taken at Beamline 5.3.1, immediately following the slicing, and at Beamline 1.4, three-fourths of the way around the ring. They also measured the spectrum of the coherent radiation at both sites (Figure 6). Spectral measurements are difficult at the ALS because the vacuum chamber design has very poor transmission of long-wavelength radiation. Because the coherent signal is very sensitive to the width and depth of the hole, it is currently used as the primary diagnostic signal for optimizing slicing efficiency.

Given the ability to slice holes in the electron bunch, we can now consider tailoring the terahertz signal to the needs of a particular experiment. Laser technology allows us to shape the temporal profile of the laser pulse and modulate the electron bunch with a multitude of patterns. For example, if we slice the beam with a train of laser pulses, we can apply a periodic modulation on the electron bunch, generating a narrow-band terahertz signal. This signal would be tunable in frequency by varying the laser pulse spacing.

Another phenomenon peculiar to electron bunches as they radiate energy is an effect known as the microbunching instability (MBI). In a storage ring, as in linac-based FELs, the electromagnetic field associated with the synchrotron radiation emitted by a bunch passing through an insertion device and/or a bending magnet interacts with the electrons in the same bunch, modulating their en-

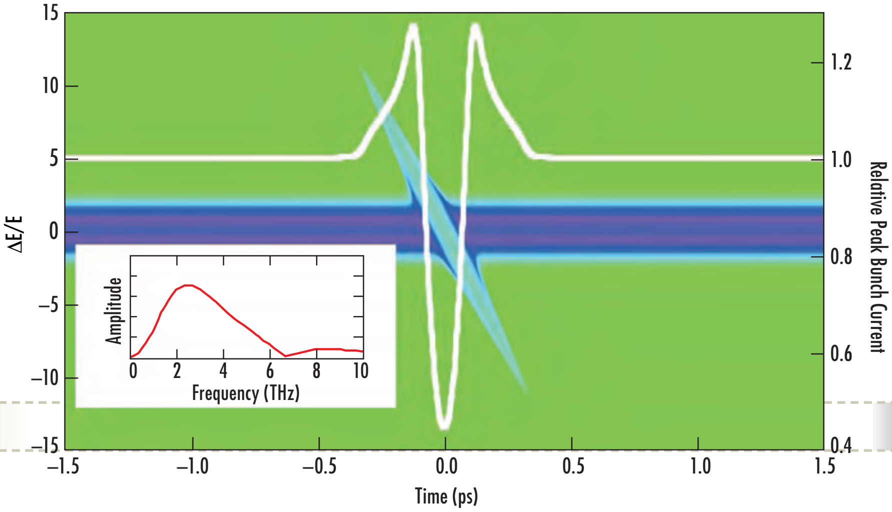

FIGURE 4. The effect of a co-propagating laser pulse on an electron bunch. The electron energy distribution (blue band) shows that electrons gaining energy (ΔE > 0) gather toward the back of the bunch (because they follow a longer path), while those that lose energy (ΔE < 0) gather toward the front (because they follow a shorter path). The relative peak bunch current (superimposed white curve) shows a "hole" in the electron bunch that emits coherent terahertz radiation (frequency spectrum shown in inset). As the bunch travels around the storage ring, the "hole" quickly spreads and fills with electrons.

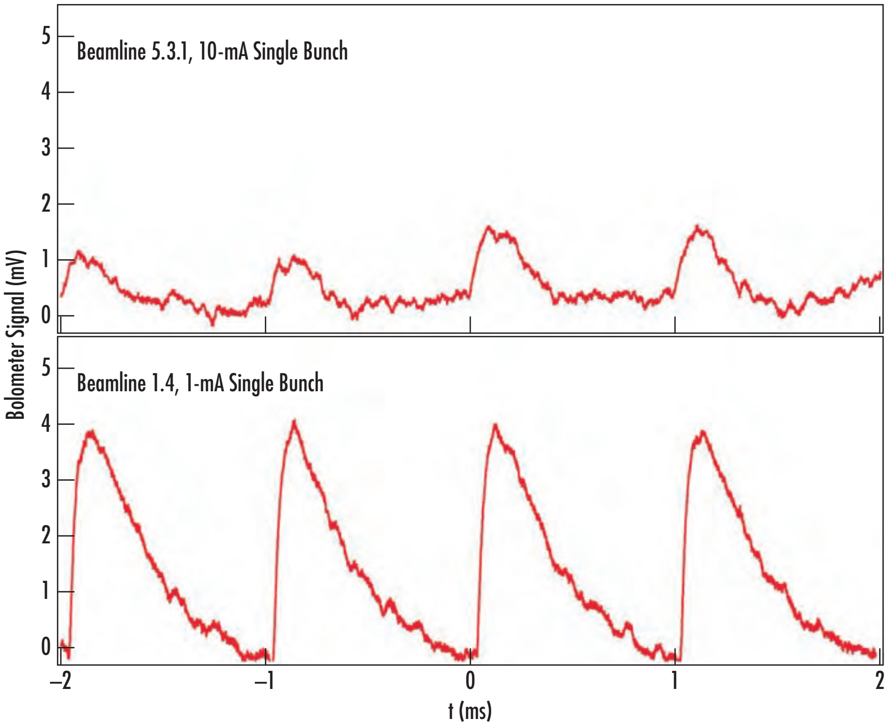

FIGURE 5. Bolometer signal observed at Beamline 5.3.1 and Beamline 1.4 with slicing on.

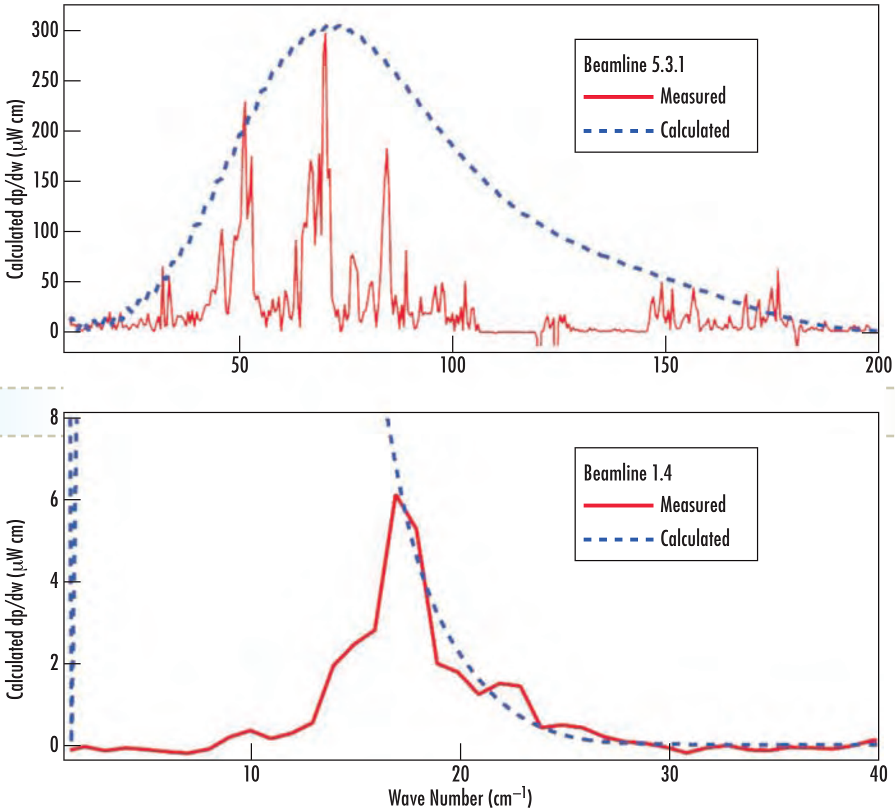

FIGURE 6. The spectral measurement of the coherent radiation at Beamline 5.3.1 and Beamline 1.4.

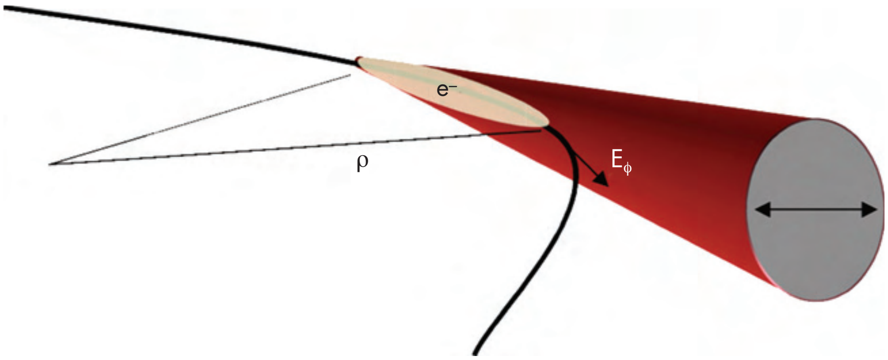

FIGURE 7. Schematic view of the interaction of an electron bunch with its own synchrotron radiation. The curvature of the electron orbit allows the radiation field to interact with the electron.

ergy (Figure 7). Electrons in the front of the bunch sense a longitudinal component of the radiation field that can either accelerate or decelerate the electron, depending on its position. Above a threshold current (number of electrons per bunch) in storage rings, the intensity becomes strong enough to exponentially amplify modulations in the bunch distribution, resulting in the MBI. Such density modulations have characteristic lengths smaller or comparable to typical terahertz radiation wavelengths and thus radiate powerful CSR pulses in that frequency range.

The gain process described above can amplify either small fluctuations (i.e., noise) in the electron-beam density or a small modulation in the density induced by interaction with a laser beam (laser seeding). Until now, the MBI was always observed in storage rings as a stochastic process starting from noise and associated with the emission of powerful CSR bursts with random repetition rates and large fluctuations in amplitude. But experiments performed at ALS Beamline 1.4.3 now show that by laser-inducing a modulation on the electron bunch above the MBI current threshold, it is possible to seed the instability in a controlled way (Figures 8 and 9). In this case, the CSR bursts become synchronous with the modulating laser, and the instability gain can be exploited for generating high-power terahertz CSR pulses.

Looking at the World with T-Ray Vision

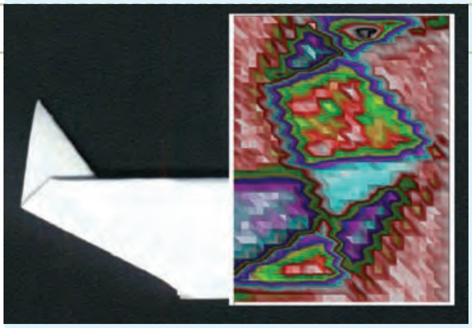

Unless they're at a temperature of absolute zero, all objects, animate and inanimate, give off terahertz radiation, the heat from molecular vibrations. This "black-body" radiation is emitted at such low intensities—typically less than a millionth of a watt per square centimeter—that we're unaware of it. We would need some pretty strong "T-ray glasses" to be able to see objects with this form of light. Thus, although the terahertz region of the electromagnetic spectrum is a frontier area for research in physics, chemistry, biology, medicine, and materials sciences, without the appropriate technology to generate and detect this type of radiation, science has for a long time overlooked the many parts of the universe that are in tune with T-rays.

Terahertz radiation, which has a fundamental period of about 1 picosecond, is uniquely suited to spectroscopic studies of systems of central importance: electrons in highly-excited atomic Rydberg states orbit at terahertz frequencies; small molecules rotate at terahertz frequencies; and collisions between gas-phase molecules at room temperature last about 1 ps. Biologically-important collective modes of proteins vibrate at terahertz frequencies. Frustrated rotations and collective modes cause polar liquids (such as water) to absorb at terahertz frequencies. Electrons in semiconductors and their nanostructures resonate at terahertz frequencies. Superconducting energy gaps are found at terahertz frequencies. Gaseous and solid-state plasmas oscillate at terahertz frequencies. The opportunities are limitless.

Terahertz radiation is also of great interest for nondestructive imaging applications in areas such as medicine and security. Relatively low-energy T-rays can penetrate and distinguish between many types of materials, including living tissue, without causing the kind of damage associated with ionizing radiation such as x rays. For example, T-rays might be used to diagnose the depth of a subcutaneous skin cancer lesion, replace or augment mammography, or detect weaknesses in a tooth or bone. T-rays can also be used to screen people and objects for security: concealed firearms, packages containing chemical and biological weapons, and buried explosives or land mines all yield their secrets under the glare of T-rays. On a less menacing note, T-ray screening might also be used for industrial quality assurance processes—checking pharmaceuticals for coating thickness or ensuring the moisture content of packaged goods, for example.

While sources of high-quality terahertz rays have been scarce, we have recently begun to fill this gap with relatively low-power table-top sources based on ultrafast lasers and semiconductors. More powerful, narrow-band-width sources are also being developed using free-electron lasers or diodes. Accelerator-based sources offer both broad band width and high power. As is often the case, new sources lead to new science in many areas, as scientists begin to become aware of the opportunities for research progress in their fields using terahertz radiation.

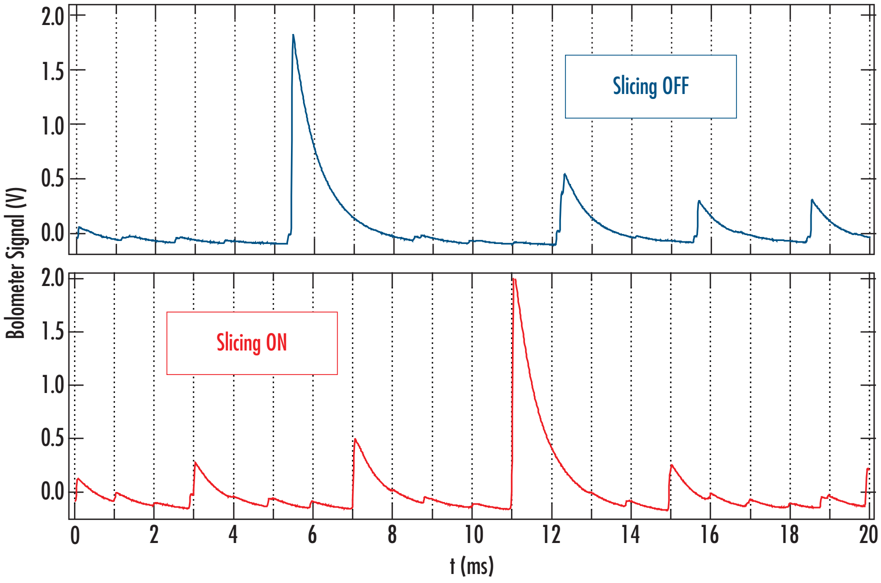

FIGURE 8. Above the current threshold for the microbunching instability (MBI), the slicing process seeds the instability. Top: Random bursts of high-intensity, coherent synchrotron radiation (CSR) associated with the MBI, as measured at the ALS. Bottom: When the slicing laser is turned on at a 1-kHz repetition rate, the bursts become synchronous with the slicing laser, as the burst onset positions match the vertical lines at 1-ms intervals on the horizontal scale.

These observations can be explained within the framework of MBI theory. Quantitative comparison of the MBI model with the ALS data shows good agreement up to currents of about 19 mA, thus indicating that the model can account for the CSR power growth (Figure 10). At higher currents, a saturation effect takes control as the MBI goes into a nonlinear regime where the theory breaks down.

The laser-seeding phenomenon could be the basis for a terahertz source. Pump–probe and other experiments not requiring shot-to-shot intensity stability could benefit from the several-orders-of-magnitude increase in power that the seeded MBI offers. In a more speculative scenario, a fraction of the terahertz signal can be brought back into the ring to co-propagate in an insertion device or in a bending magnet with a subsequent electron bunch, modulating its energy and seeding the MBI that generates a new burst that is then used in the loop for seeding a fresh bunch. By this process, one can in principle bring the CSR emission to a stable high-power saturation regime where all the bunches radiate coherently.

INVESTIGATORS

J.M. Byrd, D.S. Robin, F. Sannibale, R.W. Schoenlein, A.A. Zholents, and M.S. Zolotorev (Berkeley Lab) and Z. Hao and M.C. Martin (ALS).

PUBLICATIONS

J.M. Byrd, Z. Hao, M.C. Martin, D.S. Robin, F. Sannibale, R.W. Schoenlein, A.A. Zholents, and M.S. Zolotorev, "Tailored terahertz pulses from a laser-modulated electron beam," *Phys. Rev. Lett.* **96,** 164801 (2006).

J.M. Byrd, Z. Hao, M.C. Martin, D.S. Robin, F. Sannibale, R.W. Schoenlein, A.A. Zholents, and M.S. Zolotorev, "Laser seeding of the storage-ring microbunching instability for high-power coherent terahertz radiation," *Phys. Rev. Lett.* **97,** 074802 (2006).

FUNDING

U.S. DOE BES and Office of High Energy Physics.

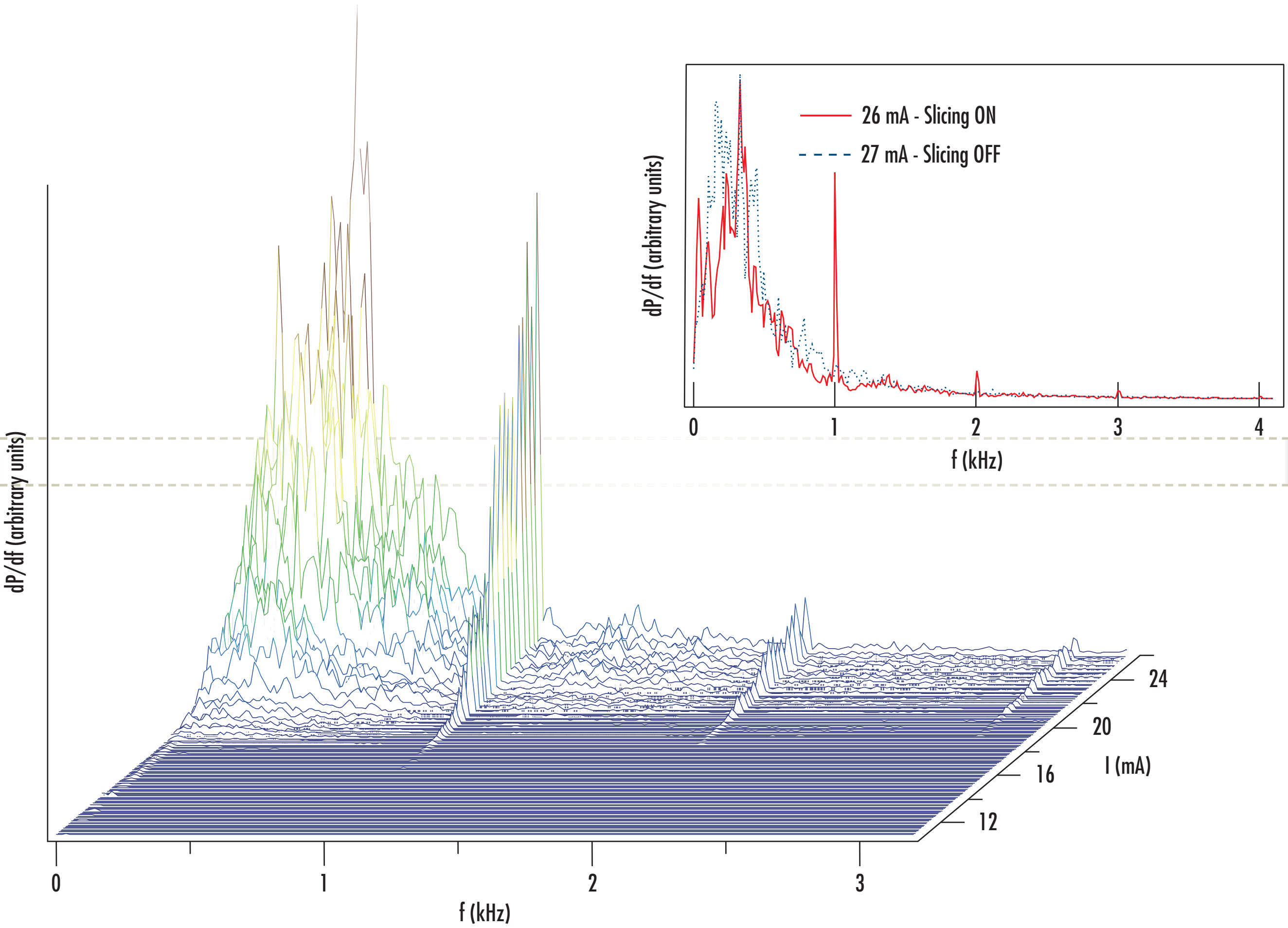

FIGURE 9. The bunch-current dependence of the terahertz detector's Fourier (frequency) spectra shows two prominent features: the onset of the MBI at around 15 mA and the match between the 1-kHz line and its harmonics with the laser repetition frequency. The inset shows two frequency spectra for currents above the MBI threshold with the slicing laser on (red) and off (blue). The 1-kHz line and harmonics clearly disappear when the laser is switched off.

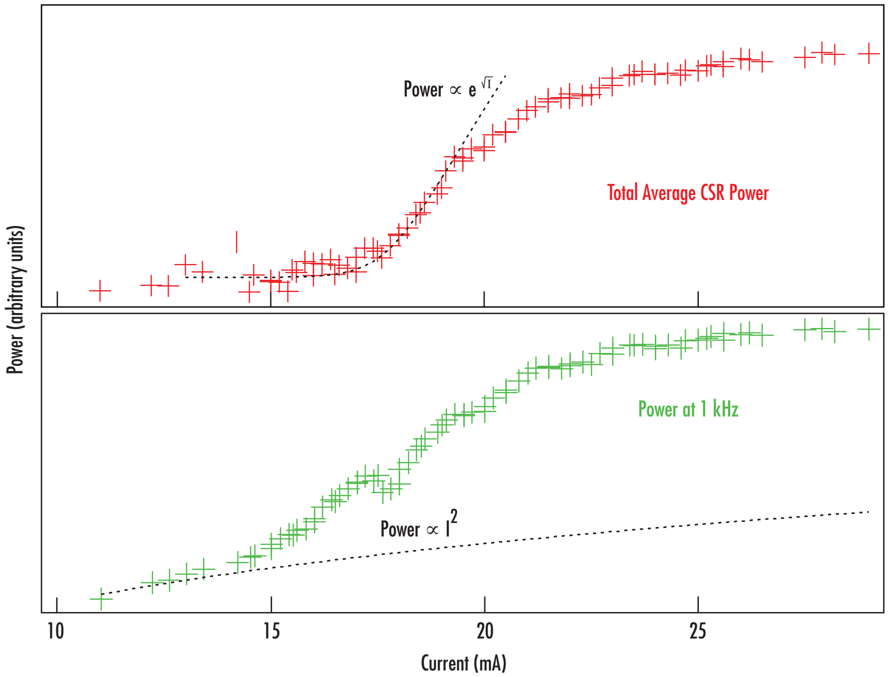

FIGURE 10. Above the MBI threshold (15 mA), the total average CSR power (red) and the power associated with the 1-kHz line (green) both grow exponentially with the single-bunch current, thanks to the gain process that increases the number of electrons emitting coherently. If the power at 1 kHz were due only to the particles in the bunch that were modulated in energy by the slicing laser, then the current dependence would be quadratic, as observed below the MBI threshold. The dashed blue curves represent theoretical calculations: the exponential curve predicted by the MBI model in the top graph and a quadratic comparison in the bottom graph.

Operations and Availability

David Robin, Division Deputy for Operations and Accelerator Development

The mission of the ALS is to support users in doing outstanding science in a safe environment. Critical to that support is the delivery of high-quality beam. Delivering beam according to the published schedule, along with an efficient, effective safety program, allows ALS researchers to make maximum use of the limited beam time. In 2006, the ALS exceeded its availability and reliability compared with any year since operation began in October 1993 [fiscal year (FY) 1994].

More than 6000 scheduled hours were delivered to users in FY 2006 (Table 1). Compared to 2005 (which was one of the previous best years), 14% more beam was delivered. The mean time between failures was 50 hours (25% improvement) and the mean time to recovery was just more than 1 hour. All told this accounted for 97.5% availability in FY 2006.

As in years past, we look very carefully at different systems to determine where to focus our resources to improve reliability. Figure 1 shows the "lost user-beam analysis" for 1999 to 2006. As the figure clearly shows, the lost beam time in FY 2006 was fairly evenly divided over the various categories—vacuum, rf, power supplies, etc. No single category accounted for more than 0.5% of the time scheduled. The total lost beam time accounted for only about 2.5% of the time scheduled, which, as previously mentioned, made FY 2006 the ALS's best year to date.

TABLE 1. Improvement in Beam Availability

	FY 2005	**FY 2006**	**COMPARISON**
Scheduled user hours	5521	6201	12% more
Delivered user hours (in schedule)	5321 (96.4%)	6045 (97.5%)	14% more
Additional unscheduled hours delivered	N/A	64	N/A
Mean time between beam interruption (hours)	40	50	25% more
Mean time to recovery (minutes)	72	64	10% less

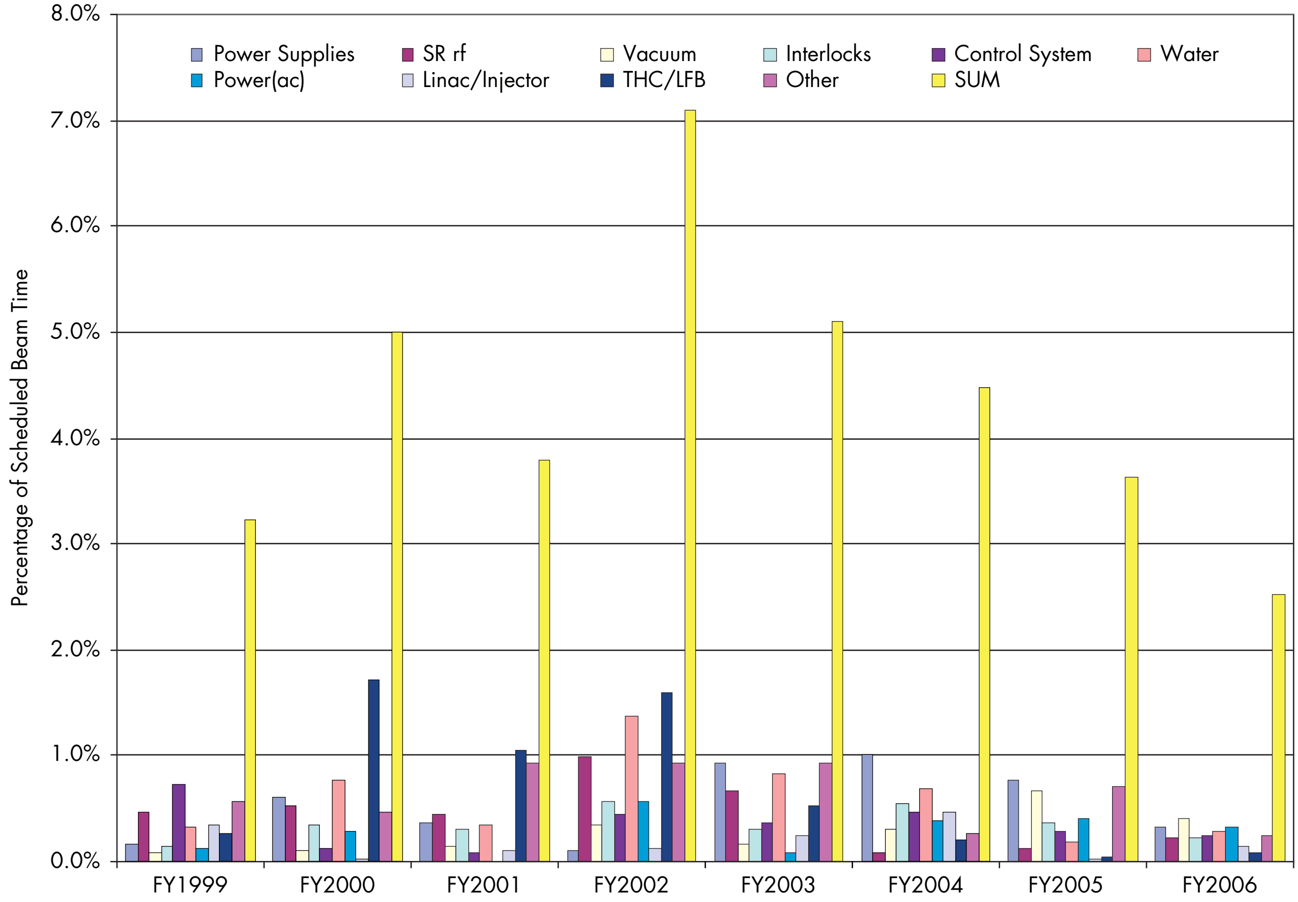

FIGURE 1. Lost beam time from FY 1999 through FY 2006.

Accelerator Physics

David Robin, Division Deputy for Operations and Accelerator Development / Christoph Steier, Deputy Leader, Operations and Accelerator Development

The Accelerator Physics Group contributes in four principal ways to achieving the ALS mission of supporting users in doing outstanding science in a safe environment. The first and foremost is to ensure the performance and reliability of the ALS so that high-quality beam is delivered to users. The second is to strive to understand and continually improve the performance of the facility, keeping it at the forefront of synchrotron radiation sources. The third is to ensure that machine upgrades are implemented smoothly with minimal adverse impact to users. The fourth is to study potential upgrades that will enhance the capabilities and capacities of the ALS.

Below is a short summary of some of the group's areas of work, as well as achievements over the last year. This is followed by longer sections that describe in more detail some of the highlights, including the ongoing top-off upgrade, the higher-brightness lattice study, and the Matlab Middle Layer work.

The undulator-based femtoslicing source, which has been described in previous reports, started routine operation during the last year. It is a very complex facility that combines a high-average-power, short-pulse laser system; two insertion devices (a wiggler as modulator and an in-vacuum undulator as radiator); complicated beam manipulations between the insertion devices using 12 local skew quadrupoles; and two advanced photon beamlines.

All accelerator components of the system work extremely well. The impact of the reduction in vertical physical aperture (from more than 8 mm to slightly more than 5 mm at the in-vacuum undulator) on the dynamic momentum aperture, and therefore the Touschek lifetime, has been extremely small. This was enabled by the sophisticated skew quadrupole scheme, which provides for vertical dispersion at the undulator to spatially separate the sliced electron beam, but at the same time provides zero global and very small local coupling at the position of the undulator.

Other systems that were implemented in conjunction with this project were vertical scrapers to localize electron losses away from the undulator, as well as a skew quadrupole feedforward system (with 20 individual skew quadrupoles). The feedforward system keeps the vertical emittance constant while changes are made to the photon wavelength (and therefore to the field of the in-vacuum undulator, at a position with significant vertical design dispersion for the slicing separation).

Initial studies were started to find the fundamental limits of the ALS magnet arrangement. These studies identified several families of possible lattices with smaller emittances or smaller momentum compaction factors than currently possible at the ALS. Some of the lower-emittance lattices were studied in more detail, and dynamic aperture simulations confirmed that, with moderate changes to magnets and some additional power supplies (namely, the addition of two more sextupole families), a significant reduction in the natural horizontal emittance of the ALS appears possible. These studies will be pursued further in the coming year and will hopefully lead to an upgrade project that would allow the emittance of the ALS to be reduced to values similar to or smaller than the ones for Diamond (one of the newest third-generation light sources, currently being commissioned in the United Kingdom).

DYNAMIC MULTIPOLE SHIMMING OF ELLIPTICALLY POLARIZING UNDULATORS

The ALS has added several APPLE II-type elliptically polarizing undulators (EPUs) over the years, capable of generating high-brightness photon beams with variable linear, elliptical, or circular polarization characteristics. The existing devices have a period of 50 mm. A 90-mm-period device is currently being installed for the new meV-resolution beamline (MERLIN).

Interaction of the existing devices with the stored electron beam has been intensely studied at the ALS. The biggest concern is that beam-based measurements and simulations show that the transverse dynamic aperture of the beam is reduced by the EPU fields. The effect is both tuneshift- and gap-dependent and is noticeable in existing ALS operations; it will become intolerable with top-off operation, when electrons will be injected with large offsets with the EPUs in operation. It is caused by "dynamic field integrals" that result from the combination of the undulating trajectories and the intrinsically fast transverse field roll-off of the magnetic fields in EPUs.

For longer-period devices like the MERLIN EPU, the effect can be so strong that no beam could be stored without mitigating the effects. As described last year, the mitigation consists of small iron shims that are placed such that static field integrals with similar (but opposite polarity) nonlinear behaviors are created. This technique has been used successfully during the last year on one of the existing EPUs with a 50-mm period. After the shimming, the nonlinearities in the horizontal kick as a function of horizontal displacement in the device have been nearly eliminated (Figure 1). As a result, the dynamic momentum aperture is no longer affected by the shimmed EPU.

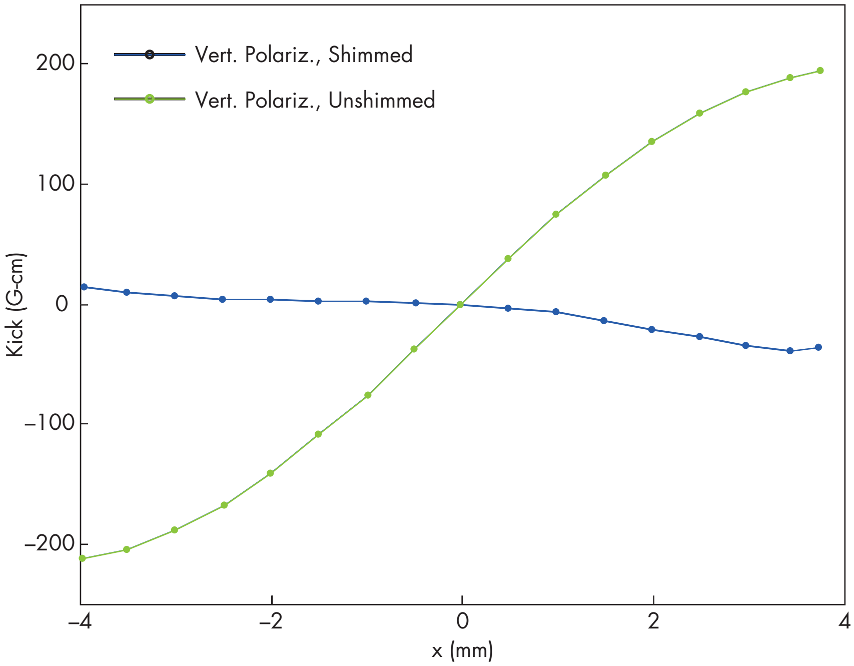

FIGURE 1. Measurement of the horizontal kick due to one of the 50-mm-period EPUs as a function of horizontal displacement. This measures the sum of the dynamic plus static field integrals. In the case of the shimmed device, the kicks are strongly reduced and the nonlinearity of the kick disappeared almost completely.

TOP-OFF

Christoph Steier

To provide higher brightness and better stability, the ALS is being upgraded to top-off injection. A main part of the top-off modification is an upgrade of the booster, as well as extraction and injection elements and the transfer line, for full energy. Further upgrades include new diagnostics, an improved controls and timing system, and new radiation safety systems (monitors and interlocks).

MOTIVATION AND BACKGROUND

The ALS was one of the earliest third-generation light sources, and after operating for more than a decade, it continues to generate forefront science in many areas. However, storage rings currently being commissioned will provide higher brightness than has been achievable at the ALS.

The main possibilities for improving the brightness of the ALS are increasing the time-averaged current, reducing the beam size, and reducing the insertion-device gaps. Currently, those changes would result in (unacceptably) short beam lifetimes. With continuous injection (top-off), the importance of this lifetime impediment can be reduced significantly. Figure 2 shows a comparison of the brightness of planned, new ALS insertion devices with the upgraded beam parameters (IU20) to the typical brightness of a current ALS undulator (U50). It also shows the brightness expected with proposed insertion devices at newer intermediate-energy light sources. One can see that the upgraded ALS will remain competitive, with the main improvements coming from the smaller vertical emittance and the smaller physical gaps of the undulators.

PROGRESS TOWARD TOP-OFF

The last year saw major progress toward the realization of top-off at the ALS. The major installation shutdown to upgrade the complete injector system for full-energy injection was completed. Furthermore, there was tremendous progress in studying all relevant radiation safety aspects, culminating in a successful outside review of the radiation safety tracking studies and controls.

The fall/winter 2006 installation shutdown was the longest since the ALS began operations in 1993. The focus of the shutdown was to complete the installations necessary for top-off injection. The many other significant achievements included replacement of the front-end optics at the protein crystallography beamlines in Sector 5, installation of a higher-order-mode damper in one of the storage ring radio frequency (rf) cavities, preparations for the installation of an experimental "camshaft" bunch kicker, replacement of 24 beam-position-monitor button assemblies to prepare

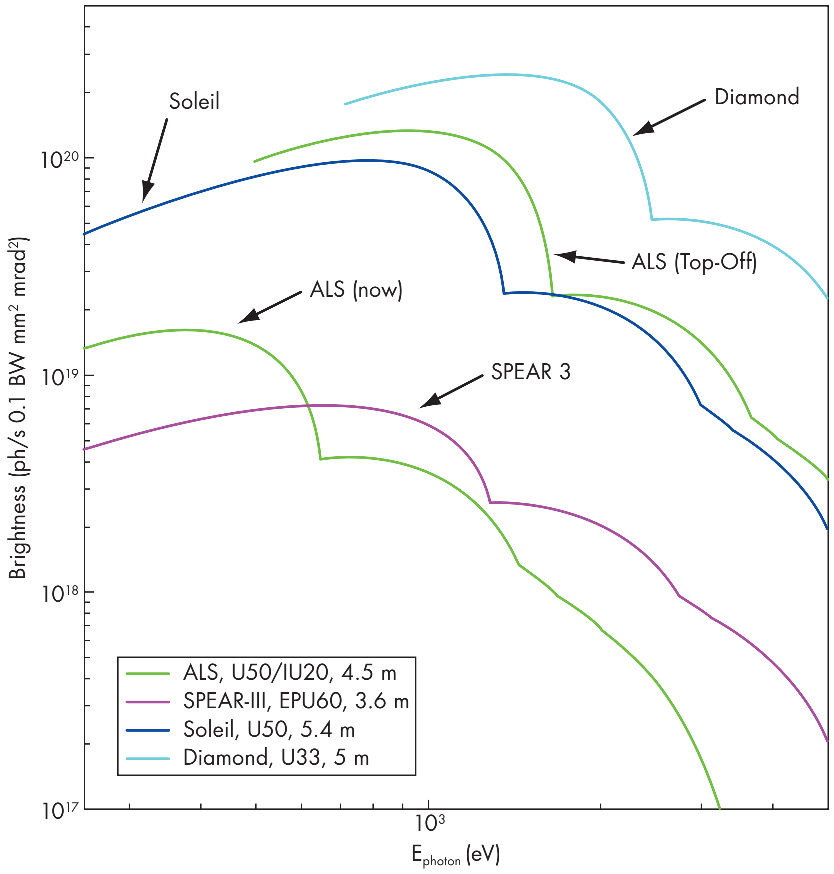

FIGURE 2. Comparison of the brightness around 1 keV of a 4.5-m long U50 with the current ALS parameters and an in-vacuum IU20 with top-off beam parameters to the brightness of proposed undulator sources at newer intermediate-energy light sources.

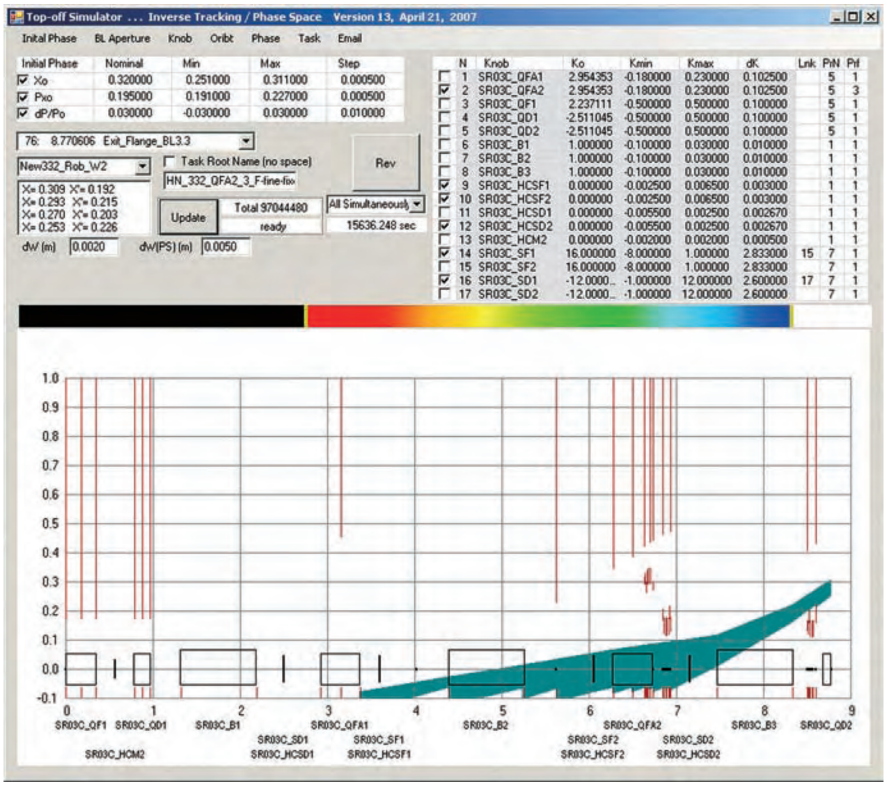

Initial Phase	Nominal	Min	Max	Step
☑ Xo	0.320000	0.251000	0.311000	0.000500
☑ Pxo	0.195000	0.191000	0.227000	0.000500
☑ dP/Po	0.030000	-0.030000	0.030000	0.010000

76: 8.770606 Exit_Flange_BL3.3

New332_Rob_W2

☐ Task Root Name (no space)

HN_332_QFA2_3_F-fine-fix

X= 0.309 X'= 0.192
X= 0.293 X'= 0.215
X= 0.270 X'= 0.203
X= 0.253 X'= 0.226

Total 97044480

ready

All Simultaneously

15636.248 sec

dW (m) 0.0020

dW(PS) (m) 0.0050

	N	Knob	Ko	Kmin	Kmax	dK	Lnk	PrN	Prf
☐	1	SR03C_QFA1	2.954353	-0.180000	0.230000	0.102500		5	1
☑	2	SR03C_QFA2	2.954353	-0.180000	0.230000	0.102500		5	3
☐	3	SR03C_QF1	2.237111	-0.500000	0.500000	0.100000		5	1
☐	4	SR03C_QD1	-2.511045	-0.500000	0.500000	0.100000		5	1
☐	5	SR03C_QD2	-2.511045	-0.500000	0.500000	0.100000		5	1
☐	6	SR03C_B1	1.000000	-0.100000	0.030000	0.010000		1	1
☐	7	SR03C_B2	1.000000	-0.100000	0.030000	0.010000		1	1
☐	8	SR03C_B3	1.000000	-0.100000	0.030000	0.010000		1	1
☑	9	SR03C_HCSF1	0.000000	-0.002500	0.006500	0.003000		1	1
☑	10	SR03C_HCSF2	0.000000	-0.002500	0.006500	0.003000		1	1
☐	11	SR03C_HCSD1	0.000000	-0.005500	0.002500	0.002670		1	1
☑	12	SR03C_HCSD2	0.000000	-0.005500	0.002500	0.002670		1	1
☐	13	SR03C_HCM2	0.000000	-0.002000	0.002000	0.000500		1	1
☑	14	SR03C_SF1	16.000000	-8.000000	1.000000	2.833000	15	7	1
☐	15	SR03C_SF2	16.000000	-8.000000	1.000000	2.833000		7	1
☑	16	SR03C_SD1	-12.0000...	-1.000000	12.000000	2.600000	17	7	1
☐	17	SR03C_SD2	-12.0000...	-1.000000	12.000000	2.600000		7	1

FIGURE 3. Result of radiation safety tracking studies for the ALS. The figure shows the trajectories of backward-propagating particles launched inside the acceptance of one ALS beamline. The results indicate that for a wide range of error conditions (including magnet shorts), no particles can propagate backwards to a point close to injection. Therefore no injected particles can travel down a beamline (if certain interlocks for beam and magnet currents and configuration controls for aperture locations are in place).

orbit feedback enhancements, shimming of one EPU to correct for nonlinear dynamics effects, upgrades of bend-magnet photon stop assemblies, and annual maintenance of the cryogenic systems on the superconducting bend magnets (superbends).

This long shutdown also afforded tremendous progress on less glamorous maintenance items, such as the replacement of the nearly four miles of low-conductivity-water lines, replacement of less-reliable magnetic limit switches on EPUs, and painting of the beamline floor. Beamline staff performed a variety of maintenance and upgrade projects.

The most significant work, which determined the duration of the shutdown, was associated with the top-off upgrade. It included a complete replacement of the booster rf transmitter and waveguides, replacement of the four booster-to-storage ring dipole magnet power supplies, replacement of the two booster quadrupole magnet power supplies, replacement of the booster dipole magnet power supply, new pulsers and upgrades to the pulsed magnet systems, additions to the timing system, a new control system for the new equipment as well as many existing power supplies, new interlock systems, and new collimators for radiation safety.

Generally the work went well and was completed on time. However, toward the end of the shutdown, there was a serious failure in the new booster dipole power supply. The failure occurred during the last day of testing by the power-supply vendor and just before the recommissioning of the booster synchrotron with beam was to begin. The power supply is composed of two separate units that work in unison to supply the needed power. Therefore contingency plans needed to be developed; those were implemented very successfully. However, the problem resulted in a loss of user operation time and also meant slightly longer refill times and lower stability because the storage ring injection for several months had to be done using just half of the new power supply at 1.2 GeV (instead of 1.5 GeV with the old equipment). The plan is to finish the power supply in summer 2007 and start full-energy injection immediately thereafter.

With the completion of the 2006 shutdown and commissioning period, the major hardware work for the top-off upgrade was complete. Further hardware work will be relatively limited, involving additional radiation safety interlock systems and the gating signal distribution chassis. These can be installed without a major shutdown.

The main activity that needs to be completed before top-off operation can begin is a set of very extensive radiation safety studies. There has been good progress recently, culminating in an outside peer review of the tracking studies, demonstrating that injection with the safety shutters open is safe, given certain controls involving interlock systems and verification of apertures. Figure 3 shows the result of backtracking studies for one ALS beamline. Challenges include the unusual (very large) oscillation amplitudes of the particles as well as the extremely large number of parameter combinations and initial phase-space conditions to be studied. We plan to start the process that leads to regulatory approval for top-off operation in late summer 2007. We hope to receive approval that fall and plan to start top-off operation immediately thereafter.

HIGHER-BRIGHTNESS LATTICE

Hiroshi Nishimura

Many experiments at the ALS would benefit by increasing the horizontal brightness. Horizontal brightness is a function of many parameters: it is proportional to flux and inversely proportional to the beam size and beam divergence. The emittance varies strongly with horizontal tune (Nux) and horizontal dispersion (eta). The storage ring nominally operates at tunes (Nux, Nuy) = (14.25, 9.20) and eta = 0.06 m (dispersion at the center of the long straight sections) with an emittance of 6.8 x 10^{-9} m-rad at 1.9 GeV. The dependence of emittance on Nux and eta is shown in Figure 4. Figure 4 shows that operating with a lattice tuned to Nux of 16.25 m and a dispersion of 0.15 m gives an emittance of 2.2 x 10^{-9} m-rad, which is less than one-third of the nominal lattice emittance.

The optics of one of the 12 cells in the present ALS lattice and in the low-emittance lattice are shown in Figures 5 and 6, respectively. The major quantitative changes are that the dispersion and the horizontal beta function are larger in the straight sections and smaller in the center bend. Table 1 shows the major parameters of these modes.

Comparing the parameters of the two lattices in Table 1, one sees that the new lattice has smaller beam sizes than the nominal lattice. The comparison is particularly good in the central bend beamlines where the beam size is about 2.5 times smaller. This would directly translate into a 2.5-times improvement in brightness for these beamlines.

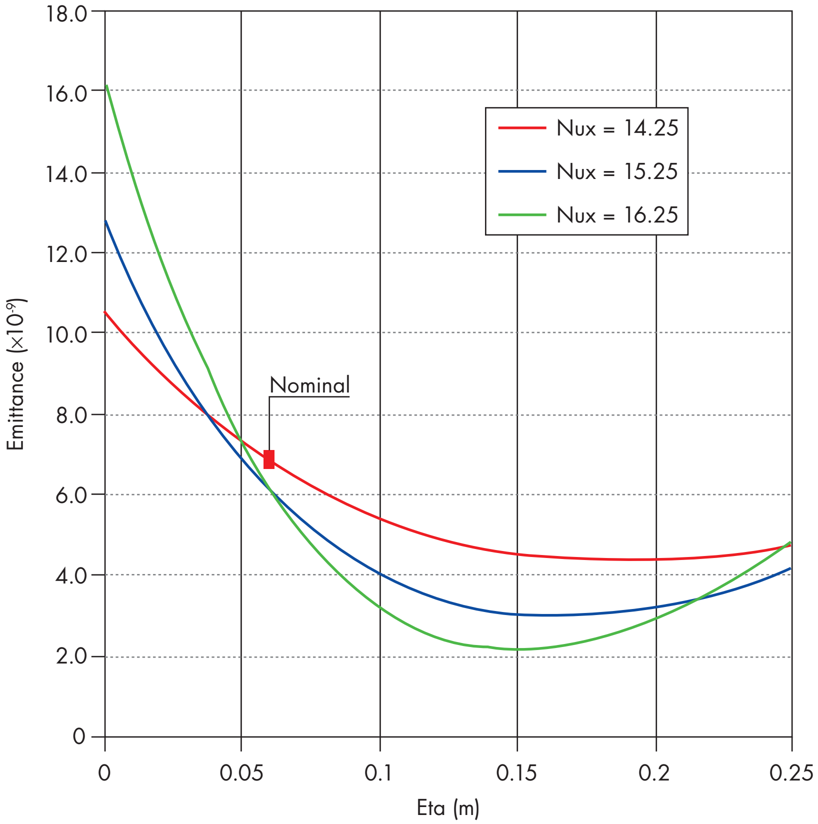

FIGURE 4. Emittance of the ALS at 1.9 GeV as a function of horizontal tune and dispersion in the straight section.

Why can't the ALS just operate with this new lattice? At present, there are only two families of sextupoles, SF and SD, located inside the ALS cell arc (Figure 7). The existing sextupoles are not sufficient to correct the large chromaticities of the low-emittance lattice. Operating with the new lattice requires that an additional two families of sextupoles be added to the lattice on the ends of the straight section. Because there is no additional space in the straight section to install magnets, the alternative would be to include sextupole components in existing magnets. In this case, the two options are to include sextupoles in the QF and QD magnets by adding additional windings, or to replace the corrector magnets with combined-function magnets. These possibilities are currently being studied.

In preparation for either of these possibilities, beam dynamics calculations have begun. The initial results indicate that there is sufficient dynamic aperture for good lifetime and injection efficiency. More detailed simulations are in progress. If successful, such a lattice modification would allow for the possibility of significantly increased brightness—thus keeping the ALS at the forefront of synchrotron light sources.

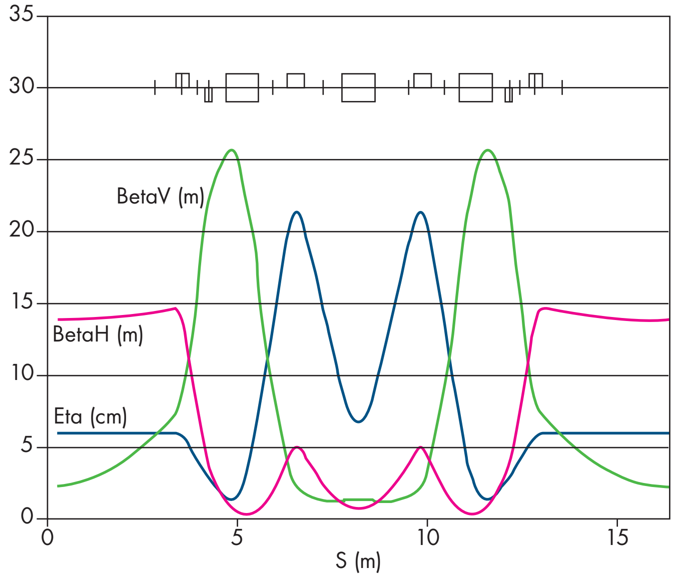

FIGURE 5. Optics of the nominal mode.

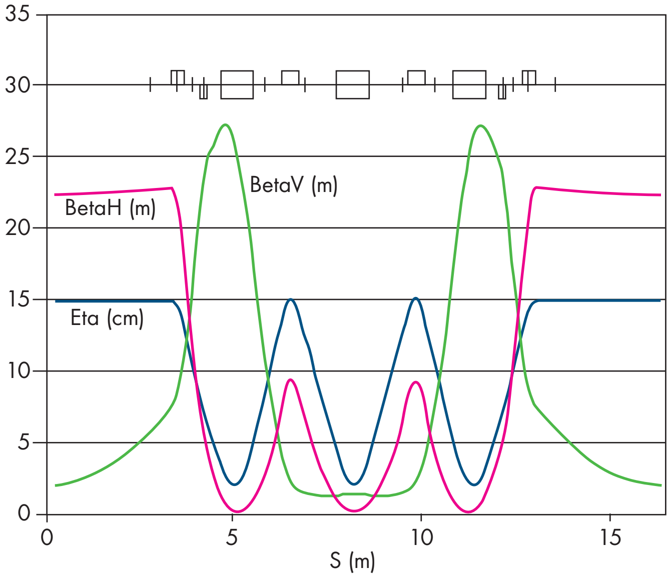

FIGURE 6. Optics of the low-emittance mode.

TABLE 1. Major Parameters: Nominal Mode vs Low-Emittance Mode

PARAMETER	NOMINAL	LOW EMITTANCE
Nux	14.25	16.25
Nuy	9.2	9.2
Dispersion* (m)	0.06/0.79	0.15/0.022
Beta H* (m)	13.85/0.79	22.39/0.31
Beta V (m)	2.26	2.07
Mom. compaction	1.37×10^{-3}	8.72×10^{-4}
Energy spread	9.77×10^{-4}	9.57×10^{-4}
Chromaticity H	–27.02	–50.02
Chromaticity V	–32.33	–35.06
Emittance	6.81×10^{-9}	2.17×10^{-9}
Beam size* (mm)	0.31/0.78	0.26/0.033

*Straight section/center bend

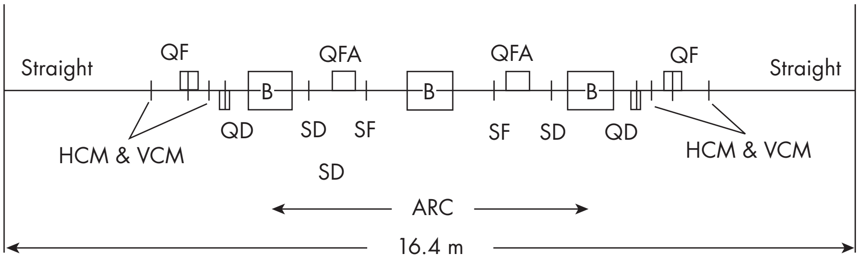

FIGURE 7. Magnets in the ALS unit cell.

A MATLAB MIDDLE LAYER (MML)

Gregory Portmann

The ability to build more-complex and better-performing accelerators is in part due to better computers and software tools. Unfortunately, history has shown that one of the most likely deliverables to go over cost and schedule, even with scope reduction, is software. And the day it is delivered, there begins a "feature creep" that only ends when the accelerator is turned off. This increased demand for software has outpaced most software budgets as well.

One possible solution is collaboration. At all levels of software effort, laboratories around the world are making large efforts to share resources and burden. EPICS and TANGO are two examples of large accelerator control systems running at multiple facilities that were written by a group effort. Accelerator tracking codes are another example. High-level control of particle accelerators has probably seen less sharing of software, but that is rapidly changing. SDDS from APS and XAL from Oak Ridge National Laboratory are examples of sharable high-level software for doing accelerator physics. In a joint effort between the ALS and SPEAR3 at SLAC, a Matlab-based high-level control software system has been gaining popularity in the world.

THE BROADENING USE OF MATLAB

Matlab has been used in particle physics at many institutions for a long time. It was first used at the ALS in the early 1990s, shortly after commissioning. In the beginning, it was primarily used as a scripting language for machine physics shifts but has grown into a larger and more general high-level control tool. The name Matlab Middle Layer is no longer appropriate, since it is much more than a middle layer, but the MML acronym stuck.

Matlab is a matrix manipulation language originally developed to be a convenient language for using and developing algorithms. Matlab does cost money, but it comes with a huge and ever-expanding function library. The ever-expanding part also implies an active worldwide developer base. An advantage of using a commercial product is that some of the feature creep is done by a company and not the laboratory. Actually, many more features are added every year than we need, but the incremental cost is very small, and having room to grow is practically required in a research and development environment.

The software collaboration that started with the ALS and SPEAR3 expanded to the Canadian Light Source, Pohang Light Source, the NSLS vacuum ultraviolet (VUV) and x-ray rings at Brookhaven, and the Duke FEL. The MML project has substantially expanded in the past year, with the three new light sources—Soleil, Diamond, and the Australian Synchrotron Project—making extensive use of the MML software for commissioning and operations. The next two light sources in the world at Shanghai (SSRF) and Barcelona (ALBA) are planning to join the collaboration as well. Lastly, the light source in Thailand (SPS) is presently commissioning the MML software.

The MML is very appealing for countries where both funds and experience in particle physics are limited because they can quickly come up to speed and try algorithms used all around the world. Since the MML software uses the AT (accelerator toolbox) simulator, one can also test algorithms on any of the above accelerators. In total, eleven accelerators are presently using the MML software and at least two more will be using it in the next year.

FROM RESEARCH AND DEVELOPMENT INTO OPERATIONS

Although the MML software was designed to be a scripting tool for designing and testing complex algorithms predominantly during physics shifts, it has also migrated into machine operations. This is quite a departure from the more standard programming languages used in the control room. However, the reliability and speed of Matlab have proven to be more than adequate for machine operations.

Typical uses in storage ring operations include lattice configuration save/restore, energy ramp, global orbit correction, slow orbit feedback, and insertion-device compensation. The core functionality of the MML software is focused on accelerator setup. This includes orbit control, beam-based alignment, tune correction, chromaticity correction, response matrix measurement, local control (LOCO), insertion-device compensation, photon-beam steering, and general scripting for machine-physics studies. As the complexity of accelerators and the need for precision increases, the need for more advanced and flexible programming environments that can support a collaborative effort increases. What makes Matlab so appealing for accelerator physics is the combination of a matrix-oriented programming language, an active workspace for system variables, powerful graphics capability, built-in math libraries, and platform independence.

The collaboration mentioned earlier has produced three Matlab toolboxes written for accelerator physics—MML, AT, and LOCO. All three are well integrated and have proven to be quite useful for machine studies and control at several operating machines. The relatively user-friendly software and almost computer-independent programming language (writing software in a computer-independent way is more time consuming, but the final product tends to be better written and more robust) have fostered a number of collaborations. Most scientists find the syntax quite intuitive, making it possible for visitors to participate in machine development studies with minimal training. Having multiple laboratories use the same high-level software has proven to be quite convenient. Not every laboratory has to spend the resources to write the same algorithms. For new laboratories, this provides a very inexpensive and fast way to acquire high-level control and simulation software that has also been thoroughly tested on other machines. Software development is not only expensive from a labor point of view, it is very expensive to test and commission new software from a beam-time perspective.

Having the same software package debugged at many laboratories has also improved reliability. Thousands of dedicated accelerator hours have been spent testing, improving, debugging, and exercising the MML, AT, and LOCO software packages. As with the EPICS collaboration, software expansion, suggestions, and new ideas come from a big pool of people. The number of physicists and engineers trained on the Middle Layer is growing rapidly. Thus, visiting scientists can work immediately on the new accelerator with very little training. This is particularly useful during the commissioning phase of an accelerator. Running the same code on different accelerators makes it easier to find their similarities and differences. This is very helpful when trying to reach the design performance of an accelerator. Finally, being able to switch between so many different accelerators in a simulated mode is very informative when developing new algorithms and testing designs for future accelerators.

Figure 8 shows the same beam-based alignment algorithm run at the Canadian Light Source and at SPEAR3—different accelerators, same software. It is also very helpful to know ahead of time what the experimental results should look like. A good guess comes from running the algorithm on the machine simulator and comparing experimental data with a similar type of accelerator. Often the first time an online measurement is attempted, the results are not very clean, so having this information greatly speeds up troubleshooting. The ultimate goal of the MML collaboration is to speed up the implementation of known ideas so that there is more time left to experiment with new ones.

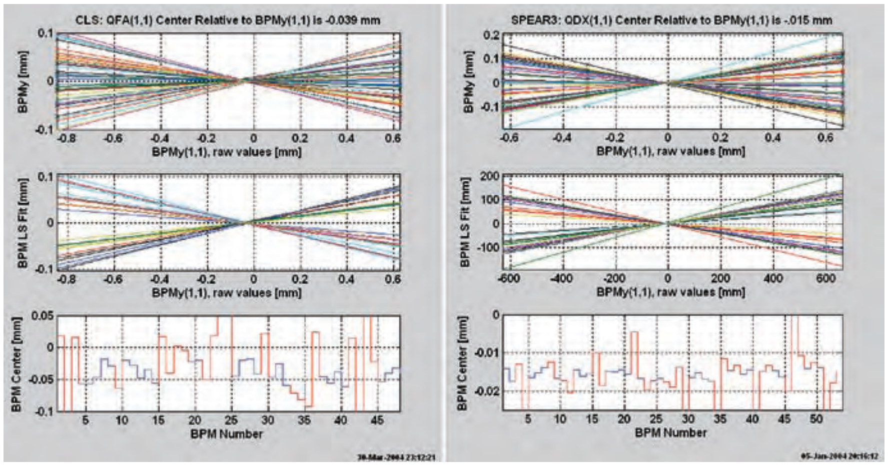

FIGURE 8. Beam-based alignment of a quadrupole magnet at the Canadian Light Source (left) and SPEAR3 (right).

Experimental Systems

The role of the Experimental Systems Group (ESG) (Figure 1) can be split into several categories: (1) to design and build beamlines and endstations based on the demands of the user program, (2) to conduct forefront research in science and instrumentation that will push the boundaries of the application of synchrotron radiation techniques, and (3) to give support to existing user programs, usually in areas of high technical complexity. Approximately 50% of the group's activity is in this latter area of direct user support. This short report gives several examples of work in the two former areas and summarizes our group's activity over the broader range of its work.

FIGURE 1. Row 1: Howard Padmore; Row 2: John Spence, Jonathan Kirschman, Yekaterina Opachich, Martin Kunz, Corin Michael Greaves, Richard Kirian, and Sander Caldwell; Row 3: Anton Chakhmatov, Nobumichi Tamura, Anthony Young, Richard Celestre, Thornton Glover, Steve Irick, and Philip Heimann; Row 4: Valeriy Yashchuk, Jamshed Patel, Emanuele Pedersoli, Dmytro Voronov, Wim Bras, Kyle Engelhorn, and Philippe Goudeau.

Row 1: Alberto Comin, Alexander Hexemer, Christopher Coleman-Smith, Deborah Smith, Eliot Gann, Eric Schaible, and Jamie Nasiatka; Row 2: Tim Kellogg, Malcolm Howells, Jun Feng, Simon Clark, Alastair MacDowell, Wayne McKinney, and Matthew Marcus; Row 3: Andreas Bartelt, Andreas Scholl, Andrew Doran, Gregory Morrison, James Glossinger, Matthew Church, and Anthony Warwick; Row 4: Jason Knight, Simon Morton, Simon Teat, Sirine Fakra, Bob Batterman, Stefano Marchesini, and Bruce Rude.

OPTICAL METROLOGY

The Optical Metrology Laboratory (OML) at the ALS, under the leadership of V. Yashchuk, is tasked with characterizing, understanding, and developing synchrotron radiation optics. The OML staff is actively working to improve metrology instruments (Figure 2) and to develop new measurement techniques, with improved accuracy and resolution, for characterization of x-ray optics with surface slope errors of less than 0.25 µrad (rms). The need for higher-precision metrology is driven by a need to improve optics commensurate with the steady increase in storage-ring performance over the last few years and the increased emphasis on experiments where coherence preservation is required.

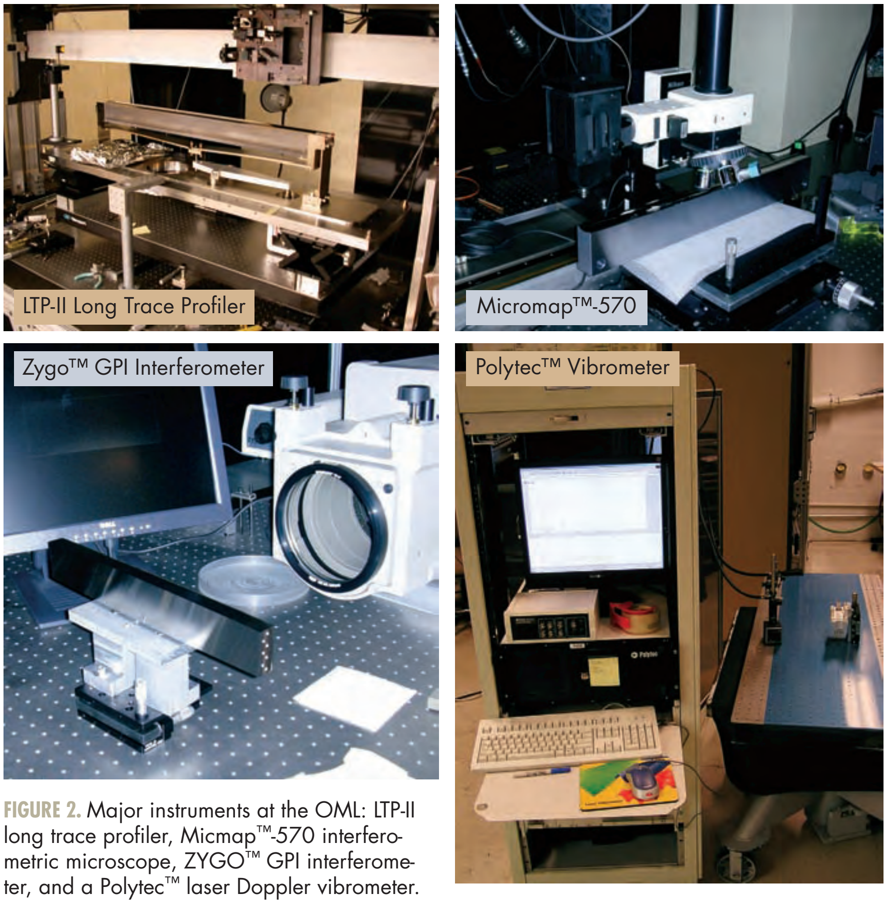

FIGURE 2. Major instruments at the OML: LTP-II long trace profiler, Micmap™-570 interferometric microscope, ZYGO™ GPI interferometer, and a Polytec™ laser Doppler vibrometer.

The long trace profiler (LTP) was last upgraded about 10 years ago. At that time, an optical reference channel was added, allowing for monitoring the LTP systematic error on the level of ~1 µrad. To incorporate the reference channel, a detector based on two linear photodiode arrays was used. Over the years, the detector and the dedicated data acquisition system have become the most unreliable parts of the instrument. They became dated and very difficult to replace and upgrade. Because of detector failure, we were forced to accelerate the modernization of this LTP.

In just two months of extremely intensive work, the LTP modernization was successfully completed. This included (1) reassembly and readjustment of the LTP-II linear translation stage to allow assured operation under the National Instruments (NI) motion control system, with the increased load of a new detector; (2) a distance-measuring interferometer, incorporated into the system for precise positioning of the LTP optical head; (3) development of motion control and data acquisition software based on the NI LabView™ platform; (4) design and fabrication of a new detector system based on a high-resolution (7.4 x 7.4 µm^2 pixel size) CCD camera (Figure 3); (5) assembly and use of an efficient experimental setup for precise, ~0.5%, flat-field calibration of the camera pixel-to-pixel photo-response nonuniformity; and (6) development of new software for carrying out LTP measurements and data analysis.

After the modernization and calibration and testing were completed, the first metrology work with the upgraded LTP was performed on a superpolished grating substrate with a spherical radius of ~18.7 m, fabricated by InSync, Inc. for the MERLIN project. The rms slope variation for the substrate was specified to be < 0.5 µrad. The measurement performed at the OML indicates a slope variation of < 0.37 µrad for the central part of the substrate (Figure 4). Such measurements have only been possible because of the upgraded LTP. With further improvements, we expect that the overall accuracy of LTP measurements will improve to the 0.1-µrad level.

LTP metrology of this substrate became possible because of the use of a novel technique developed at the OML for suppression and measurement of the LTP systematic error. The technique utilizes the new two-dimensional de-

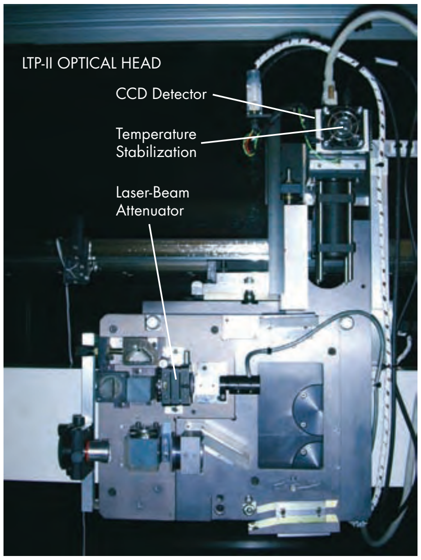

FIGURE 3. Optical sensor of the upgraded LTP with a new detector system based on a precisely calibrated CCD camera with homemade active temperature stabilization. A new laser-beam attenuator was designed to simplify alignment of the instrument.

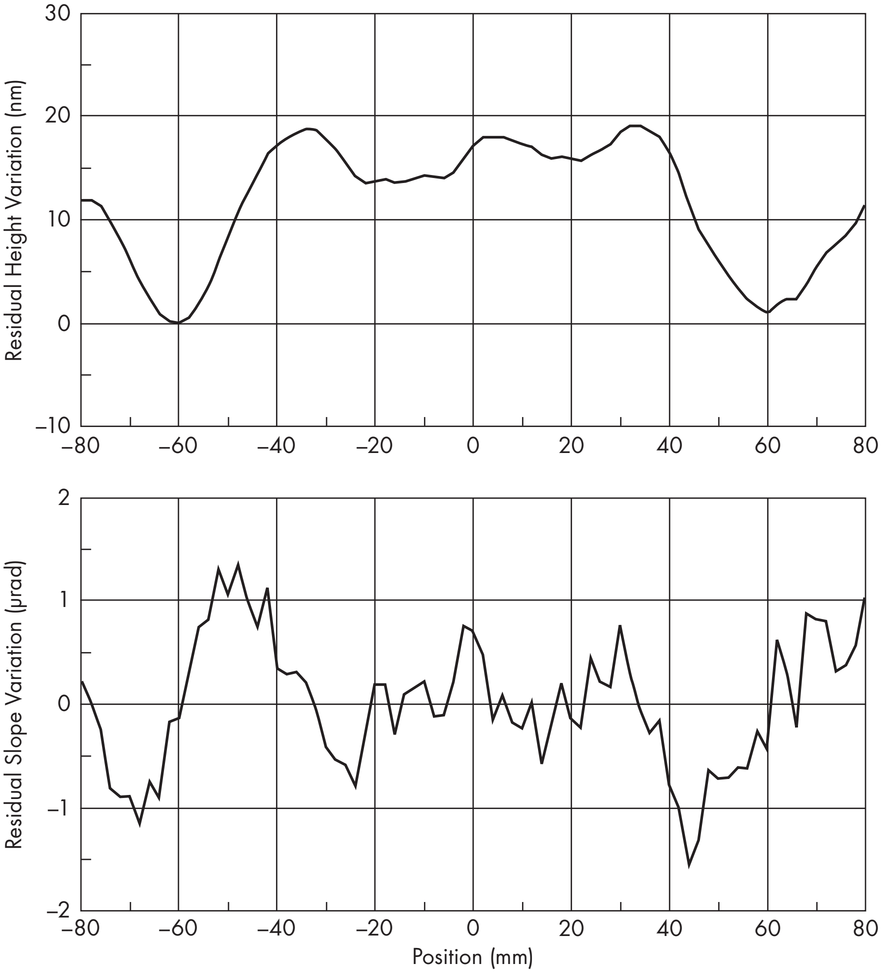

FIGURE 4. Residual slope and corresponding height profiles of the superpolished grating substrate with a spherical radius of ~18.7 m, fabricated by InSync, Inc. for the MERLIN project. The slope variation of the central part of the substrate as measured with the modernized LTP is less than 0.37 µrad (rms).

tector of the LTP. With this detector, it is possible to perform repeated measurements over the same trace on the mirror surface, but at different sagittal tilts of the mirror with respect to the LTP. By averaging over these measurements, the higher-spatial-frequency systematic errors of the LTP optics are significantly suppressed.

We still need a sophisticated calibration system for precise calibration and control for the lower-spatial-frequency systematic errors of the upgraded LTP. The current calibration, extracted from the test measurement of the 40-m curved "round robin" mirror, provides only a one-point calibration and does not account for all of the nonlinearity of LTP curvature measurements. Ideas for a more sophisticated technique for calibration of slope-measuring instruments (based on a universal test mirror to simulate a mirror with a known shape) has been developed at the OML and is being fabricated in collaboration with a worldwide collaboration of the ALS, BESSY, and the PTB (the German national standards institute).

A new generation of high-brightness sources (LCLS, NSLS-II, ALS at low-emittance top-off mode) is being developed in the United States to enable nanofocusing applications and high-coherence experiments including diffraction imaging, scattering, and speckle measurements. To deliver on this potential, beamline optics of unprecedented quality are required. The corresponding metrology will be essential in order to achieve high-efficiency sub-100-nm focusing. The beamline optics will have to have sub-100-nrad slope error tolerances. This is now the worldwide goal for manufacturing and metrology of x-ray optics. The next generation of mirror-measurement tools must achieve sensitivity and accuracy well below these values. It has become apparent that without a concentrated nationwide research and development effort in x-ray metrology, costly increases in source brightness may not translate into increased experimental capabilities because "if you cannot measure, you cannot make it, nor use it."

COSMIC AND MAESTRO AT SECTOR 7

Two large scientific proposals are currently under consideration: COSMIC, a facility for coherent soft x-ray imaging and scattering and MAESTRO, a facility for nanoscale angle-resolved photoemission (Figure 5). Taken together, these will require the rebuild of the undulator beam lines at Sector 7, replacing one of the original ALS spherical grating monochromators with a pair of modern beamlines designed specifically for these two programs.

The optical design of this dual facility was completed by the ESG in an effort led by T. Warwick, and a successful optical design review took place with an international review committee. The reviewers reported, "We are unanimous in our belief that these conceptual designs will be turned into high-performance, robust operation, highly productive beamlines." Preliminary engineering studies will begin soon.

The key to a successful rebuild of ALS Sector 7 is a properly scoped project, carefully planned. At the design stage, this means that the beamlines should fit the floor space available, taking careful account of user space needs for future endstation development and sample preparation. The project will need ten or so state-of-the-art reflecting optics, and the design calls for state-of-the-art specifications for each of these, with managed risk. Beamline performance is optimized, and the performance requirements are met with consideration of the effects that could limit the delivered flux and resolution. Optical aberrations and thermal deformation have been assessed, and consultation is underway with the potential vendors of the mirrors and gratings.

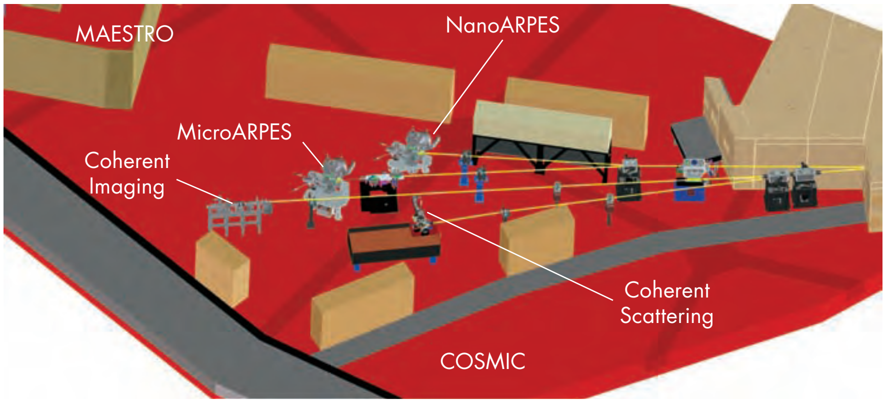

FIGURE 5. Depiction of the COSMIC and MAESTRO beamlines on the ALS floor at Sector 7.

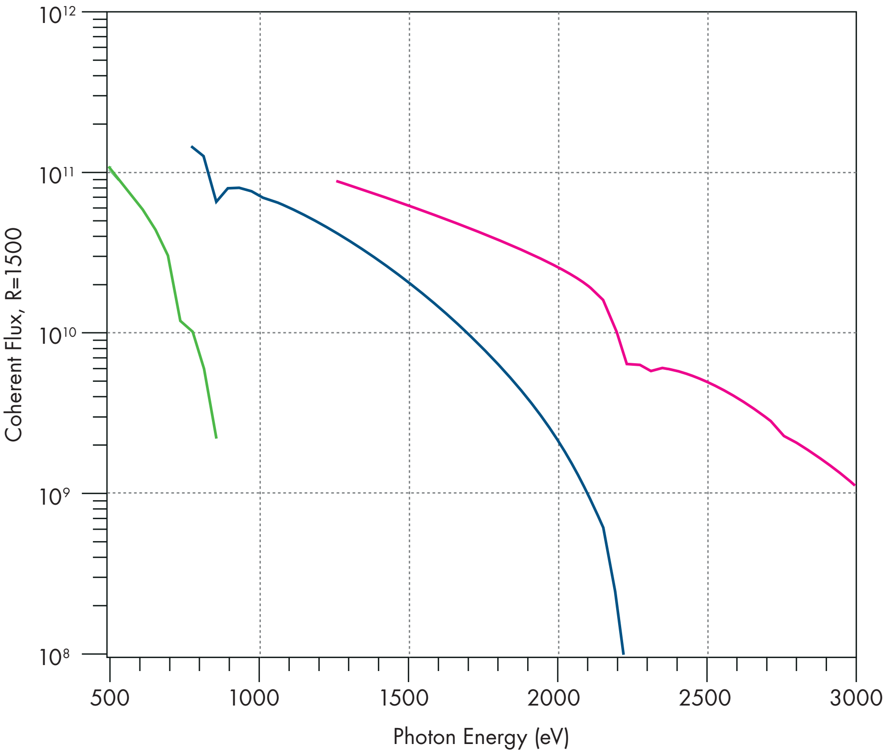

FIGURE 6. Coherent flux at R = 1500 in the coherent imaging branch of COSMIC. The three traces are computations using the undulator first, third, and fifth harmonics from the corresponding diffraction grating, of which there are three.

The COSMIC beamlines will be served by a 34-mm-period EPU and branch to serve two endstations. One will be for coherent scattering and speckle measurements from organic and magnetic materials from 250 to 1800 eV. The other will be for lensless diffractive imaging using phase retrieval techniques from 500 eV to 3 keV (Figure 6). In each case, the facility will provide full polarization control and will be optimized for modest spectral resolution (R < 1500) and maximum coherent photon flux. The reduced vertical brightness of the ALS with top-off operation will be exploited and preserved in the beamline.

The MAESTRO beamlines will be served by a 70-mm-period EPU and branch to serve two endstations for angle-resolved photoemission, from 60 to 600 eV with added range down to 20 eV and up to 1000 eV (Figure 7). High spectral resolution is required and the design promises 2-meV resolution at 60 eV. One branch will generate a small spot on the order of 10 µm and illuminate the currently operating Electronic Structure Factory endstation. The second branch will be for a zone-plate nanofocus for microscopic studies using ARPES with an x-ray spot on the order of 10 nm.

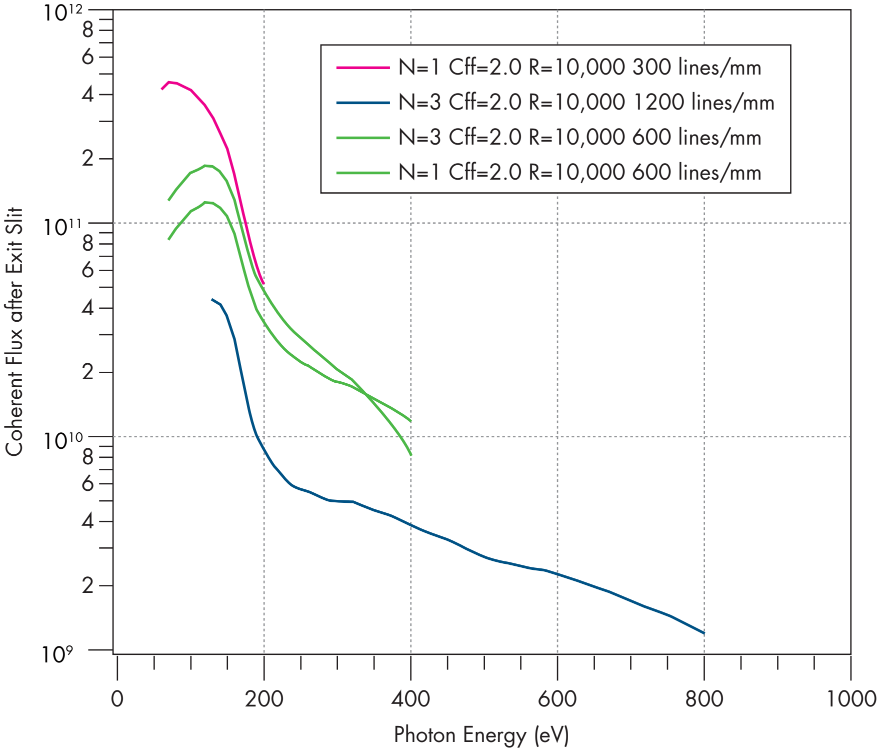

FIGURE 7. Coherent flux at R = 10,000 for MAESTRO.

X-RAY MICRODIFFRACTION ON SUPERBEND BEAMLINE 12.3.2

The move of the successful x-ray microdiffraction program from bend-magnet Beamline 7.3.3 to the super-bend Beamline 12.3.2 was made possible by a funded NSF instrumentation proposal submitted by E. Ustundag (Iowa State University) together with support from the ALS. This team effort was led by A. MacDowell, N. Tamura, and T. Warwick together with R. Celestre, S. Fakra, M. Church, and J. Glossinger. The move stemmed from the need for a smaller spot size and access to higher-energy photons, to enable better strain/stress sensitivity for more precise insights into the micromechanics of engineered samples and for development of bulk-sensitive three-dimensional x-ray microdiffraction techniques.

Beamline 12.3.2 was completed early in 2007 and the hutch received first light on April 17, 2007. Assembly of the optical components inside the hutch as well as initial commissioning of parts being installed in the station (Figure 8) were started soon afterward. The source for this beamline is a 6-T peak field superconducting bend magnet shared with the 12.3.1 SIBYLS beamline. The available energy range has been extended from 5–12 keV (on regular bend magnet 7.3.3) to 5–24 keV on the new superbend. The nominal source size is 240 (h) x 40 (v) µm (FWHM). At 13 m from the source lies a horizontally deflecting 0.7-m long silicon toroidal mirror (M1) coated with a Pt–Rh bilayer that refocuses the source at the entrance of the experimental hutch, which is situated a further 9.4 m downstream. The working grazing incidence angle is 3.5 mrad. Characterization of the M1 mirror performance has been carried out and shows that it behaves close to expectations. Like the previous bend-magnet station, water-cooled tungsten rotary slits placed at the M1 focus just behind the entrance to the hutch are used as a size-ad-

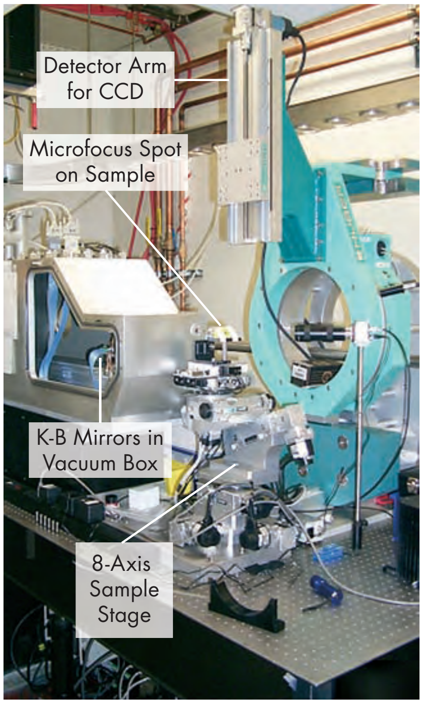

FIGURE 8. New microdiffraction endstation being assembled during the commissioning of Beamline 12.3.2.

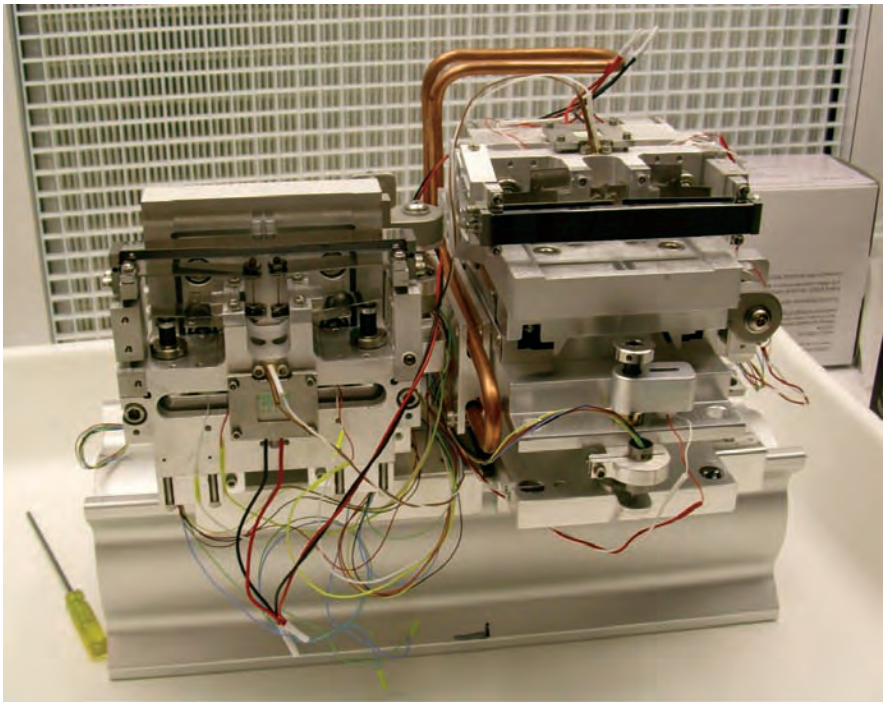

FIGURE 9. New Kirkpatrick-Baez mirror assemblies for Beamline 12.3.2.

justable secondary source for the microfocus instrument inside the hutch. This secondary source size is close to the expected value of 175 (h) x 30 (v) µm (FWHM).

Besides the M1 mirror, all the other optical components of the beamline are placed in the hutch inside a vacuum chamber. The Kirkpatrick-Baez (K-B) mirror pairs (Figure 9) are placed 2.13 m (horizontally focusing) and 2.265 m (vertically focusing) downstream of the rotary slits. They are 100-mm-long, 12.5-mm-wide, and 4-mm-thick silicon mirrors coated with rhodium. The focal point on the sample is at 270 mm and 135 mm, respectively, from the horizontal and vertical focusing mirrors. Each mirror has four degrees of freedom: translation in-out of the beam, pitch, and two bends. The bending of the mirrors to the required elliptical shape is performed using flat flexure and tie rods instead of weak leaf springs as in the original 7.3.3 design in order to minimize misalignment. The tie rods are short to minimize thermal drift effects. The new set of K-B benders also contains a more sensitive and stable mirror detwist mechanism. The new K-B system has been shaped in the OML and installed at the beamline for initial characterization and commissioning. Measurements of the figure errors and roughness indicate that the new set of mirrors should provide a beam size ~100 nm. Initial measurements of spot size were around 1 micron before detailed optimization. An air-conditioning system maintains the temperature inside the hutch to within ±0.1 °C, while initial vibration measurements performed during the shutdown indicate a system stability of less than about 100 nm. The beamline will work mostly in white-beam mode, but a number of experiments also require monochromatic focused beam. This will be provided by a four-bounce monochromator consisting of two Si(111) channel cuts mounted on encoded rotary stages that would allow rapid switching between white and monochromatic beam while illuminating the same spot on the sample.

The sample stage has eight degrees of motion. Three XYZ motors at the base allow alignment of the stage's center of rotation with the focal position of the x-ray beam. A chi cradle can change the angle of incidence of the beam onto the sample from 0 to 45 degrees, permitting both transmission and reflection experiments. Three translations and a phi rotation stage allow for the scanning of the sample under the beam. The position reproducibility of the upper stage is 50 nm. Diffraction patterns will be collected by an x-ray CCD detector mounted on a two-theta arm allowing it to be positioned for transmission as well as high-angle mode. The beamline is expected to become fully operational and available for users during the summer of 2007. The in-house code for analyzing the thousands of diffraction patterns generated by a single two-dimensional scan has been adapted to run on a 24-dual-processor-node Linux cluster for fast real-time processing of data to yield strain/stress, deformation, orientation, crystalline phase distribution maps of the sample.

The microdiffraction program covers very diverse areas of science and has been a tremendous success. The new combination of a high-energy superbend beamline having enhanced flux and high-energy coverage with high-power computing, state-of-the-art detectors, and 100-nm spatial resolution will be truly revolutionary, and we are set for a very bright future in applying the new system to the study of materials microstructures.

SMALL- AND WIDE-ANGLE X-RAY SCATTERING (SAXS/WAXS)

The previous home of the x-ray microdiffraction facility described above, Beamline 7.3.3, has been transformed under a strategic Laboratory Directed Research and Development (LDRD)-funded program into a simultaneous small-angle and wide-angle x-ray scattering (SAXS/WAXS) beamline (Figure 10). This work has been headed by A. Hexemer and H. Padmore, together with R. Kirian, A. MacDowell, R. Celestre, M. Church, E. Gann, J. Glossinger, and (ESRF collaborator) W. Bras.

Currently the beamline is in the initial stages of commissioning. The modification to Beamline 7.3.3 to accommodate a SAXS/WAXS endstation has been minor in comparison to constructing a completely new beamline. A multilayer monochromator has been installed in front of the M1 mirror. The multilayer is made of 250 layers of Mo alternating with B_4C each with a d-spacing of 2.0 nm. The x-ray energy in normal operation mode is fixed at 10 keV and yields an x-ray flux of 1.7×10^{12} at the sample position inside the hutch. Two sets of slits have been installed to reduce the parasitic scattering. In addition, two identical detectors, one for SAXS and one for WAXS, have been mounted. The detectors are on loan from the Berkeley Center for Structural Biology (BSCB) through the LDRD's co-principal investigator, P. Adams. They are ADSC Quantum 4R CCD detectors with an active area of 188 x 188 mm (2304 x 2304 pixels) and a dynamic range of 16 bits. The readout time varies between 9 and 3 s depending on imaging mode. The SAXS detector is mounted on a rail system to easily change the sample–detector distance between 1 and 4.30 m (Figure 11). The WAXS detector is suspended on a five-axis mount providing a large degree of freedom in positioning the detector around the sample. With the possibility of measuring SAXS and WAXS at the same time, the total q-range of the system is between 0.004 $Å^{-1}$ and 8.7 $Å^{-1}$. In real space this corresponds to feature sizes between 1500 Å and about 0.8 Å.

A major focus during the design of the SAXS/WAXS endstation was to accommodate a wide variety of samples, stages, and environments. In the beginning, however, the focus will be on three main research areas.

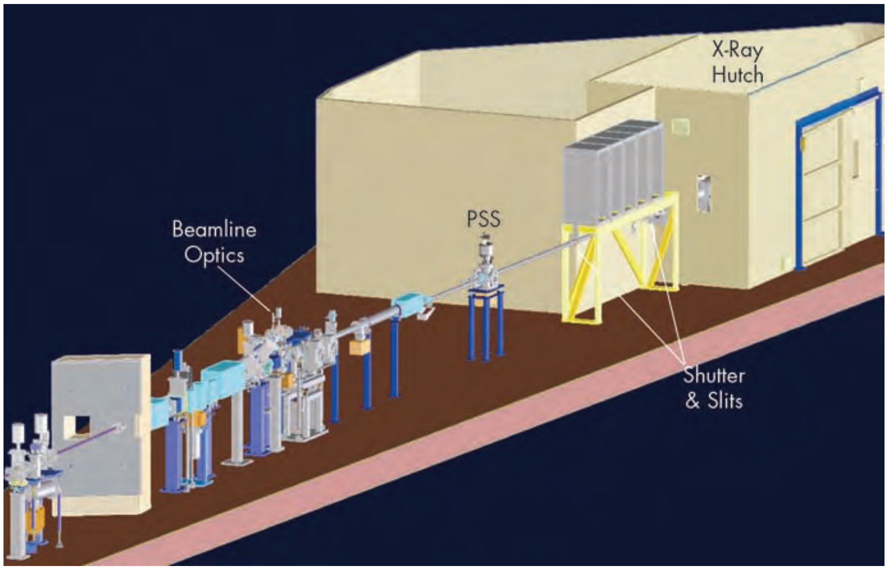

FIGURE 10. Layout of the SAXS/WAXS Beamline 7.3.3.

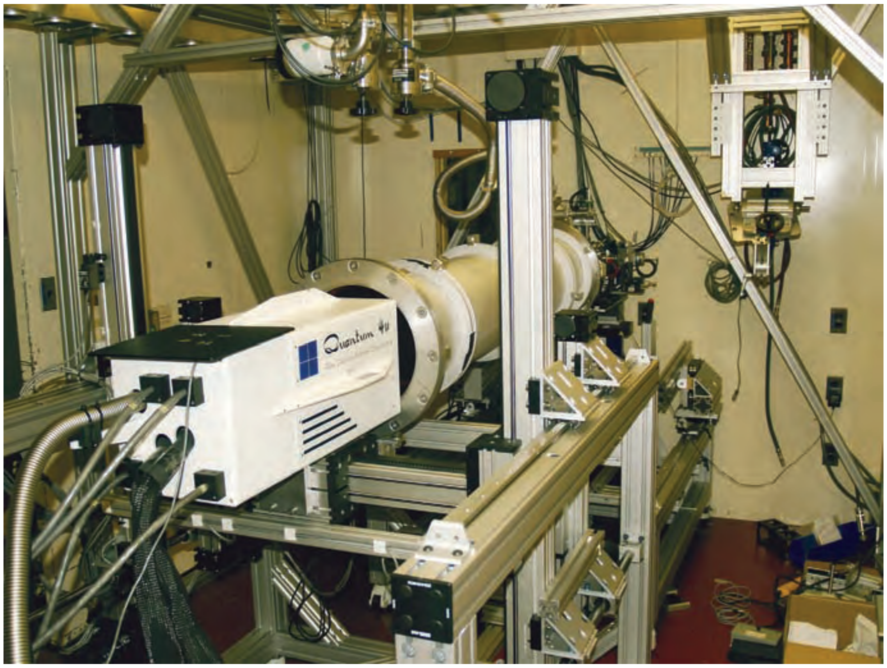

FIGURE 11. SAXS detector with flight tube.

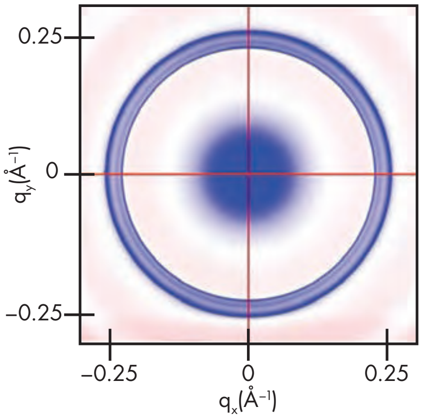

FIGURE 12. SAXS pattern of a smectic liquid crystal.

First, Beamline 7.3.3 will allow SAXS measurements of proteins and protein complexes. The value of protein SAXS is illustrated by three problems with standard protein crystallography: first, certain proteins and complexes are difficult or impossible to crystallize, an issue that is avoided in SAXS since proteins are measured in solution; second, a protein's structure in a crystalline lattice may well differ in important respects from its structure in physiologically relevant conditions; finally, large complexes typically exist in a very large array of states in order to perform their functions, and it is inconceivable that all these states and the transition from one to another can be followed with traditional crystallography.

The second research area will focus on polymer systems and liquid crystals. SAXS provides the primary means of determining the nanophase structure and disordering transitions in block copolymers by the development of periodic features commensurate with microphase separation. Subtle changes in structure, such as a nanometer increase in domain spacing due to molecular reorientation or changes from interdigitated to bilayer structures, can be detected and explored as a function of temperature. The first experiment at Beamline 7.3.3 was in collaboration with B. Freelon, a member of the UC Berkeley group of R. Birgeneau. The sample was a thermotropic liquid crystal changing from an isotropic phase to a nematic to a smectic phase as a function of temperature. The SAXS data was taken in situ while the sample was cooled from 80 to 45 °C. Figure 12 shows the collected SAXS pattern for an exposure time of 20 s at 51 °C. The liquid crystal is in a smectic phase at this temperature.

The third focus area will be work in nanoscience—for example, studies of the growth kinetics of nanoparticle complexes in solution.

OTHER ACTIVITIES

ESG staff members continue to support other technically demanding user programs. The photoemission electron microscopy (PEEM) program involves the continued operation of Beamline 7.3.1 and the development of PEEM3 at Beamline 11.0.1. A laser-based subpicosecond magnetization dynamics program is under development at the same beamline. High-pressure diffraction is under continued development at Beamline 12.2.1. MicroXAFS and fluorescence analysis operates at Beamline 10.3.2. ESG staff support and develop Beamlines 6.0.1 and 6.0.2 for laser-sliced femtosecond x-ray research. Lensless imaging is supported at Beamline 9.0.1. A dedicated small-molecule crystallography station is operational at Beamline 11.3.1. Finally, an x-ray microtomography program is being developed on superbend Beamline 8.3.2.

Scientific Support

Zahid Hussain, Division Deputy for Scientific Support / Eli Rotenberg, Deputy Leader, Scientific Support Group

INTRODUCTION

The primary mission of the Scientific Support Group (SSG) (Figure 1) is to support the efforts of researchers at the ALS through scientific and technical collaboration and scientific outreach. Working with the users, the SSG plays an important role in developing novel instrumentation that enables cutting-edge science. Depending on the needs of the user, the degree of collaboration can range from technical assistance with the beamline and instrumentation to full partnership in developing new research programs.

SCIENTIFIC OUTREACH

The SSG strives to expand the scientific program of the ALS and broaden its user base through publications and presentations. The group organizes a variety of seminars, including the weekly ALS/Center for X-Ray Optics (CXRO) seminar series and a targeted weekly SSG lecture series. The weekly lectures cover a wide range of topics and are given by world-renowned scientists. The group also organizes the quarterly ALS Colloquium. This year, R. Birgeneau, Chancellor of UC Berkeley, also gave one of the ALS Colloquia.

FIGURE 1. Left to right: Per-Anders Glans, Yulin Chen, Adriana Reza, Zhihui Pan, Cinthia Piamonteze, Shan Qiao, Jinghua Guo, Evelyn Cruz, Elke Arenholz, Zahid Hussain, Michael Martin, Wanli Yang, Eddie Red, Jonathan Spear, Tolek Tyliszczak, Jessica McChesney, Zhao Hao, Matthew Brown, Simon Mun, Gennadi Lebedev, Geoffrey Gaines, Yi-De Chuang, and Aaron Bostwick.

Working together with the UEC, the SSG also helps to organize workshops exploring new scientific opportunities and needs for new beamlines or experimental facilities. During the 2006 ALS Users' Meeting, ten such workshops were heavily attended by enthusiastic scientists, triggering many fruitful discussions that should spark further advances at the ALS.

The ALS offers two types of research fellowships: the Doctoral Fellowship in Residence and the newly instituted Postdoctoral Fellowship.

The ALS Doctoral Fellowship in Residence program, established in 2001, has been very popular among doctoral students and has been received with much appreciation. Doctoral fellowships enable students to acquire hands-on scientific training and develop professional maturity for independent research. More details are given at the ALS Web site (www-als.lbl.gov/als/fellowships/). A selection committee consisting of C. Heske (chair, UEC), C. Larabell, Z. Hussain, S. Bader (chair, Scientific Advisory Committee), and N. Smith recommended the following recipients for doctoral fellowships for academic year 2006 (Figure 2): Matthew Brown (UC Irvine, ambient-pressure XPS);

FIGURE 2. From left to right: Zhihui Pan, Xiaowei Yu, Eddie Red (E.O. Lawrence Postdoctoral Fellow), Shuyun Zhou, and Matthew Brown.

Ileana Dumitriu (Western Michigan University, inner-shell photodetachment of negative ions of C_{60} and nickel clusters Negative Ions); Mohammed Hussain (University of British Columbia, ARPES and XAS); Zhiqiang Li (UC San Diego, infrared microscopy of charge injection in organic field-effect transistors); Zhihui Pan (Boston College, photoemission study of strongly correlated electron systems); Cheng Wang (North Carolina State University, resonant scattering); Jie Wu (UC Berkeley, nanomagnetism with photoemission electron microscopy); Xiaowei Yu (Stanford University, time-resolved imaging/magnetic phase transitioning); Shuyun Zhou (UC Berkeley, ARPES).

The purpose of the new ALS Postdoctoral Fellowship program is to identify outstanding individuals in new and emerging scientific and engineering research fields and provide advanced training in synchrotron radiation science. Fellows become integral members of ALS research teams. Applicants must have received a doctoral research degree from an accredited academic institution in an appropriate scientific or engineering discipline within three years of the appointment start date. Applications are reviewed on a quarterly basis. Awards are initially for one year with the possibility of renewal for a second or third year, contingent on satisfactory annual performance reviews and funding availability. Salary is competitive with current ALS/Berkeley Lab postdoctoral fellows, ranging from $60,000 to $66,000 per year, depending on the number of years since receipt of the doctoral degree. Postdoctoral fellows are also eligible for midlevel career benefits. More details are given at the ALS Web site (www-als.lbl.gov/als/fellowships/).

SUPPORT

SSG members are responsible for the operation, upgrade, and maintenance of most of the facility beamlines and many of the permanent endstations at the ALS. Each of the undulator-based beamlines—4.0.2, 7.0.1, 8.0.1, 10.0.1, a photoemission branchline on 12.0.1, and a coherent science branchline 12.0.2—typically have one or two SSG staff members responsible for their continued operation. This year the SSG has also taken responsibility for operation of Beamline 6.3.1 which was developed and operated by CXRO. The group is also playing an active role in the operation of the molecular environmental science Beamline 11.0.2 and the upgrade of the chemical dynamics complex (Beamline 9.0.2), which are operated by Berkeley Lab's Chemical Sciences Division (CSD) under separate funding from DOE BES. Members of the SSG put great emphasis on making the development of novel instrumentation more efficient and user friendly. In 2006, working with the Engineering group, the SSG has made significant progress in the development of MERLIN Beamline 4.0.3 (see details below). The group has also designed and developed several new experimental systems, some of which are described below.

MEMBER RESEARCH

Staff scientists within SSG are expected to maintain scientific and technical excellence in areas of synchrotron radiation research. Participation in active scientific programs is essential for such development, and all of the SSG scientists are active members of research programs at the ALS.

CARBON ARRIVES AT THE ELECTRONIC STRUCTURE FACTORY

Graphene is a single layer of carbon atoms tiled in a honeycomb array; it is the building block of carbon nanotubes, graphite, fullerenes, and other exotic carbon-based materials that have been widely studied in the last two decades. Graphene-based devices might very well address the fundamental limitations of silicon-based technology, expected to be reached in the next decade or so. These limitations are not only in the size of devices, but also in power consumption. The latter is especially important considering that the present high rate of power consumption is one of the most significant environmental impacts of computers and other electronic devices. Graphene also has bizarre electronic properties: the charge carriers have an effectively zero mass and move through the material at a constant speed, much as massless photons have a constant speed of light. This makes graphene an unusual playground for studying relativistic particle physics, and its carriers are referred to as Dirac fermions, after the equation that describes their motion.

The Electronic Structure Factory is a high-resolution, high-throughput ARPES endstation, dedicated in part to studies of complex materials grown in situ at Beamline 7.0.1. Because of these capabilities, this endstation is well-situated to study the electronic structure of in situ grown graphene-based materials.

In a recent article in the journal *Science*, a collaboration between the ALS and two groups in Germany have proved the feasibility of making a unique electronic switch only two graphene layers thick (see "Controlling Graphene's Electronic Structure" in the Condensed Matter Physics section of the Science Highlights). The researchers verified theoretical predictions that upon controlling the electronic charge in each layer, such a bilayer can be readily switched from being a metal to being an electrical insulator. Furthermore, work by this group and others has shown that the current traveling through graphene layers dissipates very little energy, so a switch based on this effect would work efficiently with less heat dissipation than present electronic devices.

The change in the electrical conduction occurs upon application of an electrical field across the bilayer graphene sample as a consequence of symmetry breaking. When there is no net field perpendicular to the layers, the individual graphene sheets are identical, and calculations predict a gapless, semimetallic band structure. With a bias across the sample, the graphene layers are no longer identical and the electronic band structure acquires an energy gap, which can be clearly seen in the experiment (Figure 3). This control of the band structure means that if the Fermi level is adjusted to be near the band crossing, a semimetal-to-insulator transition can be induced by applying an electric field. While the experiments at the ALS used alkali metal overlayers to control the field, similar control in a device could be readily achieved using standard voltage gating techniques.

In an article published in the journal *Nature Physics,* the same research team showed for the first time the effect of plasmon scattering on the electronic lifetime in a single graphene sheet. To probe the effect, the researchers grew graphene layers doped with a slight amount of excess charge, amounting to about 1 electron per 1000 carbon atoms. While small, this excess charge was sufficient to create a dilute metal, which shows up in the ARPES measurements as a tiny circular Fermi surface (Figure 4, left). The underlying energy bands have a very special character: they consist of two bands that were predicted to cross without any energy gaps where they overlap (Figure 4, center). This can easily be seen in the experiment. What is strange is that at the crossing point, also called the Dirac energy (E_D), the bands are significantly broadened, and furthermore, rather than passing in a straight line, they show a notable kink in their shape. This is most easily seen for a specific

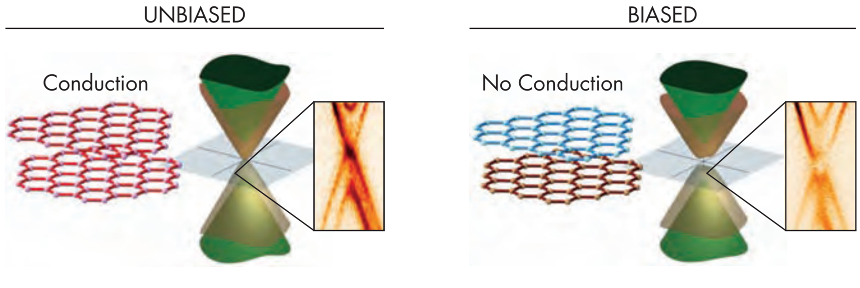

FIGURE 3. Left: When the graphene film has no net applied field, the symmetry of the film dictates, and ARPES data confirm, that two electronic bands cross without an energy gap. Right: Upon application of an electric field, the symmetry is broken and a gap is opened in the energy spectrum.

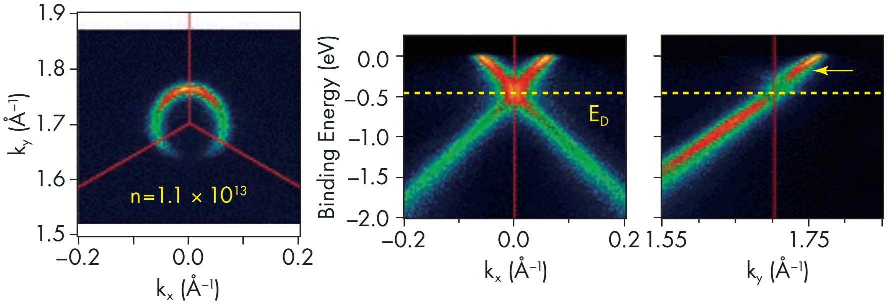

FIGURE 4. Electronic structure of n-doped graphene. Left: The Fermi surface of graphene grown on silicon carbide, for charge density n = 1.1 x 10^{13} electrons/cm^2. Center, right: Energy bands taken along horizontal and vertical directions through momentum space.

slice of momentum space in which one of the two bands is suppressed by a symmetry effect (Figure 4, right).

These effects can only be explained by some many-body interaction, namely the decay of the quasiparticles by plasmon emission. This is the first demonstration of such electron–plasmon coupling and is significant because such coupling might be a new pairing mechanism for the superconductivity observed in carbon nanotubes. It is also significant because strong electron–plasmon coupling is a prerequisite for applications in plasmonics, which is the technology of confining and controlling light on a length scale much smaller than the light's wavelength. This is a relatively new area and is expected to impact not only information technology and nanotechnology, but also biological and medical science.

What is remarkable about both these experiments is the high degree of momentum resolution achieved. The Fermi surface areas were less than a tenth of a percent of the Brillouin zone area, which means that the observed Fermi surfaces (e.g., Figure 4, left) are only about 1 degree wide. In order to say anything meaningful about the lifetime of states, it was necessary to have an angular resolution at least 10 times higher. It also required fine control of the sample motion: the polar scan shown in Figure 4 required scanning the polar angle (vertical direction in the figure) in steps of only 0.025 degrees.

INVESTIGATORS

A. Bostwick, T. Ohta, J.L. McChesney, and E. Rotenberg (ALS); K. Emtsev and T. Seyller (Universität Erlangen-Nürnberg, Germany); and Karsten Horn (Fritz Haber Institute, Germany).

PUBLICATIONS

T. Ohta et al., "Controlling the electronic structure of bilayer graphene," *Science* **313**, 951 (2006).

A. Bostwick et al., "Quasiparticle dynamics in graphene," *Nat. Phys.* **3**, 36 (2007).

MERLIN

Beamline 4.0.3, the meV-resolution beamline (MERLIN), is currently under construction at Sector 4 of the ALS. MERLIN is designed to have an unsurpassed energy resolution, on the order of 1 to 2 meV, for most of its operating energies from 10 to 150 eV. Besides high energy resolution, it will provide full polarization control to satisfy the experimental needs of ARPES and resonant inelastic x-ray scattering (RIXS) spectroscopies.

To provide full polarization control with reduced contamination from the high harmonics commonly seen in low-energy beamlines, the MERLIN undulator adopts a brand new quasi-periodic EPU (QEPU) design. It uses a 90-mm-period EPU to maximize flux/brightness. The periodicity is modified by properly shimming the magnetic blocks (Figure 5, top) to shift the anharmonic photon peaks to noninteger multiples of the fundamental; these high harmonics can be then be filtered out by the monochromator. The calculated flux of the 90-mm QEPU and regular EPU at 9-eV photon energy is shown in Figure 5. With the quasi-periodicity, the intensity at integer multiples of the fundamental is greatly reduced.

The MERLIN beamline layout is shown in Figure 6 It consists of two upstream mirrors, M301 and M302, which deflect the beam away from the storage ring and focus it vertically at the entrance slit and horizontally at the exit slit. The M302 pitch/yaw/roll mechanisms are motorized and can be used to establish a feedback loop with the zero-order monitor right after the grating to maintain the throughput at the entrance slit. These two mirrors also serve as a power filter to remove unwanted heat from high harmonics, preserving the figures of resolution-determining optics.

The monochromator is a variable-included-angle spherical grating monochromator, with one plane mir-

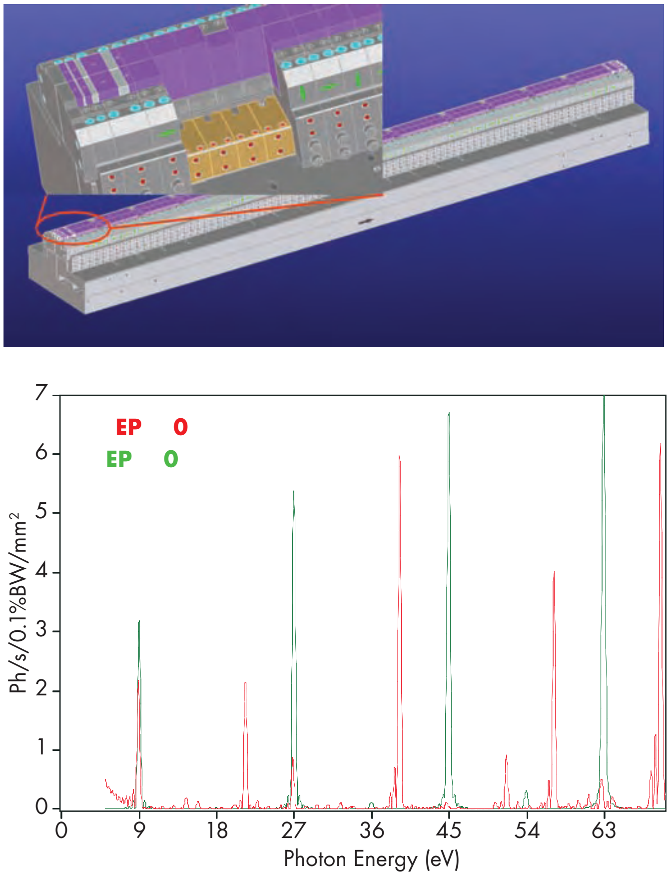

FIGURE 5. Top: Schematic showing the design of the QEPU. The quasi-periodicity is achieved by shimming the magnetic blocks. Bottom: Calculated performance of 90-mm QEPU (red) versus regular EPU (green).

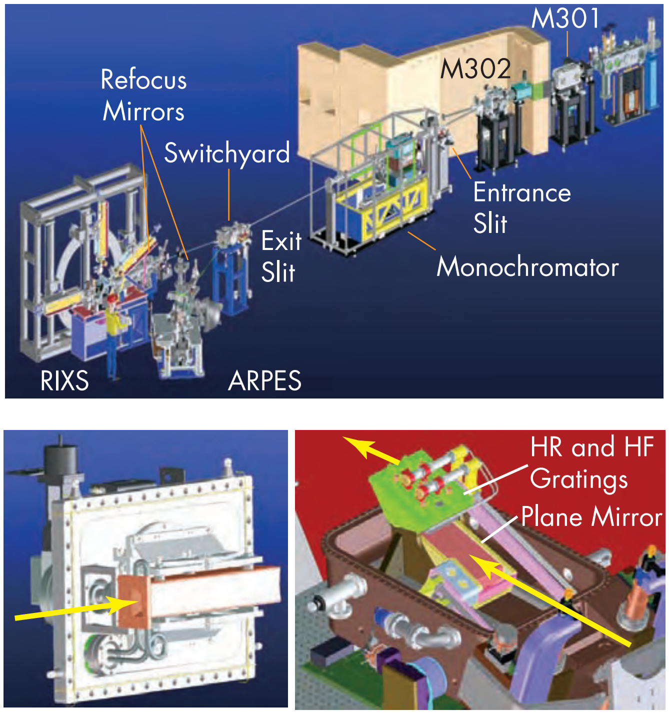

FIGURE 6. Top: Schematic plot of MERLIN beamline layout. Bottom left: Schematic plot showing the pitch/roll/yaw mechanism of M302. Bottom right: Schematic plot showing the internal structure of the monochromator. The beam direction is marked by yellow arrows.

ror and two sets of spherical gratings in a single tank. The mechanical drawing of the monochromator is shown in Figure 6 (mirror faces up and gratings face down). Selection of the grating is done by shuttling the monochromator tank transverse to the beam trajectory. The included angle of the gratings can be varied by changing the angle of the plane mirror. By combing this capability with the ability to translate the monochromator tank 1.30 m along the beam trajectory, the Rowland circle focusing condition can be satisfied for most of the photon energies without even moving the entrance and exit slits. This unique aspect preserves the throughput (tight focusing from M302) at the entrance slit and source image (the exit slit) of the downstream refocusing optics. Hence we are able to design the tight refocusing optics. The high-resolution gratings, with line densities of 900, 1800, and 3600 line/mm on a single substrate, will provide high energy resolution that lives up to the name of the beamline. To satisfy photon-hungry RIXS experiments with less demanding energy resolution, high-flux gratings with 1/3 the line densities can be used. With the options of selecting either high energy resolution or high photon flux, this beamline can meet different demands for ARPES and RIXS experiments.

After the exit slit, a wedge-shaped switchyard mirror is used to deflect the beam into the ARPES and RIXS branches. A refocus mirror set, with a fixed-radius Si mirror and a 17-4PH bendable mirror, will perform the refocusing. The Si mirror will deflect the beam vertically and sagittally focus the beam at the sample position. The 17-4PH mirror, with proper side profile designed to achieve the desired elliptical shape, will produce a nice Gaussian profile in the vertical direction, which is critical for an entrance-slitless RIXS spectrometer.

To achieve the best performance of the beamline, high-quality optics play

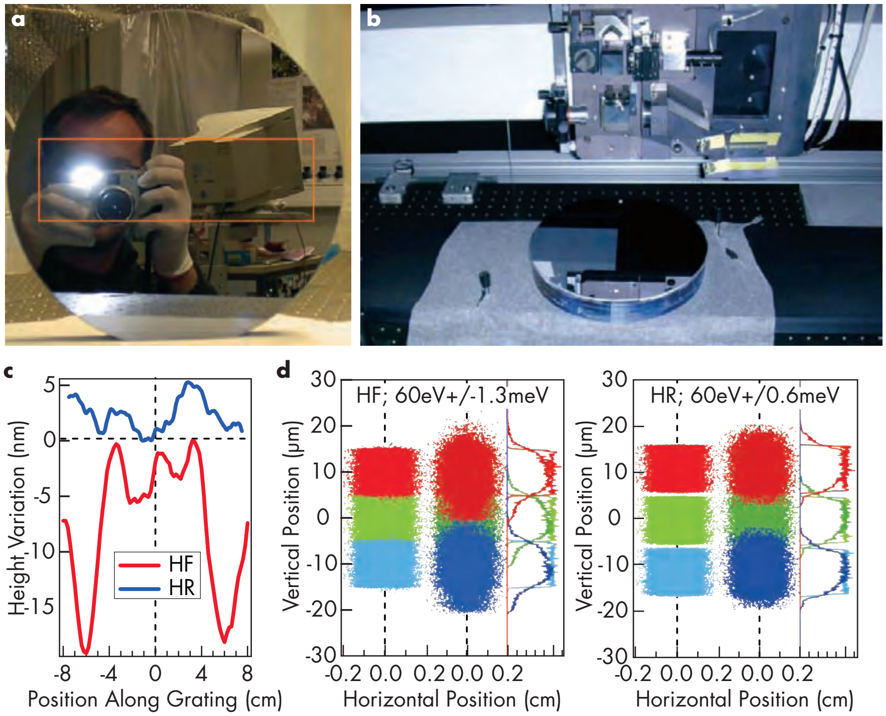

FIGURE 7. (a) Image of HR grating taken at the OML at BESSY II. (b) Image of HF grating substrate taken at the OML at the ALS. (c) Height variation of the substrates (from ideal sphere). (d) Ray-tracing program (SHADOW) simulation showing the beam image at the exit slit with 10-µm entrance slit setting. The energy difference is 1.3 meV for HF gratings and 0.6 meV for HR gratings. The central energy is 60 eV.

important roles. This is a very challenging demand for optics vendors. With extreme effort, we have acquired high-quality grating substrates for both high-resolution (HR) and high-flux (HF) gratings. The HR substrate was previously measured at the OML at BESSY II and the HF substrate was measured at the OML at the ALS. Images of the HR and HF grating substrates are shown in Figure 7. The measured rms slope error is around 0.25 µrad for the HR substrate and ~0.5 µrad for the HF substrate. The corresponding height variations (deviation from ideal sphere, in nm) along the central tangential line of both substrates are shown in Figure 7c. The height variation is very small, on the order of 10 nm for the HF substrate and better than 5 nm for the HR substrate. With height variation information, we are able to simulate the performance of these two gratings. Here we use the high-density rulings (1200 line/mm for HF and 3600 line/mm for HR) and the entrance slit is set to be 10 µm at 60 eV. The energy difference is 1.3 meV for HF and 0.6 meV for HR. As expected, for ideal gratings, a beautiful step-like image is observed at the exit location. Inclusion of the surface error will produce tails beside the step and the full width increases by 100% for the HF grating and 50% for the HR grating. Hence we will be expecting ~2.5-meV energy resolution for the HF grating and 0.9 meV for the HR grating at 60 eV, a conservative estimate (in fact, the FWHM shows minute change).

During the 2007 shutdown, front-end components, M301 and M302 mirror tanks will be installed. The monochromator assembly, entrance and exit slits will be installed before the end of 2007. By early 2008, the rest of the optics are expected to be installed and the commissioning process will start.

The lead engineer for the MERLIN project is N. Kelez, and the lead scientist is the beamline scientist, Y.-D. Chuang. J. Denlinger will be the second beamline scientist, responsible for photoemission activity at MERLIN starting in the fall of 2007. Other scientists actively involved in the project are Z. Hasan (Princeton University), A. Lanzara (MSD, Berkeley Lab), Z.-X. Shen (Stanford University) and Z. Hussain (ALS).

ULTRAHIGH-VACUUM (UHV) BENDABLE REFOCUS MIRRORS

A standardized design for UHV-compatible, elliptically bent refocus optics has been under development since 2003 for use at various ALS beamlines, including seven new refocus mirrors as part of an upgrade to the Beamline 8.0.1 optical layout. A key motivation for the new design is the desire for smaller refocus spots requiring higher demagnification configurations of one mirror (or one K-B pair) positioned close to each endstation as opposed to a single high-quality mirror pair servicing multiple endstations. The close proximity of the optics to the UHV endstation requires that the optics assembly and vessel also be UHV compatible. The increased total number of optical elements needed, each with different demagnification requirements, motivates the use of less-expensive mirror flats in a standardized bending mechanism for approximating a range of elliptical curvatures.

The mirror assembly design (Figure 8) features standard Conflat mounting flanges with 6- to 12-in. outer diameters (ODs), accommodating mirror lengths from 78 to 228 mm with a single standardized external feedthrough configuration for pitch and bending control. Two external linear drive feedthroughs (custom-designed for forces greater than 50 lb) actuate leaf-spring bending couples, and a single bellows accommodates pitch motion as well as an optional linear drive for lateral translation of the mirror into and out of the x-ray beam.

The need for mild baking of the optics assembly (< 100 °C) to achieve UHV pressures precluded the use of silicon mirror flats with glued end mounts. Instead, metallic substrates of nickel-coated Glidcop, polished to less than 5-Å rms roughness and < 1-μrad slope error (InSync, Inc.), were mounted to the bending flexures with a glueless end-clamping design.

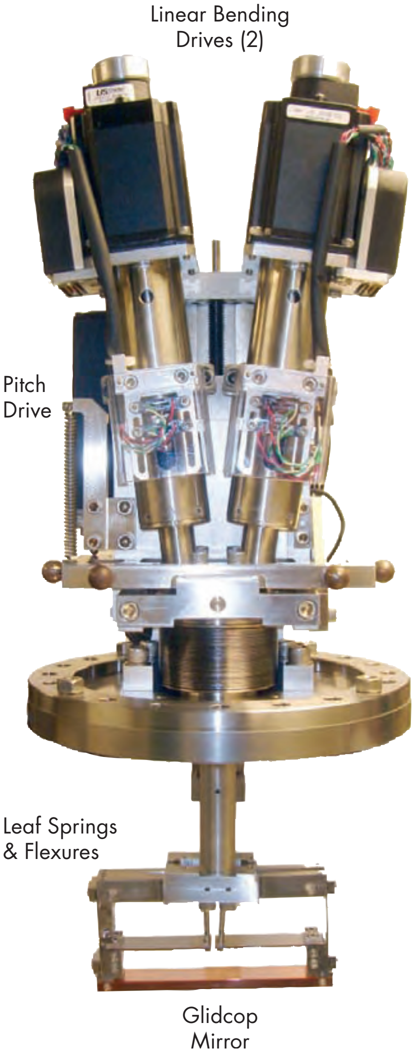

FIGURE 8. Bendable UHV refocus mirror design.

In the fall 2006 shutdown, two 12-in. OD Conflat mirror benders were installed in a horizontal switchyard tank (Figure 9) as the first phase in the Beamline 8.0.1 optical upgrade.

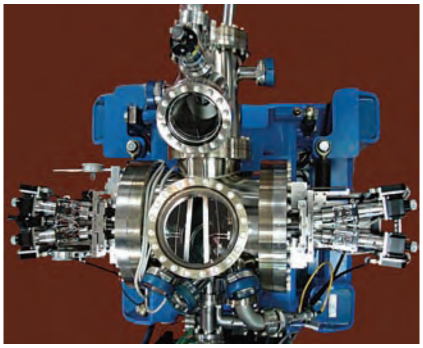

FIGURE 9. Horizontal mirror switchyard for Beamline 8.0.1.

The new switchyard provides more rapid changeover between two branchlines than the previous rotating air-platform, which was dismantled and retired after 10 years of service. In combination with an 8-in. OD Conflat vertical mirror bender mounted 0.5 m from the new NanoNEXAFS main chamber (see 2002 Activity Report, p. 90), a focal spot of 100 x 15 microns was delivered for use by a new entrance-slitless variable-line-spacing (VLS) grating x-ray emission spectrometer optimized for efficient detection of the C, N, and O K edges. The second-phase upgrade, planned for 2007, involves the installation of the remaining four 6-in. OD Conflat mirror benders directly in front of different endstations for optimal demagnification. In addition, the UHV bender standardized design has been adopted for use at other beamlines at the ALS.

ALS technical support included K. Franck (main UHV bender design engineer), T. Miller (high-force linear feedthrough design) and D. MacGill (bender assembly). The lead scientist is the beamline scientist, J. Denlinger, with help from W. Yang and J. Spear.

HIGH-EFFICIENCY X-RAY EMISSION SPECTROMETER

An advanced entrance-slitless VLS grating soft x-ray emission spectrometer project at the ALS, initiated in 2001, has produced multiple instruments for specific applications of RIXS at C, N, and O K edges and transition-metal $L_{2,3}$ and $M_{2,3}$ edges. The key components of the emission spectrograph (Figure 10) are a combination of a spherical focusing premirror, a VLS grating, and a back-illuminated CCD for detection of the dispersed soft x rays. To achieve high resolution, the spectrometer utilizes a CCD with small (13.5 micron) pixel size and, due to the entrance-slitless design, a finely focused x-ray beam spot in the dispersive direction (less than 30 microns). The combination of smaller focal spot, optimized grating blaze angles, and a high-quantum efficiency CCD detector gives a theoretical prediction of significantly enhanced detection efficiency compared to standard x-ray emission spectrograph designs.

The initial spectrograph prototype was funded through LDRD funds (Z. Hasan, Princeton University, and Z. Hussain, principal investigators), and subsequent spectrographs have been co-funded by particular research groups. The latest VLS spectrograph construction was designed by O. Fuchs and E. Umbach (University of Würzburg, Germany) in collaboration with L. Weinhardt and C. Heske (University of Nevada, Las Vegas). The design was optimized for the study of biologically relevant systems in a liquid-flow cell. Initial liquid-flow-cell experiments with the existing SXF endstation, as well as commissioning of the new VLS spectrometer, were performed at Beamline 8.0.1. In the new NanoNEXAFS endstation at Beamline 8.0.1, which features a new, high-demagnification UHV bendable refocus optic, a less than 20-micron vertical beam spot was achieved as the source point for the entrance-slitless VLS spectrometer.

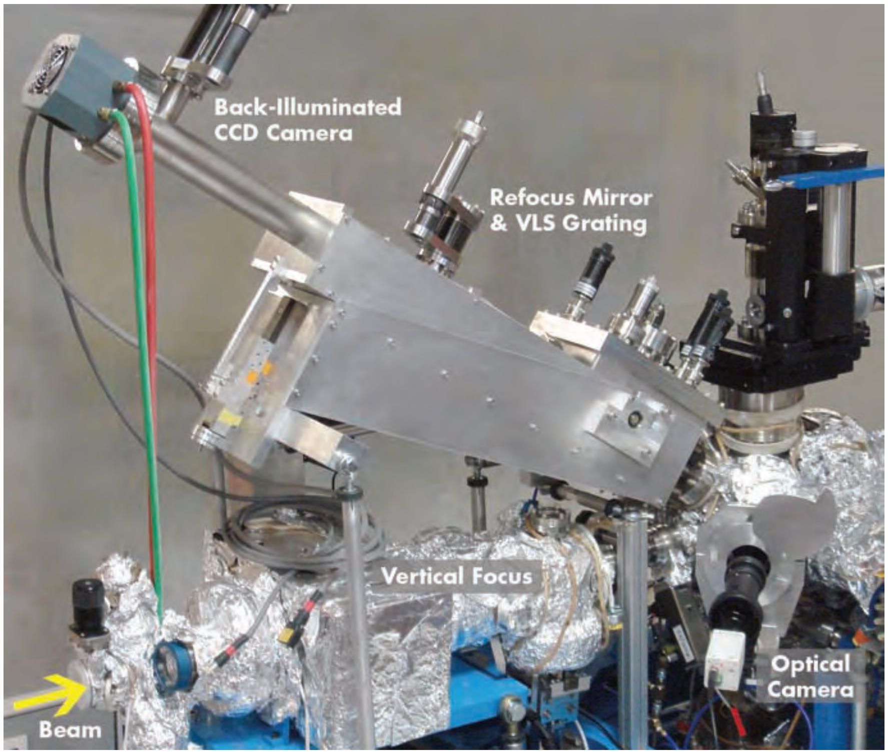

FIGURE 10. VLS grating spectrometer installed in the Beamline 8.0.1 NanoNEXAFS endstation.

Ray tracing and optical specification were performed by O. Fuchs with assistance by W. McKinney. CXRO assisted in fabrication, including mechanical design by P. Batson and grating efficiency measurements by E. Gullikson. The spectrograph, employing a single 600-line/mm VLS grating manufactured by Zeiss, was optimized for maximum efficiency and resolution in the energy range of 120 to 540 eV. It covers the sulfur L edge as well as the C, N, and O K edges for the investigation of liquids and organic systems. Since such a wide energy range cannot be satisfactorily covered with a single grating, the native energy range of the spectrometer is limited to 120 to 220 eV, while the higher energies up to 540 eV are detected in the second, third, and even fourth diffraction order. An overall efficiency gain of approximately 10x (for S, N, and O) and up to 150x (for C) was found in comparison to the existing SXF spectrometer at Beamline 8.0.1 for an equivalent resolving power of $E/\Delta E = 1000$.

The increased efficiency (and thus rapid data acquisition) changes the experimental paradigm from the measurement of a limited selection of excitation energies at a particular absorption edge to the acquisition of a complete RIXS map with a uniform small step size for all edges of interest. Such map images (Figure 11) can reveal a much richer structure of effects. In addition, with dwell times of a few seconds, time-dependent beam-damage studies are more feasible, albeit with a trade-off for the more concentrated beam spot. Also, the large energy-detection window (including the higher orders) allows the VLS spectrograph to simultaneously monitor relative intensities of a wide range of elements in a manner reminiscent of higher energy-dispersive SiLi for Ge detectors.

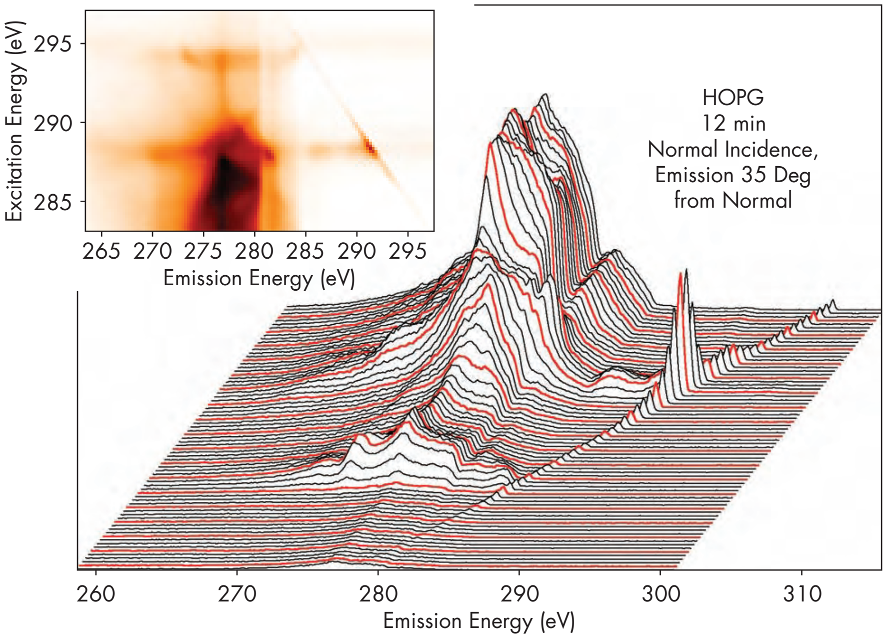

FIGURE 11. Example of an x-ray emission map for highly ordered pyrolytic graphite (HOPG) using the VLS spectrograph at Beamline 8.0.1.

SPIN-TOF: TIME-OF-FLIGHT ANALYZER FOR SPIN-RESOLVED ARPES

Despite the large amount of activity and discoveries in the field of ARPES, propelled by enormous progress in instrumentation in the past decades, rapid growth in spin-resolved ARPES has remained largely elusive due to the major difficulties of measuring electron spin. Recent explosions of interest in complex magnetic systems in particular have made this powerful technique even more compelling. The ALS formed a diverse interdisciplinary collaboration spread through Berkeley Lab and the UC Berkeley campus to develop an entirely new time-of-flight (TOF)-based instrument for highly efficient spin-resolved ARPES.

The ARPES technique was revolutionized by the development of the two-dimensional electrostatic hemispherical analyzer used throughout the ALS and the world. It allows efficient simultaneous collection of data in two dimensions (electron kinetic energy and emission angle along one direction) with high resolution. State-of-the art spin detectors (so-called "mini-Mott detectors"), however, are single-channel instruments based on the spin–orbit-induced spin-dependent scattering of relativistic electrons from a gold-foil target. This spin-resolving measurement itself involves a large loss in count rates, mainly due to the small cross sections at the greater than 20-keV kinetic energies required. When coupled to a standard hemispherical analyzer, a time-consuming zero-dimensional analyzer results.

The TOF spin-resolved ARPES project attacks these problems with a double-edged sword. First, the spin-detection element is completely redesigned to be based on low-kinetic-energy exchange scattering from a magnetic target, similar to Bertacco et al. (Ref. 1). As opposed to the relativistic Mott detectors, photoelectrons are retarded to less than 10 eV and back-scattered from a ferromagnetic target with approximately two orders

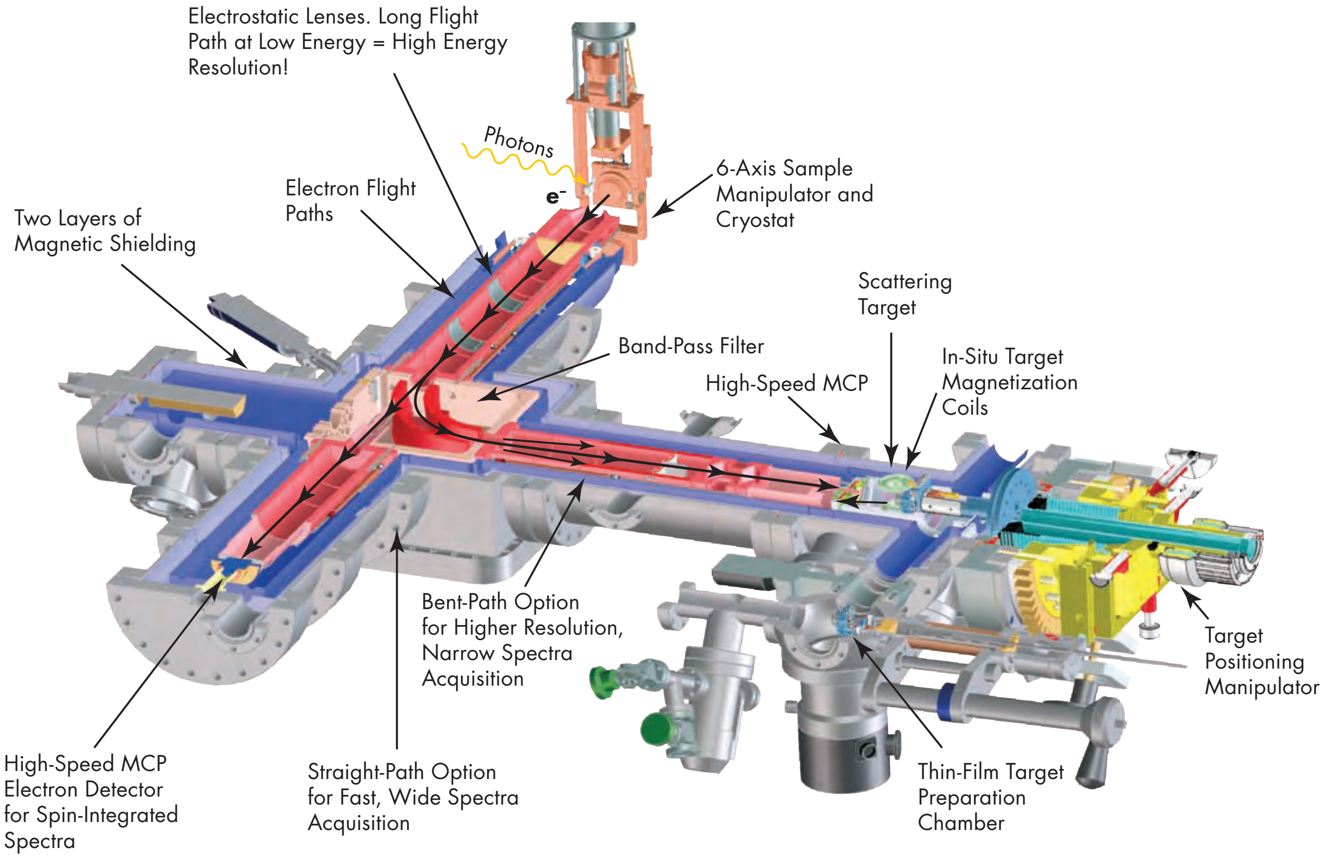

FIGURE 12. Layout of the spin-TOF instrument including electrostatic lens system, exchange scattering spin detector, magnetic shielding, and vacuum chamber.

of magnitude increased reflectivity. The reflectivity is spin dependent, and flipping the magnetization of the scattering target allows efficient spin resolution of incident photoelectrons. In contrast to Bertacco, our design is based on thin-film targets that have negligible stray fields. We have characterized the spin-resolving power of such thin-film targets using the spin-polarized low-energy electron microscope (SPLEEM) at the Berkeley Lab's National Center for Electron Microscopy (NCEM) and found that we could indeed achieve efficiencies 100 times higher than the best mini-Mott detectors (Ref. 2).

Secondly, instead of being based on the ubiquitous hemispherical analyzer, the energy analyzing element is based on the TOF technique. Taking advantage of the inherent pulsed nature of the ALS and the growing number of ultraviolet lasers, the instrument resolves photoelectron energy by precise measurement of the time between an incident light pulse and the arrival of a photoelectron at the final high-speed multichannel-plate (MCP) detector. We have designed from scratch a complete electrostatic lens system for collecting photoelectrons and guiding them to the final detectors at desired drift energies with high efficiency and energy resolution. Because photoelectron energy is detected through temporal dispersion, when our TOF lens system is coupled to a single *spatial* channel (multi-*temporal* channel) spin detector, an efficient one-dimensional analyzer results.

A schematic view of the full TOF instrument including the spin detector is shown in Figure 12. Figure 13 shows a photo of the recently assembled TOF lens system (without spin detector), including a long input column, two shorter exit columns, and a 90-degree band-pass filter to couple the entrance and second exit columns. A single-column prototype was previ-

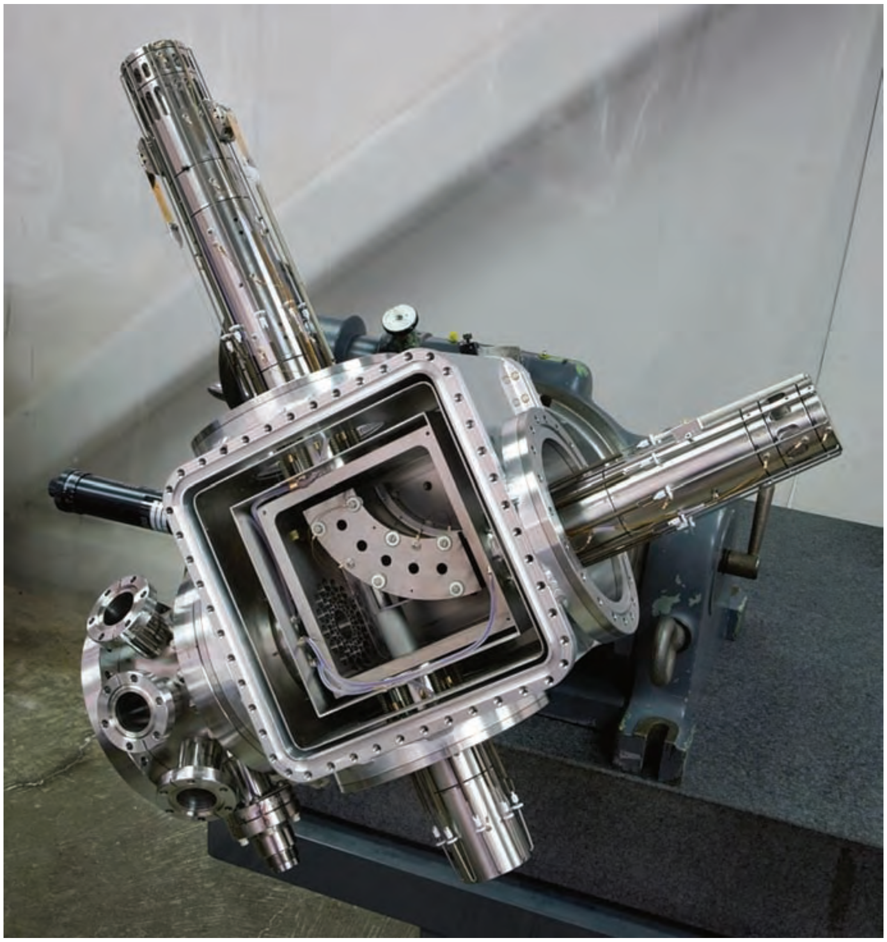

FIGURE 13. View of the assembled TOF electrostatic lens system.

ously built and tested at Beamline 12.0.1 to evaluate the TOF technique without spin resolution during a two-bunch run. Polycrystalline gold spectra were successfully taken, showing instrumental energy resolutions nearing 10 meV, which will be further improved in the final instrument.

Coupled together, the final spin-resolved TOF analyzer will be able to perform spin-resolved ARPES experiments with at least 100 times the efficiency of current state-of-the-art instruments, making way for a large leap in the field. Electronics and software for the final device, including the spin detector, are currently being completed. A 6-eV laser is presently coming on-line and will be extensively used with the spin-resolved TOF analyzer between two-bunch runs at the ALS.

This effort is a collaboration between the ALS (Z. Hussain and G. Lebedev) and MSD (A. Lanzara), forming the Ph.D. project of C. Jozwiak (UC Berkeley). Other collaborators include N. Andresen and J. Pepper (Engineering), J. Graf and A. Schmid (MSD), and A. Belkacem (CSD).

REFERENCES

1. R. Bertacco, D. Onofrio, and F. Ciccacci, *Rev. Sci. Instr.* 70, 3572 (1999).

2. J. Graf, C. Jozwiak, A.K. Schmid, Z. Hussain, and A. Lanzara, *Phys. Rev. B* 71, 144429 (2005).

NANOSCALE METAMATERIALS

Recently, artificial metamaterials have been reported to have a *negative* index of refraction (Ref. 1), which allows a flat slab of the material to behave as a "perfect" lens (Ref. 2), possibly even creating subdiffraction-limited focusing. These novel materials have numerous potential applications (Ref. 3), especially if their behavior can be extended to the near-infrared and visible region. The first steps toward scaling the dimensions of these metamaterials have recently been taken with the fabrication of structures showing magnetic resonances at about 1 THz (Refs. 4–5) and 100 THz (Ref. 6).

The primary goal of this LDRD-funded project is to create fully left-handed nanoscale metamaterials with features small enough to resonate in the near-infrared by taking advantage of Berkeley Lab's nanofabrication expertise within the CXRO and infrared spectromicroscopy capabilities of the ALS's infrared Beamlines 1.4.2, 1.4.3, and 1.4.4. An example of an array of double split-ring resonator (DSSR) structures with scaled line widths and lattice spacing dimensions are shown in Figure 14. Each test structure has feature widths between 20 and 100 nm and is written in a pattern covering a 100-square-micron SiN window, with 2-mm spacing to the next test sample.

FTIR spectromicroscopy measurements were performed in transmission and reflection geometries as a function of incident angle and polarization angle. Examples of mid- and near-infrared transmission data with the light polarization along y and an angle of incidence of θ = 30° are shown in Figure 15. Strong resonant absorptions are observed consistent with a negative magnetic permeability.

Ongoing work continues to explore various split-ring resonator sample geometries, lattice spacings, and materials to optimize performance at high frequency. We aim to achieve full negative index of refraction structures at

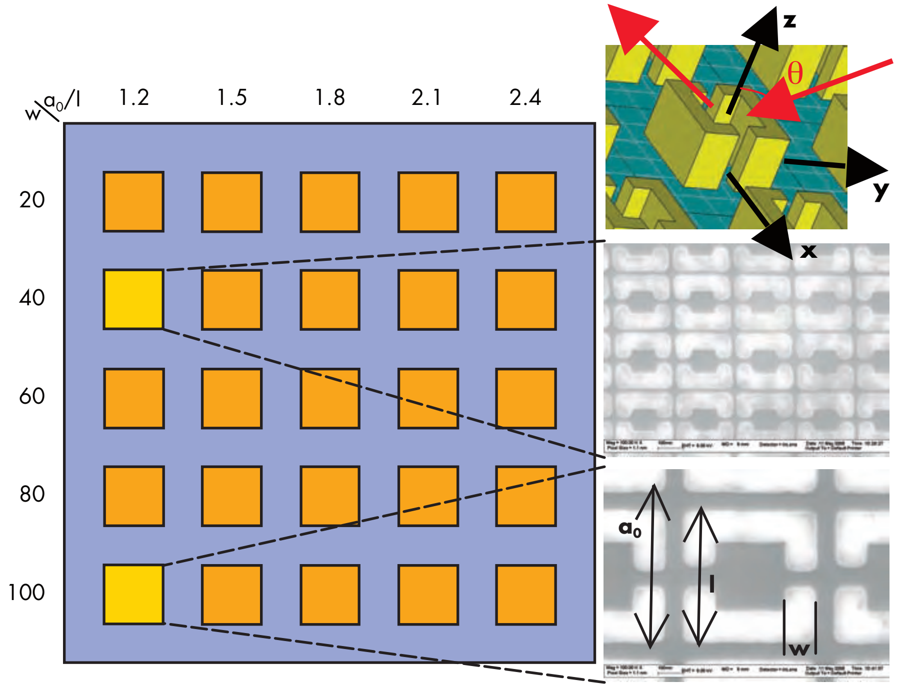

FIGURE 14. A nanofabricated array of DSSR metamaterials having varying line widths (w) from 20 to 100 nm and varying lattice spacing (a_0) relative to the unit cell size (l). At right are two example SEM photos and the optical measurement axes related to the DSRR structures.

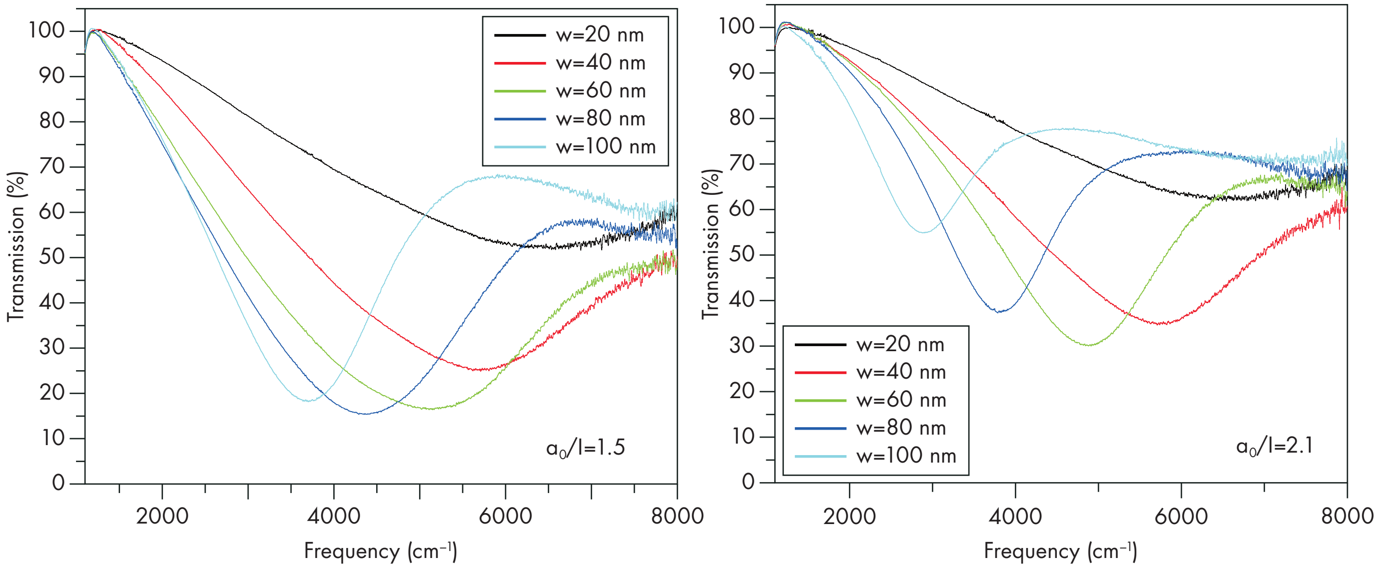

FIGURE 15. Infrared transmission results showing a strong absorption peak that shifts in frequency with feature size and scales in intensity with lattice spacing.

optical wavelengths. This research was performed by Z. Hao and M.C. Martin (ALS), B. Harteneck and S. Cabrini (MSD), and A. Liddle and E. Anderson (CXRO).

REFERENCES

1. D.R. Smith, W.J. Padilla, D.C. Vier, S.C. Nemat-Nasser, and S. Schultz, *Phys. Rev. Lett.* **84,** 4184 (2000); R.A. Shelby, D.R. Smith, and S. Schultz, *Science* **292,** 77 (2001); J. Pendry, *Nature* **423,** 22 (2003); A.A. Houck, J.B. Brock, and I.L. Chuang, *Phys. Rev. Lett.* **90,** 137401 (2003); C.G. Parazzoli, R.B. Greegor, K. Li, B.E.C. Koltenbah, and M. Tanielian, *Phys. Rev. Lett.* **90,** 107401 (2003).

2. J.B. Pendry, *Phys. Rev. Lett.* **85,** 3966 (2000).

3. M.C.K. Wiltshire, J.B. Pendry, I.R. Young, D.J. Larkman, D.J. Gilderdale, and J.V. Hajnal, *Science* **291,** 849 (2001).

4. T.J. Yen, W.J. Padilla, N. Fang, D.C. Vier, D.R. Smith, J.B. Pendry, D.N. Basov, and X. Zhang, *Science* **303,** 1494 (2004).

5. M.C. Martin, Z. Hao, A. Liddle, E.H. Anderson, W.J. Padilla, D. Schurig, and D.R. Smith, *Proceedings of the Joint 30th International Conference on Infrared and Millimeter Waves and 13th International Conference on Terahertz Electronics* (IRMMW-THz2005).

6. S. Linden, C. Enkrich, M. Wegener, J. Zhou, T. Koschny, and C.M. Soukoulis, *Science* **306,** 1351 (2004).

UPGRADES AT THE PHOTOEMISSION BRANCH OF BEAMLINE 12.0.1

The high-resolution angle-resolved photoemission (HARP) station at Beamline 12.0.1 has become an instrument very popular among research groups studying strong electron correlations in complex materials by means of photoelectron spectroscopy. Within the past three years, data taken at the beamline have made their way into eleven papers in *Physical Review Letters*, three in *Nature*, and one in *Science*. The electron spectrometer endlessly pumping out these data is a Gammadata-Scienta SES 100. Since its development circa 1999, the company has taken steps toward improving the throughput of its analyzers. The latest product is the R3000 spectrometer, which shares the basic layout of the SES 100 but is capable of collecting data in an angular window almost four times greater. Upgrading our SES 100 to the new R3000 is a logical (and easy) step toward increasing the productivity of the beamline. The ALS has placed an order for one new spectrometer, and delivery will occur before the fall of 2007. We anticipate completion of the installation and commissioning by the following December.

The performance of the beamline itself was improved by installing two new gratings. The 200-line/mm grating is optimized for low photon energies (~20–40 eV) while the 1200-line/mm grating will have a good efficiency above ~200 eV. The latter grating will be also be used for experiments requiring high energy resolution above ~100 eV, where the resolving power of the existing gratings rapidly deteriorates. Figure 16 displays the measured efficiencies of both new gratings. The lead scientist for this project is A. Fedorov.

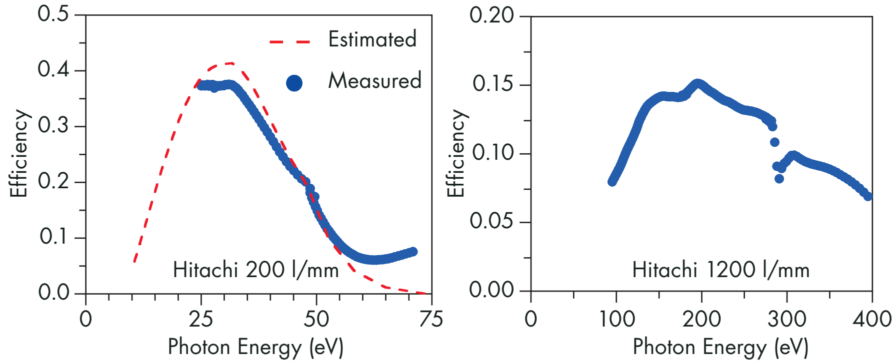

FIGURE 16. Measured efficiencies of new gratings (200 l/mm and 1200 l/mm) for Beamline 12.0.1.

FAST-SWITCHING SUPERCONDUCTING MAGNETS FOR SPECTROSCOPY

It is the goal of this LDRD project to develop the core technology for a superconducting magnet providing a peak field of about 5 T with arbitrary field orientation and capable of full field reversal in approximately 5 s. Magnetic fields of this magnitude are needed to align the magnetic moments along the hard magnetization directions in many novel materials such as molecular magnets, magnetic nanoclusters, ferromagnetic semiconductors, functional oxides, etc. Arbitrary field directions will allow us to take full advantage of the strengths of combined soft x-ray magnetic linear and circular dichroism measurements. Rapid field ramping suitable for point-by-point field reversal in spectroscopy experiments will provide much improved sensitivity, enabling new insights into the properties of magnetic nanostructures impossible today.

Based on a detailed magnetic analysis to determine a) the impact of conductor specifications on device performance, b) optimal geometric design parameters, and c) the impact of cryogenic design/capacity on device performance, a prototype magnet will be fabricated. The thorough experimental evaluation of the pole will test our model calculations, both in terms of peak operating field and allowable switching rate. The design of the full eight-pole system (Figure 17) will be optimized to account for the results of the prototype testing. The lead scientists for this project are E. Arenholz (ALS) and Soren Prestemon (Engineering).

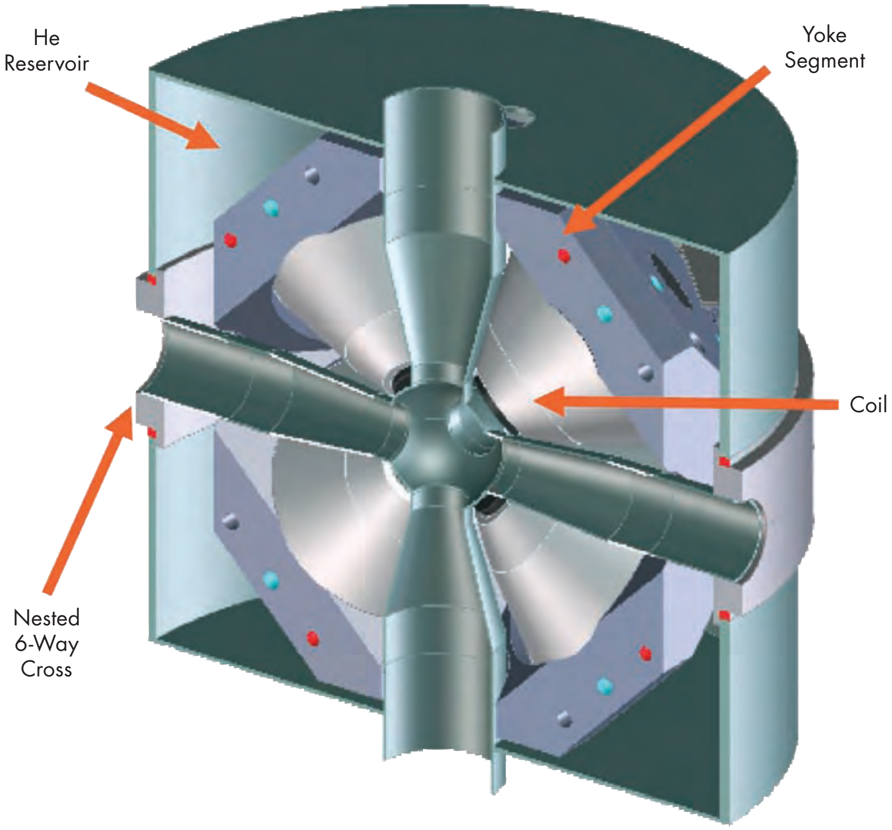

FIGURE 17. Design sketch of 6-T eight-pole magnet.

IN SITU PHOTON-IN/PHOTON-OUT SOFT-X-RAY SPECTROSCOPY AT BEAMLINE 7.0.1

ATMOSPHERIC CORROSION OF METAL FILMS

Atmospheric corrosion, taking place between metal surfaces and the surrounding atmosphere, is ubiquitous and generates enormous costs for society (several percent of the gross national product in industrialized countries). It affects areas such as information technology, communication technology, national defense, and cultural heritage. Therefore, it is highly desirable to find ways to avoid and reduce atmospheric corrosion, which involves chemical, electrochemical, and physical processes in three phases (solid, liquid, and gas) and two interfaces (solid–liquid and liquid–gas).

A user group from Uppsala, Sweden, led by L. Duda and J. Nordgren, has constructed a versatile chamber, an "atmospheric corrosion cell," for soft x-ray absorption/emission spectroscopy of metal surfaces in a corrosive atmosphere, allowing novel in situ electronic structure studies. An experiment, conducted on Beamline 7.0.1 by J. Forsberg, A. Olsson, T. Schmitt, and J. Andersson, has provided initial results on the corrosion of iron and copper surfaces in humidified synthetic air.

A small, thin membrane (typically 0.25 x 1 mm^2 in area and 100 nm thick) of silicon nitride or carbon separates the vacuum of the analysis chamber from the reaction-cell environment (Figure 18). The membrane allows both the incoming and scattered soft x rays to pass through, making it possible to irradiate the sample film and record an emission spectrum. These membranes have been tested for pressure differences of up to a few atmospheres, depending on material, geometry, and area. A quartz crystal microbalance (QCM) is covered by a film of the metal to be studied, in this case iron, deposited by evaporation. NaCl is deposited on the surface of the film, to act as a corrosion-accelerating agent. This is typically done by dissolving the salt in ethanol and applying a small drop of the solution on the surface.

The frequency curve flattens out toward the end of the sequence, indicating that most of the iron film is corroded. The total change in frequency is 3000 Hz, which corresponds to a mass change of approximately 13 µg/cm^2. This is consistent with an increase in mass corresponding to complete corrosion of an approximately 100-nm-thick iron film into FeOOH.

Soft x-ray measurements were conducted at the beginning and end of the process. Figure 19 displays iron L-edge absorption and emission data from the iron film made before the corrosion (blue) and after several hours of corrosion (red). A distinct energy shift is observed in the iron L-absorption spectra (inset), in agreement with expectations that the onset of iron L absorption will be shifted to

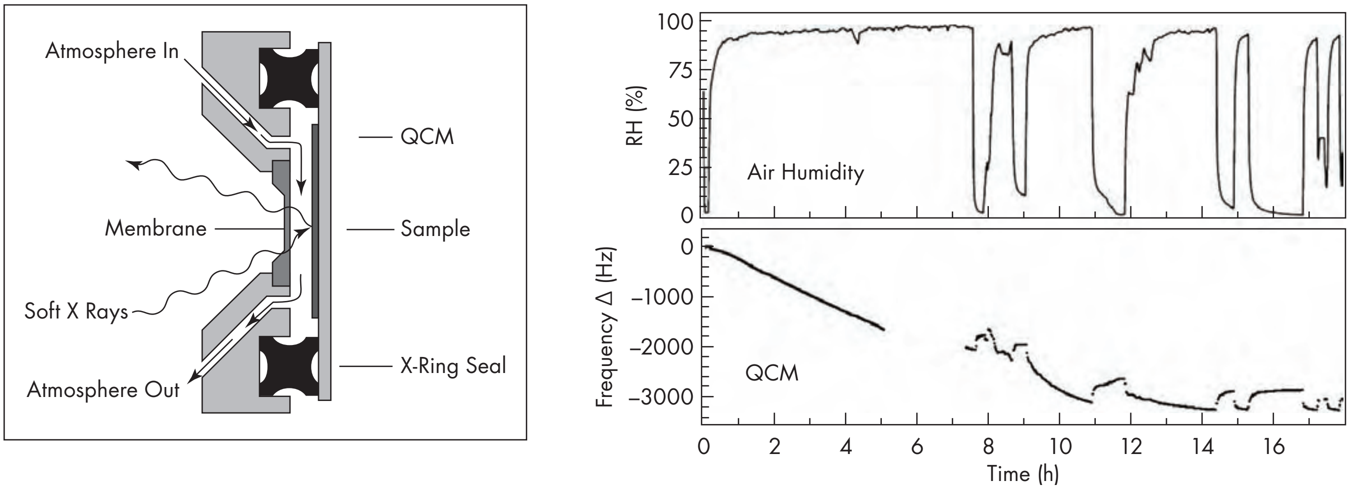

FIGURE 18. Left: Conceptual sketch of the atmospheric corrosion cell. Right: Atmospheric corrosion of an iron film with NaCl, monitored by QCM frequency (a measurement of small changes in mass) and humidity sensors. QCM frequency is displayed as difference from start value.

higher energies in oxidized iron due to a chemical shift. The iron L-emission spectra, taken at several different excitation energies, show even stronger contrast between the two stages. It is clear that the surface of the iron film has gone through a chemical change.

HYDROGEN ADSORPTION

Hydrogen storage is the most challenging task for a potential hydrogen economy. Solid-state hydrogen storage by chemisorption and/or physisorption is attractive from a technology point of view, but it has encountered tremendous challenges in terms of storage capacity and kinetics. Our goal is to study the electronic properties of hydrogen storage materials to gain insight into hydrogen adsorption in metal and complex hydrides, doping- and defect-induced hydrogen adsorption/desorption, combined chemisorption and physisorption mechanisms for hydrogen storage using metastable nanoporous hydride materials and carbon nanostructures, and new classes of hydrogen storage materials—for example, metal-organic frameworks (MOFs). The challenge is to get the hydrogen adsorption binding energy within the desirable range of 20–60 kJ/mol, which would increase hydrogen uptake on MOF and carbon-based materials at higher temperatures (closer to room temperature) and increase hydrogen release from chemical hydrides at lower temperatures (also, closer to room temperature).

Interesting candidates for the dense storage of hydrogen include different types of carbon-based nanomaterials: single-walled carbon nanotubes (SWNTs), multiwalled carbon nanotubes, and graphene layers. SWNTs for hydrogen storage has become the subject of active research. Different mechanisms for the interaction of H_2 and SWNTs have been reported. HOPG has similarities with the carbon systems mentioned above. Photon-in/photon-out soft x-ray spectroscopies are well suited for measurements of the electronic structure of these materials under ambient hydrogen pressure. XAS and XES measurements have been performed on SWNTs and HOPG under different hydrogen pressures (Figure 20). The lead scientist for this project is J. Guo.

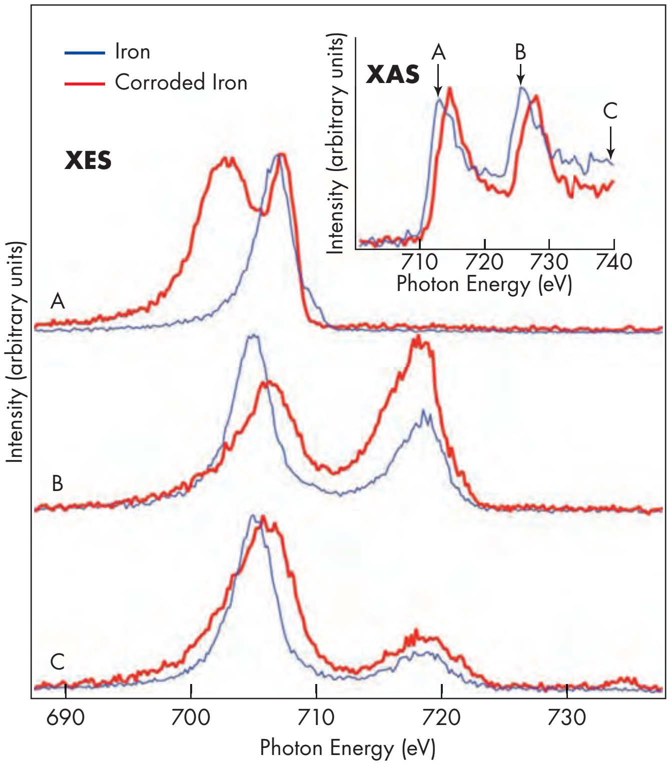

FIGURE 19. L-edge x-ray absorption (XAS, inset) and emission (XES) spectra taken at different excitation energies.

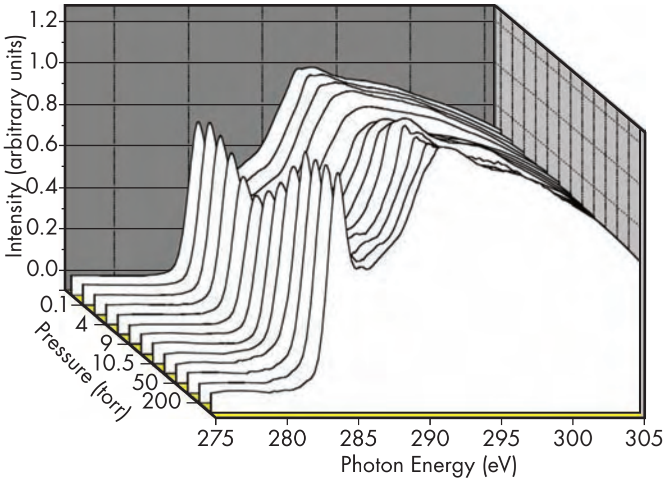

FIGURE 20. Carbon K-edge absorption spectra recorded at different hydrogen pressures.

PORTABLE UHV "MINIATURE" STXM

The ALS-designed scanning transmission x-ray microscopes (STXMs) at Beamlines 5.3.2 and 11.0.2 have been very successful in enabling the research of many users. These microscopes have seen full operational functionality for over four years. They are very versatile, user-friendly instruments and exhibit the best performance for their class of microscopes. Other synchrotron light sources are now adopting this proven laser-controlled configuration to achieve the same high performance.

The high demand for the ALS STXMs as well as the need for new functionality provided the impetus for a new and innovative microscope. To achieve this aim and enable the pursuit of further novel and interesting research, a number of new designs have been evaluated and tested. The foremost goal is to achieve a UHV-compatible, high-precision, and high-stability instrument that can be readily adapted to different beamlines. This can be accomplished by the use of innovative "nanocube" stages from nanoCube Systems.

The existing STXMs have a large footprint and are positioned on a 700-kg polymer concrete block for vibration isolation. The new "miniSTXM" has a 6-cm^2 footprint and can be readily inserted into a UHV chamber (Figure 21). With accessible ports, one can readily adapt to additional configurations, such as those required for magnetic domain and lab-on-a-chip studies.

The compact design of this microscope allows it to be portable. It could be placed on any beamline that delivers x rays with energies ranging from 100 eV to 3 keV and beam sizes of 200 to 1500 µm^2. A portable optical table provides the necessary vibration isolation as well as a platform for precise adjustment to the photon beam. The positional registry of less than 40 nm with respect to the orthogonal requirements of the photon beam (z), sample (x,y) and zone-plate (z) stages is assured by using differential interferometers working in a feedback loop to control the piezo scanners within the attocubes. Figure 22 shows a 25-nm raster scan of the sample. The vibrations are on the order of 1 nm (rms). High precision, low vibrations, UHV compatibility, and portability should make this microscope a valuable addition to the already wide selection of x-ray microscopes at the ALS. T. Tyliszczak and D. Kilcoyne (ALS) and D. Shuh (CSD) are finalizing construction of this new miniSTXM. The lead scientist for this project is T. Tyliszczak.

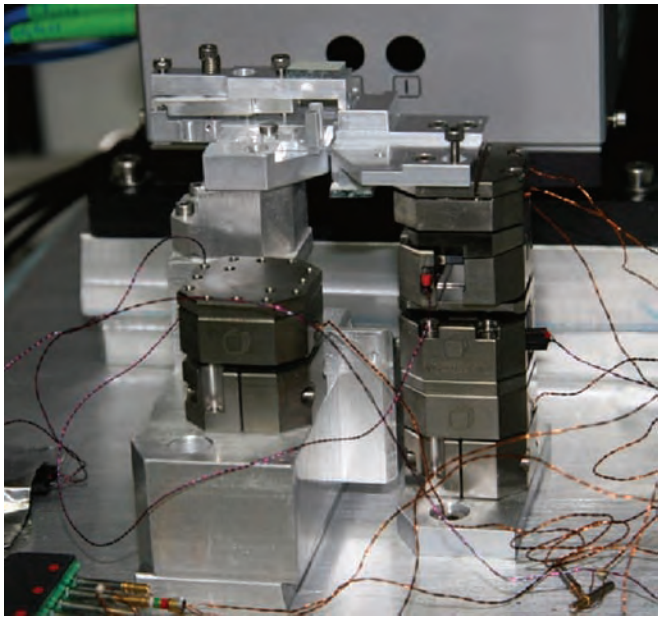

FIGURE 21. Test assembly of the new miniSTXM.

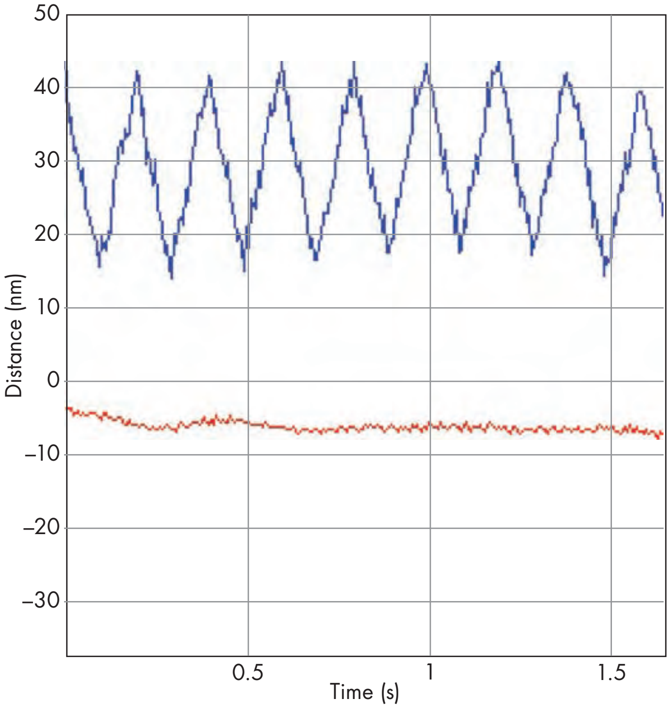

FIGURE 22. Sample (blue) and zone plate (red) position during a 25-nm test scan of the sample stages.

User Services

The User Services Group mission is to provide a friendly and efficient interface to the ALS focusing on safety for users and visitors. The group is made up of four sections: the User Services Office, Experimental Setup Coordination, Material Management, and Communications. These groups work together to provide users with a wide range of services.

USER SERVICES OFFICE

FIGURE 1. Clockwise from top: Jeff Troutman, Olga Poblete, Sharon Fujimura, Carmen Escobar, and Ken Winters.

The goal of the User Services Office is to provide a seamless interface between the user and the ALS and Berkeley Lab while ensuring the highest safety standards. The User Services Office is managed by Jeff Troutman and includes Carmen Escobar, Sharon Fujimura, Olga Poblete, Ken Winters, and Valerie Wysinger (Figure 1). This six-member team offers the following administrative services to the users:

- Proposals and beam time allocation: General sciences user proposals are administered by the User Services Office twice a year. The Office also administers the protein crystallography proposals, with reviews on a bimonthly basis. Carmen Escobar is the administrative contact for proposals; she also administers the beam time allocation and notification processes.
- Users' Meetings and Conferences: Carmen is the lead for the annual ALS Users' Meeting, with support from the rest of the office.
- Guest Processing: When users first come to the ALS, they are greeted in the mezzanine by Sharon Fujimura or Olga Poblete. They provide users with assistance in registration, badging, and basic safety training. Olga also helps users through the parking permit process.
- Apartments: Ken Winters is in charge of the ALS apartments as well as the publications database.
- Travel and Stipends: Valerie Wysinger is in charge of stipends, invitation letters for visas, and office space assignments.
- Administrative workforce management and planning for the User Services Office is the responsibility of Jeff Troutman. He also works on developing long-term running schedules, planning for UEC meetings, and DOE BES reporting.

In addition, the User Services Office administers critical databases in which users record their experiments and publications:

- End-of-Run Reports: Upon completion of every experiment, every experimenter must complete an end-of-run report.
- Publications: In addition, all publications resulting from experiments or work done at the ALS are recorded by the User Services Office for the DOE, after the user adds his or her publication to the database.

The ALS User Services Office, located in the mezzanine of Building 6 (Room 2212), is open from 8 A.M. to noon and 1 to 5 P.M. Stop by, or contact them by phone (510-486-7745) or email (alsuser@lbl.gov). Other user resources include the online User Guide (http://www-als.lbl.gov/als/ quickguide/).

EXPERIMENTAL SETUP COORDINATION

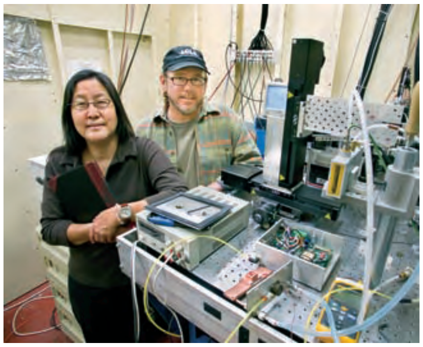

FIGURE 2. Donna Hamamoto and David Malone.

The Experimental Setup Coordination group consists of Donna Hamamoto and David Malone (Figure 2). They make early contact with experimenters to confirm the samples and hardware for each experiment, coordinate Experiment Safety Sheet inspections for new and returning experiments, and serve as the main point of contact for experiment-related needs. The group also provides assistance with the setup of toxic gases, ALS Chemistry Lab access, and waste disposal. Users should contact Donna (DJHamamoto@lbl.gov) or David (DJMalone@lbl.gov) anytime regarding the addition of new samples, equipment, and people to their experiments.

MATERIAL MANAGEMENT

The Material Management group is managed by Gary Giangrasso and includes Todd Anderson, Derrick Crofoot, and Jason De Ponte (Figure 3). This section provides shipping, receiving, gas-bottle ordering, refilling and servicing of liquid nitrogen dewars, temporary storage, endstation setup services, and movement/asembly of office and lab equipment. The group maintains a stockroom of parts and equipment, including safety devices, commonly needed by ALS users and technicians (Figure 4). Stockroom supplies are accessible by key card 24 hours a day. Another service provided is the generation of purchase requisitions for ALS

FIGURE 3. Todd Anderson, Jason De Ponte, Derrick Crofoot, and Gary Giangrasso.

staff and users requesting new supplies and equipment. Also, new barcode system has been implemented for tracking chemicals that arrive at the ALS on a daily basis.

Material management is also in charge of property management for ALS Division. ALS now has implemented a new property management office adjacent to the warehouse to handle property issues and questions in regards to custodian and location changes for DOE assets. Also generated at the new office are property passes for laptop computers and equipment that will be taken off site for business travel or home use.

FIGURE 4. Commonly needed parts and equipment are kept in a user stock room available 24 hours a day by key card.

COMMUNICATIONS

Led by Liz Moxon, the Communications group includes Julie McCullough, Art Robinson, Lori Tamura, and Greg Vierra (Figure 5). This group is responsible for communicating about the science, people, and events of the ALS user community to scientists of all disciplines, students, teachers, the local community, Berkeley Lab staff, members of Congress, DOE program managers, and people who just love science. If you have recently published in a high-profile journal, need a cover, have a newsworthy item for ALSNews, lightsources.org, or a Lab press release, contact us at alscommunications@lbl.gov.

Here's how we get the word out:

- ALS Science Highlights: We work with users to create profiles of research conducted at the ALS. These highlights are presented in several ways: through the Activity Report, ALSNews, the ALS Web site, posters, and the ALS Science Bulletin, which is emailed to the stakeholders at the DOE and other government agencies.
- ALSNews: This Web-based monthly e-newsletter turns the spotlight on what's going on around the facility (beamline upgrades, user services, safety updates), in the news (budget updates), and within the user community (awards and recognition).
- ALS Web Site: We provide the latest information for users and staff on ALS scientific meetings, conferences, and events.
- Annual Activity Report: This tangible record is where we formally document our high-profile research, equipment and facility developments, and special events.
- Posters, Displays, Technical Illustrations, and Graphic Design: A picture can be worth a thousand words. We work with the researchers to create original illustrations and revise and enhance existing ones. We provide art for print and Web media, user events, conferences, and open houses.
- Educational Outreach: We provide tours and hands-on demonstrations for students and the general public.

FIGURE 5. Clockwise from top: Lori Tamura, Art Robinson, Greg Vierra, Julie McCullough, and Liz Moxon.

USER DEMOGRAPHICS IN 2006

The User Services Group collects user demographics and publication information, available in this Activity Report as well as online (http://www-als.lbl.gov/als/publications/). As a national user facility, the ALS is required to report these statistics annually to the U.S. DOE. The ALS continued to grow rapidly in 2006. Figure 6 shows the growth in particular scientific fields and the overall user growth from 1998–2006. The breakdown of different types of institutions that make up our user base is shown in Figure 7. The growth of the user community over the past 10 years is mirrored by the growth in beamlines and publications, as shown in Figure 8. As the number of beamlines approaches the capacity of the storage ring, new beamlines will be created by chicaning straight sections and revamping some of the older bend-magnet beamlines.

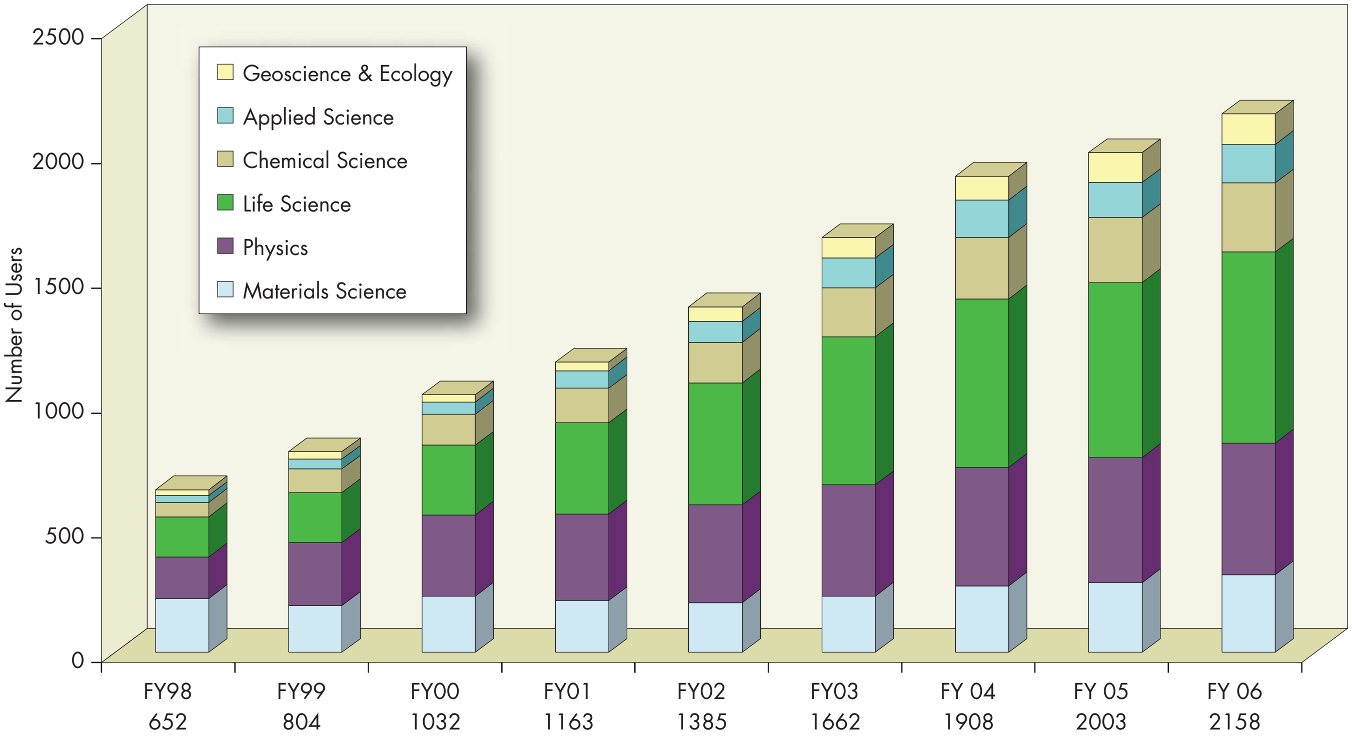

FIGURE 6. Bar graph showing growth in areas of science.

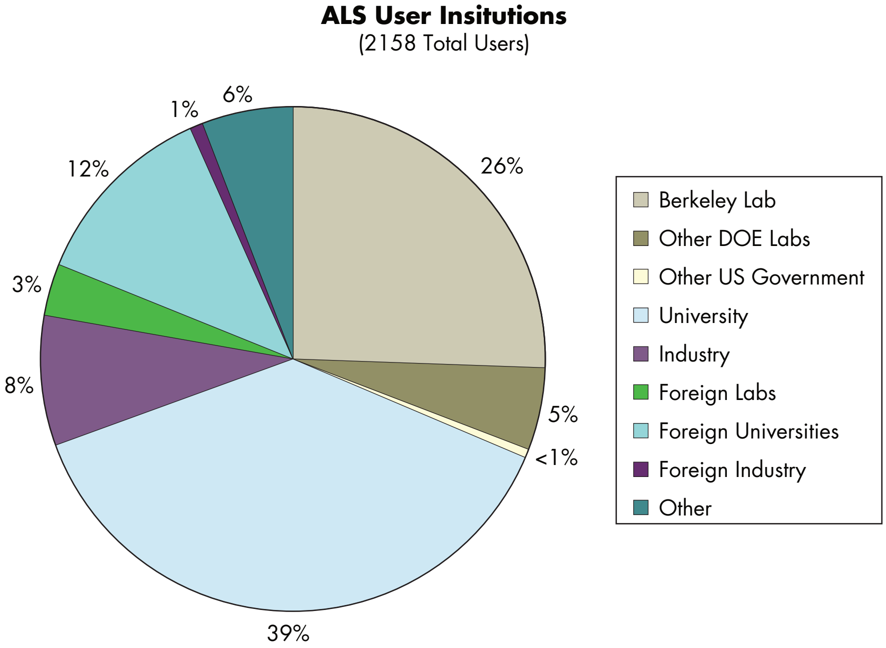

FIGURE 7. Pie chart showing percentages of different types of user institutions.

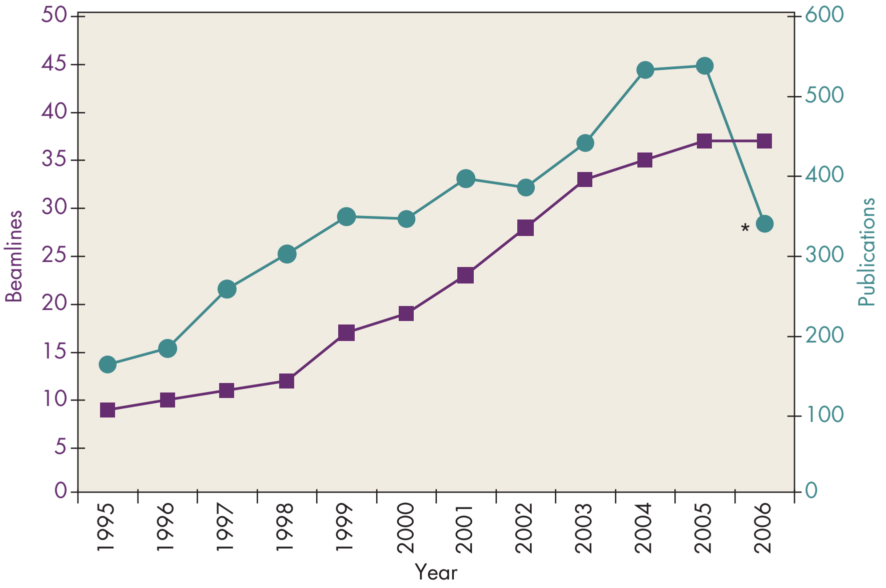

FIGURE 8. Graph of growth in beamlines (pink) and publications (blue). *Note that publications for 2006 were still being collected at the time this section was being written.

Special Events

VISITORS AND EVENTS

From opening new beamlines to opening the doors of the ALS to visitors from the U.S. and abroad, ALS scientists and staff had a very busy year. In August, hundreds of current and former Berkeley Lab employees toured the ALS as part of Founders' Day, the 75th anniversary of the Lab. At the end of the summer, more than 400 students attending the National Student Leadership Conference on Engineering at UC Berkeley were shown around the ALS by scientist volunteers.

In May, acting ALS Director Janos Kirz guided Clay Sell, executive at the U.S. DOE and deputy to Secretary Samuel Bodman, as he toured the ALS. Accompanied by Berkeley Lab Director Steve Chu, the tour included a visit to Beamline 5.0.2 to view examples of protein crystallography research and to the planned site of the new User Support Building.

Also in May, Neville Smith (left, standing) and Zahid Hussain (second from right, kneeling) welcomed Jefferson Fellows from the East-West Center to the ALS. The Jefferson Fellowship program exposes middle and senior journalists from throughout the Asia-Pacific region to a wide range of research and education issues in the U.S. The group visiting the ALS was particularly interested in energy science and climate change.

Cutting the ribbon that officially opened the new National Center for X-Ray Tomography (NCXT) were (from left) Roland Hirsch (DOE), Allan Basbaum (UC San Francisco), Carolyn Larabell (Berkeley Lab), Barbara Alving (NIH), Amy Swain (NIH), and Roger Falcone (ALS). NXCT features the first soft x-ray transmission microscope to be designed specifically for biological and biomedical applications. Among its many unique capabilities will be "CAT scans" for biological cells.

The Stanford chapter of the Optical Society of America visited the ALS in November. Following an overview of the facility by ALS Division Director Roger Falcone and beamline talks about lithography, the students posed for a photo under the dome.

ALS USERS' MEETING

OCTOBER 9–11

This year's meeting featured a record 470 attendees, 12 workshops, scientific highlights, a well-attended public lecture, the introduction of a new director, and a special session dedicated to the scientific contributions of ALS Scientific Director Neville Smith.

UC Berkeley Chancellor Robert Birgeneau welcomed a full house of users and staff to the 2006 ALS Users' Meeting. He was followed by DOE BES Associate Director of Science Pat Dehmer, who provided an overview of U.S. light sources and techniques, funding, and the rapid growth of competing international facilities.

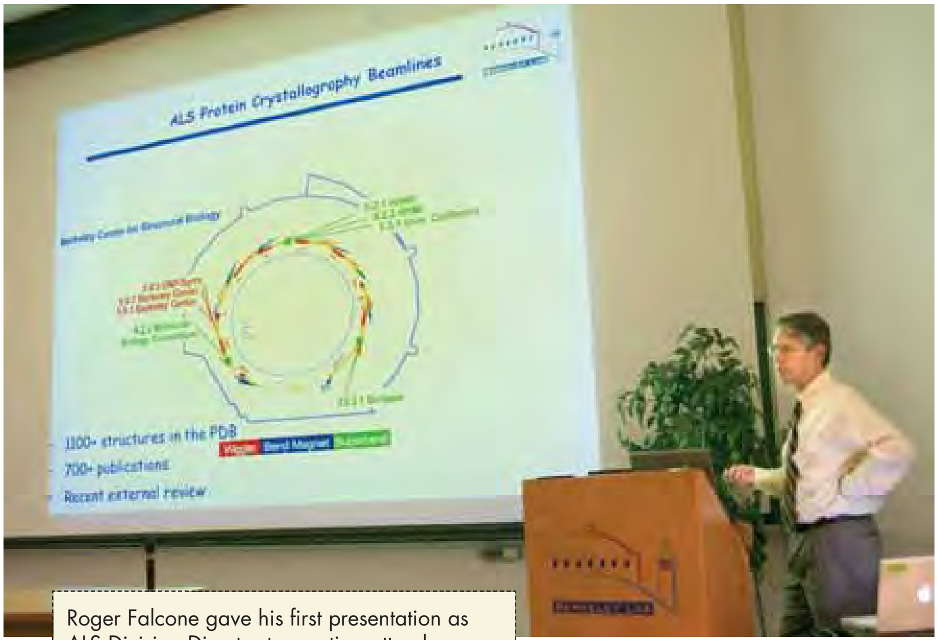

Roger Falcone gave his first presentation as ALS Division Director to meeting attendees.

Invited speaker Andrew Westphal (Space Sciences Laboratory, UC Berkeley) intrigued the audience with recent results in his talk, "Synchrotron analysis of Stardust samples."

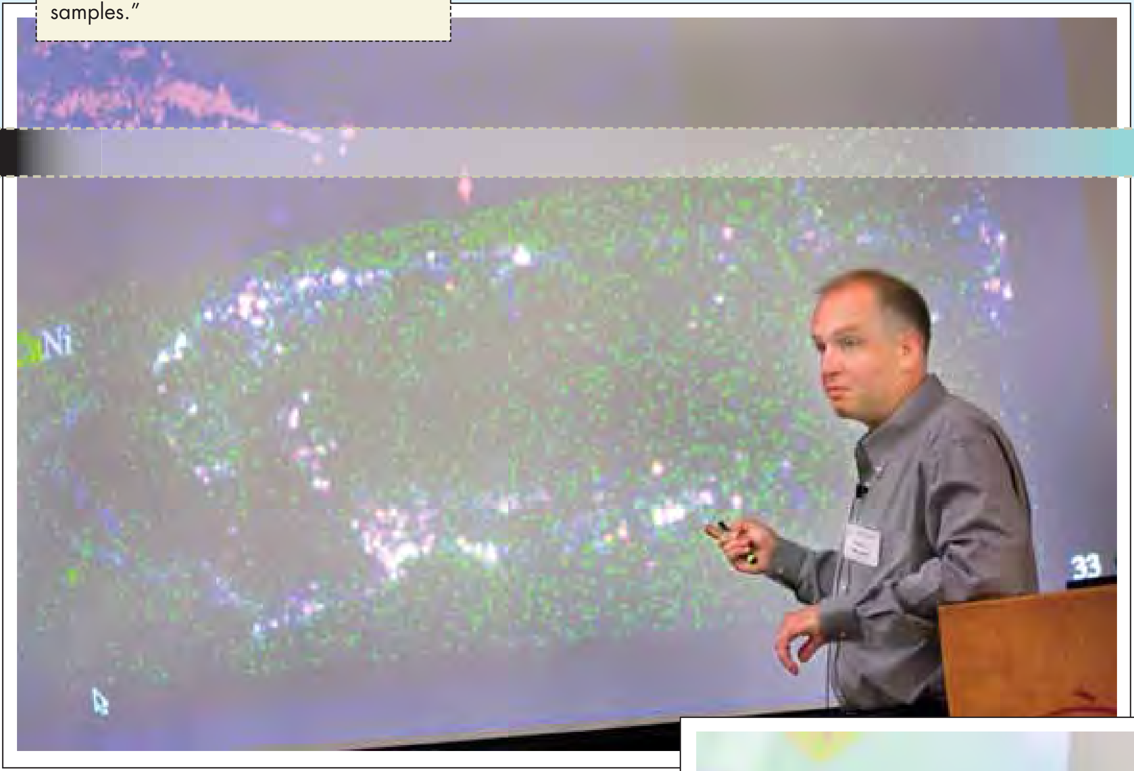

During the morning plenary session, keynote speaker Carolyn Bertozzi, director of the Molecular Foundry, described the exciting scientific opportunities in nanoscience at the new facility and future prospects for ALS–Molecular Foundry collaborations.

The Halbach Award for innovative instrumentation was won by Carl Cork and John Taylor (Physical Biosciences Division); Robert Nordmeyer, Earl Cornell, and Jim O'Neill (Engineering Division); and Gyorgy Snell (Takeda San Diego) for the development of automated crystal-mounting robots for high-throughput macromolecular crystallography. Carl Cork presented the group's work during the plenary session.

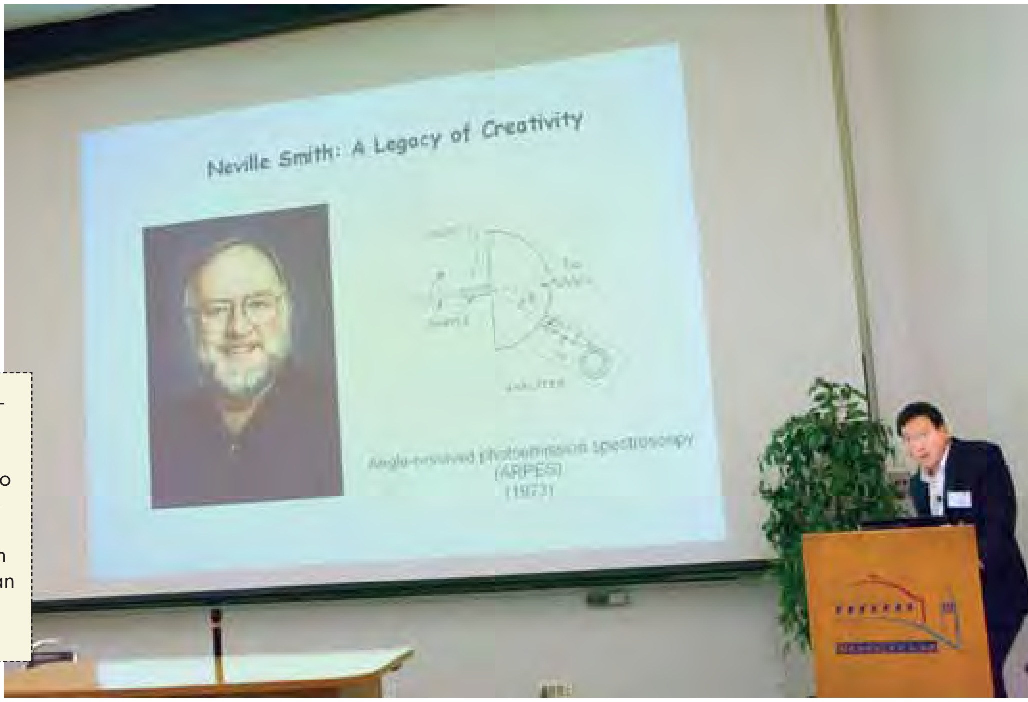

On the fist day of the meeting, ALS Scientific Advisor Janos Kirz hosted a session dedicated to Neville Smith. Collaborators past and present noted Neville's immense scientific contributions to photoemission science and the synchrotron community as well as his unique and outstanding sense of humor. Speakers included Peter Johnson (Brookhaven National Laboratory) Stephen Kevan (University of Oregon), Z.Q. Qiu (UC Berkeley), and (right) Z.X. Shen (Stanford University).

During the evening banquet, Peter Johnson (right) chaired a special presentation dedicated to the life of Neville as Betsy Smith (left) looked on. The event included a slide show and many stories of Neville's kindness and support of young scientists over the years.

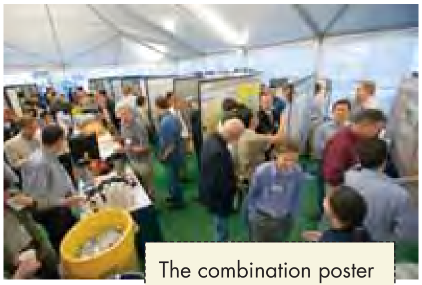

The combination poster session, student poster competition, and reception for exhibitors again attracted capacity crowds to the tent and ALS patio.

More than 25 entries vied for the student poster competition awards this year. Standing with UEC Chair Clemens Heske from right are first-place student poster award winner Rajesh Chopdekar (Cornell University), second-place winner Regan Wilks (University of Saskatchewan, Canada), and third-place recipient Geza Szigethy (UC Berkeley).

The Shirley Award for scientific achievement went to Andreas Scholl (ALS) and Hendrik Ohldag (SSRL) for their outstanding work in using photoemission electron microscopy in the study of magnetic materials.

The Renner User Service Award went to Warren Byrne for his exceptional efforts in providing the highest quality beam and assistance to ALS users.

Following the conclusion of the formal meeting, 12 focused workshops, six of which were held jointly with SSRL, were held around the Lab. Some of the topics discussed included ultrafast dynamics, inelastic x-ray scattering, tomography, angle-resolved photoemission, and advanced magnetic spectroscopy.

About the ALS

ALS Staff

This is a cumulative list of all those who worked at the ALS during the 2006 calendar year. The list includes visitors, students, as well as staff members from other divisions who were matrixed to the ALS.

Division Management

D. Chemla†
R. Falcone
J. Kirz
B. Feinberg
P. Oddone
N. Smith

Accelerator Physics

D. Robin, Group Leader
C. Steier, Deputy Leader
W. Byrne
A. Loftsdottir*
H. Nishimura
G. Portmann
H. Sannibale
T. Scarvie
W. Wan
W. Wittmer**

Administration

G. Flores
A. Reza
N. Sallee
D. Smith
J. Troutman

Budget

L. Griffin
J. Kekos
M. Lewis

Computer Protection

E. Williams

Controls

A. Biocca, Group Leader
C. Timossi, Deputy Leader
T. Campbell
E. Domning
H. Huang
C. Ikami
S. Jacobson
T. Kellog
Y. Lou
B. Smith
R. Steele
M. Urashka
E. Williams

Electrical Engineering

W. Barry, Group Leader
G. Stover, Deputy Leader
B. Bailey
M. Balagot
K. Baptiste
M. Bell
R. Candelario
P. Casey
M. Chin
R. Colston
S. Cooper
P. Cull
J. Elkins
M. Fahmie
R. Gassaway
R. Gervasoni
L. Holzer
J. Julian
T. Kuneli
E. Lee
P. Molinari
R. Mueller
J. Nomura
F. Ottens
S. Rogoff
P. Rosado
M. Sawada
A. Sippio
R. Slater
G. Stover
M. Vinco
J. Weber
K. Woolfe

Environment, Safety, and Health

R. Baker
R. Donahue
B. Fairchild
J. Floyd
M. Kritscher
T. Kuneli
G. Perdue
W. Thur

Experimental Systems

H. Padmore, Group Leader
A. Warwick, Deputy Leader
R. Celestre
M. Church
S. Clark
A. Doran
S. Fakra
J. Feng
J. Glossinger
E. Glover
P. Heimann
M. Howells
S. Irick
T. Kellog
A. MacDowell
M. Marcus
W. McKinney
G. Morrison
S. Morton
J. Nasiatka
B. Rude
E. Schaible
A. Scholl
N. Tamura
S. Teat
V. Yashchuck
A. Young

Magnetic Systems Engineering

R. Schlueter, Group Leader
M. Coleman
J.-Y. Jung
S. Marks
P. Pipersky
S. Prestemon

Mechanical Engineering

R. Duarte, Group Leader
N. Kelez, Deputy Leader
R. Beggs
D. Calais
A. Catalano
D. Colomb
C. Cummings
M. Decool
A. DeMello
S. Dimaggio
D. Ellis
J. Fischer
K. Franck
A. Gavidia
D. Gibson
F. Gicquel
C. Hernikl
C. Hopkins
D. Hull
D. Jones
S. Klingler
M. Kritscher
K. Krueger
R. Low
D. MacGill
P. McKean
H. Meyer
T. Miller
V. Moroz
G. Morrison
D. Munson
E. Palmerston
J. Pepper
K. Peterman
D. Plate
A. Rawlins
K. Sihler
A. Smith
T. Stevens
M. Thomas
W. Thur
E. Wong
D. Yegian
F. Zucca

Operations

R. Bloemhard, Group Leader
W. Byrne, Deputy Leader
M. Beaudrow
D. Brothers
K. Osborne
A. Pearson
D. Richardson
D. Riley-Cole
S. Stricklin

Procedure Center

R. Jones

Project Management

A. Catalano
S. Rossi

Quality Assurance

D. Richardson

Scientific Support

Z. Hussain, Group Leader
E. Rotenberg, Deputy Leader
G. Ackerman
E. Arenholz
W. Bates
A. Bostwick
Y.-D. Chuang**
E. Cruz
J. Denlinger
A. Fedorov
J. Guo
A. Guy
Z. Hao**
D. Kilcoyne
G. Lebedev
M. Martin
S. Mun
J. Pepper
C. Piamonteze
M. Pfeifer**
F. Schlachter
J. Spear
T. Tyliszczak
W. Yang

User Services

G. Krebs, Group Leader
A. Robinson, Deputy Leader
T. Anderson
J. De Ponte
C. Escobar
S. Fujimura
G. Giangrasso
D. Hamamoto
D. Malone
E. Moxon
B. Phillips
O. Poblete
J. Pruyn
L. Tamura
J. Troutman
G. Vierra
K. Winters
V. Wysinger

Visitors and Students

T. Araki**
M. Awadallah
I. Babin
A. Bartelt**
H. Barth
B. Batterman
R. Bilodeau**
M. Boots
V. Brown
S. Caldwell
A. Chakmatov
F. Chaudry
L. Chen
P. Chung
C. Coleman
A. Comin**
C. Cui**
A. Das
B. Freelon**
I. Furtado
E. Gann
P. Glans**
M. Greaves
Z. Hao*
M.-Z. Hasan
A. Hexemer
M. Hindi
S. Kashtanov
J. Kirschman
A. Kotani
O. Kuprin
K. Lee
N. Mannella**
J. McChesney
G. Meyer

S. Morton
B. Nellis
M. Nip
T. Ohta*
K. Opachich*
J. Patel
M. Pfeiffer**
E. Poliakoff
D. Rolles
M. Rossi
S. Roy
T. Sasagawa
H.-J. Shin
D. Shiraki
L. Sorenson
J. Spence
Z. Sun
L. Svec
K. Tanaka
T. Tong
C. Tonnessen
J. Turner
F. Wang
W. Wang
B. Watts
A. Wray
M. Xia
W. Yang
J. Zhong

ALS Doctoral Fellows

Y. Chen*
I. Dumitriu*
A. Hudson*
T. Learmonth*
Z. Li*
Z. Pan*
P. Strachan*
M. Weinberger*

†On leave
*Graduate Student
Research Assistant
**Postdoc

ALS Advisory Panels

Scientific Advisory Committee

Neil Ashcroft, Cornell University
Samuel Bader (chair), Argonne National Laboratory
Jeffrey Bokor, UC Berkeley
Phil Bucksbaum, Stanford University
Jennifer Doudna, Physical Biosciences Division, Berkeley Lab
Wolfgang Eberhardt, BESSY GmbH, Germany
Pascal Elleaume, European Synchrotron Radiation Facility
Clemens Heske (ex-officio), University of Nevada, Las Vegas
Peter Johnson (ex-officio), Stony Brook University
Stephen D. Kevan, University of Oregon
Samuel Krinsky, Brookhaven National Laboratory
Carolyn Larabell, Life Sciences Division, Berkeley Lab
John Parise, State University of New York
Erwin Poliakoff, Louisiana State University
Miquel Salmeron, Materials Sciences Division, Berkeley Lab
Sunil Sinha, UC San Diego
J. Friso van der Veen, Paul Scherrer Institut
Linda Young, Argonne National Laboratory

Users' Executive Committee

Elke Arenholz, Advanced Light Source, Berkeley Lab
Gregory Denbeaux (past chair), University at Albany, State University of New York
Jinghua Guo, Advanced Light Source, Berkeley Lab
Clemens Heske (chair), University of Nevada, Las Vegas
Amanda Hudson, University of Nevada, Las Vegas
Alessandra Lanzara, UC Berkeley and Materials Sciences Division, Berkeley Lab
Simon Morton, Physical Biosciences Division, Berkeley Lab
Hendrik Ohldag, Stanford Synchrotron Radiation Laboratory
Corie Ralston, Physical Biosciences Division, Berkeley Lab
Tony van Buuren (vice chair), Lawrence Livermore National Laboratory
Ed Westbrook, Molecular Biology Consortium

Facts and Figures

USING THE ADVANCED LIGHT SOURCE

The ALS, a DOE national user facility, welcomes researchers from universities, industry, and government laboratories. Qualified users have access as general users or as members of either a participating research team (PRT) or approved program (AP). PRTs and APs (groups of researchers with related interests from one or more institutions) construct and operate beamlines and have primary responsibility for experiment endstation equipment. The Scientific Advisory Committee awards the PRTs or APs a percentage of their beamline's operating time commensurate with the resources that they have contributed to the beamline. Through the additional peer-review process of the Proposal Study Panel, the remaining beam time is granted to general user proposals. These users may provide their own endstation or negotiate access to a PRT- or AP-owned endstation.

The ALS does not charge users for beam access if the research is nonproprietary. Users performing proprietary research are charged a fee based on full cost recovery. All users are responsible for the day-to-day costs of research (e.g., supplies, phone calls, technical support).

The nominal operating energy of the ALS storage ring is 1.9 GeV, although it can run from 1.0 to 1.9 GeV, allowing flexibility for user operations. At 1.9 GeV, the normal maximum operating current is 400 mA in multibunch operation. The spectral range of undulator and wiggler beamlines extends from photon energies of roughly 5 eV to 21 keV; on superbend beamlines the range is between 2.4 and 60 keV. Bend magnets produce radiation from the infrared to about 20 keV.

The ALS is capable of accommodating approximately 50 beamlines and more than 100 endstations. The first user beamlines began operation in October 1993, and there were 39 operating beamlines, with several more under construction, by the end of 2006.

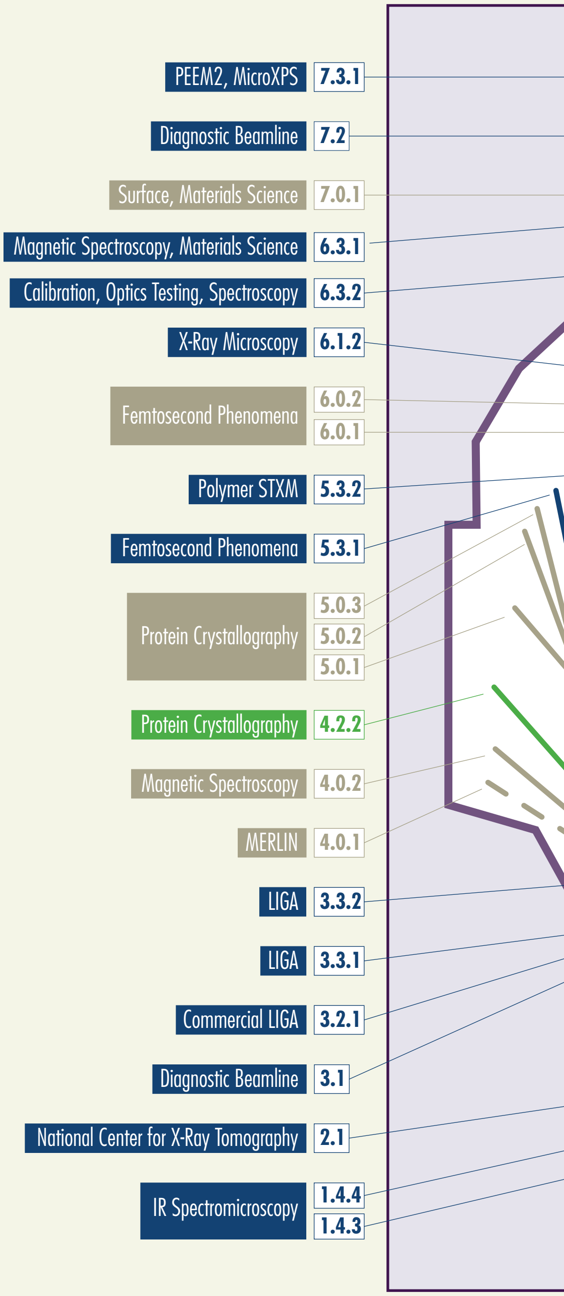

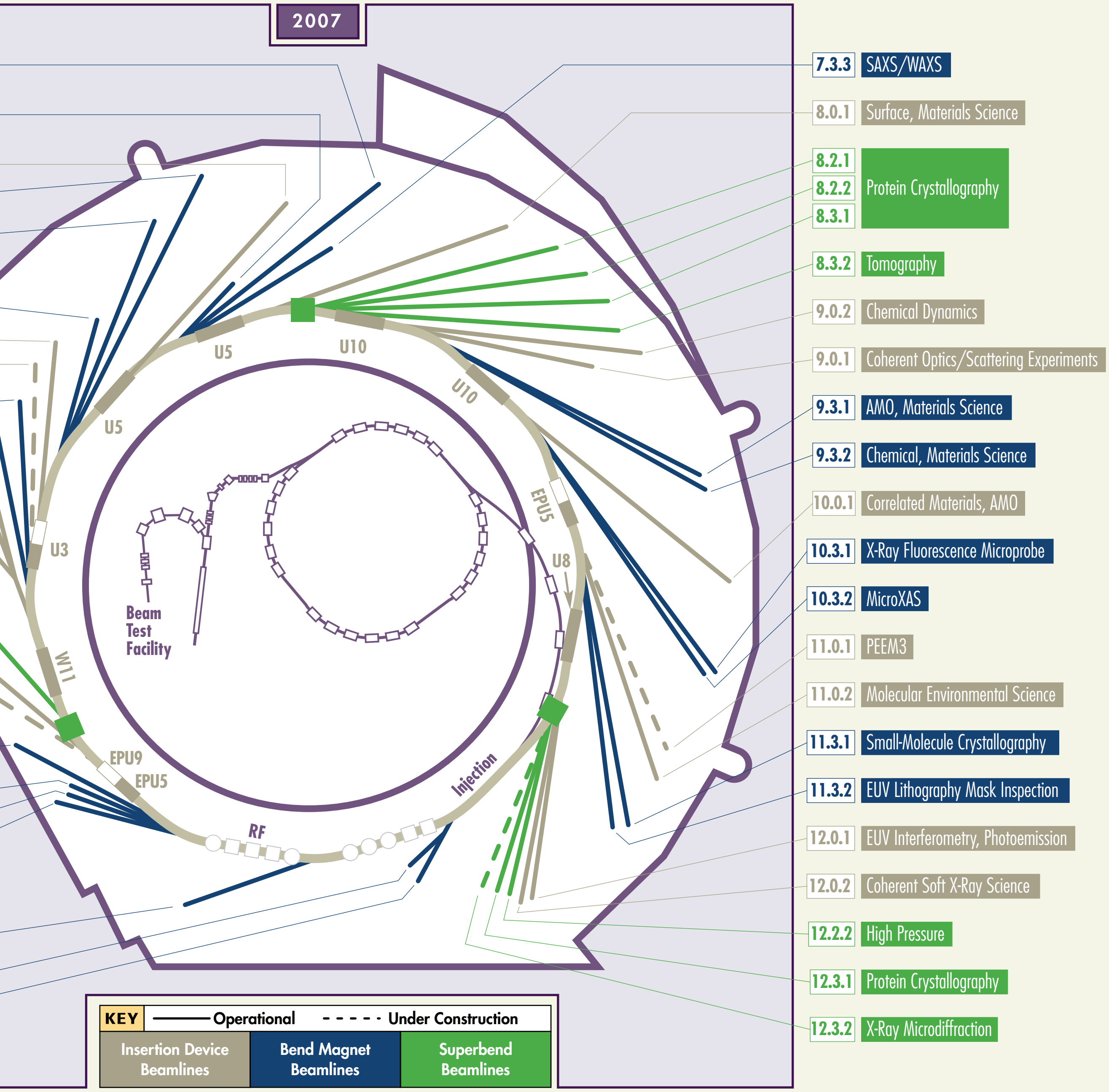
2007
7.3.3 SAXS/WAXS
8.0.1 Surface, Materials Science
8.2.1
8.2.2
8.3.1
Protein Crystallography
8.3.2 Tomography
9.0.2 Chemical Dynamics
9.0.1 Coherent Optics/Scattering Experiments
9.3.1 AMO, Materials Science
9.3.2 Chemical, Materials Science
10.0.1 Correlated Materials, AMO
10.3.1 X-Ray Fluorescence Microprobe
10.3.2 MicroXAS
11.0.1 PEEM3
11.0.2 Molecular Environmental Science
11.3.1 Small-Molecule Crystallography
11.3.2 EUV Lithography Mask Inspection
12.0.1 EUV Interferometry, Photoemission
12.0.2 Coherent Soft X-Ray Science
12.2.2 High Pressure
12.3.1 Protein Crystallography
12.3.2 X-Ray Microdiffraction
U5
U10
U10
U5
U3
EPU5
U8
W11
EPU9
EPU5
RF
Injection
Beam Test Facility
KEY
Operational
Under Construction
Insertion Device Beamlines
Bend Magnet Beamlines
Superbend Beamlines

ALS BEAMLINES (2006)

BEAMLINE	SOURCE	AREAS OF RESEARCH/TECHNIQUES	MONOCHROMATOR	ENERGY RANGE	OPERATIONAL
1.4.3	Bend	Infrared spectromicroscopy	Interferometer	0.05–1.2 eV (600–10,000 cm^{-1})	Now
1.4.4	Bend	Infrared spectromicroscopy	Interferometer	0.05–1.5 eV (400–12,000 cm^{-1})	Now
2.1	Bend	National Center for X-Ray Tomography (XM-2)	Zone-plate linear	200 eV–7 keV	Now
3.1	Bend	Diagnostic beamline	Mirror/filter	1–2 keV	Now
3.2.1	Bend	Commercial deep-etch x-ray lithography (LIGA)	None	3–12 keV	Now
3.3.1	Bend	Deep-etch x-ray lithography (LIGA)	None	3–12 keV	Now
3.3.2	Bend	Deep-etch x-ray lithography (LIGA)	None	3–12 keV	Now
4.0.1	EPU9	High-resolution spectroscopy of complex materials (MERLIN)	Variable-included-angle SGM	10–150 eV	2008
4.0.2	EPU5	Magnetic spectroscopy			
		Advanced photoelectron spectrometer/diffractometer	Variable-included-angle PGM	80–1900 eV	Now
		L-edge chamber with superconducting spectrometer	Variable-included-angle PGM	80–1900 eV	Now
		XMCD chamber (6 T, 2 K)	Variable-included-angle PGM	80–1900 eV	Now
		Eight-pole electromagnet	Variable-included-angle PGM	80–1900 eV	Now
4.2.2	SB	Multiple-wavelength anomalous diffraction (MAD) and monochromatic protein crystallography	Double crystal	5–17 keV	Now
5.0.1	W11	Monochromatic protein crystallography	Curved crystal	12.4 keV	Now
5.0.2	W11	Multiple-wavelength anomalous diffraction (MAD) and monochromatic protein crystallography	Double crystal	4–16 keV	Now
5.0.3	W11	Monochromatic protein crystallography	Curved crystal	12.4 keV	Now
5.3.1	Bend	Femtosecond phenomena	Double crystal	1.8–12 keV	Now
5.3.2	Bend	Polymer scanning transmission x-ray microscopy	SGM	250–700 eV	Now
6.0.1	U3	Femtosecond phenomena	Double crystal	2–10 keV	2007
6.0.2	U3	Femtosecond phenomena	VLS-PGM	200–1800 eV	Now
6.1.2	Bend	High-resolution zone-plate microscopy	Zone-plate linear	300–1300 eV	Now
6.3.1	Bend	Magnetic spectroscopy	VLS-PGM	300–2000 eV	Now
6.3.2	Bend	Calibration and standards; EUV optics testing; atomic, molecular, and materials science	VLS-PGM	50–1300 eV	Now
7.0.1	U5	Surface and materials science, spectromicroscopy			
		Scanning photoemission microscope (SPEM)	SGM	100–800 eV	Now
		Electronic Structure Factory (ESF)	SGM	60–1200 eV	Now
		Advanced x-ray inelastic scattering (AXIS)	SGM	80–1200 eV	Now
7.2	Bend	Diagnostic beamline	Filter/none	Far IR–17 keV	Now
7.3.1	Bend	Magnetic microscopy, spectromicroscopy	SGM	175–1500 eV	Now
7.3.3	Bend	Small- and wide-angle x-ray scattering (SAXS/WAXS)	Double multilayer	10 keV	Now
8.0.1	U5	Surface and materials science, imaging photoelectron spectroscopy, soft x-ray fluorescence			
		Ellipsoidal-mirror electron energy analyzer (EMA)	SGM	65–1400 eV	Now
		Soft x-ray fluorescence spectrometer(SXF)	SGM	65–1400 eV	Now

BEAMLINE	SOURCE	AREAS OF RESEARCH/TECHNIQUES	MONOCHROMATOR	ENERGY RANGE	OPERATIONAL
8.2.1	SB	Multiple-wavelength anomalous diffraction (MAD) and monochromatic protein crystallography	Double crystal	5–17 keV	Now
8.2.2	SB	Multiple-wavelength anomalous diffraction (MAD) and monochromatic protein crystallography	Double crystal	5–17 keV	Now
8.3.1	SB	Multiple-wavelength anomalous diffraction (MAD) and monochromatic protein crystallography	Double crystal	2.4–18 keV	Now
8.3.2	SB	Tomography	Double crystal, multilayer, white light	5–60 keV	Now
9.0.1	U10	Coherent optics/scattering experiments	None or off-axis zone plate	10–800 eV	Now
9.0.2	U10	Chemical dynamics			
		Molecular-beam photoelectron/photoion imaging and spectroscopy	White light, Off-plane Eagle	5–30 eV	Now
		Flame chamber	White light, Off-plane Eagle	5–30 eV	Now
		Ablation chamber	White light, Off-plane Eagle	5–30 eV	Now
		Aerosol chamber	White light, Off-plane Eagle	5–30 eV	Now
		Kinetics machine	White light, Off-plane Eagle	5–30 eV	Now
9.3.1	Bend	Atomic, molecular, and materials science			
		Angle-resolved time-of-flight electron spectrometer	Double crystal	2.2–5.5 keV	Now
		Ion time-of-flight spectrometer	Double crystal	2.2–5.5 keV	Now
		Magnetic mass analyzer	Double crystal	2.2–5.5 keV	Now
		Polarized-x-ray emission spectrometer	Double crystal	2.2–5.5 keV	Now
		X-ray absorption cell	Double crystal	2.2–5.5 keV	Now
		XAFS station	Double crystal	2.2–5.5 keV	Now
9.3.2	Bend	Chemical and materials science, circular dichroism, spin resolution			
		Advanced materials chamber (AMC)	SGM	30–1400 eV	Now
		Ambient pressure photoemission	SGM	30–1400 eV	Now
10.0.1	U10	Photoemission of highly correlated materials; high-resolution atomic, molecular, and optical physics			
		High energy resolution spectrometer (HERS)	SGM	17–340 eV	Now
		High-resolution atomic and molecular electron spectrometer (HiRAMES)	SGM	17–340 eV	Now
		Ion-photon beamline (IPB)	SGM	17–340 eV	Now
		Electron spin polarization (ESP)	SGM	17–340 eV	Now
10.3.1	Bend	X-ray fluorescence microprobe	White light, multilayer mirrors	3–20 keV	Now
10.3.2	Bend	Environmental and materials science, micro x-ray absorption spectroscopy	White light, two crystal	2.5–17 keV	Now
11.0.1	EPU5	Magnetic microscopy, spectromicroscopy (PEEM3)	VLS-PGM	100–2000 eV	2007
11.0.2	EPU5	Molecular environmental science			
		Wet spectroscopy	Variable-included-angle PGM	95–2000 eV	Now
		High-pressure photoemission spectroscopy	Variable-included-angle PGM	95–2000 eV	Now
		Scanning transmission x-ray microscope (STXM)	Variable-included-angle PGM	130–2000 eV	Now

continued

ALS BEAMLINES (2006) *continued*

BEAMLINE	SOURCE	AREAS OF RESEARCH/TECHNIQUES	MONOCHROMATOR	ENERGY RANGE	OPERATIONAL
11.3.1	Bend	Small-molecule crystallography	Channel-cut Si(111)	6–17 keV	Now
11.3.2	Bend	Inspection of EUV lithography masks	VLS-PGM	50–1000 eV	Now
12.0.1	U8	EUV optics testing and interferometry, angle- and spin-resolved photoemission			
		Angle- and spin-resolved photoemission (12.0.1.1)	VLS-PGM	24–350 eV	Now
		EUV interferometer (12.0.1.2)	VLS-PGM	60–320 eV	Now
		EUV interferometer (12.0.1.3)	VLS-PGM	60–320 eV	Now
12.0.2	U8	Coherent soft x-ray science			
		Coherent optics	VLS-PGM	200–1000 eV	Now
		Coherent scattering	VLS-PGM	200–1000 eV	Now
12.2.2	SB	California High-Pressure Science Observatory (CALIPSO)			
		Nanoscience/materials chemistry	Double crystal	6–40 keV	Now
		Solid-state physics/geoscience	Double crystal	6–40 keV	Now
12.3.1	SB	Structurally Integrated Biology for Life Sciences (SIBYLS)	Double crystal and double multilayer	5.5–17 keV	Now
12.3.2	SB	X-ray microdiffraction	White light and four crystal	6–22 keV	2007
BTF	Linac	Beam Test Facility	None	50-MeV electrons	Now

Bend = bend magnet
SB = superconducting bend magnet
EPUx = x-cm-period EPU
Ux = x-cm-period undulator
Wx = x-cm-period wiggler

ALS INSERTION DEVICE PARAMETERS (2006)

DEVICE	BEAMLINE	STATUS	ENERGY RANGE AT 1.5 GeV (eV)	ENERGY RANGE AT 1.9 GeV (eV)	PERIOD (cm)	NO. OF PERIODS	OPERATING GAP RANGE (cm)	PEAK EFFECTIVE FIELD RANGE (T)
U3	6.0.2	Operational	73–3100 eV	120–5000 4000–11000[a]	3	50	0.55–2.7	1.5–0.13
U5	8.0.1	Operational	50–1000	80–3000	5	89	1.4–4.5	0.85–0.10
U5	7.0.1	Operational	50–1000	80–3000	5	89	1.4–4.5	0.85–0.10
U8	12.0.1	Operational	18–1200	20–1900	8	55	2.47–8.3	0.80–0.07
U10	9.0.1	Operational	5–950	8–1500	10	43	2.27–11.6	0.98–0.05
U10	10.0.1	Operational	8–950	12–1500	10	43	2.31–11.6	0.80–0.05
EPU5	4.0.2	Operational	45–1000[b]	73–3000[b]	5	36.5	1.40–5.5	0.86–0.10[c] 0.58–0.10[d]
EPU5	11.0.1	Operational	47–1000[b]	75–3000[b]	5	36.5	1.43–5.5	0.86–0.10[c] 0.58–0.10[d]
EPU5	11.0.2	Operational	44–1000[b]	71–3000[b]	5	37	1.38–5.5	0.86–0.10[c] 0.58–0.10[d]
W11	5.0.2	Operational	6000–13000	6–21[a]	11.4	29	1.25–18.0	1.94–0.03

[a] Wiggler mode [b] Elliptical polarization mode [c] Vertical field [d] Horizontal field

ALS STORAGE RING PARAMETERS

PARAMETER	VALUE
Beam particle	Electron
Beam energy	1.0–1.9 GeV
Injection energy	1.0–1.5 GeV
Beam current	
Multibunch mode	400 mA
Two-bunch mode	2 x 25 mA
Filling pattern (multibunch mode)	276 to 320 bunches possibility of 10-mA "camshaft" bunch in filling gap
Bunch spacing	
Multibunch mode	2 ns
Two-bunch mode	328 ns
Circumference	196.8 m
Number of straight sections	12
Current number of insertion devices	10
Radio frequency	499.642 MHz
Beam size in straight sections, rms (1.9-GeV multibunch mode)	310 microns horiz. x 16 microns vert.

PARAMETER	VALUE AT 1.5 GeV	VALUE AT 1.9 GeV
Beam lifetime		
multibunch mode[a]	~3.5 hours at 400 mA	~8.0 hours at 400 mA
two-bunch mode	not used	~60 min. at 40 mA
Horizontal emittance	4.2 nm-rad	6.3 nm-rad
Vertical emittance[b]	0.2 nm-rad	0.13 nm-rad
Energy spread (ΔE/E, rms)	8 x 10^{-4}	1 x 10^{-3}

[a] In multibunch mode, the storage ring is typically filled every eight hours at 1:00 A.M., 9 A.M., and 5 P.M. For 1.5-GeV operation, injection occurs every four hours and in two-bunch mode, every two hours.

[b] Vertical emittance is deliberately increased to improve beam lifetime.

PUBLICATIONS

Listed below are publications (e.g., journal articles, conference papers, theses, and book chapters) that were published in calendar year 2006 and are based on data obtained in whole or in part at the ALS as well as publications containing descriptions of experiment, beamline, or accelerator systems developed at the ALS.

Accardi, A., S. Lobet, C.Williams, C., Miller, and R. Dutzler, “Synergism between halide binding and proton transport in a CLC-type exchanger,” *J. Mol. Biol.* **362,** 691 (2006).

Acremann, Y., J.P. Strachan, V. Chembrolu, S.D. Andrews, T. Tyliszczak, J.A. Katine, M.J. Carey, B.M. Clemens, H.C. Siegmann, and J. Stöhr, “Time-resolved imaging of spin transfer switching: Beyond the macrospin concept,” *Phys. Rev. Lett.* **96,** 217202 (2006).

Addlagatta, A., and B.W. Matthews, “Structure of the angiogenesis inhibitor ovalicin bound to its noncognate target, human type 1 methionine aminopeptidase,” *Protein Sci.* **15,** 1842 (2006).

Addlagatta, A., L. Gay, and B.W. Matthews, “Structure of aminopeptidase N from *Escherichia coli* suggests a compartmentalized, gated active site,” *Proc. Natl. Acad. Sci. USA* **103,** 13339 (2006).

Aguilar, A., J.D. Gillaspy, G.F. Gribakin, R.A. Phaneuf, M.F. Gharaibeh, M.G. Kozlov, J.D. Bozek, and A.L.D. Kilcoyne, “Absolute photoionization cross sections for Xe^{4+}, Xe^{5+}, and Xe^{6+} near 13.5 nm: Experiment and theory,” *Phys. Rev. A* **73,** 3 (2006).

Allendorph, G.P., W.W. Vale, and S. Choe, “Structure of the ternary signaling complex of a TGF-beta superfamily member,” *Proc. Natl. Acad. Sci. USA* **103**, 7643 (2006).

Angers, S., T. Li, X. Yi, M.J. MacCoss, R.T. Moon, and N. Zheng, “Molecular architecture and assembly of the DDB1-CUL4A ubiquitin ligase machinery,” *Nature* **443**, 590 (2006).

Anstrom, D.M., and S.J. Remington, “The product complex of *M. tuberculosis* malate synthase revisited,” *Protein Sci.* **15,** 2002 (2006).

Appleton, B.A., P. Wu, and C. Weismann, “The crystal structure of murine coronin-1: A regulator of actin cytoskeletal dynamics in lymphocytes,” *Structure* **14**, 1 (2006).

Appleton, B.A., Y. Zhang, P. Wu, J.P. Yin, W. Hunziker, N.J. Skelton, S.S. Sidhu, and C. Wiesmann, “Comparative structural analysis of the erbin PDZ domain and the first PDZ domain of ZO-1: Insights into determinants of PDZ domain specificity,” *J. Biol. Chem.* **281**, 31 (2006).

Araki, T., H. Ade, J.M. Stubbs, D.C. Sundberg, G.E. Mitchell, J.B. Kortright, and A.L.D Kilcoyne, “Resonant soft x-ray scattering from structured polymer nanoparticles,” *Appl. Phys. Lett.* **89**, 12 (2006).

Arenholz, E., K. Liu, Z. Li, and I.K. Schuller, “Magnetization reversal of uncompensated Fe moments in exchange biased Ni/FeF_2 bilayers,” *Appl. Phys. Lett.* **88**, 7 (2006).

Argiriadi, M.A., E.R. Goedken, I. Bruck, M. O’Donnell, and J. Kuriyan, “Crystal structure of a DNA polymerase sliding clamp from a gram-positive bacterium,” *BMC Struct. Biol.* **6**, 2 (2006).

Arndt, J.W., Q. Chai, T. Christian, and R.C. Stevens, “Structure of botulinum neurotoxin type D light chain at 1.65 Å resolution: Repercussions for VAMP-2 substrate specificity,” *Biochemistry–US* **45**, 3255 (2006).

Ashworth, J., J.J. Havranek, C.M. Duarte, D. Sussman, and R.J. Monnat, “Computational redesign of endonuclease DNA binding and cleavage specificity,” *Nature* **441**, 656 (2006).

Attwood, D., “Nanotomography comes of age,” *Nature* **422**, 642 (2006).

Attwood, D., W. Chao, E. Anderson, J.A. Liddle, B. Harteneck, P. Fischer, G. Schneider, M. Le Gros, and C. Larabell, “Imaging at high spatial resolution: Soft x-ray microscopy to 15 nm,” *J. Biomed. Nanotech.* **2**, 75 (2006).

Avvakumov, G.V., J.R.Walker, S. Xue, P.J. Finerty, Jr., F. Mackenzie, E.M. Newman, and S. Dhe-Paganon, “Amino-terminal dimerization, NRDP1-rhodanese interaction, and inhibited catalytic domain conformation of the ubiquitin-specific protease 8 (USP8),” *J. Biol. Chem.* **281**, 38061 (2006).

Bahng, M.-K., X. Xing, S.J. Baek, X. Qian, and C.Y. Ng, “A combined VUV synchrotron pulsed field ionization-photoelectron and IR-VUV laser photoion depletion study of ammonia,” *J. Phys. Chem. A* **110**, 8488 (2006).

Bailey, S., Wing, R.A., Steitz, T.A. “The Structure of *T. aquaticus* DNA polymerase III is distinct from eukaryotic replicative DNA polymerases,” *Cell* **126**, 893 (2006).

Bale, H.A., J.C. Hanan, and N. Tamura, “4D XRD for strain in many grains using triangulation,” *Powder Diffr.* **21**, 184 (2006).

Bao, Y., C.L. White, and K. Luger, “Nucleosome core particles containing a Poly(dA$\cdot$dT) sequence element exhibit a locally distorted DNA structure,” *J. Mol. Biol.* **361**, 617 (2006).

Baron, M.K., T.M. Boeckers, B. Vaida, S. Faham, M. Gingery, M.R. Sawaya, D. Salyer, E.D. Gundelfinger, and J.U. Bowie, “An architectural framework that may lie at the core of the postsynaptic density,” *Science* **311**, 531 (2006).

Benzerara, K., N. Menguy, P. López-García, T.H. Yoon, J. Kasmierczak, T. Tyliszczak, F. Guyot, and G.E. Brown, Jr., “Nanoscale detection of organic signatures in carbonate microbialities,” *Proc. Natl. Acad. Sci.* **103**, 9440 (2006).

Berben, L.A., M.C. Faia, N.R.M. Crawford, and J.R. Long, “Angle-dependent electronic effects in 4,4′-bipyridine-bridged Ru_3 triangle and Ru_4 square complexes,” *Inorg. Chem.* **45**, 6378 (2006).

Berrah, N., R.C. Bilodeau, J.D. Bozek, C.W. Walter, N.D. Gibson, and G.D. Ackerman, “Double-Auger decay, Feshbach and shape resonances in negative ions,” *Radiat. Phys. Chem.* **75**, 1447 (2006).

Bethune, M.T., P. Strop, Y. Tang, L.M. Sollid, and C. Khosla, “Heterologous expression, purification, refolding, and structural-functional characterization of EP-B2, a self-activating barley cysteine endoprotease,” *Chem. Bio.* **13**, 637 (2006).

Bhattacharyya, R.P., A. Remenyi, M.C. Good, C.J. Bashor, A.M. Falick, and W.A. Lim, “The Ste5 Scaffold allosterically modulates signaling output of the yeast mating pathway," *Science* **311**, 822 (2006).

Bilodeau, R.C., C.W. Walter, I. Dumitriu, N.D. Gibson, G.D. Ackerman, J.D. Bozek, B.S. Rude, R. Santra, L.S. Cederbaum, and N. Berrah, "Photo double detachment of CN^-: Electronic decay from an inner-valence hole in molecular anions," *Chem. Phys. Lett.* **426**, 237 (2006).

Bilodeau, R.C., J.D. Bozek, G.D. Ackerman, N.D. Gibson, C.W. Walter, A. Aguilar, G. Turri, I. Dumitriu, and N. Berrah, "Multi-Auger decay in negative ion photodetachment," *AIP Conf. Proc.* **811**, 120 (2006); Thirteenth International Symposium on Polarization and Correlation in Electronic and Atomic Collisions and International Symposium on (e,2e) Double Photoionization, and Related Topics, Buenos Aires, Argentina, July 28–30, 2005.

Bilodeau, R.C., J.D. Bozek, G.D. Ackerman, A. Aguilar, and N. Berrah, "Photodetachment of He^- near the 1s threshold: Absolute cross-section measurements and postcollision interactions," *Phys. Rev. A* **73**, 034701 (2006).

Biswal, B.K., G. Garen, M.M. Cherney, C. Garen, and M.N. James, "Cloning, expression, purification, crystallization and preliminary x-ray studies of epoxide hydrolases A and B from *Mycobacterium tuberculosis*," *Acta Crystallogr. F* **62**, 136 (2006).

Biswal, B.K., K. Au, M.M. Cherney, C. Garen, and M.N. James, "The molecular structure of Rv2074, a probable pyridoxine 5′-phosphate oxidase from *Mycobacterium tuberculosis*, at 1.6 angstroms resolution," *Acta Crystallog. F.* **62**, 735 (2006).

Biswal, B.K., M. Wang, M.M. Cherney, L. Chan, C.G. Yannopoulos, D. Bilimoria, J. Bedard, and M.N.G. James, "Non-nucleoside inhibitors binding to hepatitis C virus NS5B polymerase reveal a novel mechanism of inhibition," *J. Mol. Biol.* **361**, 33 (2006).

Blasiak, L.C., F.H. Vaillancourt, C.T. Walsh, and C.L. Drennan, "Crystal structure of the non-haem iron halogenase SyrB2 in syringomycin biosynthesis," *Nature* **440**, 368 (2006).

Bluhm, H., J. Andersson, T. Araki, K. Benzerara, G.E. Brown, J.J. Dynes, S. Ghosal, M.K. Gilles, H.-Ch. Hansen, J.C. Hemminger, A.P. Hitchcock, G. Ketteler, A.L.D. Kilcoyne, E. Kneedler, J.R. Lawrence, G.G. Leppard, J. Majzlam, B.S. Mun, S.C.B. Myneni, A. Nilsson, H. Ogasawara, D.F. Ogletree, K. Pecher, M. Salmeron, D.K. Shuh, B. Tonner, T. Tyliszczak, and T.H. Yoon, "Soft x-ray microscopy and spectroscopy at the Molecular Environmental Science Beamline at the Advanced Light Source," *J. Electron Spectrosc.* **150**, 86 (2006).

Blum, M., "X-ray and electron spectroscopy of WO_3 and $CdS/Cu(In,Ga)Se_2$ thin films for photoelectrochemical and photovoltaic devices," masters thesis, University of Würzburg, Germany (2006).

Bolte, M., R. Eiselt, G. Meier, D.-H. Kim, and P. Fischer, "Real space observation of dipolar interaction in arrays of Fe microelements," *J. Appl. Phys.* **99**, 08H301 (2006).

Borchers, C., T.I. Khomenko, O.S. Morozova, A.V. Galakhov, E.Z. Kurmaev, J. MacNaughton, M.V. Yablonskikh, and A. Moewes, "Influence of graphite addition on the reactivity of Ti powder with H_2 under ball milling," *J. Phys. Chem. B* **110**, 196 (2006).

Bosch, J., M.A. Robien, C. Mehlin, E. Boni, A. Riechers, F.S. Buckner, W.C. Van Voorhis, P.J. Myler, E.A. Worthey, G. DeTitta, J.R. Luft, A. Lauricella, S. Gulde, L.A. Anderson, O. Kalyuzhniy, H.M. Neely, J. Ross, T.N. Earnest, M. Soltis, L. Schoenfeld, F. Zucker, E.A. Merritt, E. Fan, C.L. Verlinde, and W.G.J. Hol, "Using fragment cocktail crystallography to assist inhibitor design of *Trypanosoma brucei* nucleoside 2-deoxyribosyltransferase," *J. Med. Chem.* **49**, 5939 (2006).

Bosch, J., S. Turley, T.M. Daly, S.M. Bogh, M.L. Villasmil, C. Roach, N. Zhou, J.M. Morrisey, A.B. Vaidya, L.W. Bergman, and W.G. Hol, "Structure of the MTIP-MYOA complex, a key component of the malaria parasite invasion motor," *Proc. Natl. Acad. Sci. USA* **103**, 4852 (2006).

Bozek, J.D., J.E. Furst, T.J. Gay, H. Gould, A.L.D. Kilcoyne, J.R. Machacek, F. Martin, K.W. McLaughlin, and J.L. Sanz-Vicario, "Production of excited atomic hydrogen and deuterium from H_2 and D_2 photodissociation," *J. Phys. B: At. Mol. Opt. Phys.* **39**, 4871 (2006).

Braun, A., F.E. Huggins, K.E. Kelly, B.S. Mun, S.N. Ehrlich, and G.P. Huffmann, "Impact of ferrocene on the structure of diesel exhaust soot as probed with wide-angle x-ray scattering and C(1s) NEXAFS spectroscopy," *Carbon* **44**, 2904 (2006).

Braun, A., S. Wirick, A. Kubatova, B.S. Mun, and F.E. Huggins, "Photochemically induced decarboxylation in diesel soot extracts," *Atmos. Environ.* **40**, 5837 (2006).

Brenk, R., S.W. Vetter, S.E. Boyce, D.B. Goodin, and B.K. Shoichet, "Probing molecular docking in a charged model binding site," *J. Mol. Biol.* **357**, 1449 (2006).

Bridges, K.G., R. Chopra, L. Lin, K. Svenson, A. Tam, G. Jin, R. Cowling, F. Lovering, T.N. Akopian, E. DiBlasio-Smith, B. Annis-Freeman, T.H. Marvell, E.R. LaVallie, R.S. Zollner, J. Bard, W.S. Somersa, M.L. Stahl, and R.W. Kriz, "A novel approach to identifying β-secretase inhibitors: Bis-statine peptide mimetics discovered using structure and spot synthesis," *Peptides* **27**, 1877 (2006).

Brimhall, N., J.C. Painter, M. Turner, S.V. Voronov, R.S. Turley, M. Ware, and J. Peatross, "Construction of an extreme ultraviolet polarimeter based on high-order harmonic generation," *Proc. SPIE* **6317**, 63170Y-01 (2006).

Brimhall, N.F., A.B. Grigg, R.S. Turley, and D.D. Allred, "Thorium dioxide thin films in the extreme ultraviolet," *Proc. SPIE* **6317**, 631710 (2006).

Brouet, V., W.L. Yang, X.J. Zhou, Z. Hussain, and Z.X. Shen, "Dependence of the band structure of C_{60} monolayers on molecular orientations and doping observed by angle resolved photoemission," *J. Phys. Chem. Solids* **67**, 218 (2006).

Brown, M.A., T.-S. Park, A. Rosakis, E. Ustundag, Y. Huang, N. Tamura, and B.C. Valek, "A comparison of x-ray microdiffraction and coherent gradient sensing in measuring discontinuous curvatures in thin film-substrate systems," *J. Appl. Mech.* **73**, 723 (2006).

Brownlee, D., et al., "Comet 81P/Wild 2 under a microscope," *Science* **314,** 1711 (2006).

Budiman, A.S., N. Tamura, B.C. Valek, K. Gadre, J. Maiz, R. Spolenak, J.R. Patel, and W.D. Nix, "Electromigration-induced plastic deformation in Cu damascene interconnect lines as revealed by synchrotron x-ray microdiffraction," *Proc. 2006 MRS Spring Meeting* **914**, F06-05 (2006); 2006 MRS Spring Meeting, San Francisco, CA, April 17–21, 2006.

Budiman, A.S., W.D. Nix, N. Tamura, B.C. Valek, K. Gadre, J. Maiz, R. Spolenak, and J.R. Patel, "Crystal plasticity in Cu damascene interconnect lines undergoing electromigration as revealed by synchrotron x-ray microdiffraction," *Appl. Phys. Lett.* **88**, 233515 (2006).

Buonassisi, T., A.A. Istratov, M.D. Pickett, J.-P. Rakotoniaina, O. Breitenstein, M.A. Marcus, S.M. Heald, and E.R. Weber, "Transition metals in photovoltaic-grade ingot-cast multicrystalline silicon: Assessing the role of impurities in silicon nitride crucible lining material," *J. Cryst. Growth* **287**, 402 (2006).

Buonassisi, T., A.A. Istratov, M.D. Pickett, M. Heuer, J.P. Kalejs, G. Hahn, M.A. Marcus, B. Lai, Z. Cai, S.M. Heald, T.F. Ciszek, R.F. Clark, D.W. Cunningham, A.M. Gabor, R. Jonczyk, S. Narayanan, E. Sauar, and E. R. Weber, "Chemical natures and distributions of metal impurities in multicrystalline silicon materials," *Prog. Photovolt: Res. Appl.* **14,** 513 (2006).

Buonassisi, T., A.A. Istratov, M.D. Pickett, M.A. Marcus, T.F. Ciszek, and E.R. Weber, "Metal precipitation at grain boundaries in silicon: Dependence on grain boundary character and dislocation decoration," *Appl. Phys. Lett.* **89**, 042102 (2006).

Byrd, J.M., Z. Hao, M.C. Martin, D.S. Robin, F. Sannibale, R.W. Schoenlein, A.A. Zholents, and M.S. Zolotorev, "Tailored terahertz pulses from a laser-modulated electron beam," *Phys. Rev. Lett.* **96**, 164801 (2006).

Byrd, J.M., Z. Hao, M.C. Martin, D.S. Robin, F. Sannibale, R.W. Schoenlein, A.A. Zholents, and M.S. Zolotorev, "Laser seeding of the storage-ring microbunching instability for high-power coherent terahertz radiation," *Phys. Rev. Lett.* **97**, 074802 (2006).

Cain, J.P., P.P. Naulleau, and C.J. Spanos, "Resist-based measurement of the contrast transfer function in a 0.3-numerical aperture extreme ultraviolet microfield optic," *J. Vac. Sci. Technol. B* **24**, 326 (2006).

Cain, J.P., P.P. Naulleau, E.M. Gullikson, and C.J. Spanos, "Lithographic characterization of the flare in the Berkeley 0.3 numerical aperture extreme ultraviolet microfield optic," *J. Vac. Sci. Technol. B* **24**, 1234 (2006).

Cappa C.D., J.D. Smith, B.M. Messer, R. C. Cohen, and R.J. Saykally, "The electronic structure of the hydrated proton: A comparative x-ray absorption study of aqueous HCl and NaCl solutions," *J. Phys. Chem. B.* **110**, 1166 (2006).

Cappa, C.D., J.D. Smith, B.M. Messer, R.C. Cohen, and R.J. Saykally, "Effects of cations on the hydrogen bond network of liquid water: New results from x-ray absorption spectroscopy of liquid microjets," *J. Phys. Chem. B* **110**, 5301 (2006).

Cardoso, R.M.F., F.M Brunel, S. Ferguson, M. Zwick, D.R. Burton, P.E. Dawson, and I.A. Wilson, "Structural basis of enhanced binding of extended and helically constrained peptide epitopes of the broadly neutralizing HIV-1 antibody 4E10," *J. Mol. Biol.* **365**, 1533 (2006).

Caruthers, J.M., Y. Hu, and D.B. McKay, "Structure of the second domain of the Bacillus subtilis DEAD-box RNA helicase $Y_{xi}N$," *Acta Crystallogr. F* **62**, 1191 (2006).

Castelnau, O., P.Goudeau, G. Geandier, N. Tamura, J.-L Béchade, M. Bornert, and D. Caldemaison, "White beam microdiffraction experiments for the determination of the local plastic behaviour of polycrystals," *Mater. Sci. Forum* **524**, 103 (2006).

Chang, C., A. Sakdinawat, P. Fischer, E. Anderson, and D. Attwood, "Single-element objective lens for soft-x-ray differential interference contrast microscopy," *Opt. Express* **31**, 1564 (2006).

Chang, G.S., A. Moewes, S.H. Kim, J. Lee, K. Jeong, C.N. Whang, D.H. Kim, and S.C. Shin, "Uniaxial in-plane magnetic anisotropy of a CoPt thin film induced by ion irradiation," *Appl. Phys. Lett.* **88**, 092504 (2006).

Chang, G.S., E.Z. Kurmaev, D.V. Boukhvalov, L.D. Finkelstein, D.H. Kim, T.-W. Noh, A. Moewes, and T.A. Callcott, "Clustering of impurity atoms in Co-doped anatase TiO_2 thin films probed with soft x-ray fluorescence," *J. Phys.: Condens. Matter* **18**, 4243 (2006).

Chang, G.S., E.Z. Kurmaev, L.D. Finkelstein, N.A. Babushkina, T. Pederson, A. Moewes, and T.A. Callcott, "Probing changes in the Mn 3d band of $Sm_{0.525}Sr_{0.475}MnO_3$ induced by oxygen isotope substitution," *Phys. Rev. B* **74**, 125105 (2006).

Chao, W., B. D. Harteneck, J.A. Liddle, E. H. Anderson and D. T. Attwood, "Zone plate microscopy to sub-15 nm spatial resolution with XM-1 at the ALS," *Proc. 8th Int. Conf.* **7**, 4 (2006); 8th International Conference on X-ray Microscopy, Himeji City, Japan, July 26–30, 2005.

Chen, G., C.Wang, C., C. Fuqua, L.H. Zhang, and L. Chen, "Crystal structure and mechanism of TraM2, a second quorum-sensing antiactivator of *Agrobacterium tumefaciens* strain A6," *J. Bacteriol.* **188**, 8244 (2006).

Chen, Y., A. Iyo, W.L. Yang, X.J. Zhou, D. Lu, H. Eisaki, T.P. Devereaux, Z. Hussain, and Z.X. Shen, "Anomalous Fermi-surface dependent pairing in a self-doped high-T_c superconductor," *Phys. Rev. Lett.* **97**, 236401 (2006).

Chen, Z., J. Zang, J. Whetstine, X. Hong, F. Davrazou, T.G. Kutateladze, M. Simpson, Q. Mao, C.-H. Pan, S. Dai, J. hagman, K. Hansen, Y. Shi, and G. Zhang, "Structural insights into histone demethylation by JMJD2 family members," *Cell* **125**, 691 (2006).

Cheng, J.C., "Chitosan as a MEMS Engineering Material," masters thesis, University of California, Berkeley (2006).

Cherney, M.M., P. Marcato, G.L. Mulvey, G.D. Armstrong, M.E. Fraser, and M.N.G. James, "Binding of adenine to Stx2, the protein toxin from *Escherichia coli* O157:H7," *Acta Crystallogr.* **62**, 627 (2006).

Chikan, V., F. Fournier, S.R. Leone, and B. Nizamov, "State-resolved dynamics of the CH(A2Delta) channels from single and multiple photon dissociation of bromoform in the 10–20 eV energy range," *J. Phys. Chem. A* **110**, 2850 (2006).

Cho, U.S., M.W. Bader, M.F. Amaya, M.E. Daley, R.E. Klevit, S.I. Miller, and W. Xu, "Metal bridges between the PHOQ sensor domain and the membrane regulate transmembrane signaling," *J. Mol. Biol.* **356**, 1193 (2006).

Chou, K.W., A. Puzic, H. Stoll, G. Schuetz, B. Van Waeyenberge, T. Tyliszczak, K. Rott, G. Reiss, H. Brueckl, I. Neudecker, D. Weiss, and C.H. Back, "Vortex dynamcs in coupled ferromagnetc multilayer structures," *J. Appl. Phys.* **99**, 08F305 (2006).

Chrencik, J.E., A. Brooun, M.I. Recht, M.L. Kraus, M. Koolpe, A.R. Kolatkar, R.H. Bruce, G. Martiny-Baron, H. Widmer, E.B. Pasquale, and P. Kuhn, "Structure and thermodynamic characterization of the EPHB4/ephrin-B2 antagonist peptide complex reveals the determinants for receptor specificity," *Structure* **14**, 321 (2006).

Colakerol, L., T.D. Veal, H.K. Jeong, L. Plucinski, A. DeMasi, T. Learmonth, P.A. Glans, S. Wang, Y. Zhang, L.F.J Piper, P.H. Jefferson, A.V. Fedorov, T.-C. Chen, T.D. Moustakas, C.F. McConville, and K.E. Smith, "Quantized electron accumulation states in indium nitride studied by angle-

resolved photoemission spectroscopy," *Phys. Rev. Lett.* **97**, 237601 (2006).

Compaan, D.M., and Hymowitz, S.G., "The crystal structure of the costimulatory OX40-OX40L complex," *Structure* **14**, 1321 (2006).

Corbett, K.D., and J.M. Berger, "Structural basis for topoisomerase VI inhibition by the anti-Hsp90 drug radicicol," *NAR* **34**, 4269 (2006).

Cronk, J.D., R.S. Rowlett, K.Y.J. Zhang, C. Tu, J.A. Endrizzi, J. Lee, P.C. Gareiss, and J.R. Preiss, "Identification of a novel non-catalytic bicarbonate binding site in eubacterial beta-carbonic anhydrase," *Biochemistry* **45**, 4351 (2006).

Danzenbächer, S., Y. Kucherenko, C. Laubschat, D.V. Vyalikh, Z. Hossain, C. Geibel, X.J. Zhou, W.L. Yang, N. Mannella, Z. Hussain, Z.-X. Shen, and S.L. Molodtsov, "Energy dispersion of 4f-derived emissions in photoelectron spectra of the heavy-fermion compound YbIr$_2$Si$_2$," *Phys. Rev. Lett.* **96**, 106402 (2006).

Das A., E.D. Poliakoff, R.R. Lucchese, and J.D. Bozek, "Launching a particle on a ring: $b_{2u} \rightarrow ke_{2g}$ ionization of C$_6$F$_6$," *J. Chem. Phys.* **125**, 164316 (2006).

Dash, R., J. Chmiola, G. Yushin, Y. Gogotsi, G. Laudisio, J. Singer, J. Fisher, and S. Kucheyev, "Titanium carbide derived nanoporous carbon for energy-related applications," *Carbon* **44**, 2489 (2006).

De Stasio, G., D. Rajesh, J.M. Ford, M.J. Daniels, R.J. Erhardt, B.H. Frazer, T. Tyliszczak, M.K. Gilles, R.L. Conhaim, S.P. Howard, J.F. Fowler, F. Esteve, and M.P. Mehta, "Motexafin-gadolinium taken up in vitro by at least 90% of glioblastoma cell nuclei," *Clin. Cancer Res.* **12**, 206 (2006).

Denbeaux G., P. Fischer, F. Salmassi, K. Dunn, and J. Evertsen, "Reflection mode imaging with high resolution x-ray microscopy," *Proc. 8th Int. Conf.* **7**, 375 (2006); 8th International Conference on X-ray Microscopy, Himeji City, Japan, July 26–30, 2005.

Di Stasio, S., and A. Braun, "Comparative NEXAFS study on soot obtained from an ethylene/air flame, a diesel engine, and graphite," *Energy Fuels* **20**, 187 (2006).

Dinca, M., A.F. Yu, and J.R. Long, "Microporous metal-organic frameworks incorporating 1,4-benzeneditetrazolate: Syntheses, structures, and hydrogen storage properties," *J. Am. Chem. Soc.* **128**, 8904 (2006).

Dong, C.L., M. Mattesini, A. Augustsson, X.G. Wen, W.X. Zhang, S.H. Yang, C. Persson, R. Ahuja, J. Luning, C.L. Chang, and J.-H. Guo, "Electronic structure and surface structure of Cu$_2$S nanorods from polarization dependent x-ray absorption spectroscopy," *J. Electron Spectrosc.* **151**, 64 (2006).

Doolittle, R.F., A. Chen, and L. Pandi, "Differences in binding specificity for the homologous γ- and β-chain "holes" on fibrinogen: Exclusive binding of Ala-His-Arg-Pro-amide by the β-chain hole," *Biochemistry* **45**, 13962 (2006).

Drake, I.J., Y. Zhang, M.K. Gilles, C.N.T. Liu, P. Nachimuthu, R.C.C. Perera, H. Wakita, and A.T. Bell, "An in situ Al K-Edge XAS investigation of the local environment of H$^+$- and Cu$^+$-exchanged USY and ZSM-5 zeolites," *J. Phys. Chem. B* **110**, 11665 (2006).

Dressler, R.A., Y. Chiu, D.J. Levandier, X.N. Tang, Y. Hou, C. Chang, C. Houchins, H. Xu, and C.-Y. Ng, "The study of state-selected ion-molecule reactions using the vacuum ultraviolet pulsed field ionization-photoion technique," *J. Chem. Phys.* **125**, 132306 (2006).

Du, Z., J.K. Lee, R. Tjhen, S. Li, H. Pan, R.M. Stroud, and T.L. James, "Crystal structure of the first KH domain of human poly(C)-binding protein-2 in complex with a C-rich strand of human telomeric DNA at 1.7 Å," *J. Biol. Chem.* **280**, 38823 (2005).

Dynes, J.J., J.R. Lawrence, D.R. Korber, G.DW. Swerhone, G.G. Leppard, and A.P. Hitchcock, "Quantitative mapping of chlorhexidine in natural river biofilms," *Sci. Total Environ.* **369**, 369 (2006).

Dynes, J.J., T. Tyliszczak, T. Araki, J.R. Lawrence, G.D. Swerhone, G.G. Leppard, and A.P. Hitchcock, "Speciation and quantitative mapping of metal species in microbial biofilms using scanning transmission x-ray microscopy," *Environ. Sci. Technol.* **40**, 1556 (2006).

Ebke, D., J. Schmalhorst, N.-N. Liu, A. Thomas, G. Reiss, and A. Huetten, "Large tunnel magnetoresistance in tunnel junctions with Co$_2$MnSi/Co$_2$FeSi multilayer electrode," *Appl. Phys. Lett.* **89**, 162506 (2006).

Eddins, M.J., C.M. Carlile, K.M. Gomez, C.M. Pickart, and C. Wolberger, "Mms$_2$-Ubc$_{13}$ covalently bound to ubiquitin reveals the structural basis of linkage-specific polyubiquitin chain formation," *NSMB* **13**, 915 (2006).

Edmonds, K.W., G. van der Laan, A.A. Freeman, N.R. Farley, T.K. Johal, R.P. Campion, C.T. Foxon, B.L. Gallagher, and E. Arenholz, "Angle-dependent x-ray magnetic circular dichroism from (Ga,Mn)As: Anisotropy and identification of hybridized states," *Phys. Rev. Lett.* **96**, 117207 (2006).

Edwards, T.E., and A.R. Ferre-D'Amare, "Crystal Structures of the thi-box riboswitch bound to thiamine pyrophosphate analogs reveal adaptive RNA-small molecule recognition," *Structure* **14**, 1459 (2006).

Eich, D., O. Fuchs, U. Groh, L. Weinhardt, R. Fink, E. Umbach, C. Heske, A. Fleszar, W. Hanke, E.K.U. Gross, C. Bostedt, T. van Buuren, N. Franco, L.J. Terminello, L.J. Keim, G. Reuscher, H. Lugauer, and A. Waag, "Resonant inelastic soft x-ray scattering of Be chalcogenides," *Phys. Rev. B* **73**, 115212 (2006).

Eriksson, F., N. Ghafoor, F. Schafers, E.M. Gullikson, and J. Birch, "Interface engineering of short-period Ni/V multilayer x-ray mirrors," *Thin Solid Films 500,* **84** (2006).

Erzberger, J.P., M.L. Mott, and J.M. Berger, "Structural basis for ATP-dependent DnaA assembly and replication-origin remodeling," *Nat. Struct. Mol. Biol.* **13**, 676 (2006).

Evans, W.R., S.C. Barton, M. Clemens, and D.D. Allred, "Understanding DC-bias sputtered thorium oxide thin films useful in EUV optics," *Proc. SPIE*, **6316**, 631711-01 (2006); Advances in X-Ray/EUV Optics, Components, and Applications, Optics and Photonics 2006, San Diego California, August 13–17, 2006.

Faiz M., N. Tabet, A. Mekki, B. S. Mun, Z. Hussain," X-ray absorption near edge structure investigation of vanadium-doped ZnO thin films," *Thin Solid Film* **515**, 1377 (2006).

Fan, L., A.S. Arvai, P.K. Cooper, S. Iwai, F. Hanaoka, and J.A. Tainer, "Conserved XPB core structure and motifs for DNA unwinding: Implications for pathway selection of transcription or excision repair," *Mol. Cell* **22**, 27 (2006).

Fassbender, J., L. Bischoff, R. Mattheis, and P. Fischer, "Magnetic domains and magnetization reversal of ion-induced magnetically patterned Ruderman-Kittel-Kasuya-Yoshida-coupled Ni$_{81}$Fe$_{19}$/Ru/Co$_{90}$Fe$_{10}$ films," *J. Appl. Phys.* **99**, 08G301 (2006).

Feinberg, H., R. Castelli, K. Drickamer, P.H. Seeberger, and W.I. Weis, "Multiple modes of binding enhance the affinity of DC-SIGN for high-mannose N-linked glycans found on viral glycoproteins," *J. Biol. Chem.* **282**, 4202 (2006).

Felten, A., H. Hody, C. Bittencourt, J.-J. Pireaux, D. Hernandez Cruz, and A.P. Hitchcock, "Scanning transmission x-ray microscopy of isolated multiwall carbon nanotubes," *Appl. Phys. Lett.* **89**, 093123 (2006).

Felts, R.L., T.J. Reilly, and J.J. Tanner, "Structure of *Francisella tularensis* AcpA: Prototype of a unique superfamily of acid phosphatases and phospholipases C," *J. Biol. Chem.* **281**, 30289 (2006).

Felts, R.L., T.J. Reilly, M.J. Calcutt, and J.J. Tanner, "Cloning, purification and crystallization of *Bacillus anthracis* class C acid phosphatase," *Acta Crystallogr., Sec. F: Struct. Biol. Cryst. Comm.* **62**, 705 (2006).

Felts, R.L., T.J. Reilly, M.J. Calcutt, and J.J. Tanner, "Crystallization of a newly discovered histidine acid phosphatase from *Francisella tularensis*," *Acta Crystallogr., Sec. F: Struct. Biol. Cryst. Comm.* **62**, 32 (2006).

Finazzi, M., A. Brambilla, P. Biagioni, J. Graf, G.-H. Gweon, A. Scholl, A. Lanzara, and L. Duò, "Interface coupling transition in a thin epitaxial antiferromagnetic film interacting with a ferromagnetic substrate," *Phys. Rev. Lett.* **97**, 097202 (2006).

Finkelshtein, L.D., I.A. Nekrasov, A.V. Lukoyanov, E.Z. Kurmaev, V.I. Anisimov, S. Kucas, A. Kyniene, A. Moewes, J.-L. Wang, and Z. Zeng, "The origin of an elastic line in the L_3 x-ray emission spectrum of metallic manganese," *Phys. Solid State* **48**, 420 (2006).

Fischer, P., "Studies of magnetic microstructures with soft x-ray transmission microscopy," *IEEE J. Quantum Electron.* **42**, 36 (2006).

Fischer, P., D.-H. Kim, B. Kang, W. Chao, and E.H. Anderson, "Magnetic microstructures and their dynamics studied by x-ray microscopy," *Micron* **37**, 296 (2006).

Fischer, P., D.-H. Kim, B.-S. Kang, W. Chao and E. H. Anderson, "Achievements and perspectives of magnetic soft x-ray transmission microscopy," *Proc. 8th Int. Conf.* **7**, 252; 8th International Conference on X-ray Microscopy, Himeji City, Japan, July 26–30, 2005.

Fischer, P., D.H. Kim, W. Chao, J.A. Liddle, E.H. Anderson, and D.T. Attwood, "Soft x-ray microscopy of nanomagnetism," *Mater. Today* **9**, 26 (2006).

Flynn, G.J., et al., "Elemental composition of Comet 81P/Wild 2 samples collected by Stardust," *Science* **314**, 1731 (2006).

Fraser, M.E., K. Hayakawa, M.S. Hume, D.G. Ryan, and E.R. Brownie, "Interactions of GTP with the ATP-grasp domain of GTP-specific succinyl-CoA synthetase," *J. Biol. Chem.* **281**, 11058 (2006).

Fraser, M.E., M.M. Cherney, P. Marcato, G.L. Mulvey, G.D. Armstrong, and M.N. James, "Binding of adenine to Stx2, the protein toxin from *Escherichia coli* O157:H7," *Acta Crystallogr., Sec. F: Struct. Biol. Cryst. Comm.* **62**, 627 (2006).

Freedman, D.E., M.V. Bennett, and J.R. Long, "Symmetry-breaking substitutions of $[Re(CN)_8]^{3-}$ into the centered, face-capped octahedral clusters $(CH_3OH)_{24}M_9M'_6(CN)_{48}$ (M = Mn,Co; M′ = Mo,W)," *Dalton Trans.* **23**, 2829 (2006).

Freedman, T.S., Sondermann, H., Friedland, G.D., Kortemme, T., Bar-Sagi, D., Marqusee, S., Kuriyan, J. "A Ras-induced conformational switch in the Ras activator Son of sevenless," *Proc. Natl. Acad. Sci.* **103**, 16692 (2006).

Freelon, B., A. Augustsson, J.-H. Guo, P. G. Medaglia, A. Tebano, and G. Balestrino, "Electron correlation and charge transfer in $[(Ba_{0.9}Nd_{0.1})CuO_{2+\delta}]_2/[CaCuO_2]_2$ superconducting superlattices," *Phys. Rev. Lett.* **96**, 017003 (2006).

Freeman, A.A., K.W. Edmonds, G. van der Laan, N.R.S. Farley, T.K. Johal, E. Arenholz, R.P. Campion, C.T. Foxon, and B.L. Gallagher, "Giant anisotropy in x-ray magnetic linear dichroism from (Ga,Mn)As," *Phys. Rev. B* **73**, 233303 (2006).

Freeman, J.L., C.F. Quinn, M.A. Marcus, S. Fakra, and E.H. Pilon-Smits, "Selenium-tolerant diamondback moth disarms hyperaccumulator plant defense," *Curr. Biol.* **16**, 2181 (2006).

Freeman, J.L., L.H. Zhang, M.A. Marcus, S. Fakra, S.P. McGrath, and E.A.H. Pilon-Smits, "Spatial imaging, speciation and quantification of selenium in the hyperaccumulator plants *Astragalus bisulcatus* and *Stanleya pinnata*," *Plant Physiol.* **142**, 124 (2006).

Fu, J., "Linear dichroism in the NEXAFS spectroscopyof n-alkane thin films," Ph.D. thesis, University of Saskatchewan, Canada (2006).

Fuh, G., P. Wu, W.C. Liang, M. Ultsch, C.V. Lee, B. Moffat, and C. Wiesmann, "Structure-function studies of two synthetic anti-vascular endothelial growth factor Fabs and comparison with the Avastin™ Fab," *J. Biol. Chem.* **281**, 6625 (2006).

Fuhrmann, C.N., M.D. Daugherty, and D.A. Agard, "Subangstrom crystallography reveals that short ionic hydrogen bonds, and not a His-Asp low-barrier hydrogen bond, stabilize the transition state in serine protease catalysis," *J. Am. Chem. Soc.* **128**, 9086 (2006).

Gay, L.M., H.L. Ng, and T. Alber, "A conserved dimer and global conformational changes in the structure of apo-PknE Ser/Thr protein kinase from *Mycobacterium tuberculosis*," *J. Mol. Biol.* **360**, 409 (2006).

Gergaud, P., P. Goudeau, O. Sicardy, N. Tamura, and O. Thomas, "Residual stress analysis in micro- and nano-structured materials by x-ray diffraction," *Int. J. Mater. Prod. Technol.* **26**, 354 (2006).

Gilbert, B., H. Zhang, B. Chen, M. Kunz, F. Huang, and J.F. Banfield, "Compressibility of zinc sulfide nanoparticles," *Phys. Rev. B* **74**, 115405 (2006).

Gilbert, S.D., S.J. Mediatore, and R.T. Batey, "Modified pyrimidines specifically bind the purine riboswitch," *J. Am. Chem. Soc.* **128**, 14214 (2006).

Gloaguen E., E. R. Mysak, S. R. Leone, M. Ahmed, and K. R. Wilson "Investigating the chemical composition of mixed organic-inorganic particles by 'soft' VUV photoionization: The reaction of ozone with anthracene on sodium chloride particles," *Int. J. Mass Spectrom.* **258**, 74 (2006).

Goldberg, K.A., A. Barty, Y. Liu, P. Kearney, Y. Tezuka, T. Terasawa, J.S. Taylor, H.S. Han, and O.R. Wood II, "Actinic inspection of EUV programmed multilayer defects and cross-comparison measurements," *J. Vac. Sci. Technol. B* **24**, 2824 (2006).

Goldstein, D.M., T.A. Alfredson, J. Bertrand, M.F. Browner, K. Clifford, S. Dalrymple, J. Dunn, J. Freire-Moare, S.F. Harris, S.S. Labadie, J. La Fargue, J.M. Lapierre, S. Larrabee, F. Li, E. Papp, D. McWeeney, C. Ramesha, R. Roberts, D. Rotstein, B. San Pablo, E. Sjogren, O.Y. So, F.X. Talamas, W. Tao, A. Trejo, A. Villasenor, M. Welch, T. Welch, P. Weller, P.E. Whiteley, K. Young, and S. Zipfel, "Discovery of *S*-[5-amino-1-(4-fluorophenyl)-1H-pyrazol-4-yl]-[3-(2,3-dihydroxypropoxy)phe nyl]methanone (RO3201195), an orally bioavailable and highly selective inhibitor of p38 map kinase," *J. Med. Chem.* **49**, 1562 (2006).

Gomez, G.A., C. Morisseau, B.D. Hammock, and D.W. Christianson, "Human soluble epoxide hydrolase: Structural basis of inhibition by 4-(3-cyclohexylureido)-carboxylic acids," *Protein Sci.* **15**, 58 (2006).

Gopalsamy, A., R. Chopra, K. Lim, G. Ciszewski, M. Shi, K.J. Curran, S.F. Sukits, K. Svenson, J. Bard, J.W. Ellingboe, A. Agarwal, G. Krishnamurthy, A.Y. Howe, M. Orlowski, B. Feld, J. O'Connell, and T.S. Mansour, "Discovery of proline sulfonamides as potent and selective hepatitis C virus NS5b polymerase inhibitors. Evidence for a new NS5b polymerase binding site," *J. Med. Chem.* **49**, 3052 (2006).

Goudeau, P., D. Faurie, B. Girault, P.-O. Renault, E. Le Bourhis, P. Villain, F. Badawi, O. Castelnau, R. Brenner, J.-L. Bechade, G. Geandier, and N. Tamura, "Strains, stresses and elastic properties in polycrystalline metallic thin films: In situ deformation combined with x-ray diffraction and simulation experiments," *Residual Stresses VII* **524**, 735 (2006); 7th European Conference on Residual Stresses, Berlin Germany, September 13–15, 2006.

Greco, A., J.G.S. Ho, S.-J. Lin, M.M. Palcic, M. Rupnik, and K.K.-S. Ng, "Carbohydrate recognition by *Clostridium difficile* toxin A," *NSMB* **13**, 460 (2006).

Grodsky, N., Y. Li, D. Bouzida, R. Love, J. Jensen, B. Nodes, J. Nonomiya, and S. Grant, "Structure of the catalytic domain of human protein kinase C beta II complexed with a bisindolylmaleimide inhibitor," *Biochemistry* **45**, 13970 (2006).

Guan, L., I.N. Smimova, G. Verner, S. Nagamori, and H.R. Kaback, "Manipulating phospholipids for crystallization of a membrane transport protein," *Proc. Natl. Acad. Sci. USA* **103**, 1723 (2006).

Guo, J.-H., "X-ray absorption and emission spectroscopy in nanoscience and lifesciences," in *Nanosystem Characterization Tools in the Life Sciences,* p. 259 (Wiley-VCH Verlag GmbH & Co. KgaA, Weinheim, 2006).

Hamburger, Z.A., A.E. Hamburger, A.P. West, and W.I. Weis, "Crystal structure of the *S. cerevisiae* exocyst component Exo70p," *J. Mol. Biol.* **356**, 9 (2006).

Hansen, N., S.J. Klippenstein, C.A. Taatjes, J.A. Miller, J. Wang, T.A. Cool, B. Yang, R. Yang, L. Wei, C. Huang, J. Wang, F. Qi, M.E. Law, and P.R. Westmoreland, "Identification and chemistry of C_4H_3 and C_4H_5 isomers in fuel-rich flames," *J. Phys. Chem. A* **110**, 3670 (2006).

Hansen, N., S.J. Klippenstein, J.A. Miller, J. Wang, T.A. Cool, M.E. Law, P.R. Westmoreland, T. Kasper, and K. Kohse-Hoinghaus, "Identification of C_5H_x isomers in fuel-rich flames by photoionization mass spectrometry and electronic structure calculations," *J. Phys. Chem. A* **110**, 4376 (2006).

Harries, J.R., J.P. Sullivan, P. Hammond, and Y. Azuma, "Photoionization of He in the 3*lnl*′ double-excited state energy region: Angular distribution of the fluorescence from the residual ion $He^+(2p)^2P$," *J. Phys. B: At. Mol. Opt. Phys.* **39**, 4819 (2006).

Harrison, A.J., T. Gardenborg, M. Yu, M, Middleditch, R.J. Ramsay, E.N. Baker, and J.S. Lott, "The structure of MbtI from *Mycobacterium tuberculosis*, the first enzyme in the biosynthesis of the siderophore mycobactin, reveals it to be a salicylate synthase," *J.Bacteriol.* **188**, 6081 (2006).

Hasan M.Z., D. Qian, M.L. Foo, and R.J. Cava, "Are cobaltates conventional? An ARPES viewpoint," *Ann. Phys.* **321**, 1568 (2006).

Havermeier, T., "Photoionisation und doppelt angeregte Zustände in Wasserstoff- und Deuterium-Molekülen," masters thesis, University of Frankfurt, Germany (2006).

Head-Gordon, T., and M.E. Johnson, "Tetrahedral structure or chains for liquid water," *Proc. Natl. Acad. Sci. USA* **103**, 7973 (2006).

Heffron, S.E., R. Moeller, and F. Jurnak, "Solving the structure of *Escherichia coli* elongation factor Tu using a twinned data set," *Acta Crystallogr., Sect. D* **62**, 433 (2006).

Heitmann, L.M., A.B. Taylor, P.J. Hart, and A.R. Urbach, "Sequence-specific recognition and cooperative dimerization of N-terminal aromatic peptides in aqueous solution by a synthetic host," *J. Am. Chem. Soc.* **128**, 12574 (2006).

Hemmers, O., R. Guillemin, D. Rolles, A. Wolska, D.W. Lindle, E.P. Kanter, B. Krässig, S.H. Southworth, R. Wehlitz, B. Zimmermann, V. McKoy, and P.W. Langhoff, "Low-energy nondipole effects in molecular nitrogen valence-shell photoionization," *Phys. Rev. Lett.* **97**, 103006 (2006).

Hernandez Cruz, D., M.-E. Rousseau, M.M. West, M. Pezolet, and A.P. Hitchcock, "Quantitative mapping of the orientation of fibroin beta-sheets in *B. mori* cocoon fibers by scanning transmission x-ray microscopy," *Biomacromolecules* **7**, 836 (2006).

Heuer, M., T. Buonassisi, M.A. Marcus, A.A. Istratov, M.D. Pickett, T. Shibata, and E.R. Weber, "Complex intermetallic phase in multicrystalline silicon doped with transition metals," *Phys. Rev. B* **73**, 235204 (2006).

Heyderman L., F. Nolting, D. Backes, S. Czekaj, L. Lopez-Diaz, M. Kläui, U. Rüdiger, C.A.F. Vaz, J.A.C. Bland, R.J. Matelon, U.G. Volkmann, and P. Fischer, "Magnetization reversal in cobalt antidot arrays," *Phys. Rev. B*, **73**, 214429 (2006).

Hoang, C., J. Chen, C.A. Vizthum, J.M. Kandel, C.S. Hamilton, E.G. Mueller, and A.R. Ferre-D'Amare, "Crystal structure of pseudouridine synthase RluA: Indirect sequence readout through protein-induced RNA structure," *Mol. Cell*, **24**, 535 (2006).

Hoffmann, P., D. Schmeisser, H.-J. Engelmann, E. Zschech, H. Stegmann, F. Himpsel, and J. Denlinger, "Characterization of chemical bonding in low-k dielectric materials for interconnect isolation: A XAS and EELS study," *Materials, Technology and Reliability of Low-k Dielectrics and Copper Interconnects* **914**, F01 (2006); Materials Research Society Spring Meeting, San Francisco California, April 17–21, 2006.

Hoink, V., M.D. Sacher, J. Schmalhorst, G. Reiss, D. Engel, T. Weis, and A. Ehresmann, "Thermal stability of magnetic nanostructures in ion-bombardment-modified exchange-bias systems," *Phys. Rev. B* **73**, 224428 (2006).

Holman, H.-Y.N., and M.C. Martin, "Synchrotron radiation infrared spectromicroscopy: A non-invasive molecular probe for biogeochemical processes," *Adv. in Agronomy* **90**, 79 (2006).

Holmes, M.A., F.S. Buckner, W.C. Van Voorhis, C.L. Verlinde, C. Mehlin, E. Boni, G. Detitta, J. Luft, A. Lauricella, L. Anderson, O. Kalyuzhniy, F. Zucker, L.W. Schoenfeld, T.N. Earnest, W.G. Hol, and E.A. Merritt, "Structure of ribose 5-phosphate isomerase from *Plasmodium falciparum*," *Acta Crystallogr., Sect. F* **62**, 427 (2006).

Horn, K., W. Theis, J.J. Paggel, S.R. Bar-

man, E. Rotenberg, Ph. Ebert, and K. Urban, “Core and valence level photoemission and photoabsorption study of icosahedral Al-Pd-Mn quasicrystals,” *J. Phys.: Condens. Matter* **18**, 435 (2006).

Hosaka, K., J. Adachi, A.V. Golovin, M. Takahashi, T. Teramoto, N. Watanabe, T. Jahnke, Th. Weber, M. Schöffler, L. Schmidt, T. Osipov, O. Jagutzki, A.L. Landers, M.H. Prior, H. Schmidt-Böcking, R. Dörner, A. Yagishita, S. K. Semenov, and N. A. Cherepkov, “Nondipole effects in the angular distribution of photoelectrons from the C *K* shell of the CO molecule,” *Phys. Rev. A: At. Mol. Opt. Phys.* **73**, 022716 (2006).

Hu, X., A. Addlagatta, B.W. Matthews, and J.O. Liu, “Identification of pyridinylpyrimidines as inhibitors of human methionine aminopeptidases,” *Angew. Chem. Int. Ed. Engl.* **45**, 3772 (2006).

Hu, X., A. Addlagatta, J. LuB.W. Matthews, and J.O. Liu, “Elucidation of the function of type 1 human methionine aminopeptidase during cell cycle progression,” *Proc. Natl. Acad. Sci. USA*, **103**, 18148 (2006).

Huang, L., G. Sun, D. Cobessi, A.C. Wang, J.T. Shen, E.Y. Tung, V.E. Anderson, and E.A. Berry, “3-nitropropionic acid is a suicide inhibitor of mitochondrial respiration that, upon oxidation by complex II, forms a covalent adduct with a catalytic base arginine in the active site of the enzyme,” *J. Biol. Chem.* **281**, 5965 (2006).

Huang, L.S., J.T. Shen, A.C. Wang, and E.A. Berry, “Crystallographic studies of the binding of ligands to the dicarboxylate site of Complex II, and the identity of the ligand in the ‘oxaloacetate-inhibited’ state,” *Biochim. Biophys. Acta* **1757**, 1073 (2006).

Huetten, A., J. Schmalhorst, A. Thomas, S. Kammerer, M. Sacher, D. Ebke, N.-N. Liu, X. Kou, and G. Reiss, “Spin-electronic devices with half-metallic Heusler alloys,” *J. Alloys Cmpd.* **423**, 148 (2006).

Hunt, A., W.Y. Ching, Y.M. Chiang, and A. Moewes, “Electronic structures of $LiFePO_4$ and $FePO_4$ studied using resonant inelastic x-ray scattering,” *Phys. Rev. B* **73**, 205120 (2006).

Hwang, W.C., Y. Lin, E. Santelli, J. Sui, L. Jaroszewski, B. Stec, M. Farzan, W.A. Marasco, and R.C. Liddington, “Structural basis of neutralization by a human anti-severe acute respiratory syndrome spike protein antibody, 80R,” *J. Biol. Chem.* **281**, 34610 (2006).

Hyre, D.E., I. Le Trong, E.A. Merritt, J.F. Eccleston, N.M. Green, R.E. Stenkamp, and P.S. Stayton, “Cooperative hydrogen-bond interactions in the streptavidin-biotin system,” *Protein Sci.* **15**, 459 (2006).

Ishino, M., P.A. Heimann, H. Sasai, M. Hatayama, H. Takenaka, K. Sano, E.M. Gullikson, and M. Koike, “Development of multilayer laminar-type diffraction gratings to achieve high diffraction efficiencies in the 1–8 keV energy region,” *Appl. Optics* **45**, 6741 (2006).

Istratov, A.A., T. Buonassisi, M.D. Pickett, M. Heuer, and E.R. Weber, “Control of metal impurities in ‘dirty’ multicrystalline silicon for solar cells,” *Mater. Sci. Eng., B* **134**, 282 (2006).

Iwata, N., “Industrial application of x-ray absorption spectroscopy and scanning transmission x-ray microscopy for materials analysis,” Ph.D. thesis, Chiba University, Japan (2006).

Iwata, N., K. Tani, A. Watada, H. Ikeura-Sekiguchi, T. Araki, and A.P. Hitchcock, “Chemical component mapping of pulverized toner by scanning transmission x-ray microscopy,” *Micron* **37**, 290 (2006).

Iwata, N., K. Tani, A. Watada, H. Ikeura-Sekiguchi, T. Araki, and A.P. Hitchcock, “Mapping very similar chemical components in micron-scale organic rods by scanning transmission x-ray microscopy,” *Proc. 8th Int. Conf.* **7**, 255 (2006); 8th International Conference on X-ray Microscopy, Himeji City, Japan, July 26–30, 2005.

Jacobs, M., K. Hayakawa, L. Swenson, S. Bellon, M. Fleming, P. Taslimi, and J. Doran, “The structure of dimeric ROCK I reveals the mechanism for ligand selectivity,” *J. Biol. Chem.* **281**, 260 (2006).

Jacobs, S.A., E.R. Podell, and T.R. Cech, “Crystal structure of the essential N-terminal domain of telomerase reverse transcriptase,” *Nat. Struct. Mol. Biol.* **13**, 218 (2006).

Jager, M., Y. Zhang, J. Bieschke, H. Nguyen, M. Dendle, M.E. Bowman, J.P. Noel, M. Gruebele, and J.W. Kelly, “Structure-function-folding relationship in a MW domain,” *Proc. Natl. Acad. Sci. USA* **103**, 10648 (2006).

Jang, S.B., L.-W. Hung, M.S. Jeong, E.L. Holbrook, X. Chen, D.H. Turner, and S.R. Holbrook, “The crystal structure at 1.5 Å resolution of an RNA octamer duplex containing tandem G:U basepairs,” *Biophys. J.* **90**, 4530 (2006).

Jin, R., A. Rummel, T. Binz, and A.T. Brunger, “Botulinum neurotoxin B recognizes its protein receptor with high affinity and specificity,” *Nature* **444**, 1092 (2006).

Joachimiak, L.A., T. Kortemme, B.L. Stoddard, and D. Baker, “Computational design of a new hydrogen bond network and at least a 300-fold specificity switch at a protein-protein interface,” *J. Mol. Biol.* **361**, 195 (2006).

Johnson, J.E., D.D. Allred, R.S. Turley, W.R. Evans, and R.L. Sandburg, “Thorium-based thin films as highly reflective mirrors in the EUV,” *2005 MRS Proc.* **893**, 207 (2006); 2005 MRS Fall Meeting, Boston MA, November 27–December 1, 2005.

Joseph, J.S., K.S. Saikatendu, V. Subramanian, B.W. Neuman, A. Brooun, M. Griffith, K. Moy, M.K. Yadav, J. Velasquez, M.J. Buchmeier, R.C. Stevens, and P. Kuhn, “Crystal structure of nonstructural protein 10 from the severe acute respiratory syndrome coronavirus reveals a novel fold with two zinc-binding motifs,” *J. Virol.* **80**, 7894 (2006).

Jungwirth, T., J. Masek, K.Y. Wang, K.W. Edmonds, M. Sawicki, M. Polini, J. Sinova, A.H. MacDonald, R.P. Campion, L.X. Zhao, N.R.S. Farley, T.K. Johal, G. van der Laan, C.T. Foxon, and B.L. Gallagher, “Low-temperature magnetization of (Ga,Mn)As semiconductors,” *Phys. Rev. B* **73**, 165205 (2006).

Kang B.-S., P. Fischer, D.-H. Kim, D. Attwood, E. Anderson, and G. Cho, “Bending magnet x-ray polarization modulation for magnetic full-field soft x-ray transmission microscopy,” *Proc. 8th Int. Conf.* **7**, 288 (2006); 8th International Conference on X-ray Microscopy, Himeji City, Japan, July 26–30, 2005.

Karshtedt, D., J. McBee, T. Bell, and T. Tilley, “Stoichiometric and catalytic arene activations by platinum complexes containing bidentate monoanionic nitrogen-based ligands,” *Organometallics* **25**, 1801 (2006).

Kawate, T., and E. Gouaux, “Fluorescence-detection size-exclusion chromatography for precrystallization screening of integral membrane proteins,” *Structure* **14**, 673 (2006).

Keatinge-Clay, A.T., and R.M. Stroud, “The structure of a ketoreductase determines the organization of the beta-carbon processing enzymes of modular polyketide synthases,” *Structure* **14**, 737 (2006).

Keller, L.P., et al., "Infrared spectroscopy of Comet 81P/Wild 2 samples returned by Stardust," *Science* **314**, 1728 (2006).

Keller, L. P., S. Bajt, G.A. Baratta, J. Borg, J. Brucato, M.J. Burchell, L. Colangeli, L. D'Hendecourt, Z. Djouadi, G. Ferrini, G. Flynn, A. Franchi, M. Fries, M.M. Grady, G. Graham, F. Grossemy, A. Kearsley, G. Matrajt, V. Mennella, L. Nittler, M.E. Palumbo, A. Rotundi, B. Wopenka, and M. Zolensky, "Infrared, UV/VIS and Raman spectroscopy of Comet Wild-2 samples returned by the Stardust mission," *Proc. 37th Lunar, and Planetary Science Conf.,* **2062** (2006); 37th Lunar, and Planetary Science Conference, League City, TX, March 13–17, 2006.

Kenney, C.J., J.D. Segal, E. Westbrook, S. Parker, J. Hasi, C. Da Via, S. Watts, and J. Morse, "Active-edge planar radiation sensors," *Nucl. Instrum. Meth. A* **565**, 272 (2006).

Kim D.-H., P. Fischer, W. Chao, E. Anderson, M.-Y. Im, S.-C. Shin, and S.-B. Choe, "Magnetic soft X-ray microscopy at 15 nm resolution probing nanoscale local magnetic hysteresis," *J. Appl. Phys.* **99**, 08H303 (2006).

Kim, B.J., H. Koh, E. Rotenberg, S.J. Oh, H. Eisaki, N. Motoyama, S. Uchida, T. Tohyama, S. Maekawa, Z.X. Shen, and C. Kim, "Distinct spinon and holon dispersions in photoemission spectral functions from one-dimensional $SrCuO_2$," *Nature Physics* **2**, 397 (2006).

Kim, J.H., D.S. Peterka, C.C. Wang, and D.M. Neumark, "Photoionization of helium nanodroplets doped with rare gas atoms," *J. Chem. Phys.* **124**, 214301 (2006).

Kim, Y.-W., A.L. Lovering, H. Chen, T. Kantner, L.P. McIntosh, N.C.J. Strynadka, and S.G. Withers, "Expanding the thioglycoligase strategy to the synthesis of alpha-linked thioglycosides allows structural investigation of the parent enzyme/substrate complex," *J. Am. Chem. Soc.* **128**, 2202 (2006).

Kinderman, F.S., C. Kim, S. von Daake, Y. Ma, B.Q. Pham, G. Spraggon, N.H. Xuong, P.A. Jennings, and S.S. Taylor, "A dynamic mechanism for AKAP binding to RII isoforms of cAMP-dependent protein kinase," *Mol. Cell*. **24**, 397 (2006).

Kirpichtchikova, T.A., A. Manceau, L. Spadini, F. Panfili, M.A. Marcus, and T. Jacqet, "Speciation and solubility of heavy metals in contaminated soil using x-ray microfluorescence, EXAFS spectroscopy, chemical extraction, and thermodynamic modeling," *Geochim. Cosmochim. Acta* **70**, 2163 (2006).

Klein, D.J., and A.R. Ferre-D'Amare, "Structural basis of *glmS* ribozyme activation by glucosamine-6-phosphate," *Science* **313**, 1752 (2006).

Kleinfelder, S., S. Li, F. Bieser, R. Gareus, L. Greiner, J. King, J. Levesque, H.S. Matis, M. Oldenburg, H.G. Ritter, F. Retiere, A. Rose, K. Schweda, A. Shabetai, E. Sichtermann, J.H. Thomas, H.H. Wieman, and H. Bichsel "A proposed STAR microvertex detector using active pixel sensors with some relevant studies on APS performance," *Nucl. Instrum. Meth. A* **565**, 132 (2006).

Kliegman, J.I., S.L. Griner, J.D. Helmann, R.G. Brennan, and A. Glasfeld, "Structural basis for the metal-selective activation of the manganese transport regulator of *Bacillus subtilis,*" *Biochemistry* **45**, 3493 (2006).

Koralek, J.D., J.F. Douglas, N.C. Plumb, Z. Sun, A.V. Fedorov, M.M. Murnane, H.C. Kapteyn, S.T. Cundiff, Y. Aiura, K. Oka, H. Eisaki, and D.S. Dessau, "Laser based angle-resolved photoemission, the sudden approximation and quasiparticle-like spectral peaks in $Bi_2Sr_2CaCu_2O_{8+\delta}$," *Phys. Rev. Lett.* **96**, 017005 (2006).

Korostelev, A., S. Trakhanov, M. Laurberg, and H.F. Noller, "Crystal structure of a 70S ribosome-tRNA complex reveals functional interactions and rearrangements," *Cell* **126**, 1065 (2006).

Korotkova, N., I. Le Trong, R. Samudrala, K. Korotkov, C.P. Van Loy, A.-L. Bui, S.L. Moseley, and R.E. Stenkamp, "Crystal structure and mutational analysis of the DaaE Adhesin of *Escherichia coli*," *J. Biol. Chem.* **281**, 22367 (2006).

Kozlov, G., P. Maattanen, J.D. Schrag, S. Pollack, M. Cygler, B. Nagar, D.Y. Thomas, and K. Gehring, "Crystal structure of the bb´ domains of the protein disulfide isomerase ERp57," *Structure* **14**, 1331 (2006).

Krishnamurthy, S., C. McGuiness, L.S. Dorneles, Ml. Venkatesan, J.M.D. Coey, J.G. Lunney, C.H. Patterson, K.E. Smith, T. Learmonth, P.-A. Glans, T. Schmitt, and J.-H. Guo, "Soft-x-ray spectroscopic investigation of ferromagnetic Co-doped ZnO," *J. Appl. Phys.* **99**, 08M111-01 (2006).

Kucheyev, S.O., T.F. Baumann, Y.M. Wang, T. van Buuren, J.J. Poco, J.H. Satcher, Jr., and A.V. Hamza, "Monolithic, high surface area, three-dimensional GeO_2 nanostructures," *Appl. Phys. Lett.* **88**, 103117 (2006).

Kuepper, K., R. Klingeler, P. Reutler, B. Buchner, and M. Neumann, " Electronic structure of $LaSrMnO_4$: X-ray photoelectron spectroscopy and x-ray emission spectroscopy studies," *J. Appl. Phys.* **99**, 08Q308 (2006).

Kuepper, K., R. Klingeler, P. Reutler, B. Büchner, and M. Neumann, "Excited and ground state properties of $LaSrMnO_4$: A combined x-ray spectroscopic study," *Phys. Rev. B* **74**, 115103 (2006).

Kuprin, A.P., M.Z. Hasan, Y.-D. Chuang, D. Qian, M. Foo, and R.J. Cava, "Low-lying electronic structure of triangular cobaltite," *J. Phys. Chem. Solids* **67**, 235 (2006).

Kvashnina, K.O., J.-H. Guo, A. V. Talyzin, A. Modin, T. Kaambre, S.M. Butorin, and J. Nordgren, "X-ray absorption, and emission study of hydrogenated fullerenes," *Hydrogen in Matter (A Collection from the Papers Presented at the Second International Symposium on Hydrogen in Matter)* **837**, 230 (2006); 2nd International Symposium on Hydrogen in Matter, Uppsala Sweden, June 13–17, 2005.

Kvashnina, K.O., S.M. Butorin, B. Hjorvarsson, J.-H. Guo, and J. Nordgren, "Influence of hydrogen on properties of rare-earth hydrides studied by resonant inelastic x-ray scattering spectroscopy," *Hydrogen in Matter (A Collection from the Papers Presented at the Second International Symposium on Hydrogen in Matter)* **837**, 255 (2006); 2nd International Symposium on Hydrogen in Matter, Uppsala Sweden, June 13–17, 2005.

La Fontaine, B., A.R. Pawloski, O. Wood, Y. Deng, H.J. Levinson, P. Denham, E. Gullikson, B. Hoef, P. Naulleau, C. Holfeld, C. Chovino, and F. Letzkus, "Demonstration of phase-shift masks for extreme-ultraviolet lithography," *Proc. SPIE*, **6151**, 61510A (2006); Microlithography 2006: Emerging Lithographic Technologies X, San Jose California, February 21, 2006.

Lam, P.J., J.K.B. Bishop, C.C. Henning, M.A. Marcus, G.A. Waychunas, and I.Y. Fung, "Wintertime phytoplankton bloom in the subarctic Pacific supported by continental margin iron," *Global Biogeochem. Cycles* **20**, GB1006 (2006).

Lamers, M.H., R.E. Georgescu, S.-G. Lee, M. O'Donnell, and J. Kuriyan, "Crystal structure of the catalytic alpha subunit of

E. coli replicative DNA polymerase III," *Cell* **126**, 881 (2006).

Lamoureux, J.S., and J.N.M. Glover, "Principles of protein-DNA recognition revealed in the structural analysis of Ndt80-MSE DNA complexes," *Structure* **14**, 555 (2006).

Lanzara, A., P.V. Bogdanov, X.J. Zhou, N. Kaneko, H. Eisaki, M. Greven, Z. Hussain, and Z.X. Shen, "Normal state spectral lineshapes of nodal quasiparticles in single layer Bi2201 superconductor," *J. Phys. Chem. Solids* **67**, 239 (2006).

Larsen, N.A., H. Lin, R. Wei, M.A. Fischbach, and C.T. Walsh, "Structural characterization of enterobactin hydrolase IroE," *Biochemistry* **45**, 10184 (2006).

Larson, J.D., J.L. Jenkins, J.P. Schuermann, Y. Zhou, D.F. Becker, and J.J. Tanner, "Crystal structures of the DNA-binding domain of *Escherichia coli* proline utilization A flavoprotein and analysis of the role of Lys9 in DNA recognition," *Protein Sci.* **15**, 2630 (2006).

Le Pogam, S., H. Kang, S.F. Harris, V. Leveque, A.M. Giannetti, S. Ali, W.-R. Jiang, S. Rajyaguru, G. Tavares, C. Oshiro, T. Handricks, K. Klumpp, J. Symons, M.F. Browner, N. Cammack, and I. Najera, "Selection and characterization of replicon variants dually resistant to thumb- and palm-binding nonnucleoside polymerase inhibitors of the hepatitis C virus," *J. Virology* **80**, 6146 (2006).

Lee, C.-S., W. Liu, P.A. Sprengeler, J.R. Somoza, J.W. Janc, D. Sperandio, J.R. Spencer, M.J. Green, and M.E. McGrath, "Design of novel, potent, and selective human β-tryptase inhibitors based on α-keto-[1,2,4]-oxadiazoles," *Bioorg. Med. Chem. Lett.* **16**, 4036 (2006).

Lee, C.V., S.G. Hymowitz, H.J. Wallweber, N.C. Gordon, K.L. Billeci, S.P. Tsai, D.M. Compaan, J. Yin, Q. Gong, R.F. Kelley, L.E. Deforge, F. Martin, M.A. Starovasnik, and G. Fuh, "Synthetic anti-BR3 antibodies that mimic BAFF binding and target both human and murine B cells," *Blood* **108**, 3103 (2006).

Lemieux, M.J., B.L. Mark, M.M. Cherney, S.G. Withers, D.J. Mahuran, and M.N.G. James, "Crystallographic structure of human β-hexosaminidase A: interpretation of Tay-Sachs mutations and loss of G_{M2} ganglioside hydrolysis," *J. Mol. Biol.* **359**, 913 (2006).

Levenson, E., P. Lerch, and M. Martin, "Infrared imaging: Synchrotrons vs. arrays, resolution vs. speed," *Infrared Phys. Technol.* **49**, 45 (2006).

Levin, J.I., J.M. Chen, L.M. Laakso, M. Du, J. Schmid, W. Xu, T. Cummons, J. Xu, G. Jin, D. Barone, and J.S. Skotnicki, "Acetylenic TACE inhibitors. Part 3: Thiomorpholine sulfonamide hydroxamates," *Bioorg. Med. Chem. Lett.* **16**, 1605 (2006).

Levinson, N.M., O. Kuchment, K. Shen, M.A. Young, M. Koldobskiy, M. Karplus, P.A. Cole, and J. Kuriyan, "A Src-like inactive conformation in the Abl tyrosine kinase domain," *PLoS Biology* **4**, 753 (2006).

Li, B., S.J. Russell, D.M. Compaan, K. Totpal, S.A. Marsters, A. Ashkenazi, A.G. Cochran, S.G. Hymowitz, and S.S. Sidhu, "Activation of the proapoptotic death receptor DR5 by oligomeric peptide and antibody agonists," *J. Mol. Biol.* **361**, 522 (2006).

Li, H., J. Igarashi, J. Jamal, W. Yang, and T.L. Poulos, "Structural studies of constitutive nitric oxide synthases with diatomic ligands bound," *J. Biol. Inorg. Chem.* **11**, 753 (2006).

Li, L., A.P. Hitchcock, N. Robar, R. Cornelius, J.L. Brash, A. Scholl, and A. Doran, "X-ray microscopy studies of protein adsorption on a phase-segregated polystyrene/polymethyl methacrylate surface. 1. Concentration and exposure-time dependence for albumin adsorption," *J. Phys. Chem. B* **110**, 16763 (2006).

Li, T., X. Chen, K.C. Garbutt, P. Zhou, and N. Zheng, "Structure of DDB1 in complex with a paramyxovirus V protein: Viral hijack of a propeller cluster in ubiquitin ligase," *Cell* **124**, 105 (2006).

Li, Z.Q., G.M. Wang, N. Sai, D. Moses, M.C. Martin, M. Di Ventra, A.J. Heeger, and D.N. Basov, "Infrared imaging of the nanometer-thick accumulation layer in organic field-effect transistors," *Nano Lett.* **6**, 224 (2006).

Liang, T., G. Zhang, P. Naulleau, A. Myers, S. Park, A. Stivers, and G. Vandentop, "EUV mask pattern defect printability," *Proc. SPIE* **6283**, 62830K (2006).

Lima, E., "The advancement of biological imaging through x-ray diffraction microscopy," Ph.D. thesis, Stony Brook University (2006).

Lima, E., D. Shapiro, P. Thibault, T. Beetz, V. Elser, M. Howells, X. Huang, C. Jacobsen, J. Kirz, H. Miao, A.M. Neiman, A. Stewart, and D. Sayre, "Diffraction microscopy: Reconstruction of the complex-valued image of a yeast cell," *Proc. 8th Int. Conf.* **7**, 392 (2006); 8th International Conference on X-ray Microscopy, Himeji City, Japan, July 26–30, 2005.

Liu, X., C.-H. Jang, F. Zheng, A. Jürgensen, J.D. Denlinger, K.A. Dickson, R.T. Raines, N.L. Abbott, and F.J. Himpsel, "Characterization of protein immobilization at silver surfaces by near edge x-ray absorption fine structure spectroscopy," *Langmuir* **22**, 7719 (2006).

Lodowski, D.T., V.M. Tesmer, J.L. Benovic, and J.J. Tesmer, "The structure of G protein-coupled receptor kinase (GRK)-6 defines a second lineage of GRKs," *J. Biol. Chem.* **281**, 16785 (2006).

Louie, G.V., M.E. Bowman, M.C. Moffitt, T.J. Baiga, B.S. Moore, and J.P. Noel, "Structural determinants and modulation of substrate specificity in phenylalanine-tyrosine ammonia-lyases," *Chem. Biol.* **13**, 1327 (2006).

Lu, H., and U. Schulze-Gahmen, "Toward understanding the structural basis of cyclin-dependent kinase 6 specific inhibition," *J. Med. Chem.* **49**, 3826 (2006).

Lu, J., R.A. Edwards, J.J.W. Wong, J. Manchak, P.G. Scott, L.S. Frost, and J.N.M. Glover, "Protonation-mediated structural flexibility in the F conjugation regulatory protein, TraM," *EMBO J.* **25**, 2930 (2006).

Lu, M., "Photoionization, and electron-impact ionization of multiply charged krypton ions," Ph.D. thesis, University of Nevada, Reno (2006).

Lu, M., G. Alna'washi, M. Habibi, M.F. Gharaibeh, R.A. Phaneuf, A.L D. Kilcoyne, E. Levenson, A.S. Schlachter, C. Cisneros, and G. Hinojosa, "Photoionization and electron-impact ionization of Kr^{3+}," *Phys. Rev. A* **74**, 062701 (2006).

Lu, M., M.F. Gharaibeh, G. Alna'washi, R.A. Phaneuf, A.L.D. Kilcoyne, E. Levenson, A.S. Schlachter, A. Müller, S. Schippers, J. Jacobi, S.W.J. Scully, and C. Cisneros, "Photoionization and electron-impact ionization of Kr^{5+}," *Phys. Rev. A* **74**, 012703 (2006).

Lunde, C.S., S. Rouhani, M.T. Facciotti, and R.M. Glaeser, "Membrane-protein stability in a phospholipid-based crystallization medium," *J. Struct. Biol.* **154**, 223 (2006).

Lyubimov, A.Y., P.I. Lario, I. Moustafa, and A. Vrielink, "Atomic resolution crystallography reveals how changes in pH shape the protein microenvironment," *Nat. Chem. Bio.* **2**, 259 (2006).

MacNaughton, J.B., "Electronic structure of DNA, and related biomaterials," Ph.D. thesis, University of Saskatchewan, Canada (2006).

MacNaughton, J.B., A. Moewes, J.S. Lee, S.D. Wettig, H.-B. Kraatz, L.Z. Ouyang, W.Y. Ching, and E.Z. Kurmaev, "Dependence of DNA electronic structure on environmental and structural variations," *J. Phys. Chem. B* **110**, 15742 (2006).

MacNaughton, J.B., E.Z. Kurmaev, L.D. Finkelstein, J.S. Lee, S.D. Wettig, and A. Moewes, "Electronic structure and charge carriers in metallic DNA investigated by soft x-ray spectroscopy," *Phys. Rev. B* **73**, 205114 (2006).

MacNaughton, J.B., M.V. Yablonskikh, A.H. Hunt, E.Z. Kurmaev, J.S. Lee, S.D. Wettig, and A. Moewes, "Solid versus solution: Examining the electronic structure of metallic DNA with soft x-ray spectroscopy," *Phys. Rev. B* **74**, 125101 (2006).

MacNaughton, J.B., R.G. Wilks, J.S. Lee, and A. Moewes, "Experimental and theoretical investigation of the electronic structure of 5-fluorouracil compounds," *J. Phys. Chem. B* **110**, 18180 (2006).

MacRae, I.J., K. Zhou, F. Li, A. Repic, A.N. Brooks, W.Z. Cande, P.D. Adams, and J.A. Doudna, "Structural basis for double-stranded RNA processing by Dicer," *Science* **311**, 195 (2006).

Magid K.R., E.T. Lilleodden, N. Tamura, J. Florando, D. Lassila, R.I. Barabash, and J.W. Morris, "Hierarchical characterization of deformation heterogeneities in BCC crystals' dislocations, plasticity, damage, and metal forming: Material response and multiscale modeling," in *Proceedings of the 11th International Symposium on Plasticity,* p. 631 (2006); Kauai, HI, 2005.

Makino, D.L., J. Day, S.B. Larson, and A. McPherson, "Investigation of RNA structure in satellite panicum mosaic virus," *Virology* **351**, 420 (2006).

Marchesini, S., H.N. Chapman, A. Barty, M.R. Howells, J.C. Spence, C. Cui, U. Weiestrall, and A.M. Minor, "Phase aberrations in diffraction microscopy," *Proc. 8th Int. Conf.* **7**, 353 (2006); 8th International Conference on X-ray Microscopy, Himeji City, Japan, July 26–30, 2005.

Marchesini, S., H.N. Chapman, A. Barty, M.R. Howells, C. Cui, J.C.H. Spence, U. Weiestrall, A. Noy, S.P. Hau-Riege, J.M. Kinney, D. Shapiro, T. Beetz, C. Jacobsen, E. Lima, A.M. Minor, and H. He, "Progress in three-dimensional coherent x-ray diffraction imaging," *Proc. 8th Int. Conf.* **7**, 380 (2006); 8th International Conference on X-ray Microscopy, Himeji City, Japan, July 26–30, 2005.

Marks, S., S. Prestemon, R.D. Schlueter, C. Steier, A. Wolsi, J.Y. Jung, and O. Chubar, "Shift dependent skew quadrupole in Advanced Light Source elliptically polarizing undulators, cause and corrections," *IEEE Trans. Appl. Supercon.* **16**, 1574 (2006).

Mattison, K., J.S. Wilbur, M. So, and R.G. Brennan, "Structure of fitAB from *Neisseria gonorrhoeae* bound to DNA reveals a tetramer of toxin-antitoxin heterodimers containing pin domains and ribbon-helix-helix motifs," *J. Biol. Chem.* **281**, 37942 (2006).

Maynes, J.T., H.A. Luu, M.M. Cherney, R.J. Andersen, D. Williams, C.F.B. Holmes, and M.N.G. James, "Crystal structures of protein phosphatase-1 bound to motuporin and dihydromicrocystin-LA: Elucidation of the mechanism of enzyme inhibition by cyanobacterial toxins," *J. Mol. Biol.* **356**, 111 (2006).

McDonough, M.A., V. Li, E. Flashman, R. Chowdhury, C. Mohr, B.M.R. Lienard, J. Zondlow, N.J. Oldham, I.J. Clifton, J. Lewis, L.A. McNeill, R.J.M. Kurzeja, K.S. Hewitson, E. Yang, S. Jordan, R.S. Syed, and C.J. Schofield, "Cellular oxygen sensing: Crystal structure of hypoxia-inducible factor prolyl hydroxylase (PHD2)," *Proc. Natl. Acad. Sci. USA* **103**, 9814 (2006).

McElroy, K., G.-H. Gweon, S.Y. Zhou, J. Graf, S. Uchida, H. Eisaki, H. Takagi, T. Sasagawa, D.-H. Lee, and A. Lanzara, "Elastic scattering susceptibility of the high temperature superconductor $Bi_2Sr_2CaCu_2O_{8+\delta}$: A comparison between real and momentum space photoemission spectroscopies," *Phys. Rev. Lett.* **96**, 067005 (2006).

McGrath, M.E., P.A. Sprengeler, B. Hirschbein, J.R. Somoza, I. Lehoux, J.W. Janc, E. Gjerstad, M. Graupe, A. Estiarte, C. Venkataramani, Y. Liu, R. Yee, J.D. Ho, M.J. Green, C.-S. Lee, L. Liu, V. Tai, J. Spencer, D. Sperandio, and B.A. Katz, "Structure-guided design of peptide-based tryptase inhibitors," *Biochemistry* **45**, 5964 (2006).

McNear, D.H., "The plant-soil interface: nickel bioavailability, and the mechanisms of plant hyperaccumulation," Ph.D. thesis, University of Delaware (2006).

McNeill, C.R., B. Watts, L. Thomsen, W.J. Belcher, A.LD. Kilcoyne, N.C. Greenham, and P.C. Dastoor, "X-ray spectromicroscopy of polymer/fullerene composites: Quantitative chemical mapping," *Small* **2**, 1432 (2006).

McNeill, C.R., B. Watts, L. Thomsen, W.J. Belcher, N.C. Greenham, and P.C. Dastoor, "Nanoscale quantitative chemical mapping of conjugated polymer blends," *Nano Lett.* **6**, 1202 (2006).

Meloni, G., P. Zou, S.J. Klippenstein, M. Ahmed, S.R. Leone, C.A. Taatjes, and D.L. Osborn, "Energy-resolved photoionization of alkylperoxy radicals, and the stability of their cations," *J. Am. Chem. Soc.* **128**, 13559 (2006).

Mikolosko, J., K. Bobyk, H.I. Zgurskaya, and P. Ghosh, "Conformational flexibility in the multidrug efflux system protein ACRA," *Structure* **14**, 577 (2006).

Mitchell, G.E., B.G. Landes, J. Lyons, B.J. Kern, M.J. Devon, I. Koprinarov, E.M. Gullikson, and J.B. Kortright, "Molecular bond selective x-ray scattering for nanoscale analysis of soft matter," *Appl. Phys. Lett.* **89**, 044101 (2006).

Montange, R.K., and R.T. Batey, "Structure of the *S*-adenosylmethionine riboswitch regulatory mRNA element," *Nature* **441**, 1172 (2006).

Mooers, B.H.M., and B.W. Matthews, "Extension to 2268 atoms of direct methods in the *ab initio* determination of the unknown structure of bacteriophage P22 lysozyme," *Acta Crystallogr. Sec. D* **62**, 165 (2006).

Moore, K.T., G. van der Laan, J.G. Tobin, B.W. Chung, M.A. Wall, and A.J. Schwartz, "Probing the population of the spin–orbit split levels in the actinide 5f states," *Ultramicroscopy* **106**, 261 (2006).

Mou, T.C., A. Gille, S. Suryanarayana, M. Richter, R. Seifert, and S.R. Sprang, "Broad specificity of mammalian adenylyl cyclase for interaction with 2′,3′-substituted purine- andpyrimidine nucleotide inhibitors," *Mol. Pharmacol.* **70**, 878 (2006).

Mougous, J.D., D.H. Lee, S.C. Hubbard, M.W. Schelle, D.J. Vocadlo, J.M. Berger, and C.R. Bertozzi, "Molecular basis for g protein control of the prokaryotic ATP sulfurylase," *Mol. Cell* **21**, 109 (2006).

Mun B.S., J.C. Moon, S.W. Hong, K.S. Kang, K. Kim, T.W. Kim, and H.L. Ju, "X-ray absorption spectroscopy studies on magnetic tunnel junctions with AlO and AlN tunnel barriers," *J. App. Phys.* **99**, 08E506 (2006).

Mun B.S., M. Watanabe, M. Rossi, V. Stamenkovic, N.M. Markovic, G. Wang, and P.N. Ross Jr., "The study of surface segregation, structure, and valence band density of states of $Pt_3Ni(100)$, (110), and (111) crystals," *Surf. Rev. Lett.* **13**, 697 (2006).

Nagar, B., O. Hantschel, M. Seeliger, J.M. Davies, W.I. Weis, G. Superti-Furga, and J. Kuriyan, "Organization of the SH3-SH2 unit in active and inactive forms of the c-Abl tyrosine kinase," *Mol. Cell* **21**, 787 (2006).

Nakagawa, T., H.W. Yeom, E. Rotenberg, B. Krenzer, S.D. Kevan, H. Okuyama, M. Nishijima, and T. Aruga, "Long-period surface structure stabilized by Fermi surface nesting: Cu(001)-($\sqrt{20} \times \sqrt{20}$)R26.6°-In," *Phys. Rev. B* **73**, 075407 (2006).

Naulleau, P., C. Anderson, R. Kim, B. La Fontaine, and T. Wallow, "Investigation of lithographic metrics for the characterization of intrinsic resolution limits in EUV resists," in *Proceedings of the EUVL Symposium* (2006), Barcelona Spain, October 15–18, 2006.

Naulleau, P., C. Anderson, and S. Horne, "Design for a stand-alone extreme ultraviolet interference lithography tool," in *Proceedings of the EUVL Symposium* (2006), Barcelona Spain, October 15–18, 2006.

Naulleau, P., F. Salmassi, and E.M. Gullikson, "Demonstration of an EUV phase-only computer-generated hologram," in *Proceedings of the EUVL Symposium* (2006), Barcelona Spain, October 15–18, 2006.

Naulleau, P., J. Cain, D. Dean, and K.A. Goldberg, "Lithographic characterization of low-order aberrations in a 0.3-NA EUV microfield exposure tool," *Proc. SPIE* **6151**, 61512Z (2006); Microlithography 2006: Emerging Lithographic Technologies X, San Jose California, February 21, 2006.

Naulleau, P., K.A. Goldberg, J.P. Cain, E.H. Anderson, K.R. Dean, P. Denham, B. Hoef, and K.H. Jackson, "Extreme ultraviolet lithography capabilities at the Advanced Light Source Using a 0.3-NA optic," *IEEE J. Quantum Elect.* **42**, 44 (2006).

Naulleau, P.P., C. Rammeloo, J.P. Cain, K. Dean, P. Denham, K.A. Goldberg, B. Hoef, B. La Fontaine, A.R. Pawloski, C. Larson, and G. Wallraff, "Investigation of the current resolution limits of advanced extreme ultraviolet (EUV) resists," *Proc. SPIE* **6151**, 61512Y (2006); Microlithography 2006: Emerging Lithographic Technologies X, San Jose California, February 21, 2006.

Naulleau, P.P., J.P. Cain, and K.A. Goldberg, "Lithographic characterization of the spherical error in an extreme ultraviolet optic by use of a programmable pupil fill-illuminator," *Appl. Optics* **45**, 1957 (2006).

Nguitragool, W., and C. Miller, "Uncoupling of a CLC Cl^-/H^+ exchange transporter by polyatomic anions," *J. Mol. Biol.* **362**, 682 (2006).

Nicolas, C., J.N. Shu, D.S. Peterka, M. Hochlaf, L. Poisson, S.R. Leone, and M. Ahmed, "Vacuum ultraviolet photoionization of C_3," *J. Am. Chem. Soc.* **128**, 220 (2006).

Nicoll, D.A., M. Sawaya, S. Kwon, D. Cascio, K.D. Philipson, and J. Abramson, "The crystal structure of the primary Ca^{2+} sensor of the Na^+/Ca^{2+} exchanger reveals a novel Ca^{2+} binding motif," *J. Biol. Chem.* **281**, 21577 (2006).

Nilsson, H.J., T. Tyliszczak, R.E. Wilson, L. Werme, and D.K. Shuh, "Soft x-ray spectromicroscopy of actinide particulates," in *Recent Advances in Actinide Chemistry,* p. 56 (Cambridge, 2006).

Nishimura, H., and C. Timossi, "Mono for cross-platform control system environment," in *PCaPAC Proceedings*, p. 37 (2006); Sixth International Workshop on Personal Computers and Particle Accelerator Controls, Newport News, Virginia, October 24–27, 2006.

Ohldag, H., H. Shi, E. Arenholz, J. Stöhr, and D. Lederman, "Parallel versus antiparallel interfacial coupling in exchange-biased Co/FeF_2 bilayers," *Phys. Rev. Lett.* **96**, 027203 (2006).

Ohta, T., A. Bostwick, T. Seyller, K. Horn, and E. Rotenberg, "Controlling the electronic structure of bilayer graphene," *Science* **313**, 951 (2006).

Okram, B., A. Nagle, F.J. Adrian, C. Lee, P. Ren, X. Wang, T. Sim, Y. Xie, X. Wang, G. Xia, G. Spraggon, M. Warmuth, Y. Liu, and N.S. Gray, "A general strategy for creating 'inactive-conformation' abl inhibitors," *Chem. Biol.* **13**, 779 (2006).

Olynick, D.L., A.V. Tivanski, M.K. Gilles, T.Tyliszczak, F. Salmassi, J.A. Liddle, K.Liang, and S.R. Leone, "Scanning X-ray microscopy investigations into the electron beam exposure mechanism of hydrogen silsesqioxane resists," *J. Vac. Sci. Tech. B* **24**, 3084, (2006).

Öström, H., H. Ogasawara, L.Å. Näslund, L.G.M. Pettersson, and A. Nilsson, "Physisorption-induced C–H bond elongation in methane," *Phys. Rev. Lett.* **96**, 146104 (2006).

Otero, E., and S.G. Urquhart, "Nitrogen 1s near-edge x-ray absorption fine structure spectroscopy of amino acids: Resolving Zwitterionic effects," *J. Phys. Chem. A* **110**, 12121 (2006).

Ou, Z., R.L. Felts, T.J. Reilly, J.C. Nix, and J.J. Tanner, "Crystallization of recombinant *Haemophilus influenzae* e (P4) acid phosphatase," *Acta Crystallogr. Sec. F* **62**, 464 (2006).

Pao, C.W., H.M. Tsai, J.W. Chiou, W.F. Pong, M.-H. Tsai, T.W. Pi, H.-J. Lin, L.Y. Jang, J.F. Lee, C.R. Wang, S.T. Lin, and J.-H. Guo, "The effect of the Mn constituent on the electronic structures of $Al_{70}Pd_{22.5}(Re_{1-x}M_{nx})_{7.5}$ quasicrystals studied by x-ray absorption and photoemission spectroscopy," *J. Phys.: Condens. Mat.* **18**, 265 (2006).

Park, Y.J., and K. Luger, "The structure of nucleosome assembly protein 1," *Proc. Natl. Acad. Sci. USA* **103**, 1248 (2006).

Parker, S.I., C.J. Kenney, D. Gnani, A.C. Thompson, E. Mandelli, G. Meddeler, J. Hasi, J. Morse, and E.M. Westbrook, "3DX: An x-ray pixel array detector with active edges," *IEEE T. Nucl. Sci.* **53**, 1676 (2006).

Patterson, A.W., W.J.L. Wood, M. Hornsby, S. Lesley, G. Spraggon, G., and J.A. Ellman, "Identification of selective, nonpeptidic nitrile inhibitors of cathepsin S using the substrate activity screening method," *J. Med. Chem.* **49**, 6298 (2006).

Payne, D.J., R.G. Egdell, A. Walsh, G.W. Watson, J. Guo, P.-A. Glans, T. Learmonth, and K.E. Smith, "Electronic origins of structural distortions in post-transition metal oxides: Experimental and theoretical evidence for a revision of the lone pair model," *Phys. Rev. Lett.* **96**, 157403 (006).

Pegan, S., C. Arrabit, P.A. Slesinger, and S. Choe, "Andersen's syndrome mutation effects on the structure and assembly of the cytoplasmic domains of KIR2.1," *Biochemistry* **45**, 8599 (2006).

Perry, J.J.P., S.M. Yanonne, L.G. Holden, C. Hitomi, A. Asaithamby, S. Han, P.K. Cooper, D.J. Chen, and J.A. Tainer, "WRN exonuclease structure, and molecular mechanism imply an editing role in DNA end processing," *NSMB* **13**, 414 (2006).

Perry, K., Y. Hwang, F.D. Bushman, and G.D. Van Duyne, "Structural basis for specificity in the poxvirus topoisomerase," *Mol. Cell* **23**, 343 (2006).

Persson, C., C.L. Dong, L. Vayssieres, A. Augustsson, T. Schmitt, M. Mattesini, R. Ahuja, J. Nordgren, C.L. Chang, A. Ferreira da Silva, and J.-H. Guo, "X-ray absorption and emission spectroscopy of ZnO nanoparticle and highly oriented ZnO microrod arrays," *Microelectron. J.* **37**, 686 (2006).

Peterka, D.S., J.H. Kim, C.C. Wang, and D.M. Neumark, "Photoionization, and photofragmentation of SF$_6$ in helium nanodroplets," *J. Phys. Chem. B* **110**, 19945 (2006).

Peters-Libeu, C.A., Y. Newhouse, D.M. Hatters, and K.H. Weisgraber, "Model of biologically active apolipoprotein E bound to dipalmitoylphosphatidylcholine," *J. Biol. Chem.* **281**, 1073 (2006).

Petrovykh, D.Y., V. Pérez-Dieste, A. Opdahl, H. Kimura-Suda, J.M. Sullivan, M.J. Tarlov, F.J. Himpsel, and L.J. Whitman, "Nucleobase orientation, and ordering in films of single-stranded DNA on gold," *J. Am. Chem. Soc.* **128**, 2 (2006).

Pfingsten, J.S., D.A. Costantino, and J.S. Kieft, "Structural basis for ribosome recruitment, and manipulation by a viral IRES RNA," *Science* **314**, 1450 (2006).

Pillai, B., M.M. Cherney, C.M. Diaper, A. Sutherland, J.S. Blanchard, J.C. Vederas, and M.N. James, "Structural insights into stereochemical inversion by diaminopimelate epimerase: An antibacterial drug target," *Proc. Natl. Acad. Sci. USA* **103**, 8668 (2006).

Pinkett, H.W., K.E. Shearwin, S. Stayrook, I.B. Dodd, T. Burr, A. Hochschild, J.B. Egan, and M. Lewis, "The structural basis of cooperative regulation at an alternate genetic switch," *Mol. Cell* **21**, 605 (2006).

Plenge, J., C. Nicolas, A.G. Caster, M. Ahmed, and S.R. Leone, "Two-color visible/vacuum ultraviolet photoelectron imaging dynamics of Br$_2$," *J. Chem. Phys.* **125**, 133315 (2006).

Pornillos, O., and G. Chang, "Inverted repeat domains in membrane proteins," *FEBS Lett.* **580**, 358 (2006).

Powers, J.P., D.E. Piper, Y. Li, V. Mayorga, J. Anzola, J.M. Chen, J.C. Jaen, G. Lee, J. Liu, M.G. Peterson, G.R. Tonn, Q. Ye, N.P. Walker, and Z. Wang, "SAR, and mode of action of novel non-nucleoside inhibitors of hepatitis C NS5b RNA polymerase," *J. Med. Chem.* **49**, 1034 (2006).

Prabu, J.R., S. Thamotharan, J.S. Khanduja, E.Z. Alipio, C.Y. Kim, G.S. Waldo, T.C. Terwilliger, B. Segelke, T. Lekin, D. Toppani, L.W. Hung, M. Yu, E. Bursey, K. Muniyappa, N.R. Chandra, and M. Vijayan, "Structure of *Mycobacterium tuberculosis* RuvA, a protein involved in recombination," *Acta Crystallogr. Sec. F* **62**, 731 (2006).

Prabu-Jeyabalan, M., E.A. Nalivaika, K. Romano, and C.A. Schiffer, "Mechanism of substrate recognition by drug-resistant human immunodeficiency virus type 1 protease variants revealed by a novel structural intermediate," *J. Virol.* **80**, 3607 (2006).

Prilliman, S.G., S.M. Clark, A.P. Alivisatos, P. Karvankova, and S. Veprek, "Strain and deformation in ultra-hard nanocomposites nc-TiN/a-BN under hydrostatic pressure," *Mater. Sci. Engr. A* **437**, 379 (2006).

Prochnow, C., R. Bransteitter, M. Klein, M. Goodman, and X. Chen, "The APOBEC-2 crystal structure and functional implications for the deaminase AID," *Nature* **445**, 447 (2006).

Qian, D., D. Hsieh, L. Wray, Y.D. Chuang, A.V. Fedorov, D. Wu, J.L. Luo, N.L. Wang, L. Viciu, R.J. Cava, and M.Z. Hasan, "Low-lying quasiparticle states and hidden collective charge instabilities in parent cobabltate superconductors," *Phys. Rev. Lett.* **96**, 216405 (2006).

Qian, D., L. Wray, D. Hsieh, D. Wu, J.L. Luo, N.L. Wang, A. Kuprin, A.V. Fedorov, R.J. Cava, L. Viciu, and M.Z. Hasan, "Quasiparticle dynamics in the vicinity of metal-insulator phase transition in Na$_x$CoO$_2$," *Phys. Rev. Lett.* **96**, 046407 (2006).

Qian, D., L. Wray, D. Hsieh, L. Viciu, R.J. Cava, J.L. Luo, D. Wu, N.L. Wang, and M.Z. Hasan, "Complete d-band dispersion relation in sodium cobaltates," *Phys. Rev. Lett.* **97**, 186405 (2006).

Radisky, E.S., J.M. Lee, C.K. Lu, and D.E. Koshland, "Insights into the serine protease mechanism from atomic resolution structures of trypsin reaction intermediates," *Proc. Natl. Acad. Sci. USA* **103**, 6835 (2006).

Rai, R., A. Kolesnikov, P.A. Sprengeler, S. Torkelson, T. Ton, B.A. Katz, C. Yu, J. Hendrix, W.D. Shrader, R. Stephens, R. Cabuslay, E. Sanford, and W.B. Young, "Discovery of novel heterocyclic factor VIIA inhibitors," *Bioorg. Med. Chem. Lett.* **16**, 2270 (2006).

Ren, X., C. Tu, D. Bhatt, J.J. Perry, J.A. Tainer, D.E. Cabelli, and D.N. Silverman, "Kinetic and structural characterization of human manganese superoxide dismutase containing 3-fluorotyrosines," *J. Mol. Struct.* **790**, 168 (2006).

Reyes, C.L., A. Ward, J. Yu, and G. Chang, "The structures of MsbA: Insight into ABC transporter-mediated multidrug efflux," *FEBS Lett.* **580**, 1042 (2006).

Reynolds, K.A., J.M. Thomson, K.D. Corbett, C.R. Bethel, J.M. Berger, J.F. Kirsch, R.A. Bonomo, and T.M. Handel, "Structural and computational characterization of the SHV-1 β-lactamase-β-lactamase inhibitor protein interface," *J. Biol. Chem.* **281**, 26745 (2006).

Richard, P., Z.-H. Pan, M. Neupane, A.V. Fedorov, T. Valla, P.D. Johnson, G.D. Gu, W. Ku, Z. Wang, and H. Ding, "*Nature* of oxygen dopant-induced states in high-temperature Bi$_2$Sr$_2$CaCu$_2$O$_{8+x}$ superconductors: A photoemission investigation," *Phys. Rev. B* **74**, 094512 (2006).

Rigden, D.J., J.E. Littlejohn, H.V. Joshi, B.L. de Groot, and M.J. Jedrzejas, "Alternate structural conformations of *Streptococcus pneumoniae* hyaluronan lyase: Insights into enzyme flexibility, and underlying molecular mechanism of action," *J. Mol. Biol.* **358**, 1165 (2006).

Riggs, J.R., H. Hu, A. Kolesnikov, E.M. Leahy, K.E. Wesson, W.D. Shrader, D. Vijaykumar, T.A. Wahl, Z. Tong, P.A. Sprengeler, M.J. Green, C. Yu, B.A. Katz, E. Sanford, M. Nguyen, R. Cabuslay, and W.B. Young, "Novel 5-azaindole factor VIIa inhibitors," *Bioorg. Med. Chem. Lett*. **16**, 3197 (2006).

Rollings, E., G.-H. Gweon, S.Y. Zhou, B.S. Mun, J.L. McChesney, B.S. Hussain, A.V. Fedorov, P.N. First, W.A. de Heer, and A, Lanzara, "Synthesis and characterization of atomically thin graphite films on a silicon carbide substrate," *J. Phys. Chem. Solids* **67**, 2172 (2006).

Rosenberg, O.S., S. Deindl, L.R. Comolli, A. Hoelz, K.H. Downing, A.C. Nairn, and

J. Kuriyan, “Oligomerization states of the association domain and the holoenyzme of Ca^{2+}/CaM kinase II,” *FEBS J.* **273**, 682 (2006).

Rotenberg, E., Y.Z. Wu, J.M. An, M.A. Van Hove, A. Canning, L.W. Wang, and Z.Q. Qiu, “Non-free-electron momentum- and thickness-dependent evolution of quantum well states in the Cu/Co/Cu(001) system,” *Phys. Rev. B* **73**, 075426 (2006).

Ruthenburg, A.J., W. Wang, D.M. Graybosch, H. Li, C.D. Allis, D.J. Patel, and G.I. Verdine, “Histone H3 recognition, and presentation by the WDR5 module of the MLL1 complex,” *NSMB* **13,** 704 (2006).

Ryser, A.L., D.G. Strawn, M.A. Marcus, S. Fakra, J.L. Johnson-Maynard, and G. Moller, “Microscopically focused synchrotron x-ray investigation of selenium speciation in soils developing on reclaimed mine lands,” *Environ. Sci. Technol.* **40**, 462 (2006).

Sagermann, M., W.A. Baase, and B.W. Matthews, “Sequential reorganization of beta-sheet topology by insertion of a single strand,” *Protein Sci.* **15**, 1085 (2006).

Salmassi, F., P.P. Naulleau, and E.M. Gullikson, “Spin-on-glass coatings for the generation of superpolished substrates for use in the extreme-ultraviolet regime,” *Appl. Optics* **45**, 2404 (2006).

Salmassi, F., P.P. Naulleau, E.M. Gullikson, D. Olynick, and J. Liddle, “Extreme ultraviolet binary phase gratings: Fabrication, and application to diffractive optics,” *J. Vac. Sci. Technol. A* **24**, 1136 (2006).

Salom, D., D.T. Lodowski, R.E. Stenkamp, I.L. Trong, M. Golczak, B. Jastrzebska, T. Harris, J.A. Ballesteros, and K. Palczewski, “Crystal structure of a photoactivated deprotonated intermediate of rhodopsin,” *Proc. Natl. Acad. Sci. USA* **103**, 16123 (2006).

Sampathkumar, P., S. Turley, C.H. Sibley, and W.G. Hol, “NADP$^+$ expels both the co-factor and a substrate analog from the *Mycobacterium tuberculosis* ThyX active site: Opportunities for anti-bacterial drug design,” *J. Mol. Biol.* **360**, 1 (2006).

Sampietro, J., C.L. Dahlberg, U.S. Cho, T.R. Hinds, D. Kimelman, and W. Xu, “Crystal structure of a beta-catenin/BCL9/Tcf4 complex,” *Mol. Cell* **24**, 293 (2006).

Sandford, S.A., et al., “Organics captured from Comet 81P/Wild 2 by the Stardust spacecraft,” *Science* **314**, 1720 (2006).

Sarret, G., E. Harada, Y.E. Choi, M.P. Isaure, N. Geoffroy, S. Fakra, M.A. Marcus, M. Birschwilks, S. Clemens, and A. Manceau, “Trichomes of tobacco excrete zinc as zinc-substituted calcium carbonate and other zinc-containing compounds,” *Plant Physiol.* **141**, 1021 (2006).

Sawaya, M.R., G.C. Cannon, S. Heinhorst, S. Tanaka, E.B. Williams, T.O. Yeates, and C.A. Kerfeld, “The structure of beta-carbonic anhydrase from the carboxysomal shell reveals a distinct subclass with one active site for the price of two,” *J. Biol. Chem.* **281**, 7546 (2006).

Schelleneberg, M.J., R.A. Edwards, D.B. Ritchie, O.A. Kent, M.M. Golas, H. Stark, R. Luhrmann, J.N.M. Glover, and A.M. MacMillan, “Crystal structure of a core spliceosomal protein interface,” *Proc. Natl. Acad. Sci. USA* **103**, 1266 (2006).

Schmalhorst, J., M.D. Sacher, V. Hoink, G. Reiss, A. Hutten, D. Engel, and A. Ehresmann, “Magnetic and chemical properties of Co$_2$MnSi thin films compared to the Co$_2$MnSi/Al-O interface,” *J. Appl. Phys.* **100**, 113903 (2006).

Schmeisser, D., P. Hoffmann, F. Zheng, F. Himpsel, H. Stegmann, and E. Zschech, “Chemical bonding in low-k dielectric materials for interconnect isolation: Characterization using XAS and EELS,” *AIP Conf. Proc.* **817**, 117 (2006); Eighth International Workshop on Stress-Induced Phenomena in Metallization, Dresden Germany, September 12–14, 2005.

Schmidt, D.A., T. Ohta, C.-Y. Lu, A.A. Bostwick, Q. Yu, E. Rotenberg, F.S. Ohuchi, and M.A. Olmstead, “Semiconducting chalcogenide buffer layer for oxide heteroepitaxy on Si(001),” *Appl. Phys. Lett.* **88**, 181903 (2006).

Schmitt, A.L., L. Zhu, D. Schmeisser, F.J. Himpsel, and S. Jin, “Metallic single-crystal CoSi nanowires via chemical vapor deposition of single-source precursor,” *J. Phys. Chem. B* **110**, 18142 (2006).

Schmitt, A.L., M.J. Bierman, D. Schmeisser, F.J. Himpsel, and S. Jin, “Synthesis and properties of single-crystal fesi nanowires,” *Nano Lett.* **6**, 1617 (2006).

Schreiter, E.R., S.C. Wang, D.B. Zamble, and C.L. Drennan, “NikR–operator complex structure and the mechanism of repressor activation by metal ions,” *Proc. Natl. Acad. Sci. USA* **103,** 13676 (2006).

Schumacher, M.A., E. Karamooz, A. Zikova, L. Trantirek, and J. Lukes, “Crystal structures of *T. brucei* MRP1/MRP2 guide-RNA binding complex reveal RNA matchmaking mechanism,” *Cell* **126**, 701 (2006).

Schumacher, M.A., G. Seidel, W. Hillen, and R.G. Brennan, “Phosphoprotein Crh-Ser^{46}-P displays altered binding to CcpA to effect carbon catabolite regulation,” *J. Biol. Chem.* **281**, 6793 (2006).

Schumacher, M.A., K. Mizuno, and H.P. Bachinger, “The crystal structure of a collagen-like polypeptide with 3(*S*)-hydroxyproline residues in the Xaa position forms a standard 7/2 collagen triple helix,” *J. Biol. Chem.* **281**, 27566 (2006).

Sciau, P., P. Goudeau, N. Tamura, and E. Dooryhee, “Micro scanning x-ray diffraction study of Gallo-Roman terra sigillata ceramics,” *Appl. Phys. A: Mater.* **83**, 219 (2006).

Scott, P.G., C.M. Dodd, E.M. Bergmann, J.K. Sheehan, and P.N. Bishop, “Crystal structure of the biglycan dimer and evidence that dimerization is essential for folding, and stability of class I small leucine-rich repeat proteoglycans,” *J. Biol. Chem.* **281**, 13324 (2006).

Scully, S.W.J., I. Alvarez, C. Cisneros, E.D. Emmons, M.F. Gharaibeh, D. Leitner, M.S. Lubell, A. Mueller, R.A. Phaneuf, R. Puettner, A.S. Schlachter, S. Schippers, W. Shi, C.P. Ballance, and B.M. McLaughlin, “Doubly excited resonances in the photoionization spectrum of Li$^+$: Experiment and theory,” *J. Phys. B: At. Mol. Opt.* **39**, 3957 (2006).

Seo, J.H., D.S. Park, S.W. Cho, C.Y. Kim, W.C. Jang, C.N. Whang, K.-H. Yoo, G.S. Chang, T. Pedersen, A. Moewes, K.H. Chae, and S.J. Cho, “Buffer layer effect on the structural, and electrical properties of rubrene-based organic thin-film transistor,” *Appl. Phys. Lett.* **89**, 163505 (2006).

Sharma, P., H. Kimura, A. Inoue, E. Arenholz, and J.-H. Guo, “Temperature and thickness driven spin-reorientation transition in amorphous Co-Fe-Ta-B thin films,” *Phys. Rev. B* **73**, 52401 (2006).

Shiau, A.K., S.F. Harris, D.R. Southworth, and D.A. Agard, “Structural analysis of *E. coli* hsp90 reveals dramatic nucleotide-dependent conformational rearrangements,” *Cell* **127**, 329 (2006).

Shim, S.-H., S. Rekhi, M.C. Martin, and R. Jeanloz, “Vibrational spectroscopy and x-ray diffraction of $Cd(OH)_2$ to 28 GPa at 300 K," *Phys. Rev. B* **74**, 024107 (2006).

Shin, D.H., J.-S. Kim, H. Yokota, R. Kim, and S.-H. Kim, "Crystal structure of the DUF16 domain of MPN010 from *Mycoplasma pneumoniae*," *Protein Sci.* **15**, 921 (2006).

Shin, D.-W., C.L. Dong, M. Mattesini, A. Augustsson, S. Mao, C.L. Chang, C. Persson, R. Ahuja, J. Nordgren, S.X. Wang, and J.-H. Guo, "Size dependence of the electronic structure of copper nanoclusters in SiC matrix," *Chem. Phys. Lett.* **422**, 543 (2006).

Shore, D.A., L. Teyton, R.A. Dwek, P.M. Rudd, and I.A. Wilson, "Crystal Structure of the TCR co-receptor CD8αα in complex with monoclonal antibody YTS 105.18 Fab fragment at 2.88 Å resolution," *J. Mol. Biol.* **358**, 347 (2006).

Shu, J.N., K.R. Wilson, M. Ahmed, and S.R. Leone, "Coupling a versatile aerosol apparatus to a synchrotron: Vacuum ultraviolet light scattering, photoelectron imaging, and fragment free mass spectrometry," *Rev. Sci. Instrum.* **77**, 043106 (2006).

Shu, J.N., K.R. Wilson, M. Ahmed, S.R. Leone, C. Graf, and E. Ruhl, "Elastic light scattering from nanoparticles by monochromatic vacuum-ultraviolet radiation," *J. Chem. Phys.* **124**, 03470707 (2006).

Shu, X., N.C. Shaner, C.A. Yarbrough, R.Y. Tsien, and S.J. Remington, "Novel chromophores, and buried charges control color in mFruits," *Biochemistry—US* **45**, 9639 (2006).

Shutthanandan V., S. Thevuthasan, T. Droubay, S.M. Heald, M.H. Engelhard, D.E. McCready, S.A. Chambers, P. Nachimuthu, and B.S. Mun, "Synthesis of room-temperature ferromagnetic Cr-doped TiO_2(1 1 0) rutile single crystals using ion implantation" *Nucl. Instrum. Methods Phys. Res., Sect. B* **242**, 198 (2006).

Si, M., T. Araki, H. Ade, A.L.D. Kilcoyne, R. Fischer, J.C. Sokolov, and M.H. Rafailovich, "Compatibilizing bulk polymer blends by using organoclays," *Macromolecules* **39**, 4793 (2006).

Silva D.A., and P.J.M. Monteiro, "The influence of polymers on the hydration of portland cement phases analyzed by soft X-ray transmission microscopy," *Cement Concrete Res.,* **36**, 1501 (2006).

Simon, M., L. Joumel, R. Guillemin, W.C. Stole, I. Minkov, F. Gel'mukhanov, P. Salek, H. Ågren, S. Camiato, R. Taïeb, A.C. Hudson, and D.W. Lindle, "Femtosecond nuclear motion of HCl probed by resonant x-ray Raman scattering in the Cl 1s region," *Phys. Rev. A* **73**, 020706 (2006).

Sinha, S.K., S. Roy, M.R. Fitzsimmons, S. Park, M. Dorn, O. Petracic, I.V. Roshchin, Z.P. Li, X. Batlle, R. Morales, A. Misra, X. Zhang, K. Chesnel, J.B. Kortright, and I.K. Schuller, "Combined neutron, and synchrotron studies of magnetic films," *Pramana* **67,** 47 (2006).

Smith, A.D., T. Pradell, J. Roque, J. Molera, M. Vendrell-Saz, A.J. Dent, and E. Pantos, "Color variations in 13th century Hispanic lustre—An EXAFS study," *J. Non-Cryst. Solids* **352**, 5353 (2006).

Smith, J.D., "X-ray, and Raman spectroscopy of water and aqueous solutions," Ph.D. thesis, University of California, Berkeley (2006).

Smith, J.D., C.D. Cappa, B.M. Messer, W.S. Drisdell, R.C. Cohen, and R.J. Saykally, "Probing the local structure of liquid water by x-ray absorption spectroscopy," *J. Phys. Chem. B* **110**, 20038 (2006).

Smith, J.D., C.D. Cappa, W.S. Drisdell, R.C. Cohen, and R.J. Saykally, "Raman thermometry measurements of free evaporation from liquid water droplets," *J. Am. Chem. Soc.* **128,** 12892 (2006).

Speziale, S., I. Lonardelli, L. Miyagi, J. Pehl, C.E. Tommaseo, and H.R. Wenk, "Deformation experiments in the diamond-anvil cell: Texture in copper to 30 GPa," *J. Phys.: Condens. Matter* **18**, S1007 (2006).

Spiegel, P.C., B. Chevalier, D. Sussman, M. Turmel, C. Lemieux, and B.L. Stoddard, "The structure of the I-CEUI homing endonuclease: Divergence, and asymmetry of DNA recognition by a homodimeric protein scaffold," *Structure* **14**, 869 (2006).

Spolenak, R., N. Tamura, and J.R. Patel "X-ray microdiffraction as a probe to reveal flux divergences in interconnects," AIP Conf. Proc. 817, 228 (2006); Eighth International Workshop on Stress-Induced Phenomena in Metallization, Dresden Germany, September 12–14, 2005.

Srajer, G., L.H. Lewis, S.D. Bader, A.J. Epstein, C.S. Fadley, E.E. Fullerton, A. Hoffmann, J.B. Kortright, K.M. Krishnan, S.A. Majetich, T.S. Rahman, C.A. Ross, M.B. Salamon, I.K. Schuller, T.C. Schulthess, and J.Z. Sun, "Advances in nanomagnetism via x-ray techniques," *J. Magn. Magn. Mater.* **307**, 1 (2006).

Stamenkovic V.R., B.S. Mun, K.J.J. Mayrhofer, P.N. Ross, and N.M. Markovic, "The effect of surface composition on electronic structure, stability, and electrocatalytic properties of Pt-transition metal alloys: Pt-skin versus Pt-skeleton surfaces," *J. Am. Chem. Soc.* **118**, 8813 (2006).

Stamenkovic V.R., B.S. Mun, K.J. J. Mayrhofer, P.N. Ross, N.M. Markovic, J. Rossmeisl, J. Greeley, and J.K. Norskov, "Changing the activity of electrocatalysts for oxygen reduction by tuning the surface electronic structure," *Angew. Chem. Int. Ed.* **18**, 2897 (2006).

Stanfield, R.L., M.K. Gorny, S. Zolla-Pazner, and I.A. Wilson, "Crystal structures of human immunodeficiency virus type 1 (HIV-1) neutralizing antibody 2219 in complex with three different V3 peptides reveal a new binding mode for HIV-1 cross-reactivity," *J. Virol.* **80**, 6093 (2006).

Stauber, D.J., E.W. Debler, P.A. Horton, K.A. Smith, and I.A. Wilson, "Crystal structure of the IL-2 signaling complex: Paradigm for a heterotrimeric cytokine receptor," *Proc. Natl. Acad. Sci. USA* **103**, 2788 (2006).

Stavropoulos, P., G. Blobel, and A. Hoelz, "Crystal structure, and mechanism of human lysine-specific demethylase-1," *Nat. Struct. Mol. Biol.* **13**, 626 (2006).

Steier, C., "What are good beam stabilization strategies and their limits in ERLs?" in *FLS 2006 Proceedings (2006)*; 37th ICFA Advanced Beam Dynamics Workshop on Future Light Sources, Hamburg Germany, May 16–19, 2006.

Steier, C., D. Robin, and T. Scarvie, "Status of the top-off upgrade of the ALS," in *EPAC 2006 Proceedings (2006)*; 10th Biennial European Particle Accelerator Conference, EPAC '06, Edinburgh UK, June 26–30, 2006.

Steier, C., S. Marks, S. Prestemon, D. Robin, R. Schlueter, W. Wan, and W. Wittmer, "Studies of the nonlinear dynamics effects of APPLE-II type EPUs at the ALS," in *EPAC 2006 Proceedings (2006)*; 10th Biennial European Particle Accelerator Conference, EPAC '06, Edinburgh UK, June 26–30, 2006.

Stephen, R., K. Palczewski, and M.C. Sousa, "The crystal structure of GCAP3 suggests molecular mechanism of GCAP-linked cone dystrophies," *J. Mol. Biol.* **359**, 266 (2006).

Sterling, N., "Light neutron-capture element abundances in planetary nebulae," Ph.D. thesis, University of Texas, Austin (2006).

Stevens, J., O. Blixt, T.M. Tumpey, J.K. Taubenberger, J.C. Paulson, and I.A. Wilson, "Structure and receptor specificity of the hemagglutinin from an H5N1 influenza virus," *Science* **312**, 404 (2006).

Stewart, S.J., M. Fernández-García, C. Belver, S.B. Mun, and F.G. Requejo, "Influence of N-doping on the structure, and electronic properties of titania nanoparticle photocatalytsts," *J. Phys. Chem. B* **110**, 16482 (2006).

Stone, P.R., M.A. Scarpulla, R. Farshchi, I.D. Sharp, E.E. Haller, O.D. Dubon, K.M. Yu, J.W. Beeman, E. Arenholz, J.D. Denlinger, and H. Ohldag, "Mn L3,2 x-ray absorption and magnetic circular dichroism in ferromagnetic $Ga_{1-x}Mn_xP$," *Appl. Phys. Lett.* **89**, 012504 (2006).

Strong, M., M.R. Sawaya, S.S. Wang, M. Phillips, D. Cascio, and D. Eisenberg, "Toward the structural genomics of complexes: Crystal structure of a PE/PPE protein complex from *Mycobacterium tuberculosis*," *Proc. Natl. Acad. Sci. USA* **103**, 8060 (2006).

Stroud, J.C., Y. Wu, D.L. Bates, A. Han, K. Nowick, S. Paabo, H. Tong, and L. Chen, "Structure of the forkhead domain of FOXP2 bound to DNA," *Structure* **14**, 159 (2006).

Suh J.O., J.W. Nah, K.N. Tu. and N. Tamura, "Synchrotron radiation based x-ray micro-diffraction study on reliability issues of solder joints in electronic packaging technology," in *ECTC 2006 Proceedings*, p. 1924 (cat. no. 1645924); 56th Electronic Components and Technology Conference Piscataway, NJ, May 30–June 2, 2006.

Suh, J.O., K.N. Tu, and N. Tamura, "A synchrotron radiation x-ray microdiffraction study on orientation relationships between a Cu_6Sn_5, and Cu substrate in solder joints," *J. Microsc.: Oxford* **58**, 63 (2006).

Sun, Z., "Angle-resolved photoemission studies on bi-layer colossal magnetoresistive oxides $La_{2-2x}Sr_{1+2x}Mn_2O_7$," Ph.D. thesis, University of Colorado, Boulder (2006).

Sun, Z., Y.D. Chuang, A.V. Fedorov, J.F. Douglas, D. Reznik, F. Weber, N. Aliouane, D.N. Argyriou, H. Zheng, J.F. Mitchell, T. Kimura, Y. Tokura, A. Revcolevschi, and D.S. Dessau, "Quasiparticlelike peaks, kinks, and electron-phonon coupling at the $(\pi,0)$ regions in the CMR Oxide $La_{2-2x}Sr_{1+2x}Mn_2O_7$," *Phys. Rev. Lett.* **97**, 056401 (2006).

Sveum, N.E., S.J. Goncher, and D.M. Neumark, "Determination of absolute photoionization cross sections of the phenyl radical," *Phys. Chem. Chem. Phys.* **8**, 592 (2006).

Swartz, L., M. Kuchinskas, H. Li, T.L. Poulos, and W.N. Lanzilotta, "Redox-dependent structural changes in the *Azotobacter vinelandii* bacterioferritin: New insights into the ferroxidase and iron transport mechanism," *Biochemistry* **45**, 4421 (2006).

Szurmant, H., H. Zhao, M.A. Mohan, J.A. Hoch, and K.I. Varughese, "The crystal structure of YycH involved in the regulation of the essential YycFG two-component system in *Bacillus subtilis* reveals a novel tertiary structure," *Protein Sci.* **15**, 929 (2006).

Taatjes, C.A., "Uncovering the fundamental chemistry of ALKYL + O_2 reactions via measurements of product formation," *J. Phys. Chem. A* **110**, 4299 (2006).

Taatjes, C.A., N. Hansen, J.A. Miller, T.A. Cool, J. Wang, P.R. Westmoreland, M.E. Law, T. Kasper, and K. Kohse-Hoinghaus, "Combustion chemistry of enols: Possible ethenol precursors in flames," *J. Phys. Chem. A* **110**, 3254 (2006).

Takahashi, O., M. Odelius, D. Nordlund, A. Nilsson, H. Bluhm, and L.G.M. Pettersson, "Auger decay calculations with core-hole excited-state molecular-dynamics simulations of water," *J. Chem. Phys.* **124**, 064307 (2006).

Takamura, Y., R.V. Chopdekar, A. Scholl, A. Doran, J.A. Liddle, B. Harteneck, and Y. Suzuki, "Tuning magnetic domain structure in nanoscale $La_{0.7}Sr_{0.3}MnO_3$ islands," *Nano Lett.* **6**, 1287 (2006).

Takenaka, H., S. Ichimaru, and E.M. Gullikson, "Development of Beam Splitters for EUV region," *Proc. 8th Int. Conf.* **7**, 198; 8th International Conference on X-ray Microscopy, Himeji City, Japan, July 26–30, 2005.

Tanaka, K., W.S. Lee, D.H. Lu, A. Fujimori, T. Fujii, Risidiana, I. Terasaki, D.J. Scalapino, T.P. Devereaux, Z. Hussain, and Z.X. Shen, "Distinct Fermi-momentum-dependent energy gaps in deeply underdoped Bi2212," *Science* **314**, 1910 (2006).

Telling, N.D., G. van der Laan, S. Ladak, R.J. Hicken, and E. Arenholz, "Evidence of a barrier oxidation dependence on the interfacial magnetism in Co/alumina based magnetic tunnel junctions," *J. Appl. Phys.* **99**, 08E505 (2006).

Telling, N.D., P.S. Keatley, G. van der Laan, R.J. Hicken, E. Arenholz, Y. Sakuraba, M. Oogane, Y. Ando, and T. Miyazaki, "Interfacial structure, and half-metallic ferromagnetism in Co_2MnSi-based magnetic tunnel junctions," *Phys. Rev. B* **74**, 224439 (2006).

Thibault, P., V. Elser, C. Jacobsen, D. Shapiro, and D. Sayre, "Reconstruction of a yeast cell from x-ray diffraction data," *Acta Crystallagr., Sec. A* **62**, 248 (2006).

Timossi, C., and H. Nishimura, "EPICS SCA clients on the .NET x64 platform," in *PCaPAC Proceedings*, p. 56 (2006); Sixth International Workshop on Personal Computers and Particle Accelerator Controls, Newport News, Virginia, October 24–27, 2006.

Tommaseo, C., J. Devine, S. Merkel, S. Speziale, and H.R. Wenk, "Texture development and elastic stress in magnesiowuestite at high pressure," *Physics Chem. Miner.* **3**, 84 (2006).

Toner B., A. Manceau, S.M., and G. Sposito, "Zinc sorption to biogenic hexagonal-birnessite particles within a hydrated bacterial biofilm," *Geochim. Cosmochim. Acta.* **70**, 27 (2006).

Tully, D.C., H. Liu, A.K. Chatterjee, P.B. Alper, R. Epple, J.A. Williams, M.J. Roberts, D.H. Woodmansee, B.T. Masick, C. Tumanut, J. Li, G. Spraggon, M. Hornsby, J. Chang, T. Tuntland, T. Hollenbeck, P. Gordon, J.L. Harris, and D.S. Karanewsky, "Synthesis and SAR of arylaminoethyl amides as noncovalent inhibitors of cathepsin S: P3 cyclic ethers," *Bioorg. Med. Chem. Lett.* **16**, 5112 (2006).

Tully, D.C., H. Liu, P.B. Alper, A.K. Chatterjee, R. Epple, M.J. Roberts, J.A. Williams, K.T. Nguyen, D.H. Woodmansee, C. Tumanut, J. Li, G. Spraggon, J. Chang, T. Tuntland, J.L. Harris, and D.S. Karanewsky, "Synthesis and evaluation of arylaminoethyl amides as noncovalent inhibitors of cathepsin S. Part 3: Heterocyclic P3," *Bioorg. Med. Chem. Lett.* **16**, 1975 (2006).

Turner, J.M., J. Graziano, G. Spraggon, and P.G. Schultz, "Structural plasticity of an aminoacyl-TRNA synthetase active site," *Proc. Natl. Acad. Sci. USA* **103**, 6483 (2006).

Valla, T., A.V. Fedorov, J. Lee, J.C. Davis, and G.D. Gu, "The ground state of the pseudogap in cuprate superconductors," *Science* **314**, 1914 (2006).

Van Waeyenberge, B., A. Puzic, H. Stoll, K.W. Chou, T. Tyliszczak, R. Hertel, M. Fähnle, H. Brückl, K. Rott, G. Reiss, I. Neudecker, D. Weiss, C.H. Back, and G. Schütz, "Magnetic vortex core reversal by excitation with short bursts of an alternating field," *Nature* **444**, 461 (2006).

Vespa, M., "Influence of the inherent heterogeneity of cement on the uptake mechanisms of Ni, and Co: A micro-spectroscopic study," Ph.D. thesis, Swiss Federal Institute of Technology, Zürich, Switzerland (2006).

Vespa, M., R. Dähn, D. Grolimund, M. Harfouche, E. Wieland, and A.M. Scheidegger, "Speciation of heavy metals in cement-stabilized waste forms: A micro-spectroscopic study," *J. Geochem. Explor.* **88**, 77 (2006).

Vespa, M., R. Dähn, E. Gallucci, D. Grolimund, E. Wieland, and A.M. Scheidegger, "Microscale investigations of Ni uptake by cement using a combination of scanning electron microscopy and synchrotron based techniques," *Environ. Sci. Technol.* **40**, 7702 (2006).

Vijaykumar, D., P.A. Sprengeler, M. Shaghafi, J.R. Spencer, B.A. Katz, C. Yu, R. Rai, W.B. Young, B. Schultz, and J. Janc, "Discovery of novel hydroxy pyrazole based factor IXa inhibitor," *Bioorg. Med. Chem. Lett.* **16**, 2796 (2006).

Walter C.W., N.D. Gibson, R.C. Bilodeau, N. Berrah, J.D. Bozek, G.D. Ackerman, and A. Aguilar, "Shape resonance in K-shell photodetachment from C^-," *Phys. Rev. A* **73**, 062702 (2006).

Walter, M.J., R.G. Tronnes, L.S. Armstrong, O.T. Lord, W.A. Caldwell, and S.M. Clark, "Subsolidus phase relations and perovskite compressibility in the system $MgO–AlO_{1.5}–SiO_2$ with implications for Earth's lower mantle," *Earth Planet. Sci. Lett.* **248**, 77 (2006).

Walukiewicz, W., J. W. Ager III, K. M. Yu, Z. Liliental-Weber, J. Wu, S. X. Li, R. E. Jones, and J. D. Denlinger, "Structure, and electronic properties of InN and In-rich group III-nitride alloys," *J. Phys. D Appl. Phys.* **39**, R83 (2006).

Wang, D., D.A. Bushnell, K.D. Westover, C.D. Kaplan, and R.D. Kornberg, "Structural basis of transcription: Role of the trigger loop in substrate specificity and catalysis," *Cell* **127**, 941 (2006).

Wang, J.C., "Photoionization and electron-impact ionization of Ar^{5+}," masters thesis, University of Nevada, Reno (2006).

Wang, S., R.T. Fleming, E.M. Westbrook, P. Matsumura, and D.B. McKay, "Structure of the *Escherichia coli* FlhDC complex, a prokaryotic heteromeric regulator of transcription," *J. Mol. Biol.* **355**, 798 (2006).

Wang, S., Y. Hu, M.T. Overgaard, F.V. Karginov, O.C. Uhlenbeck, and D.B. McKay, "The domain of the *Bacillus subtilis* DEAD-box helicase YxiN that is responsible for specific binding of 23S rRNA has an RNA recognition motif fold," *RNA* **12**, 959 (2006).

Wang, S.X., K.C. Pandey, J.R. Somoza, P.S. Sijwali, T. Kortemme, L.S. Brinen, R.J. Fletterick, P.J. Rosenthal, and J.H. McKerrow, "Structural basis for unique mechanisms of folding and hemoglobin binding by a malarial protease," *Proc. Natl. Acad. Sci. USA* **103**, 11503 (2006).

Wang, X., R.H. Baloh, J. Milbrandt, and K.C. Garcia, "Structure of artemin complexed with its receptor GFRα3: Convergent recognition of glial cell line-derived neurotrophic factors," *Structure* **14**, 1083 (2006).

Wang, Y., M. Rafailovich, J. Sokolov, D. Gersappe, T. Araki, Y. Zou, A.D.L. Kilcoyne, H. Ade, G. Marom, and A. Lustiger, "Substrate effect on the melting temperature of thin polyethylene films," *Phys. Rev. Lett.* **96**, 028303 (2006).

Wei, R.R., J.R. Schnell, N.A. Larsen, P.K. Sorger, J.J. Chou, and S.C. Harrison, "Structure of a central component of the yeast kinetochore: The Spc24p/Spc25p globular domain," *Structure* **14**, 1003 (2006).

Weinhardt, L., O. Fuchs, A. Peter, E. Umbach, C. Heske, J. Reichardt, M. Bar, I. Lauermann, I. Kotschau, A. Grimm, A. Sokoll, M.Ch. Lux-Steiner, T.P. Niesen, S. Visbeck, and F. Karg, "Spectroscopic investigation of the deeply buried $Cu(In,Ga)(S,Se)_2$/Mo interface in thin-film solar cells," *J. Chem. Phys.* **124**, 074705 (2006).

Weinhardt, L., O. Fuchs, D. Gross, E. Umbach, C. Heske, N.G. Dhere, A.A. Kadam, and S.S. Kulkarni, "Surface modifications of $Cu(In,Ga)S_2$ thin film solar cell absorbers by KCN and H_2O_2/H_2SO_4 treatments," *J. Appl. Phys.* **100**, 024907 (2006).

Wenk, H.-R., I. Lonardelli, S. Merkel, L. Miyagi, J. Pehl, S. Speziale, and C.E. Tommaseo, "Deformation textures produced in diamond anvil experiments, analysed in radial diffraction geometry," *J. Phys.: Condens. Mat.* **18**, S933 (2006).

Westmoreland, P.R., M.E. Law, T.A. Cool, J. Wang, C.A. Taatjes, N. Hansen, and T. Kasper, "Analysis of flame structure by molecular-beam mass spectrometry using electron-impact and synchrotron-photon ionization," *Combust. Expl. Shock Waves*, **42**, 672 (2006).

Wilks, R.G., J.B. MacNaughton, H.-B. Kraatz, T. Regier, and A. Moewes, "Combined x-ray absorption spectroscopy and density functional theory examination of ferrocene-labeled peptides," *J. Phys. Chem. B* **110**, 5955 (2006).

Wilson, K.R., D.S. Peterka, M. Jimenez-Cruz, S.R. Leone, and M. Ahmed, "VUV photoelectron imaging of biological nanoparticles: Ionization energy determination of nanophase glycine and phenylalanine-glycine-glycine," *Phys. Chem. Chem. Phys.* **8**, 1884 (2006).

Wilson, K.R., J. Jimenez-Cruz, C. Nicolas, L. Belau, S.R. Leone, and M. Ahmed, "Thermal vaporization of biological nanoparticles: Fragment-free vacuum ultraviolet photoionization mass spectra of tryptophan, phenylalanine-glycine-glycine, and beta-carotene," *J. Phys. Chem. A* **110**, 2106 (2006).

Wilson, K.R., L. Belau, C. Nicolas, M. Jimenez-Cruz, S.R. Leone, and M. Ahmed, "Direct identification of the ionization energy of histidine with VUV synchrotron radiation," *Int. J. Mass Spectrom.* **249**, 155 (2006).

Witt, S., Y.D. Kwon, M. Sharon, K. Felderer, M. Beuttler, C.V. Robinson, W. Baumeister, and B.K. Jap, "Proteasome assembly triggers a switch required for active-site maturation," *Structure* **14**, 1179 (2006).

Wood, Z.A., L.H. Weaver, P.H. Brown, D. Beckett, and B.W. Matthews, "Co-repressor induced order and biotin repressor dimerization: A case for divergent followed by convergent evolution," *J. Mol. Biol.* **357**, 509 (2006).

Woods, K.N., S.A. Lee, H.-Y.N. Holman, and H. Wiedemann, "The effect of solvent dynamics on the low frequency collective motions of DNA in solution and unoriented films," *J. Chem. Phys.* **124**, 224706 (2006).

Wozei, E., H.-Y.N. Holman, S.W. Hermanowicz, and S. Borglin, "Detecting estrogenic activity in water samples with estrogen-sensitive yeast cells using spectrophotometry and fluorescence microscopy," in Proceedings of the 2006 UNC Environmental Symposium, Safe Drinking Water: Where Science Meets Policy, Chapel Hill, North Carolina, March 16–17, 2006.

Wright, H.M N., J.J. Roberts, and K.V. Cashman, "Permeability of anisotropic tube pumice: Model calculations and measurements," *Geophys. Res. Lett.* **33**, L17316 (2006).

Wright, H.M., "Physical and chemical signatures of degassing in volcanic systems," Ph.D. thesis, University of Oregon (2006).

Wu, Y., M. Borde, V. Heissmeyer, M. Feuerer, A.D. Lapan, J.C. Stroud, D.L. Bates, L. Gou, A. Han, S.F. Ziegler, D. Mathis, C. Benoist, L. Chen, and A. Rao, "FOXP3 controls regulatory T cell function through cooperation with NFAT," *Cell* **126**, 375 (2006).

Wu, Y.Z., C. Won, E. Rotenberg, H.W. Zhao, Q.-K. Xue, W. Kim, T.L. Owens, N.V. Smith, and Z.Q. Qiu, "Resonant interaction between two Cu quantum wells investigated by angle-resolved photoemission spectroscopy," *Phys. Rev. B* **73**, 125333 (2006).

Yablonskikh, M.V., J. Braun, M.T. Kuchel, A.V. Postnikov, J.D. Denlinger, E.I. Shreder, Y.M. Yarmoshenko, M. Neumann, and A. Moewes, "X-ray 2p photoelectron and L_α resonant x-ray emission spectra of the 3d metals in Ni_2MnZ (Z = In,Sn,Sb) Heusler alloys," *Phys. Rev. B* **74**, 085103 (2006).

Yablonskikh, M.V., R. Berger, U. Gelius, R. Lizarraga, T.B. Charikova, E.Z. Kurmaev, and A. Moewes, "On the bonding situation in $TlCo_2Se_2$," *J. Phys.: Condens. Mat.* **18**, 1757 (2006).

Yang, Q., T. Hamilton, C. Xiao, A. Hirose, and A. Moewes, "Plasma enhanced synthesis of diamond nanocone films," *Thin Solid Films* **494**, 110 (2006).

Yang, X-L., F.J. Otero, K.L. Ewalt, J. Liu, M.A. Swairjo, C. Köhrer, U.L. RajBhandary, R.J. Skene, D.E. McRee, and P. Schimmel, "Two conformations of a crystalline human tRNA synthetase–tRNA complex: Implications for protein synthesis," *EMBO J.* **25**, 2919 (2006).

Yao, W., G. Balooch, M. Balooch, Y.B. Jiang, R.K. Nalla, J. Kinney, T.J. Wronski, and N.E. Lane, "Sequential treatment of ovariectomized mice with bFGF and risedronate restored trabecular bone microarchitecture and mineralization," *Bone* **39**, 460 (2006).

Yin, J., L.X. Xu, M.M. Cherney, E. Raux-Deery, A.A. Bindley, A. Savchenko, J.R. Walker, M.E. Cuff, M.J. Warren, and M.NG. James, "Crystal structure of the vitamin B12 biosynthetic cobaltochelatase, CbiXs, from *Archaeoglobus fulgidus*," *J. Struct. Funct. Genom.* **7**, 37 (2006).

Yin, J., M.M. Cherney, E.M. Bergmann, J. Zhang, C. Huitema, H. Pettersson, L.D. Eltis, J.C. Vederas, and M.N. James, "An episulfide cation (thiiranium ring) trapped in the active site of HAV 3C proteinase inactivated by peptide-based ketone inhibitors," *J. Mol. Biol.* **361**, 673 (2006).

Yin, Y., X. He, P. Szewczyk, T. Nguyen, and G. Chang, "Structure of the multidrug transporter EmrD from *Escherichia coli*," *Science* **312**, 741 (2006).

Yoder, J.D., and P.R. Dormitzer, "Alternative intermolecular contacts underlie the rotavirus VP5* two- to three-fold rearrangement," *EMBO J.* **25**, 1559 (2006).

Yoon, T. H., K. Benzerara, S. Ahn, R.G. Luthy, T. Tyliszczak, and G.E. Brown, "Nanometer-scale chemical heterogeneities of black carbon materials and their impacts on PCB sorption properties: Soft x-ray spectromicroscopy study," *Environ. Sci. Technol.* **40**, 5923 (2006).

Youn, B., G.E. Sellhorn, R.J. Mirchel, B.J. Gaffney, H.D. Grimes, and C. Kang, "Crystal structures of vegetative soybean lipoxygenase VLX-B and VLX-D, and comparisons with seed isoforms LOX-1 and LOX-3," *Proteins* **65**, 1008 (2006).

Youn, B., R. Camacho, S.G. Moinuddin, C. Lee, L.B. Davin, N.G. Lewis, and C.H. Kang, "Crystal structures, and catalytic mechanism of the *Arabidopsis* cinnamyl alcohol dehydrogenases AtCAD5, and AtCAD4," *Org. Biomol. Chem.* **4**, 1687 (2006).

Youn, B., S. Kim, S.G. Moinuddin, C. Lee, D.L. Bedgar, A.R. Harper, L.B. Davin, N.G. Lewis, and C. Kang, "Mechanistic and structural studies of Apoform, binary, and ternary complexes of the *Arabidopsis* alkenal double bond reductase At5g16970," *J. Biol. Chem.* **281**, 40076 (2006).

Young, M.A., N.P. Shah, L.H. Chao, M. Seeliger, Z.V. Milanov, W.H. Biggs, D.K. Treiber, H.K. Patel, P.P. Zarrinkar, D.J. Lockhart, C.L. Sawyers, and J. Kuriyan, "Structure of the kinase domain of an imatinib-resistant Abl mutant in complex with the Aurora kinase inhibitor VX-680," *Cancer Res.* **66**, 1007 (2006).

Young, W.B., J. Mordenti, S. Torkelson, W.D. Shrader, A. Kolesnikov, R. Rai, L. Liu, H. Hu, E.M. Leahy, M.J. Green, P.A. Sprengeler, B.A. Katz, C. Yu, J.W. Janc, K.C. Elrod, U.M. Marzec, and S.R. Hanson, "Factor VIIA inhibitors: Chemical optimization, preclinical pharmacokinetics, pharmacodynamics, and efficacy in an arterial baboon thrombosis model," *Bioorg. Med. Chem. Lett.* **16**, 2037 (2006).

Yousef, M.S., N. Bischoff, C.M. Dyer, W.A. Baase, and B.W. Matthews, "Guanidinium derivatives bind preferentially and trigger long-distance conformational changes in an engineered T4 lysozyme," *Protein Sci.*, **15**, 853 (2006).

Zajonc, D.M., G.D. Ainge, G.F. Painter, W.B. Severn, and I.A. Wilson, "Structural characterization of mycobacterial phosphatidylinositol mannoside binding to mouse CD1d," *J. Immunol.* **177**, 4577 (2006).

Zalatan, J.G., T.D. Fenn, A.T. Brunger, and D. Herschlag, "Structural and functional comparisons of nucleotide pyrophosphatase/phosphodiesterase and alkaline phosphatase: Implications for mechanism and evolution," *Biochemistry* **45**, 9788 (2006).

Zhang, G.P., and T.A. Callcott, "Resolving dd transitions in NaV_2O_5 using angle-resolved resonant inelastic x-ray scattering at the V L edge," *Phys. Rev. B* **73**, 125102 (2006).

Zhang, L., Z. Li, Y. Tan, G. Lolli, N. Sakulchaicharoen, F.G. Requejo, B.S. Mun, and D.E. Resasco, "Influence of a top crust of entangled nanotubes on the structure of vertically aligned forests of single-walled carbon nanotubes," *Chem. Mater.* **18**, 5624 (2006).

Zhang, T., X.N. Tang, K.C. Lau, C.Y, Ng, C. Nicolas, D.S. Peterka, M. Ahmed, M.L. Morton, B. Ruscic, R. Yang, L.X. Wei, C.Q. Huang, B. Yang, J. Wang, L.S. Sheng, Y.W. Zhang, and F. Qi, "Direct identification of propargyl radical in combustion flames by vacuum ultraviolet photoionization mass spectrometry," *J. Chem. Phys.* **124**, 074302 (2006).

Zhang, X., J. Gureasko, K. Shen, P.A. Cole, and J. Kuriyan, "An allosteric mechanism for activation of the kinase domain of epidermal growth factor receptor," *Cell*, **125**, 1137 (2006).

Zhang, X.N., J.P. Johnson, J.W. Kampf, and A.J. Matzger, "Ring fusion effects on the solid-state properties of α-oligothiophenes," *Chem. Mater.* **18**, 3470 (2006).

Zhang, Y., Y. Kim, N. Genoud, J. Gao, J.W. Kelly, S.L. Pfaff, G.N. Gill, J.E. Dixon, and J.P. Noel, "Determinants for dephosphorylation of the RNA polymerase II C-terminal domain by Scp1," *Mol. Cell*. **24**, 1 (2006).

Zhao, T., A. Scholl, F. Zavaliche, K. Lee, M. Barry, A. Doran, M.P. Cruz, Y.H. Chu, C. Ederer, N.A. Spaldin, R.R. Das, D.M. Kim, S.H. Baek, C.B. Eom, and R. Ramesh, "Electrical control of antiferromagnetic domains in multiferroic $BiFeO_3$ films at room temperature," *Nat. Mater.* **5**, 823 (2006).

Zhao, X., H. Yu, S. Yu, F. Wang, J.C. Sacchettini, and R.S. Magliozzo, "Hydrogen peroxide-mediated isoniazid activation catalyzed by *Mycobacterium tuberculosis* catalase-peroxidase (KatG) and its S315T mutant," *Biochemistry* **45**, 4131 (2006).

Zhou, S.Y., G.-H. Gweon, and A. Lanzara, "Low energy excitations in graphite: The role of dimensionality and lattice defects," *Ann. Phys.* **321**, 1730 (2006).

Zhou, S.Y., G.-H. Gweon, J. Graf, A.V. Fedorov, C.D. Spataru, R.D. Diehl, Y. Kopelevich, D.-H. Lee, S.G. Louie, and A. Lanzara, "First direct observation of Dirac fermions in graphite," *Nat. Phys.* **2**, 595 (2006).

Zhu, X., T.J. Dickerson, C.J. Rogers, G.F. Kaufmann, J.M. Mee, K.M. McKenzie, K.D. Janda, and I.A. Wilson, "Complete reaction cycle of a cocaine catalytic antibody at atomic resolution," *Structure* **14**, 205 (2006).

Zolensky, M.E., et al., "Mineralogy and petrology of Comet 81P/Wild 2 nucleus samples," *Science* **314**, 1735 (2006).

Zou, Y., T. Araki, G. Appel, A.L.D. Kilcoyne, and H. Ade, "Solid state effect in the NEXAFS spectra of alkane-based van der Waals crystal: Breakdown of molecular model," *Chem. Phys. Lett.* **430**, 287 (2006).

ACRONYMS AND ABBREVIATIONS

AC	autocorrelation
AF	antiferromagnet, antiferromagnetic
AFM	atomic-force microscopy
ALS	Advanced Light Source
AP	approved program
APS	Advanced Photon Source
ARPES	angle-resolved photoelectron spectroscopy
AT	accelerator toolbox
ATP	adenosine triphosphate
BES	Basic Energy Sciences, DOE Office of
BESSY	Berliner Elektronenspeicherring-Gesellschaft für Synchrotronstrahlung
BCSB	Berkeley Center for Structural Biology
BNCO	$[(Ba_{0.9}Nd_{0.1})CuO_{2+\delta}]_2$
BZ	Brillouin zone
CCD	charge-coupled device
CCO	$[CaCuO_2]_2$
CNT	carbon nanotube
CR	charge reservoir
CSD	Chemical Sciences Division, Berkeley Lab
CSR	coherent synchrotron radiation
CT	charge transfer
CXRO	Center for X-Ray Optics
DFT	density functional theory
DMS	diluted magnetic semiconductor
DNA	deoxyribonucleic acid
DOE	Department of Energy
DOS	density of states
dsRNA	double-stranded RNA
DSSR	double split-ring resonator
EGFR	epidermal growth factor receptor
EM	electron microscope
EPU	elliptically polarizing undulator
ESG	Experimental Systems Group
ESRF	European Synchrotron Radiation Facility
EUV	extreme ultraviolet
EXAFS	extended x-ray absorption fine structure
F8BT	poly(9,9′-dioctylfluorene-*co*-benzothiadiazole)
FEL	free-electron laser
FET	field-effect transistor
FM	ferromagnet, ferromagnetic
FT	Fourier transform
FTIR	Fourier-transform infrared
FWHM	full width at half maximum
FY	fiscal year
GMR	giant magnetoresistance
HA	hemagglutinin
HARP	high-resolution angle-resolved photoemission
HF	high-flux (grating)
HOPG	highly ordered pyrolytic graphite
HR	high-resolution (grating)
HTH	helix-turn-helix (motif)
HTSC	high-temperature superconductor
IL	infinite layer
IR	infrared
JPL	Jet Propulsion Laboratory
K-B	Kirkpatrick-Baez
LBCO	$La_{2-x}Ba_xCuO_4$
LCLS	Linac Coherent Light Source
LDRD	Laboratory Directed Research and Development
LED	light-emitting diode
LEED	low-energy electron diffraction
LER	line-edge roughness
LOCO	local control
LSCO	$(La_{2-x}Sr_x)CuO_4$
LTP	long trace profiler
LWR	line-width roughness
MBE	molecular-beam epitaxy
MBI	microbunching instability
MCP	multichannel plate
MERLIN	meV-resolution beamline
miRNA	MicroRNA
MML	Matlab Middle Layer
MOF	metal-organic framework
MRAM	magnetic random-access memory
mRNA	messenger RNA
MSD	Materials Sciences Division, Berkeley Lab
NASA	National Aeronautics and Space Administration
NCEM	National Center for Electron Microscopy
NCXT	National Center for X-Ray Tomography

NEXAFS	near-edge x-ray absorption fine-structure spectroscopy
NI	National Instruments
NIH	National Institutes of Health
NIST	National Institute of Standards and Technology
NSF	National Science Foundation
NSLS	National Synchrotron Light Source
NTP	nucleoside triphosphate
OD	outer diameter
OML	Optical Metrology Laboratory
OSC	organic solar cell
PDOS	partial density of states
PE	polyethylene
PEEM	photoemission electron microscopy
PET	preliminary examination team
PGM	plane grating monochromator
PI	polyimide
PIE	photoionization efficiency
PRT	participating research team
PSS	personnel safety shutter
PTB	Physikalisch-Technische Bundesanstalt
QCM	quartz crystal microbalance
QEPU	quasi-periodic elliptically polarizing undulator
RAM	random-access memory
rf	radiofrequency
RISC	RNA-induced silencing complex
RIXS	resonant inelastic x-ray scattering
rms	root-mean-square
RNA	ribonucleic acid
SAXS	small-angle x-ray scattering
SEM	scanning electron microscope/microscopy
SGM	spherical grating monochromator
siRNA	short interfering RNA
SL	superlattice
SLAC	Stanford Linear Accelerator Center
SNUG	Synchrotron and Neutron Users' Group
SPLEEM	spin-polarized low-energy electron microscope
SPring-8	Super Photon ring, 8 GeV (Large-Scale Synchrotron Radiation Facility, Japan)
SPS	Siam Photon Source
SRC	Synchrotron Radiation Center, University of Wisconsin
ssDNA	single-stranded DNA
SSG	Scientific Support Group
SSRF	Shanghai Synchrotron Radiation Facility
SSRL	Stanford Synchrotron Radiation Laboratory
STM	scanning tunneling microscopy
STXM	scanning transmission x-ray microscope/microscopy
SWCN	single-walled (carbon) nanotubes
SXF	soft x-ray fluorescence
TFB	poly(9,9-dioctylfluorene-*co*-*N*-(4-butylphenyl)diphenylamine)
TM	transition metal
TOF	time of flight
tRNA	transfer RNA
UC	University of California
UEC	Users' Executive Committee
UHV	ultrahigh vacuum
U.K.	United Kingdom
U.S.	United States
VLS	variable line spacing
VUV	vacuum ultraviolet
WAXS	wide-angle x-ray scattering
XAFS	x-ray absorption fine structure
XANES	x-ray absorption near-edge spectroscopy
XAS	x-ray absorption spectra/spectroscopy
XES	x-ray emission spectra/spectroscopy
XMCD	x-ray magnetic circular dichroism
XMLD	x-ray magnetic linear dichroism
XPS	x-ray photoelectron spectroscopy
ZRS	Zhang-Rice singlet

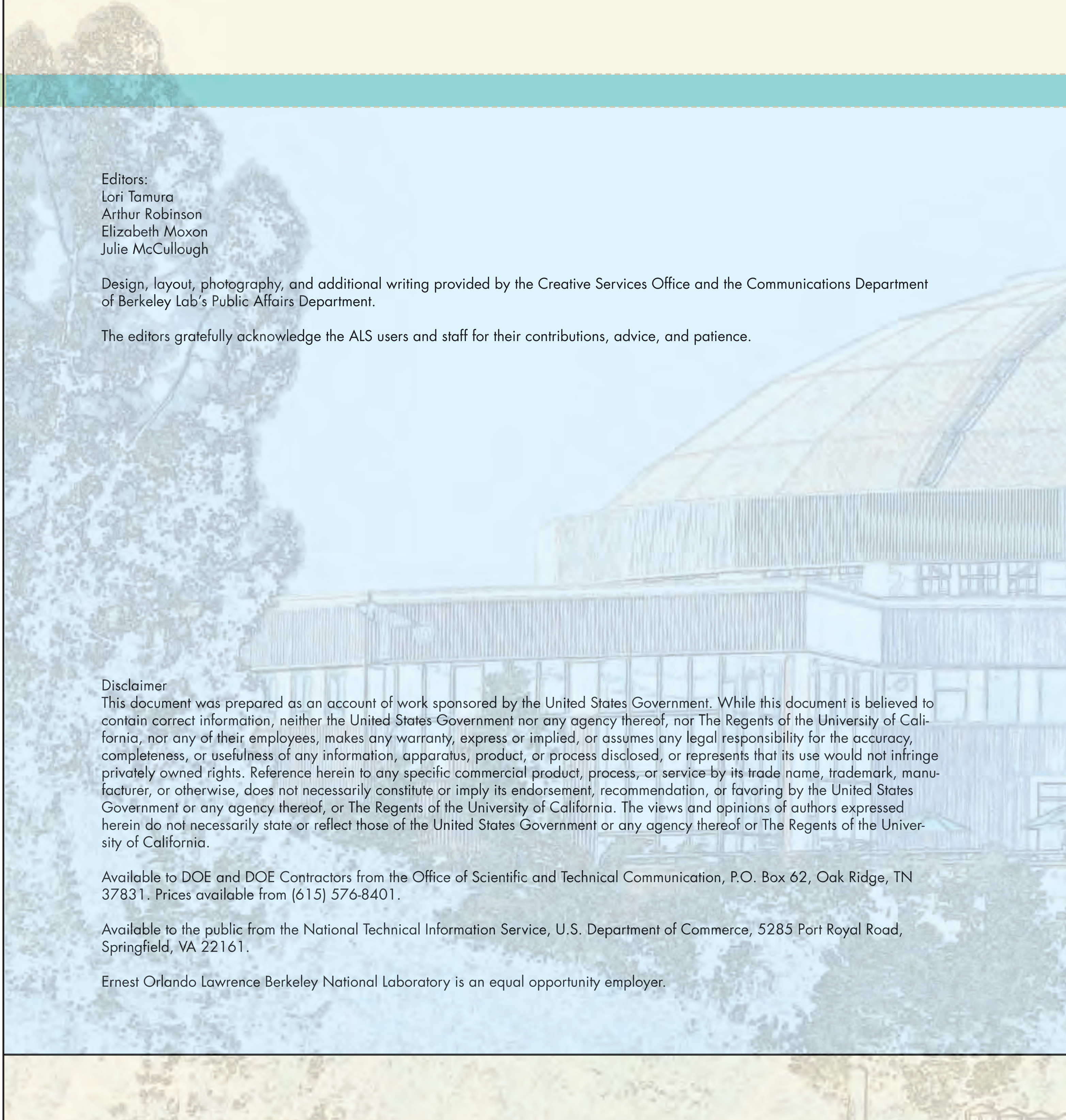

Editors:
Lori Tamura
Arthur Robinson
Elizabeth Moxon
Julie McCullough

Design, layout, photography, and additional writing provided by the Creative Services Office and the Communications Department of Berkeley Lab's Public Affairs Department.

The editors gratefully acknowledge the ALS users and staff for their contributions, advice, and patience.

Available to DOE and DOE Contractors from the Office of Scientific and Technical Communication, P.O. Box 62, Oak Ridge, TN 37831. Prices available from (615) 576-8401.

Available to the public from the National Technical Information Service, U.S. Department of Commerce, 5285 Port Royal Road, Springfield, VA 22161.

FOR MORE INFORMATION

For information about using the ALS, contact

Jeffrey Troutman
User Services Administrator
Advanced Light Source
Lawrence Berkeley National Laboratory
MS 6R2100
Berkeley, CA 94720-8226
Tel: (510) 495-2001
Fax: (510) 486-4773
Email: alsuser@lbl.gov

ALS home page
http://www-als.lbl.gov/

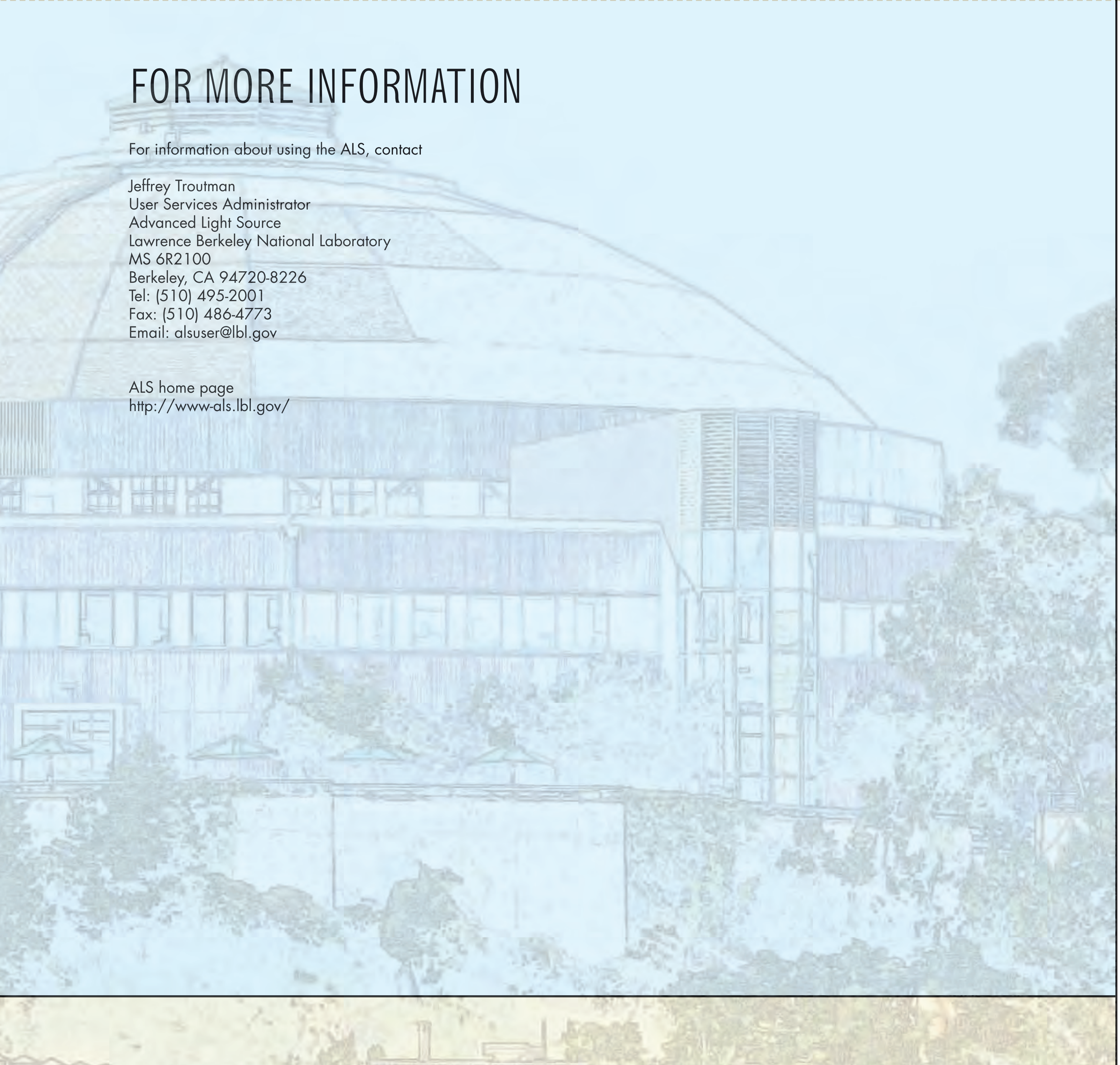

Supported by the U.S. Department of Energy under Contract No. DE-AC02-05CH11231

Advanced Light Source
Ernest Orlando Lawrence Berkeley National Laboratory
University of California
Berkeley, California 94720